Report
R-17-22
December 2019

Modelling of radionuclide retention by matrix diffusion in a layered rock model

James Crawford
Martin Löfgren

SVENSK KÄRNBRÄNSLEHANTERING AB

SWEDISH NUCLEAR FUEL
AND WASTE MANAGEMENT CO

Box 3091, SE-169 03 Solna
Phone +46 8 459 84 00
skb.se

SVENSK KÄRNBRÄNSLEHANTERING

ISSN 1402-3091
SKB R-17-22
ID 1619044
December 2019

Modelling of radionuclide retention by matrix diffusion in a layered rock model

James Crawford, Kemakta Konsult AB

Martin Löfgren, Niressa AB

Keywords: Radionuclide transport, Matrix diffusion, Geosphere retardation model.

Abstract

This report describes calculations that have been made in support of PSAR for the final repository for spent nuclear fuel at Forsmark investigating the impact of more complex representations of the rock matrix and their consequences for far-field radiotoxicity flux. The work is, in part, a continuation of the earlier work by Löfgren and Crawford (2014) in response to a request for supplementary information by SSM (2013a). In the present work, the impact of material property heterogeneity was studied by considering a multilayer rock matrix conceptualisation and several fracture classes representing different rock matrix microstructural properties distributed in (what we believe to be) a more realistic fashion along migration flowpaths leading from a KBS-3 type repository to the surface.

The modelling results suggest that the simplified, homogeneous rock matrix representation based on material properties of unaltered rock used in SR-Site was cautious and mostly results in overestimation of radiological risks. Additional theoretical analyses were also performed to attribute the depth of rock matrix associated with the bulk of the retardation effects experienced by migrating radionuclides where the central corrosion case of SR-Site was considered as a reference scenario. We have also derived a closed-form, continuous probability density function describing the depth of rock matrix associated with transport retardation for transient breakthrough of migrating radionuclides along a flowpath. To the authors' best knowledge such an analysis has not been previously described in the scientific literature.

For the hydrodynamic conditions associated with the SR-Site reference case, the bulk of the retardation can be largely tied to the first few cm to perhaps a dm of the rock matrix for single decaying radionuclides. Further detailed calculations considering the $4n+2$ decay chain suggest a similar depth of retardation attribution for actinide chains when simultaneously accounting for ingrowth of daughter nuclides along a flowpath.

Sammanfattning

Denna rapport beskriver beräkningar som har utförts till stöd för PSAR kärnbränsleförvaret i vilka man har utrett inverkan av mer komplexa representationer av bergsmatrisen och följdeffekterna för radionuklidtransport i geosfären. Rapporten är delvis en fortsättning av det tidigare arbetet utfört av Löfgren och Crawford (2014) som svar på SSM:s begäran av kompletterande information (SSM 2013a). I denna rapport har inverkan av materialegenskapernas heterogenitet studerats genom beaktande av en multilagermatris och flera sprickklasser fördelade längs flödesbanor i geosfären på ett sätt som författarna anser realistiskt för ett slutförvar av typen KBS-3.

Modelleringsresultaten visar att den förenklade homogena matrisbeskrivningen som användes i SR-Site är försiktig och mestadels resulterar i en överskattning av den radiologiska riskbilden.

Ytterligare teoretiska analyser har också genomförts för att uppskatta matrisdjupet associerat med huvuddelen av retardationen längs flödesbanan där det centrala korrosionsfallet i SR-Site utgjorde ett referensfall. En kontinuerlig sannolikhetsfördelning som beskriver djupet av matrisen kopplad till olika andelar av det erhållna genombrottet av transporterade radionuklider längs en flödesbana har även utvecklats. Enligt vad författarna känner till har detta inte redovisats i den öppna litteraturen tidigare.

För de hydrodynamiska förhållandena knutna till det centrala korrosionsfallet i SR-Site kan huvuddelen av retardationen knytas till de första centimetrarna, möjligtvis någon decimeter, in i bergsmatrisen för radionuklider som inte ingår i kedjor. Ytterligare detaljerade beräkningar för aktinidkedjan $4n+2$ pekar på liknande matrisdjup kopplade till retardationen där det tas hänsyn till inväxt av dotternuklider längs flödesbanan.

Contents

1 Introduction

1.1 General background

It is well-recognised that the host rock surrounding a geological repository for spent nuclear fuel (or other kinds of radioactive waste) retards the transport of radionuclides that escape from the engineered barrier. Radionuclides that migrate over any significant distance in the host rock will generally be carried by water flowing in discrete fractures. Water-rock interactions occur at the surfaces of these fractures. Since the rock is porous, dissolved radionuclides in the fracture water can migrate by diffusion into the fracture-adjacent rock under the influence of a concentration gradient. As the porewater of the adjacent rock is effectively stagnant and since many radionuclides adsorb to mineral surfaces, this lowers the overall transport rate of radionuclides towards the biosphere.

The above mechanistic description has been invoked within the safety assessment SR-Site for the planned Swedish KBS-3 repository for spent nuclear fuel (SKB 2010b). It has also been used in a long line of earlier, and more recent, peer-reviewed safety assessments made by different organisations around the world (see e.g. RETROCK 2005, Posiva 2012, and references therein). On this basis, it would seem safe to claim that the general conceptualisation of radionuclide retardation in the host rock as outlined above is scientifically non-controversial.

The host rock, however, is not a homogeneous medium in which retardation occurs uniformly. Typically, a dual-porosity model is assumed in safety assessment modelling. Water conducting fractures then constitute one type of porosity and the microporosity of the rock matrix constitutes the other. In many previous safety assessments, the rock matrix surrounding flowpaths has been assumed to be homogeneous whereas in other, more recent, cases it has been assumed to take the form of a layered structure (e.g. Posiva 2012) where each layer constitutes a homogeneous volume with uniform retardation properties. In SR-Site, the first of these approaches was adopted, i.e. that the flowpaths are surrounded by homogeneous rock (SKB 2010a). It should be noted that this does not imply that a homogeneous representation of the surrounding rock was considered more realistic than a heterogeneous one. On the contrary, site-specific observations strongly support the notion that fracture adjacent rock is heterogeneous (e.g. Byegård et al. 2008). For the purposes of SR-Site, however, disregarding the rock heterogeneity was judged to be pessimistic and consequently a valid assumption when estimating radiological risks.

This report aims to investigate the radiological consequences of the presumption that the surrounding rock is not homogeneous but layered. The layers considered are 1) fracture coatings, 2) an alteration rim of limited depth in the rock matrix, and 3) undisturbed rock. This is achieved by using a layered rock matrix model where all layers have individualised, although uniform, retardation properties. It is also assumed that the same layered structure does not persist along the entire flowpath, but that the flowpath encounters rock volumes featuring differing retardation properties. This analysis is based on the most important deterministic scenario of radionuclide release in SR-Site as a reference case for comparison. The analysis is also informed by rock retardation properties that have been studied within the SKB site investigation programme, at the Äspö Hard Rock Laboratory, and by other organisations.

In the present work, we have restricted ourselves to only improve the representation of the fracture adjacent rock by using a layered rock model. We also use a source term and groundwater flow field that corresponds to that previously used in the safety assessment SR-Site. Furthermore, radionuclide decay including chains and ingrowth is also included in our calculations. Although the introduction of such a complex representation of rock matrix microstructure in this work is challenging due to our inability to quantify key parameters, we have approached the task as a “Fermi”-type problem (e.g. Lan 2002). We make a serious attempt to quantify the different rock layers regarding their distribution, thickness, porosity and effective diffusivity, although lack of site-specific data sometimes forces us to use rough estimates in our quantifications. Furthermore, we assign different fracture classes for various rock alteration layer parameterisations and distribute these in different ways along the flowpaths. In a series of sensitivity studies, we attempt to bound the impact of the varied retardation properties on the radionuclide flux to the biosphere. An additional sensitivity study is made that includes variation in the sorptive properties of the rock layers. Here, we uniformly increase the sorption partitioning coefficients of all sorbing species by one order of magnitude for the different alteration layers.

In a parallel, international collaborative project conducted by several research groups, even more detailed representations of the heterogeneous nature of the flowpath adjacent rock are being modelled. This project is the called *"Task 9: Increasing the Realism in Solute Transport Modelling – Modelling the Field Experiments of Repro and LTDE-SD"* (Soler et al. 2019) and is being conducted by the SKB Task Force (www.skb.se/taskforce) on Modelling of Groundwater Flow and Transport of Solutes. In this parallel project, attempts are being made to go beyond the simplified homogeneous layered approach of the present work to obtain even better realism for radionuclide transport modelling.

Resulting from these efforts, the layered rock model as it is conceptualised in this work may need to be refined in future safety assessment. It may also become apparent that the homogeneous rock representation gives results that are sufficiently fit for purpose that more complex modelling conceptualisations are not necessary. It must be remembered, however, that the adequacy of simplifications made in the representation of the true system is often judged in reference to a specific geological repository concept, hydrogeological boundary conditions, and particular requirements of safety assessment.

1.2 Requests for complementary information by SSM

In 2011, the safety assessment SR-Site was submitted to the regulatory authorities as part of an application to build a KBS-3 type repository at Forsmark. In 2013, the Swedish Radiation Safety Authority (SSM) requested supplementary information concerning, among other things, radionuclide transport calculations and retention properties of the rock. SKB responded to these requests and as part of the response, the following document, authored by Löfgren and Crawford (2014), was sent to SSM.

Modelling of radionuclide retention by matrix diffusion in a layered rock model – response to the request by SSM for supplementary information on retention of radionuclides (SSM2011-2426-110), items 4 and 6.

This is a public document that may be downloaded from the website of SSM. This present report builds on that document, although many modifications and improvements have been made. Items tackled in this report that were previously brought up by SSM in the requests (SSM 2013a, b), are (paraphrased in English):

- SSM considers that SKB should produce an analysis of the effect of mineral alterations and fracture-filling minerals in the rock on matrix diffusion and retardation of radionuclides. The analysis should highlight both the processes and characteristics that could mean improved or deteriorated retardation relative to the base case where the undisturbed rock is considered.[1]
- SSM considers that SKB should analyse the importance of reasonably probable variability of the rock diffusivity and its impact on radionuclide transport.[2]
- SKB has made a deterministic calculation for the central corrosion case and the result is shown in Figure 4-3 in SKB (2010a), but SSM believes that SKB has not fully taken into account the pulse release due to the IRF (Instant release fraction) in this calculation. In light of the above, SSM requests that SKB complement the existing calculations with deterministic calculations that include all pulse releases from the IRF (not in a separate analysis) to show the effects of risk spreading over future generations in an integrated system, that is a system that includes release from the near-field, transport through the far field, and input to the biosphere model. [3]

[1] "SSM anser att SKB bör ta fram en analys av hur mineral-omvandlingar och sprickfyllnadsmineral i berget påverkar matrisdiffusion och retardation av radionuklider. Analysen bör belysa både processer och egenskaper som kan innebära förbättrad respektive försämrad retardation i förhållande till grundfallet där det opåverkade berget beaktas."

[2] "SSM anser att SKB bör analysera betydelsen av rimlig sannolik variabilitet av bergets diffusivitet och dess inverkan på radionuklidtransport."

[3] "SKB har också gjort en deterministisk beräkning för det centrala korrosionsfallet och resultatet visas i figur 4-3 I TR-10-50, men SSM anser att SKB inte helt tagit hänsyn till pulsutsläpp på grund av IRF i denna beräkning. Mot bakgrund av ovanstående önskar SSM att SKB kompletterar gällande beräkningar med deterministiska beräkningar inklusive alla IRF pulsutsläpp (inte separat analys) för att visa på effekterna av riskspridning mellan framtida generationer i ett integrerat system, dvs ett system som inkluderar utsläpp från närområdet, transporter genom fjärrområdet och input till biosfärsmodellen."

In SSM (2013a), further reasoning behind the requested items is provided which was used as a guideline when formulating the initial response to the request. The reasoning was initially scrutinised in the response by Löfgren and Crawford (2014) that also relates to the underlying strategy, and setup of, our layered rock model to answer specific items in the request. An important consequence that relates to the wording in the request is that when quantifying our layered rock model, retardation by matrix diffusion has been our main concern. For this reason, we have focused on providing realistic values for the effective diffusivity, porosity, and thickness of the different layers of the rock as well as the distribution of these heterogeneous properties along the flowpaths. This has been done despite the paucity of site-specific information on matrix diffusion parameters for the fracture coatings and rock directly adjacent to flowpaths. To deal with this substantial uncertainty as well as to respond to some of SSM's concerns in SSM (2013a), sensitivity studies in the form of a small number of variation cases have been made.

No additional effort has been made in assigning reasonable sorption properties for the individual layers and all layers are assumed to have the same sorption properties as assigned to the undisturbed rock in SR-Site. The effect of increasing the sorption partitioning coefficient of the layers immediately adjacent to fracture surfaces (the fracture coating and alteration rim) is investigated in a sensitivity study, although the increased values used are only qualitative and based largely on empirical reasoning. This report also includes a replication of the central corrosion case of SR-Site with integration of the pulse release of the IRF in the radionuclide transport modelling chain. This is a new development relative to the initial modelling presented in Löfgren and Crawford (2014). We also model the full suite of relevant radionuclides in the present report, as suggested by SSM (SSM 2013b).

1.3 Objectives and outline

As previously stated, this report investigates the impact of using a layered rock model on radionuclide transport in the far-field. This is done in the framework of the deterministic main scenario of SR-Site which includes the failure of copper canisters due to corrosion. The outline of this report, and the objectives of the different chapters, is as follows:

Chapter 2 provides a general description of the computational codes FARF31 and MARFA, and of their abilities and limitations. The aim is to give the reader a general background on the codes. Specific issues related to these codes that we have been forced to tackle are also discussed in this chapter.

Chapter 3 presents the revisited SR-Site central calculation case that was modelled using FARF31 in SR-Site; the "central corrosion variant" of the "canister failure due to corrosion" scenario. The reference SR-Site results are first reproduced with the computational codes FARF31 and MARFA. The main exception is that we have treated the IRF source term differently to the way it was handled in SR-Site. This is done for the flowpath intersecting the position of the first failed canister, using the same flow-related properties as in SR-Site. The rock surrounding the flowpath is assumed to be homogeneous and we use the same retardation properties as in SR-Site. All 37 radionuclides included in this base case scenario are modelled and account is taken of radionuclide decay including chains and ingrowth of progeny nuclides. Our source term is the same as in SR-Site, even though we treat the IRF differently, and we use the same solubility limits and landscape dose conversion factors previously used in SR-Site. The main objective of this exercise, however, is not to show that SR-Site results are reproducible. Instead, we set up a reference baseline case for our FARF31 and MARFA model which ensures that the effect of using a layered rock model can be properly evaluated from the perspective of relevant safety assessment results for a KBS-3 repository. The same applies when we evaluate the sensitivity of the model, by varying different retention properties of the layers.

Chapter 4 presents four hypothetical fracture classes that are used to represent different rock volumes that the flowpaths might intersect on their way from the near-field to the biosphere. The fracture classes are broadly based on the general knowledge on retention properties in fractured crystalline rock surrounding a KBS-3 type repository and risk calculations for such repositories. The intention is that these fracture classes should be commonly observed, but also differentiated in terms of retention properties, where these have been characterised. Each fracture class comprises a sequence of, at most, three adjacent layers: the fracture coating, alteration rim, and undisturbed rock matrix. Due to a lack of relevant observational data, the distribution of fracture classes is mainly based on the well-known distribution of fracture minerals, and only to a minor extent based on differences in the alteration rim or underlying rock matrix.

Chapter 5 describes the task of assigning matrix diffusion properties to each layer of the various fracture classes. Given the uncertainty in underlying data, only approximately rounded values are used for some parameters. We have, however, made an effort to base these parameter values on best estimates, taking a large set of experimental data and observations into account. The matrix diffusion properties include the porosity; effective diffusivity, and layer thickness. Furthermore, the occurrence or absence of the fracture coatings has been used to assign fracture classes to portions of the flowpath that intersect different notional rock volumes. In this analysis, we have not assigned individual sorption partitioning coefficients to the different layers but instead assume uniform properties, as assumed in SR-Site. This is a weakness of the present report that we recommend be revisited in future work.

Chapter 6 presents the results from a number of case studies made using FARF31 and MARFA, where we have assumed that the entire flowpath is represented by a single fracture class, alternatively by the homogeneous rock matrix as in SR-Site.

Chapter 7 presents the results from what we hypothesise to be the most realistic rock model, where we assume that the flowpath intersects all four fracture classes. This can be regarded as the central calculation case for modelled rock heterogeneity in this report with its inherent limitations relating to the handling of sorption.

Chapter 8 presents the sensitivity case studies including: impact of a limited maximum penetration depth in the single layer case; reduced effective diffusivity in the single layer case; an analysis of the differences between the different case studies already presented in Chapter 6; impact of uniformly increasing sorptivity in fracture adjacent layers for the multilayer case; as well as a variation case where we test whether changing the order of the intersected fracture classes has an impact on the results.

Chapter 9 presents a detailed discussion of the results obtained in previous chapters with a focus on effective depths of penetration and attribution of retardation in the rock matrix for both the single-layer and multilayer rock calculation scenarios.

Chapter 10 provides conclusions drawn from this work. Importantly, we discuss the consequences of using a layered rock model, as compared to the homogeneous rock model used in SR-Site. We also discuss if the new findings warrant a re-evaluation of the annual effective doses presented in SR-Site or modifications of the rock representation in future safety assessments. Presently, the detailed site investigations for the KBS-3 repository in Forsmark are being planned, although these plans are still at an early stage. In the light of our findings, we give recommendations on whether to continue focusing on the retardation properties of undisturbed rock, or if more attention should be directed towards properties of fracture adjacent rock including fracture coatings and alteration rims.

2 Description of FAR31 and MARFA

In SR-Site, the bulk of the far-field radionuclide transport modelling was performed by the computational code FARF31 (SKB 2010a). For some special cases, the MARFA code v3.2.2 (Painter and Mancillas 2009) was used as a complement to FARF31. This was done for probabilistic cases and for variation analyses, some of which involved special features such as correlations between stochastically assigned K_d values, colloid transport, varying climatic conditions (i.e. temporally variable flow-related transport properties), and cases involving different boundary condition assumptions. Below follows a short description of the codes with focus on giving the uninitiated reader an insight into fundamental differences between the codes, how they were used in SR-Site and in the new modelling, and whether they introduce significant artefacts in the modelling. For both codes, a near-field boundary condition must be supplied by the user. In SR-Site, the code COMP23 (Vahlund and Hermansson 2006) was used to calculate the near-field boundary condition and its use is described more fully in SKB (2010a).

2.1 FARF31

The FARF31 program (Norman and Kjellbert 1990, Lindgren et al. 2002, Elert et al. 2004) is a code that has been used for radionuclide geosphere migration calculations in SR-Site (SKB 2010a) as well as in the earlier SKB safety assessments SR-97 (Lindgren and Lindström 1999) and SR-Can (SKB 2006). It is a simple model based on a Laplace space solution of the one-dimensional advection-dispersion equation in a hypothetical streamtube with one-dimensional diffusion into a homogeneous secondary porosity in a direction orthogonal to the fluid flow. Chain decay and in-growth are included in the model and it is formulated in terms of the advective travel time in the longitudinal direction as the independent variable. The Laplace space solution for a unit response transfer function is numerically inverted to the time domain and the breakthrough curve for transported radionuclides is then obtained by convolution of the response function with the input source term. A detailed description of the algorithm is given in Norman and Kjellbert (1990).

Although FARF31 was originally developed for continuum representation of water flow through the rock, it is also compatible with a discrete fracture network (DFN) representation where flow in individual fractures is represented explicitly. The variables calculated in the DFN-based groundwater flow models are the advective travel time (t_w) and hydrodynamic transport resistance (F-factor) along flowpaths which are used as inputs to the code together with the Péclet number for hydrodynamic dispersion.

The current release version of the standalone FARF31 code is subject to a number of limitations. Chief among these is that simulations are limited to a maximum of 48 radionuclides consisting of no more than 32 distinct elements and no individual chain is permitted to have more than 8 members. Moreover, the code is not capable of simulating converging or diverging radionuclide chains. In most cases, diverging chains may be considered trivial since they typically involve very short-lived nuclides that can be assumed to be in approximate secular equilibrium in their respective decay chains. Converging chains cannot be neglected, however, since they can contribute in a non-negligible fashion to the ingrowth of daughter nuclides and therefore need to be properly accounted for. In previous safety assessments including SR-Site this problem was circumvented in an approximate fashion by directly adding the inventory of the (often relatively fast decaying) parent nuclide to the inventory of the daughter to avoid the necessity to consider the converging chain explicitly.

Fortunately, many of the code restrictions outlined above for FARF31 can be circumvented by smart pre- and post-processing with the aid of a suitable script interface. In practice this is achieved by splitting the problem up into a number of sub-problems and then recombining and summing the results in post-processing. In the SR-Site case study, however, there were 37 radionuclides consisting of 25 unique elements and no explicitly modelled converging chains. This set of nuclides comes in just under the technical limit of what is possible to simulate using the release version of FARF31.

For this project, we have made use of a script program (NUDEC-Farf31) written in the Matlab scripting language that calls FARF31 as an external program with automatic input and output management via shell commands in a scratch directory (See Appendix A). Using the release version of the stand-

alone FARF31 code to make numerical calculations was considered desirable from the point of view of the fast execution speed of the native program relative to what could be achieved using internally scripted Matlab functions and also to avoid QA issues related to the creation of a purpose written code in Matlab for pre-existing functionality in FARF31. The main advantage of the scripting code in the context of the present project was to efficiently combine source terms related to the instant release fraction and corrosion/dissolution release fractions which were handled separately in SR-Site and were part of the request for additional information from SSM as described in Section 1.2.

2.2 MARFA

The MARFA code (Painter and Mancillas 2009) is based on a completely different solution premise to FARF31 and uses a particle-based Monte Carlo method to simulate the transport of radionuclides in geomedia. The code can accommodate both continuum and DFN representations of flow with the rock in a similar fashion to FARF31 and the code was specifically designed to integrate with the safety assessment workflow used by SKB. Although pathlines can be simply defined internally in input files, the program can also accept pathline trajectories from the ConnectFlow code (Wood 2018) in the form of ConnectFlow ptv-files. The pathline trajectories represent transport pathways. MARFA then solves radionuclide transport along the pathways using a time-domain particle method. With this method, particles are advanced along a pathway using deterministic spatial displacements and random transit times for each step. The code has been shown to be computationally efficient and extremely robust. Limited and unlimited matrix diffusion, equilibrium sorption, longitudinal dispersion, decay, and in-growth are represented. MARFA supports full spatial variability for all pathway properties, decay chains of any length, and full temporal variability in radionuclide source strength. The code reports radionuclide release rates (breakthrough) at the pathway endpoints. A key difference between MARFA and FARF31 is that there is no restriction on the implementation of converging chains in MARFA unlike FARF31.

It is also possible to define parametric retention tables for uniform multilayer rock matrix structures as described in Section 1.1 which are then used by the program to calculate breakthrough curves. The retention tables for MARFA are calculated using a Mathematica script based on the Laplace space solution described by Cvetkovic (2010) for a multilayer, piecewise homogeneous rock matrix. The present version of the Mathematica package distributed with the MARFA program allows for the simulation of segmented flowpaths where the individual rock units can have up to three distinct microstructural layers featuring differing sorptive and diffusive properties (i.e. material properties varying perpendicular to the fracture plane). Each layer may be assigned individual porosity, K_d-values, effective diffusivity and thickness, although the parameters are constant within a layer.

One of the more significant differences between FARF31 and MARFA is that in calculations with multiple pathways, COMP23 and FARF31 must be executed once for each pathway, but MARFA needs to be run only once with parameters for all pathways as input. For multiple pathway simulations, MARFA calculates an ensemble mean breakthrough. In the radionuclide transport report for SR-Site (SKB 2010a) it is stated that "*The Monte Carlo nature of the algorithm ensures that an unbiased statistical estimate of the ensemble mean is obtained even when too few particles are used to accurately calculate breakthrough for each pathway realisation. Moreover, the statistical uncertainty in the ensemble mean is greatly reduced relative to that of individual realisations, a property of the method with significant advantages in terms of computational efficiency*".

Simulations made for this report have been made using MARFA v.3.2.4 (Painter and Mancillas 2013) which is an updated version relative to v3.2.2 which was used in SR-Site. Since this report was commissioned newer versions of MARFA have been developed which introduce additional functionality not previously available. This includes time dependent step changes in sorption properties and an altered source term sampling algorithm. The ability to assign different sorption properties, porosities, and effective diffusivities to different sections of rock along a flowpath renders MARFA a considerably more versatile modelling tool than FARF31, and it has therefore been chosen for the multilayer rock matrix modelling cases described in this report.

Since the MARFA code is based on a Monte Carlo time domain random walk (TDRW) particle method, the resolution with which the breakthrough curve can be reconstructed is dependent on the number of particles in the breakthrough. This is in turn dependent on the number of particles initially

released for a given nuclide and the decay and ingrowth of particles representing that radionuclide during its migration to the geosphere. It may be noted, however, that this is a feature of all particle-based methods and not uniquely associated with the TDRW method itself. The TDRW part of the code essentially calculates a long list of particle arrival times corresponding to different radionuclides. To generate a breakthrough curve for the radionuclide flux, the MARFA code performs postprocessing using a kernel density estimator (Silverman 1986) to generate a smooth curve. The curve smoothing process essentially uses a normal probability density function of variable bandwidth to represent each particle and the composite breakthrough curve is then equal to the sum of all probability density functions thus represented. A drawback of this method is that there can be considerable oscillation in parts of the solution where there are very few particles. This is typically at the leading and trailing edges of the residence time distribution, although it can also have a significant impact on short-lived radionuclides that are a long way down a decay chain, or terminal members of a decay chain.

It is recognised that the MARFA version used for this response is new and has not been verified by SKB to the same extent as FARF31 and MARFA v3.2.2 have been. This requires extra care in examining potential modelling artefacts. To some extent this has been addressed in the present work through our effort to replicate the central corrosion case from SR-Site, although the work does not fulfil the requirements of a formal verification. It should be noted, though, that this version of MARFA was also used in the recent Finnish safety case for a KBS-3 repository, TURVA-2012, which was a quality assured project (Posiva 2013).

3 Replication of SR-Site deterministic results using MARFA and FARF31

3.1 Replication of the central corrosion case from SR-Site

3.1.1 Choice of scenario

A conclusion of the SR-Site safety assessment was that only a limited number of canisters are deemed likely to fail during the one-million-year time frame of the safety assessment. When they do so, they are likely to fail due to copper corrosion resulting from advective flow conditions in the deposition hole (e.g. SKB 2011, Figure 12-18), although shearing of canisters could not be ruled out. Out of the scenarios with likelihood to occur, the "central corrosion variant" of the "canister failure due to corrosion" scenario gives the highest radiological risk in SR-Site (SKB 2010a). This scenario was briefly called the "corrosion scenario" in SKB (2010a) although we adopt the description "central corrosion case" in this this present report.

It should be noted, that the boundary condition is referred to throughout the documentation of the MARFA code (Painter and Mancillas 2013) as the "source term". In this report we use the expression interchangeably with "boundary condition", although note that the expression "source term" is also used in SKB reporting to refer to the raw inventory of radionuclides with which it might be confused. In the present context, "source term" is used exclusively to refer to the radionuclide flux versus time curve describing near-field release as calculated by COMP23.

3.1.2 Description of the source term in SR-Site

In SR-Site a great number of radionuclides needed to be taken into consideration. However, in a screening process that is detailed in SKB (2010a, Appendix D), only 45 of these radionuclides were selected for radionuclide release calculations. Of these, 23 radionuclides were fission and activation products and 22 were decay chain radionuclides (SKB 2010a, Section 3.1):

- Fission and activation products: Ag-108m, C-14, Cd-113m, Cl-36, Cs-135, Cs-137, Eu-152, H-3, Ho-166m, I-129, Mo-93, Nb-93m, Nb-94, Ni-59, Ni-63, Pd-107, Se-79, Sm-151, Sn-121m, Sn-126, Sr-90, Tc-99, and Zr-93.
- Decay chain radionuclides: Pu-240, U-236, Th-232, Cm-245, Am-241, Np-237, U-233, Th-229, Cm-246, Am-242m, Pu-242, Pu-238, U-238, U-234, Th-230, Ra-226, Pb-210, Am-243, Pu-239, U-235, Pa-231, and Ac-227.

Ten of these fission and activation products could be excluded in many scenarios, as they had such short half-lives that they would only be of importance in "what-if" scenarios including initial canister defects. The longest-lived nuclide excluded from calculations was Mo-93, with a half-life of 3 500 y (SKB 2010a, Table D-6). Two of the decay chain radionuclides, Am-242m and Pu-238, had such short half-lives that they should only be of importance in cases with fast release (i.e. high transport rates through the engineered barrier and geosphere).

In the corrosion scenario, eight of the 45 above listed radionuclides were disregarded. Six of them were short-lived fission and activation products (H-3, Mo-93, Nb-93m, Cd-113m, Sn-121m, Eu-152), and disregarded since the scenario did not include an initial canister defect. The radionuclides Ag-108m, Ho-166m, Ni-63, and Sm-151 were also deemed to have sufficiently short half-lives to be excluded from the scenario. Nevertheless, they were included as they were borderline cases with regard to total radiotoxicity versus half-life, shown in SKB (2010a, Figure D-1). In principle, the same applies to Mo-93, although the choice was made to exclude this nuclide since the total radiotoxicity at deposition was only just over the 0.1 Sv screening criterion and since it forms a converging chain with the much more long-lived nuclide Zr-93 which is present at a much higher radiotoxicity screening level (Mo-93 and Zr-93 both decay to the Nb-93m daughter nuclide). The two decay chain radionuclides Am-242m and Pu-238 were also excluded from the scenario due to their short half-lives as well as the fact that they constitute converging branches of the 4n+2 decay chain. The inventory of these nuclides was therefore added directly to the inventory of Th-234. This leaves in total 37 radionuclides that were included in the central corrosion case.

In SR-Site, radionuclide release within the canister was divided into three source term sub-types; the initial release fraction (IRF), the corrosion release fraction (CRF), and the fuel dissolution release fraction (called DRF in this present report). Radionuclide release by these source terms occur on different time scales. For the IRF, radionuclides were assumed to immediately dissolve in water intruding into the interior of the canister, and their release can be approximated as a Dirac pulse. The entire IRF inventory, with the exception of Tc-99, was assumed to reach the biosphere within a year after canister failure (see Section 3.1.3). For the CRF, radionuclides were assumed to be released at a constant rate due to corrosion over a defined time interval. In the deterministic modelling scenario, this was approximated by a Heaviside step function pulse with a duration of 1 000 years. For the DRF a constant fraction of the remaining inventory of the fuel matrix was released for each modelled time step during the entire time frame of the analysis. Since the inventory changes in the fuel matrix as result of decay, the release rates are not constant.

In SR-Site, calculations of the annual effective dose were made separately for 1) the combined source term of CRF and DRF; and 2) the IRF source term (with exception for Tc-99). The combined source term of the CRF and DRF entering the far-field is displayed in Figure 3-1, in terms of equivalent radiotoxicity flux (i.e. dose rates). It should be noted in Figure 3-1 (and in all subsequent figures in this report with annotated peak dose rates) that the numerical value for the total peak dose rate given in the legend is the total at the time of peak dose rather than the sum of the individual maxima in the legend.

It should be noted that in the corrosion scenario, the bentonite buffer has eroded to the point where it is pessimistically assumed to pose no resistance to radionuclide transport (SKB 2010a, Section 3.3). Furthermore, it is pessimistically assumed that the canister itself poses no transport resistance. Hence, there is a sharp decrease in the radionuclide release rate to the geosphere as the corrosion release ends at 1 000 years. The derivation of the source term, exiting the near field and entering the far field, is further discussed in SKB (2010a).

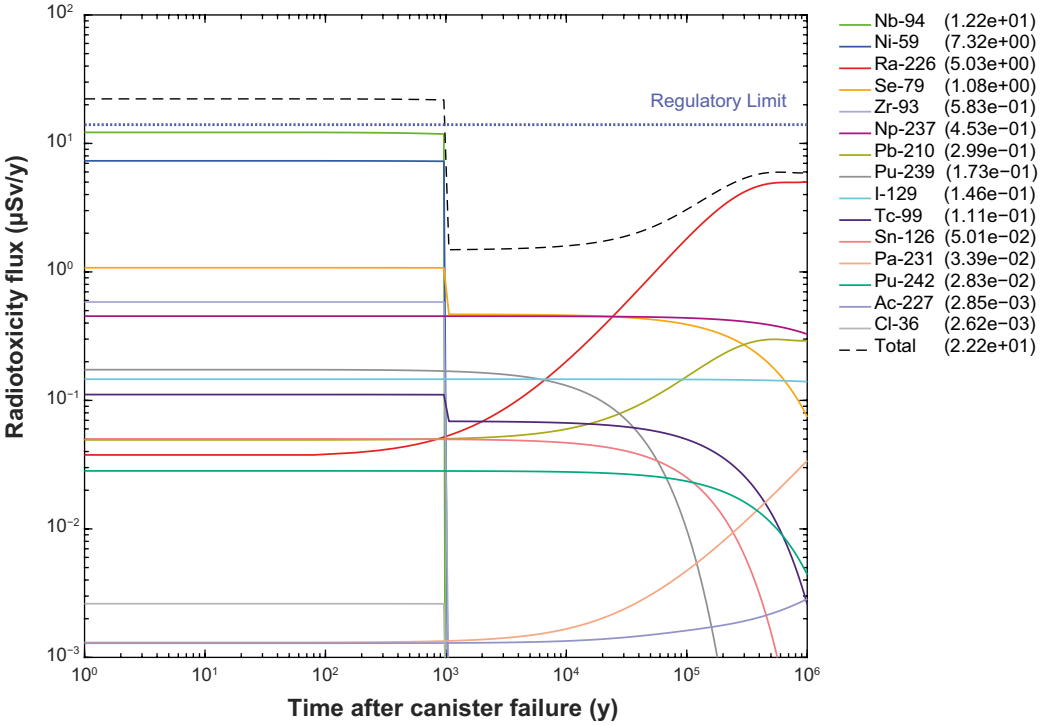

Figure 3-1. *Combined radionuclide source term of the CRF and DRF entering the far field, expressed as the annual effective dose rate in µSv/y. The legend is sorted by peak dose in the one-million-year time scale of the safety assessment where the peak dose rate is given in parentheses (also µSv/y). This plot is a replica of SKB (2010a, Figure 4-2), although the time on the x-axis is in relation to canister failure, and not repository closure in order to show more detail. Only those radionuclides contributing more than 0.1 % of the total radiotoxicity are plotted.*

3.1.3 Simplifications made for the IRF in SR-Site

For all IRF radionuclides, except for Tc-99, no modelling of retention in the far-field was performed, which would otherwise lead to pulse spreading and reduction of peak dose rates. Instead, it was assumed that the pulse comprising the entire IRF inventory would reach the biosphere within the timeframe of a year, thus contributing to the annual effective dose for that single year. This calculation approach gives a short term, high radioelement flux to the biosphere; a situation for which the basic landscape dose conversion factors (LDF's) were not strictly applicable. For this reason, an additional set of LDF's were calculated for pulse release, called the pulse LDF's (see Section 3.1.9). The IRF inventory was pessimistically set to correspond to that existing at 100 000 years for all canisters. This was done irrespective of the estimated time of canister failure, which in all cases occurred after 100 000 years.

The Tc-99 component of the IRF was given special treatment, since under reducing conditions Tc(IV) sorbs strongly to rock and its pulse will be released to the biosphere over an extended time period. Therefore, the standard LDF can be used when calculating its annual effective dose. The transport of the Tc-99 inventory of the IRF was modelled using the far-field model FARF31, but as "tagged" Tc-99. This tagged Tc-99 would have been apparent in the figures presenting the release of the CRF and DRF in the corrosion scenario (cf. SKB 2010a, Figure 4-3) if its annual effective dose would have exceeded 0.001 μSv/y, which was not the case.

3.1.4 Description of the source term in the new modelling

In the updated modelling for this report we have deviated from the SR-Site approach with respect to the treatment of the IRF, both when using FARF31 and MARFA. In SR-Site the impact of geosphere retardation on the IRF pulse was ignored, for all nuclides save for Tc-99. This approach is not suitable for this report, as its primary role is to investigate the geosphere retardation with special focus on the first few centimetres of flowpath adjacent rock. This impact will be the greatest for short pulse releases.

In our modelling with FARF31, we have separated the IRF and the combined CRF/DRF source terms in two separate runs with recombination as a post-processing step assuming linear superposition of breakthrough curves. In contrast with the SR-Site approach, however, all IRF nuclides are simulated using FARF31, thus allowing for retention and pulse spreading in the far field. We have assumed an IRF pulse as a Heaviside step function (rectangular pulse) that releases the entire IRF inventory to the geosphere at a constant rate over a period of one year. The entire inventory of the IRF (Bq/canister) should correspond to the Peak annual dose (Sv) as given in SKB (2010a, Table 4-4) divided by the pulse LRF (Sv/Bq) given in SKB (2010a, Table 3-7). Unfortunately, we have not been able to exactly replicate the numerical values in SKB (2010a, Table 4-4) so have re-calculated the values from raw data. To do so we took the initial average canister inventory for all canister types to be stored in the repository from Table C-5 of SKB (2010e), multiplied by the instant release fraction specified in Table 3-4 of SKB (2010a) and corrected for decay at 100 ky relative to the initial inventory (reference year 2045 CE). Details of the calculation are given in Table 3-1.

Table 3-1. Calculation of IRF inventory at 100 ky from specified IRF (SKB 2010a) and initial average canister inventory (SKB 2010e). The equivalent radiotoxicity is given in μSv for LDF pulse dose conversion factors with the exception of Tc-99 which is calculated assuming the Basic LDF dose conversion factor defined in SKB (2010a).

Nuclide	IRF	Inventory (total) t = 0 y	Inventory (IRF) t = 0 y	Inventory (IRF) t = 100 ky	LDF	Equivalent Radiotoxicity
	-	Bq (tot)	Bq (IRF)	Bq (IRF)	Sv/Bq	μSv
I-129	2.9×10^{-2}	2.49×10^{9}	7.21×10^{7}	7.18×10^{7}	5.56×10^{-14}	4.0
Se-79	4.2×10^{-3}	6.53×10^{9}	2.74×10^{7}	2.28×10^{7}	9.70×10^{-14}	2.2
Cs-135	2.9×10^{-2}	4.20×10^{10}	1.22×10^{9}	1.18×10^{9}	1.84×10^{-16}	0.22
Cl-36	8.6×10^{-2}	4.25×10^{8}	3.65×10^{7}	2.90×10^{7}	4.29×10^{-15}	0.12
Nb-94	1.8×10^{-2}	1.60×10^{11}	2.88×10^{9}	9.46×10^{7}	3.18×10^{-16}	0.03
Sn-126	3.0×10^{-4}	4.92×10^{10}	1.48×10^{7}	7.37×10^{6}	2.31×10^{-15}	0.017
Ni-59	1.2×10^{-2}	3.02×10^{11}	3.62×10^{9}	1.45×10^{9}	9.67×10^{-18}	0.014
Tc-99	2.0×10^{-3}	1.20×10^{12}	2.39×10^{9}	1.72×10^{9}	8.98×10^{-13}	1547

In our modelling with MARFA, we have combined the IRF, CRF, and DRF in a single source term. As for the corresponding FARF31 simulation, the IRF pulse is assumed to be a Heaviside step function where the entire inventory is released at a constant rate over a year. The problem here is that it is not possible to distinguish between IRF nuclides and CRF/DRF nuclides in any simple way in MARFA output files. Since it is necessary to apply a single LDF for each radionuclide when plotting output data, we rescale the IRF source term (Bq/y or mol/y) so that the correct transported radiotoxicity is obtained when plotting the results (Sv/y). To be able to apply the basic LDFs on the entire radionuclide flux to the biosphere, we have therefore rescaled the IRF inventory by the ratio of the pulse LDF and basic LDF for each radionuclide. This approach is further discussed in Section 3.1.9. The IRF source term has been superimposed on the source term previously shown in Figure 3-1. The combined source term entering the far field, which we have used in MARFA modelling, is shown in Figure 3-2 which is plotted here as an equivalent dose rate (µSv/y). The numerical values in the legend display the near-field peak dose rates within the assessment time frame.

As discussed in Section 3.1.5, radionuclide transport along three different flowpaths is modelled in the report (i.e. two additional sensitivity cases in addition to the flowpath corresponding to the central corrosion case). Each studied flowpath is associated with a specific canister, having a pre-defined time of failure derived from the SR-Site safety assessment (SKB 2010a). In a full safety assessment, each flowpath would ideally have an individually specified source term accounting for the different failure times. In this work, however, we have made the simplification that for each studied flowpath, the canister fails at the same time (i.e. 114 485 years). This corresponds to the time of the first canister predicted to fail in the SR-Site central corrosion case. Moreover, all canisters are assumed to have source terms identical to that shown in Figure 3-2 (including nuclides not shown in the figure). It should also be noted that there is a minor additional discrepancy in that the IRF source term is based on the inventory at 100 000 years, while the combined CRF and DRF source term is based on canister failure at 114 485 years.

The simplification of using a uniform inventory was judged to be necessary as it enables more transparent comparisons of radionuclide releases from different flowpaths. Furthermore, this simplification does not detract from the relative comparison of breakthrough curves for the layered rock model and for the reference case of undisturbed rock matrix from SR-Site.

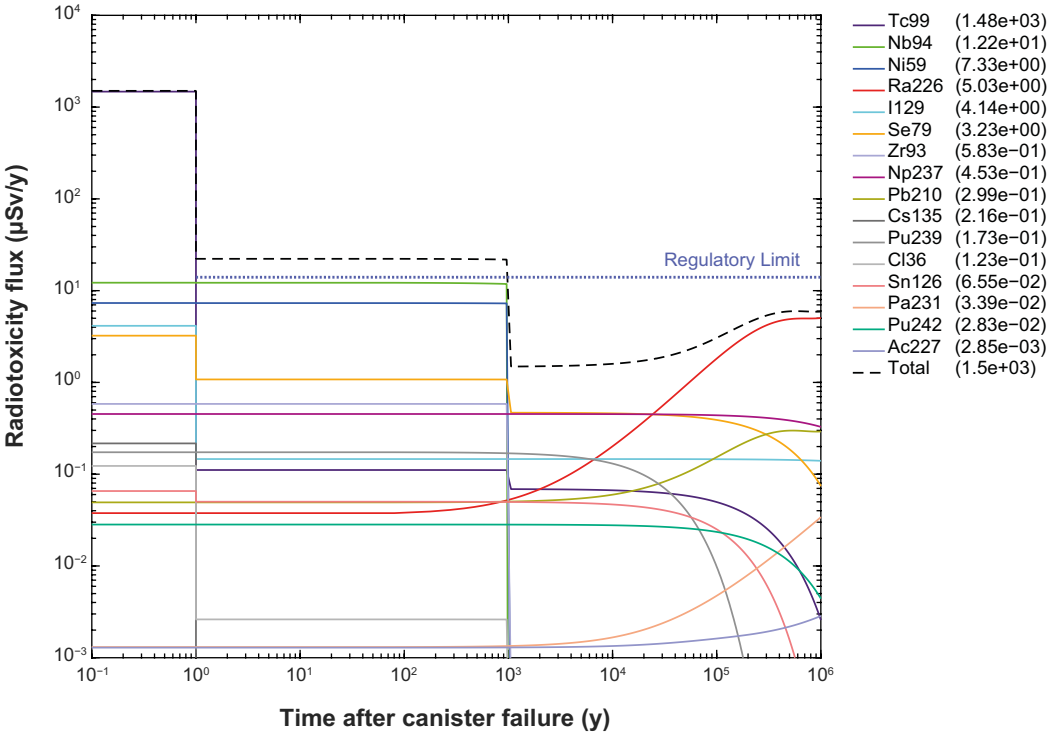

Figure 3-2. *Combined source term from the near field of the IRF, CRF, and DRF that we have used in our MARFA modelling. The time on the x-axis is in relation to canister failure. Only those radionuclides contributing more than 0.1 % of the total radiotoxicity are plotted.*

3.1.5 Flow-related migration properties of modelled flowpaths

Advective conditions in the deposition hole will only occur in canister positions that are intersected by water conducting fractures featuring relatively high flow (SKB 2011, Section 13.5). Such water-conducting fractures are frequently associated with low flow-related transport resistance (F-factor), although this is not always the case as recharge paths may have different properties than associated discharge paths. In the central corrosion case of SR-Site, each failing canister was given a specific time of failure, based on careful considerations within other parts of the safety assessment. From ten realisations of the semi-correlated Hydrogeological-DFN model, canisters at 56 different positions were predicted to fail within the assessment time frame. Their associated flow-related migration properties are shown in SKB (2010a, Table 4-3). Judging from these data, the time of failure is poorly correlated to both the advective flow through the deposition hole and the flow-related transport resistance of the flowpath, which is also called the F-factor (cf. Figure 3-3).

In the new modelling presented in this report, we do not aim to model radionuclide transport in all 56 flowpaths. For the most part, we only model the first failing canister position within the central corrosion case, and its flowpath. In a sensitivity study, however, two alternative flowpaths out of the 56 flowpaths associated with canister failure have been considered. Together with our main flowpath corresponding to the central corrosion case, the following representative flowpaths out of the pool of 56 are selected:

1. The flowpath associated with the first canister failure.
2. The flowpath having the lowest F-factor.
3. The flowpath having the median F-factor.

For flowpaths in the upper F-factor range, the retardation effect is so great that they become insignificant contributors to the radiological risk, regardless of modifications made to retention parameters. For the selected flowpaths, the data of SKB (2010a, Table 4-3) are reproduced in Table 3-2.

Table 3-2. Flow related migration properties of flowpaths intersecting the deposition holes where canisters fail due to corrosion for the ten realisations of the semi-correlated DFN model. Data reproduced from SKB (2010a, Table 4-3).

Flowpath	Time of failure (yr)	Rock transport resistance, F-factor (yr/m)	Advective travel time, t_w (yr)	Advective flow through deposition hole, q (m^3/yr)
1	114 485	53 660	6.4	0.733
2	803 247	11 330	20	0.035
3	201 037	89 910	17	0.144

As can be seen in Table 3-2, there is a large difference in time of failure for the different flowpaths that is not correlated with either the F-factor or advective travel time (cf. Figure 3-3). This supports our approach of using identical inventories for all three investigated flowpaths to identify differences arising purely due to variation of hydrodynamic transport parameters rather than the time schedule of canister failure. The first flowpath given in Table 3-2 is assumed for all variant calculations presented in this report except for Sections 8.7.1 (flowpath 2) and 8.7.2 (flowpath 3) where the impact of the hydrodynamic conditions are specifically examined.

It should be noted that the transport problem is fully specified by the F-factor and advective travel time and that the flowpath length is only needed to specify hydrodynamic dispersivity (since MARFA requires input in the form of dispersion length if hydrodynamic dispersion is modelled). In FARF31, on the other hand, the Péclet number is specified and flowpath length and equivalent dispersion length does not need to be directly considered. For the modelling presented here, the Péclet number is set to 10 in all cases which corresponds to a dispersion length of 65 m for flowpath 1 (or 10 % of the flowpath length, 650 m). The same flowpath length and dispersion length are used for flowpath 2 and 3 even though they have different physical path lengths since the Péclet number remains the same. Modelling results based on the flowpaths of Table 3-2 are judged to encompass the entire range of impacts of the variable hydrodynamic properties on radionuclide fluxes, as far as this is deemed relevant for the SR-Site radionuclide transport and dose modelling.

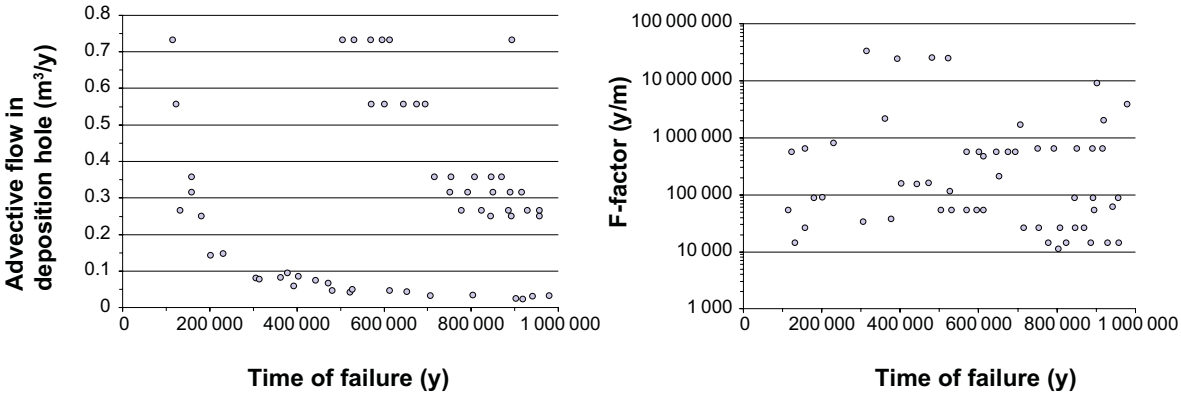

Figure 3-3. *Advective flow through deposition hole (m^3/y) and F-factor (y/m) plotted versus time of failure (y). Data from SKB (2010a, Table 4-3).*

3.1.6 Rock retention properties assumed in SR-Site

In SR-Site, the rock surrounding all flowpaths was assumed to be homogeneous. The assigned parameter values were mainly based on the site-specific data for undisturbed rock matrix that was studied extensively in the work leading up to SR-Site (e.g. Crawford 2008). Most of the rock properties used in the corrosion scenario are compiled in Table 3-3. In addition, the rock porosity was set to 0.18 % for all species. For the effective diffusivity, although not for the porosity, an anion exclusion factor of $1/\sqrt{10}$ (~ 0.32) was used for those radioelements presumed to be predominantly speciated as anions during migration (SKB 2010c, Section 6.8.10). The maximum penetration depth, while effectively infinite in the calculations, was set to 12.5 m to reflect the half-spacing between hydraulically conducting fractures and thus to ensure that the retention capacity of the rock would not be double counted (SKB 2010c, Section 6.7.10).

Table 3-3. Rock properties of the undisturbed rock used in the corrosion scenario. Table based on numerical values from SKB (2010a, Table 3-3).

Radioelement	Anion exclusion factor, f_{AE}	Effective diffusivity, D_e (m^2/s)	Sorption coefficient, K_d (m^3/kg)
Ac	1	2.0×10^{-14}	1.5×10^{-2}
Ag	1	2.0×10^{-14}	3.5×10^{-4}
Am	1	2.0×10^{-14}	1.5×10^{-2}
C	1	2.0×10^{-14}	0
Cl	0.32	6.34×10^{-15}	0
Cm	1	2.0×10^{-14}	1.5×10^{-2}
Cs	1	2.0×10^{-14}	3.5×10^{-4}
Ho	1	2.0×10^{-14}	1.5×10^{-2}
I	0.32	6.34×10^{-15}	0
Nb	1	2.0×10^{-14}	2.0×10^{-2}
Ni	1	2.0×10^{-14}	1.1×10^{-3}
Np	1	2.0×10^{-14}	5.3×10^{-2}
Pa	1	2.0×10^{-14}	5.9×10^{-2}
Pb	1	2.0×10^{-14}	2.5×10^{-2}
Pd	1	2.0×10^{-14}	5.2×10^{-2}
Po	0.32	6.34×10^{-15}	0
Pu	1	2.0×10^{-14}	1.5×10^{-2}
Ra	1	2.0×10^{-14}	2.4×10^{-4}
Se	0.32	6.34×10^{-15}	3×10^{-4}
Sm	1	2.0×10^{-14}	1.5×10^{-2}
Sn	1	2.0×10^{-14}	1.6×10^{-1}
Sr	1	2.0×10^{-14}	3.4×10^{-6}
Tc	1	2.0×10^{-14}	5.3×10^{-2}
Th	1	2.0×10^{-14}	5.3×10^{-2}
U	1	2.0×10^{-14}	5.3×10^{-2}
Zr	1	2.0×10^{-14}	2.1×10^{-2}

3.1.7 Handling of decay in SR-Site and our new modelling

In SR-Site, a number of simplifications were made to enable simulations of radionuclide transport using FARF31. Chief among these was the need to simplify decay chains to remove converging and diverging branches. Diverging decay chain branches are mostly trivial and can be neglected. This is particularly the case for the actinide chains as nuclides in all diverging branches have very short half-lives and subsequently re-converge with the main decay chain and it is generally not necessary to model these explicitly. A possible exception might be the decay of Zr-93 and Mo-93 which both can decay to either Nb-93m ($t_{½}$ 16.13 y) or Nb-93 (stable). This decay sequence is especially interesting since it is an example of both a converging and diverging decay process. Neglecting the branch fraction decaying directly to stable Nb-93 is conservative with regard to radiological risk since this assumption will slightly overpredict the activity of Nb-93m. In the FARF31 simulations it was necessary to neglect Mo-93 since the code cannot handle converging chains. Since the inventory activity of Zr-93 was much higher, it was deemed that the activity of the faster decaying Mo-93 could be reasonably neglected. The Nb-93m decay process was neglected entirely on account of its short half-life and its impact is implicitly considered in the LDF for transported Zr-93.

Very short-lived nuclides that can be expected to be in secular equilibrium with their parent nuclides are neglected in the explicit decay chain definitions, although are considered in the landscape dose factors (LDF's) for conversion of activity fluxes to dose rates. Converging branches in the actinide chains, on the other hand, are important since they contribute to inventories of subsequent daughter nuclides. The simplifications made to the actinide decay chains are shown in Figure 3-4 for the 4*n* and 4*n*+1 chains and in Figure 3-5 for the 4*n*+2 and 4*n*+3 chains.

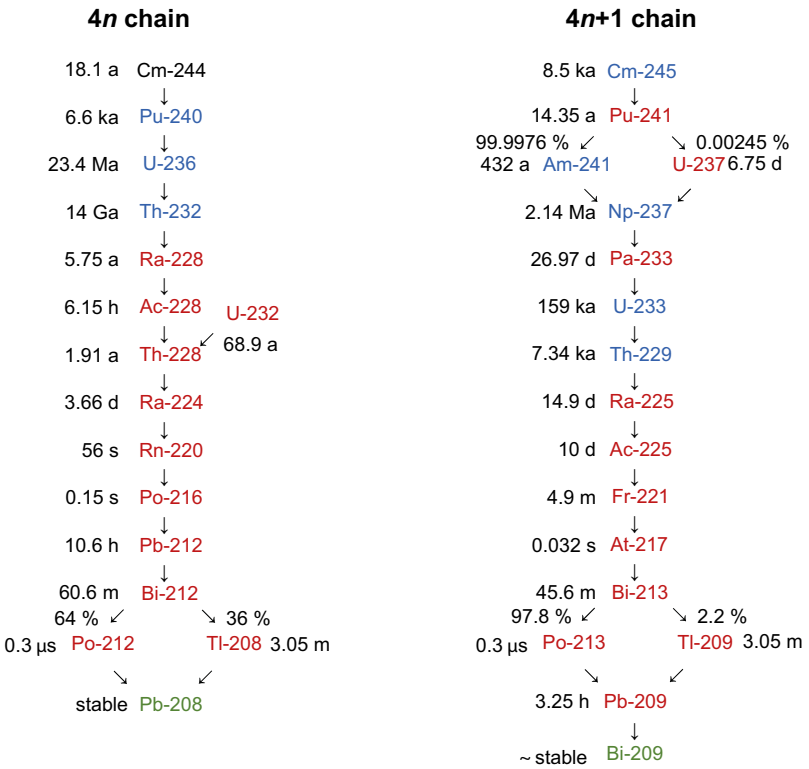

Figure 3-4. *Simplifications to the thorium (4n) and neptunium (4n+1) series radionuclide decay chains (blue – explicitly modelled radionuclides; black – radionuclides that are part of the initial inventory, but where transport is neglected and inventory is simply added to subsequent progeny nuclide; red – radionuclides implicitly modelled assuming secular equilibrium with the parent radionuclide; green – stable isotope decay chain terminator).*

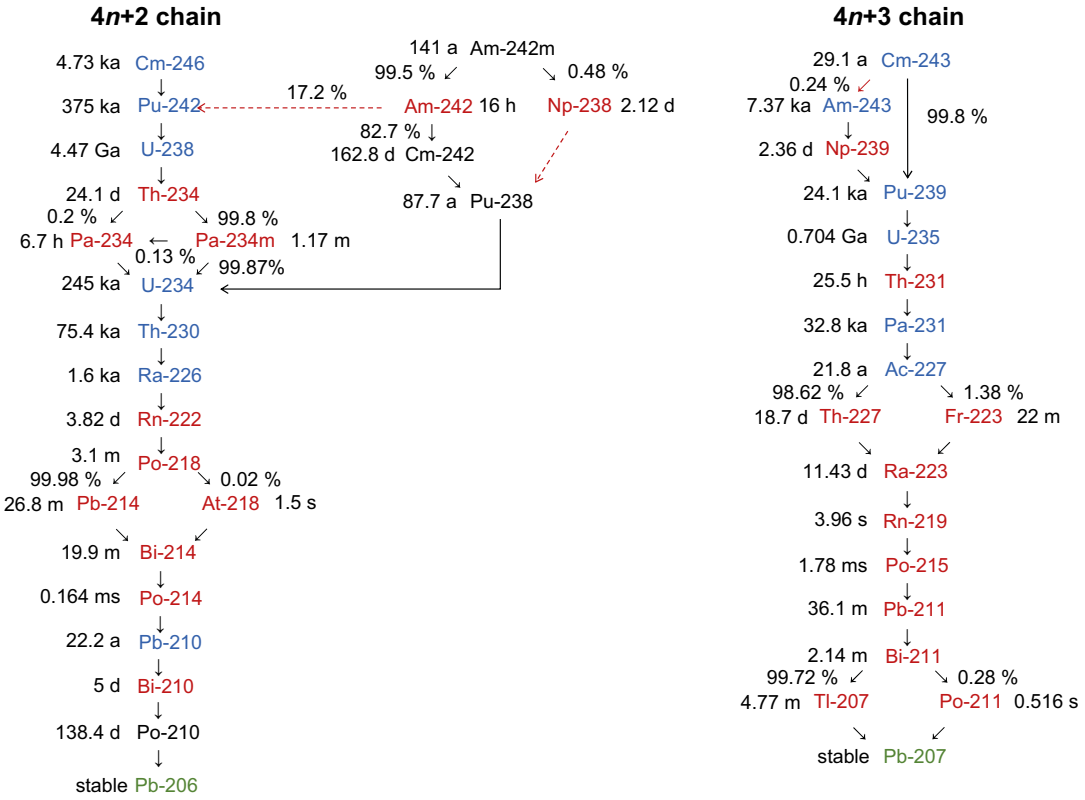

Figure 3-5. *Simplifications to the radium (4n+2) and actinium (4n+3) series radionuclide decay chains (blue – explicitly modelled radionuclides; black – radionuclides that are part of the initial inventory, but where transport is neglected and inventory is simply added to subsequent progeny nuclide; red – radionuclides implicitly modelled assuming secular equilibrium with the parent radionuclide; green – stable isotope decay chain terminator).*

On account of the short half-life of Cm-244, the 4*n* decay chain was simplified in SR-Site by adding the inventory of Cm-244 directly to that of Pu-240. Also, since FARF31 cannot handle converging decay chains, for the 4*n*+1 decay chain, the activity of U-237 was added to that of Np-237 and Pa-233 was added to that of U-233. For the 4n+2 chain, the activities of Am-242m, Pu-238, Am-242, Cm-242, Np-238, Th-234, and Pa-234m were added directly to that of U-234. For the 4n+3 chain, the activities of Cm-243 and Np-239 were added to that of Pu-239. In this way all actinide chains could be simplified to linear non-branching sequences while propagating the inventory of non-modelled converging chains in a radiologically conservative manner in the calculations.

Radionuclide half-lives were taken from the online web version of the Firestone compilation (Chu et al. 1999) with the exception of Ag-108m which was taken from Shrader (2004) and Se-79 which was taken from Bienvenue et al. (2007). It is noted that although there is a revised value for the half-life of Se-79 described by Jörg et al. (2010), we have used the previously determined value by Bienvenue (2007) to maintain consistency with the original SR-Site safety assessment. Similarly, more recent direct measurements of the decay of Sn-126 put its half-life at approximately 2.3×10^5 y (Catlow et al. 2005) which is more than double the value of 10^5 y used in SR-Site. We retain the previous value, however, to maintain consistency with the source term and the calculations made in the SR-Site transport modelling report (SKB 2010a).

Table 3-4. Decay chain simplifications, half-lives, and inventory assumptions for radionuclides considered in the SR-Site central corrosion case and as a calculation basis in this report. The column labelled "Inventory assumptions" indicates which nuclides were added together to obtain the inventory for the source term to avoid calculating converging decay chain branches.

Radionuclide	decay chain	half-life (y)	daughter	Inventory assumptions
Pu-240	4n	6 563	U-236	Pu-240, Cm-244
U-236	4n	2.342×10^{7}	Th-232	U-236
Th-232	4n	1.405×10^{10}	-	Th-232
Cm-245	4n+1	8 500	Am-241	Cm-245
Am-241	4n+1	432.2	Np-237	Am-241
Np-237	4n+1	2.144×10^{6}	U-233	Np-237, U-237
U-233	4n+1	1.592×10^{5}	Th-229	U-233, Pa-233
Th-229	4n+1	7 340	-	Th-229
Cm-246	4n+2	4 730	Pu-242	Cm-246
Pu-242	4n+2	3.733×10^{5}	U-238	Pu-242
U-238	4n+2	4.468×10^{9}	U-234	U-238
U-234	4n+2	2.455×10^{5}	Th-230	U-234, Am-242m, Pu-238, Am-242, Cm-242, Np-238, Th-234, Pa-234m
Th-230	4n+2	7.538×10^{4}	Ra-226	Th-230
Ra-226	4n+2	1 600	Pb-210	Ra-226
Pb-210	4n+2	22.3	Po-210	Pb-210
Po-210	4n+2	0.379	-	neglected (flowpath ingrowth only)
Am-243	4n+3	7 370	Pu-239	Am-243
Pu-239	4n+3	2.411×10^{4}	U-235	Pu-239, Cm-243, Np-239
U-235	4n+3	7.038×10^{8}	Pa-231	U-235
Pa-231	4n+3	3.276×10^{4}	Ac-227	Pa-231
Ac-227	4n+3	21.773	-	Ac-227
Ag-108m	-	438	-	Ag-108m
C-14	-	5 730	-	C-14
Cl-36	-	3.01×10^{5}	-	Cl-36
Cs-135	-	2.3×10^{6}	-	Cs-135
Cs-137	-	30.07	-	Cs-137
Ho-166m	-	1 200	-	Ho-166m
I-129	-	1.57×10^{7}	-	I-129
Nb-94	-	2.03×10^{4}	-	Nb-94
Ni-59	-	7.6×10^{4}	-	Ni-59
Ni-63	-	100.1	-	Ni-63
Pd-107	-	6.5×10^{6}	-	Pd-107
Se-79	-	3.77×10^{5}	-	Se-79
Sm-151	-	90	-	Sm-151
Sn-126	-	1×10^{5}	-	Sn-126
Sr-90	-	28.79	-	Sr-90
Tc-99	-	2.111×10^{5}	-	Tc-99
Zr-93	-	1.53×10^{6}	-	Zr-93

3.1.8 Solubility limits and sorption linearity

Solubility limits are assumed to have little impact on calculations in the far field, due to the low transported concentrations. According to SKB (2010a, Table 3-4), however, quantitative solubility limits for the near- and far-field were assigned. These limitations are included in the source term that was modelled in SR-Site and it is implicitly assumed in calculations that transport and retardation processes in the far-field occur at diluted concentration levels far below the solubility limit. Since radionuclide fluxes are specified instead of concentrations in the source term and since groundwater chemistry is not considered on the level of individual migration paths, it is not possible to further speculate on this and it is not given any additional consideration here.

For non-decay chain radionuclides, the sorptive retardation process as it is modelled cannot result in accumulation of solute at concentration levels exceeding the source term concentration which is already modelled as a solubility limited process. For decay chains, on the other hand, the situation is more complex since ingrowth of solubility limited radioelements can occur along flowpaths and the background aqueous concentrations of some of these (e.g U, Th, Ra) are already close to their solubility limits depending, of course, on local groundwater chemical conditions and assumed solubility controlling phases. The neglection of solubility limitations in the far-field could mean that fluxes of actinide chain radionuclides are somewhat overestimated and are thus conservative. Equally, however, the assumption of linear sorption implicit in the use of a conditionally constant K_d could also imply overestimation of sorptive retardation which could be non-conservative for far-field dose rates of certain radionuclides. This has not been quantified in the present work since it was deemed out of scope relative to the request for supplementary information (SSM2011-2426-110, items 4 and 6) as described in Section 1.2.

Although not included in the present report, the close relation between K_d and background geochemical conditions in the groundwater has been considered in considerable detail in the response to SSM's request for supplementary information (SSM2011-2426-110, item 1) which was handled as a separate issue in Crawford (2013a). It can also be noted that SKB has placed considerable effort into developing an updated methodology for anchoring K_d values used in radionuclide transport calculations to groundwater geochemistry (e.g. Crawford 2013b) including the possibility of dynamically updating of K_d values in transport calculations using MARFA (e.g. Trinchero et al. 2018). This work is ongoing and is a topic of central importance in the updated transport modelling methodology to be developed during the detailed site investigation phase at Forsmark.

3.1.9 Landscape dose conversion factors

When calculating the annual effective dose rates from radionuclide fluxes, basic landscape dose conversion factors (LDF's) were used for radionuclides that are released to the biosphere over long time periods. These include radionuclides of the CRF and DRF, and the Tc-99 component of the IRF on account of its strongly retarded transport. For radionuclides that are released over very short time periods to the biosphere, the basic LDFs are not applicable since they are based upon different underlying assumptions in the associated biosphere dose modelling (see Avila et al. 2010). Instead, pulse LDF's should be used, which are some orders of magnitude lower relative to the basic LDF's (cf. Table 3-5).

Table 3-5. Basic LDF and pulse LDF values used in deterministic modelling. Data from SKB (2010a, Table 3-7). Note that the Basic LDF has been used for Tc-99 IRF and CRF/DRF fractions on account of its strongly retarded transport.

Radionuclide	Basic LDF (Sv/y per Bq/y)	LDF pulse (Sv/y per Bq/y)
Ag-108m	7.05×10^{-13}	5.08×10^{-16}
Ac-227	1.30×10^{-11}	
Am-241	1.46×10^{-12}	
Am-243	1.53×10^{-12}	
C-14	5.44×10^{-12}	
Cl-36	5.84×10^{-13}	4.29×10^{-15}
Cm-244	8.74×10^{-13}	
Cm-245	1.58×10^{-12}	
Cm-246	1.55×10^{-12}	
Cs-135	3.96×10^{-14}	1.84×10^{-16}
Cs-137	1.20×10^{-13}	
Ho-166m	5.90×10^{-14}	
I-129	6.46×10^{-10}	5.56×10^{-14}
Nb-94	4.00×10^{-12}	3.18×10^{-16}
Ni-59	7.39×10^{-14}	9.67×10^{-18}
Ni-63	1.21×10^{-15}	
Np-237	4.83×10^{-11}	
Pa-231	8.10×10^{-12}	
Pb-210	5.07×10^{-12}	
Pd-107	6.73×10^{-15}	

Radionuclide	Basic LDF (Sv/y per Bq/y)	LDF pulse (Sv/y per Bq/y)
Po-210	8.86×10^{-12}	
Pu-239	1.94×10^{-12}	
Pu-240	1.88×10^{-12}	
Pu-242	1.89×10^{-12}	
Ra-226	3.75×10^{-12}	
Se-79	1.21×10^{-9}	9.70×10^{-14}
Sm-151	7.16×10^{-16}	
Sn-126	2.47×10^{-11}	2.31×10^{-15}
Sr-90	2.19×10^{-13}	
Tc-99	8.98×10^{-13}	2.81×10^{-15}
Th-229	3.61×10^{-12}	
Th-230	1.31×10^{-11}	
Th-232	1.72×10^{-12}	
U-233	2.50×10^{-12}	
U-234	3.62×10^{-12}	
U-235	2.76×10^{-12}	
U-236	1.85×10^{-12}	
U-238	1.85×10^{-12}	
Zr-93	2.77×10^{-14}	

In our updated modelling effort, we account for retardation in the geosphere for all IRF radionuclides. A consequence is that the IRF pulse is not released to the biosphere during a single year, as was the case in the original SR-Site calculations documented in SKB (2010a). As shown later (e.g. Figure 3-8) the pulse is released to the biosphere over a decade up to perhaps a century, depending on the radionuclide (for Tc-99 the pulse duration is even longer still). For radionuclides with prolonged release rates comparable to a human lifespan, the use of pulse LDFs may, or may not be, consistent with the underlying assumptions of the pulse LDF concept. The authors of this report have not revised the LDF values for IRF radionuclides that are released over such extended time spans since this was outside the scope the work, although it is noted as a possible weakness in the conversion of activity fluxes to dose rates as they are calculated in the present work. Instead, we have simply used the pulse LDF for the IRF specific radionuclides except for Tc-99 which is assigned a basic LDF value, as was done in SR-Site. This assumption has been deemed acceptable for the purpose of this report although it could be judged as being not entirely consistent with other underlying assumptions in the dose rate modelling.

3.2 Results for replication of SR-Site corrosion case with FARF31 and MARFA

3.2.1 FARF31 Replication Case

The SR-Site results could be adequately reproduced using FARF31 with good accuracy for most of the radionuclides of the combined CRF and DRF source term. Figure 3-6 shows the dose rates of these radionuclides, obtained in the new FARF31 modelling plotted versus time since canister failure. Numerical values of the peak radionuclide dose rates in the safety assessment time interval (10^6 y) are given in the figure legend. In the SR-Site transport modelling report (SKB 2010a), results were plotted versus absolute time, which although appropriate for the safety assessment is less useful in this work since we are interested in explaining detailed breakthrough behaviour which is not properly discernible on an absolute time scale. Figure 3-7 shows the results plotted on an absolute time scale, which is most directly comparable to that in SKB (2010a, Figure 4-3).

It should be noted that the results for a relative time scale given in Figure 3-6 and those for the absolute time scale in Figure 3-7 represent separate simulations where the source term was specified either on a relative time scale (starting from 0 y) or absolute time scale (starting from 114 485 y). This is a relevant issue because it gives rise to some small differences in the peak dose rates given in Figure 3-6 and Figure 3-7 and it is not completely clear which calculation basis was used in the original SR-Site calculations. Some of the values also differ slightly from the original breakthrough curves given in SKB (2010a, Figure 4-3).

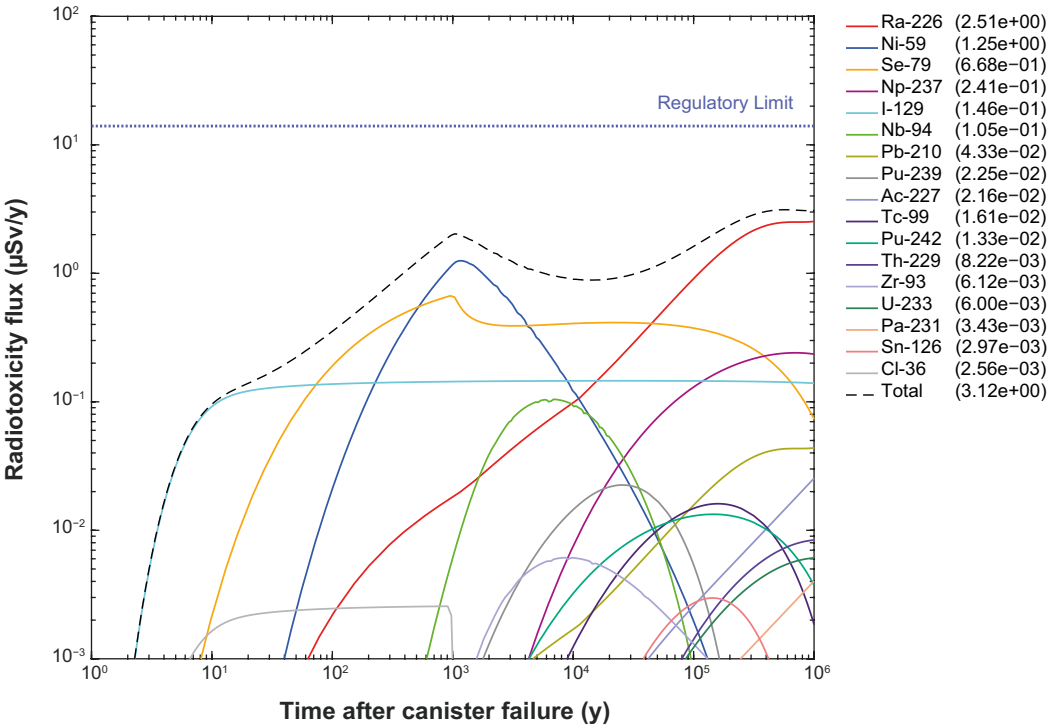

Figure 3-6. *The annual effective dose for the replicated corrosion scenario using FARF31, for the combined CRF and DRF source term only. The legend is sorted by annual effective peak dose (µSv/y) within the time frame of the assessment. The time on the x-axis is relative to canister failure. Only those radionuclides contributing more than 0.1 % of the total radiotoxicity are plotted.*

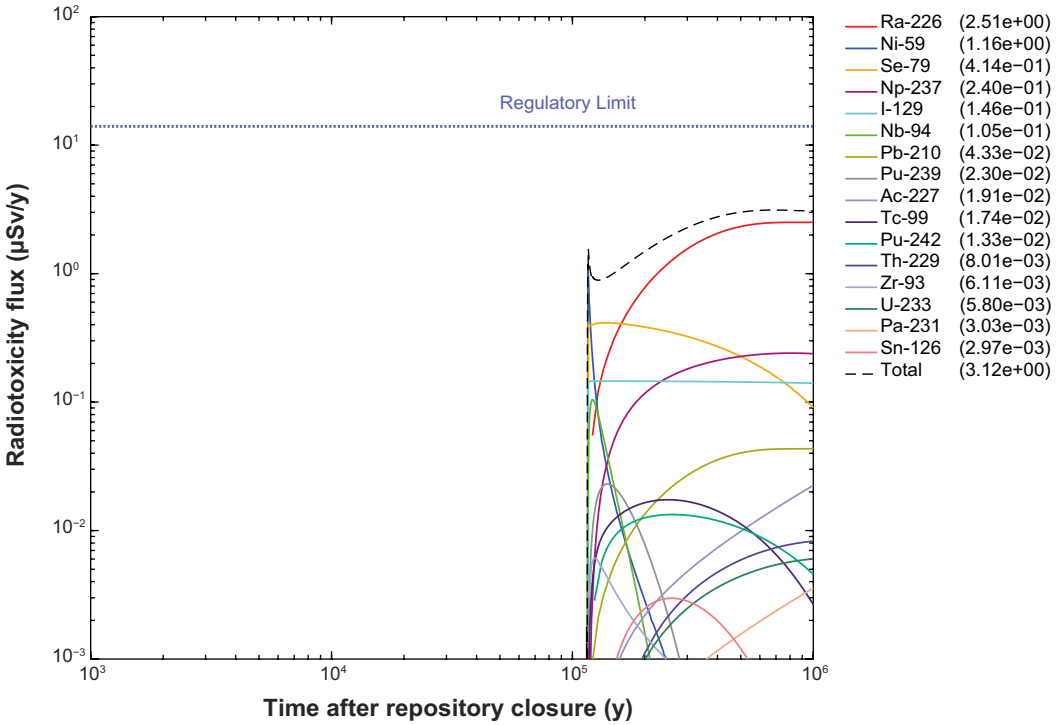

Figure 3-7. *The annual effective dose for the replicated corrosion scenario using FARF31, for the combined CRF and DRF source term only. The legend is sorted by annual effective peak dose (µSv/y) within the time frame of the assessment. The time on the x-axis is relative to repository closure. Only those radionuclides contributing more than 0.1 % of the total radiotoxicity are plotted.*

Numerical values for the top dose contributing nuclides are compiled in Table 3-6 for the original SR-Site calculations (SKB 2010a, Figure 4-3) and the new FARF31 calculations made in this work. As can be seen from the comparison, there are significant deviations for Se-79, Ac-227, Cl-36 and somewhat smaller deviations for Ra-226, Ni-59, Nb-94, and Tc-99. The deviation for Tc-99 appears to be largely attributable to the fact that the IRF fraction of Tc-99 is not included in Figure 3-6 and Figure 3-7 which would reduce the difference to less than 3 % relative to the SR-Site result if it were included. Other deviations are mostly associated with nuclides featuring early peak arrival (Ni-59, Se-79, Nb-94) or a peak that is still rising at the end of the assessment period (Ra-226, Ac-227, Pa-231). The deviation for Pu-239 and Sn-126 is small but not insignificant even though they have well resolved peaks in the middle of the assessment period for both relative and absolute calculation time frames.

Table 3-6. Peak dose rates calculating in the original SR-Site modelling and in new modelling by FARF31 as well as relative differences between the new FARF31 results and the original SR-Site values.

Nuclide	SR-Site (μS/y)	new FARF31 modelling – rel. time (μS/y)	diff. %	new FARF31 modelling – abs. time (μS/y)	diff. %
Ra-226	2.6	2.51	−3 %	2.51	−3 %
Ni-59	1.3	1.25	−4 %	1.16	−11 %
Se-79	0.68	0.668	−2 %	0.414	−39 %
Np-237	0.24	0.241	0 %	0.240	0 %
I-129	0.15	0.146	−3 %	0.146	−3 %
Nb-94	0.11	0.105	−5 %	0.105	−5 %
Pb-210	0.044	4.33×10^{-2}	−2 %	4.33×10^{-2}	−2 %
Pu-239	0.024	2.25×10^{-2}	−6 %	2.30×10^{-2}	−4 %
Tc-99	0.018	1.61×10^{-2}	−11 %	1.61×10^{-2}	−11 %
Ac-227	0.014	2.16×10^{-2}	54 %	1.91×10^{-2}	36 %
Pu-242	0.013	1.33×10^{-2}	2 %	1.33×10^{-2}	2 %
Th-229	0.0082	8.22×10^{-3}	0 %	8.01×10^{-3}	−2 %
Zr-93	0.0063	6.12×10^{-3}	−3 %	6.11×10^{-3}	−3 %
U-233	0.0060	6.00×10^{-3}	0 %	5.80×10^{-3}	−3 %
Pa-231	0.0037	3.43×10^{-3}	−7 %	3.03×10^{-3}	−18 %
Sn-126	0.0031	2.97×10^{-3}	−4 %	2.97×10^{-3}	−4 %
Cl-36	0.0013	2.56×10^{-3}	97 %	6.03×10^{-5}	−95 %
Total	3.2	3.12	−3 %	3.12	−3 %

While forensic examination of input and output files from the original SR-Site runs to identify differences is not possible since this information was not archived, the simulation of the central corrosion case using both relative and absolute timescales for the source term definition give some clues as to why differences arise. There appear to be at least four potential reasons for the numerical differences that can be identified:

1) Slightly different source terms (source flux versus time) may have been specified in SR-Site and for the new FARF31 calculations presented here.
2) Slightly different output times may have been chosen by the FARF31 inversion algorithm in the calculations presented here relative to those in SR-Site.
3) The breakthrough calculated by FARF31 may, in some cases, be poorly resolved due to the automatic selection of output times which differs for each nuclide and for different source term specifications.
4) The time period for the safety assessment is 10^6 y in an absolute time frame (i.e. post repository closure). This may be of relevance for nuclides that are still increasing in dose rate at the last timepoint in the range which may not exactly correspond to 10^6 y due to the sub-optimal resolution of the breakthrough curves.

A limitation of the release version of FARF31 used in SR-site relative to the MARFA code is that FARF31 can accept a source term with a maximum of 512 time points. Since the original source term consists of 10^4 data points, this requires a relatively severe downsampling of the data. We have copied

the same downsampling algorithm that was apparently used in the SR-Site calculations (to the extent that we have been able to reconstruct the original workflow). For most radionuclides, the rates of change in the source term are relatively even over time and quite good resolution of the source term is obtained even with a maximum of 512 data points. The downsampling algorithm, however, cannot properly handle the rapid decrease in source flux at the conclusion of the CRF source term at 1 000 y (after canister failure) so this required some manual editing to capture properly. This may not exactly correspond to how this was done in SR-Site and thus could be a source of uncertainty.

It is not clear whether the SR-Site calculations were made using a source term specified in absolute or relative time, which as Table 3-6 indicates can have a non-negligible impact on estimated peak dose rates due to the differing output times chosen by the FARF31 Laplace inversion algorithm. Since the original output files are unavailable this cannot be confirmed. It is also not clear whether the numerical values rounded to 2 significant figures in the SR-Site reporting (SKB 2010a, Figure 4-3) are interpolated to fit the exact safety assessment timeframe of 10^6 y. This may be an issue for radionuclides that are still increasing in flux at the end of the simulation time period. In general, the output times selected by FARF31 differ for each radionuclide and also are limited to a maximum of 512, although in practice the number of time points in the response function ranged from 60–126 in the SR-Site replication calculations. There is therefore a large potential for variation in the last time point in the output data for any given nuclide that is less than or equal to the safety assessment timeframe of 10^6 y.

Taking Ra-226 as a typical example, the last time point is at 989 220 y in the relative timeframe and 991 990 y in the absolute timeframe simulations. The final timepoint at which the maximum dose rate is reported for Ra-226 is therefore 8–11 ky short of the actual upper safety assessment time limit of 10^6 y. Since the far-field dose rate for Ra-226 is still increasing at the end of the simulation time, this can have an impact on the reported maximum dose rates. Larger discrepancies are noted for Ac-227 and Pa-231. Even for nuclides that peak well before the maximum safety assessment timescale, it is not clear whether the maximum peak flux estimated from the breakthrough curve is exact owing to the relatively low time resolution of the breakthrough curves. It is possible that more accurate estimates of peak flux could be made by interpolation of breakthrough curves, although this was deemed beyond the scope of what was feasible to achieve in the present work given that the differences relative to the SR-Site results are quite minor.

Another possibility which only came to light at a very late stage of editing of the present report was that a slightly different version of the FARF31 code was most likely used in SR-Site than the version that was available to the authors of this report. The updated version of the code was modified so that the restriction on the size of the boundary condition was removed and the code could then accept the boundary condition in full resolution without the need for downsampling (i.e. 10^4 data points rather than 512 in the documented release version described in Lindgren et al. 2002).

Figure 3-8 shows the results for the radionuclides of the IRF (only) after applying pulse LDF's with the exception of Tc-99 which uses the basic LDF value (see discussion in Section 3.1.9). Figure 3-9 shows the IRF results superimposed on those for the CRF/DRF fraction shown previously in Figure 3-6. It should be noted that the numerical peak doses given in Figure 3-9 are slightly less than the sum of peak doses in Figure 3-6 and Figure 3-8. This is due to the fact that the timing of the peak breakthrough differs when the breakthrough curves for the IRF and CRF/DRF are added relative to the peak timing for the IRF and CRF/DRF cases calculated separately. Another key difference is that the summed breakthrough curves in Figure 3-9 are calculated based on a concatenation of the output times for the IRF and CRF/DRF simulations followed by summing of the individual breakthrough curves interpolated to the new concatenated output time vector.

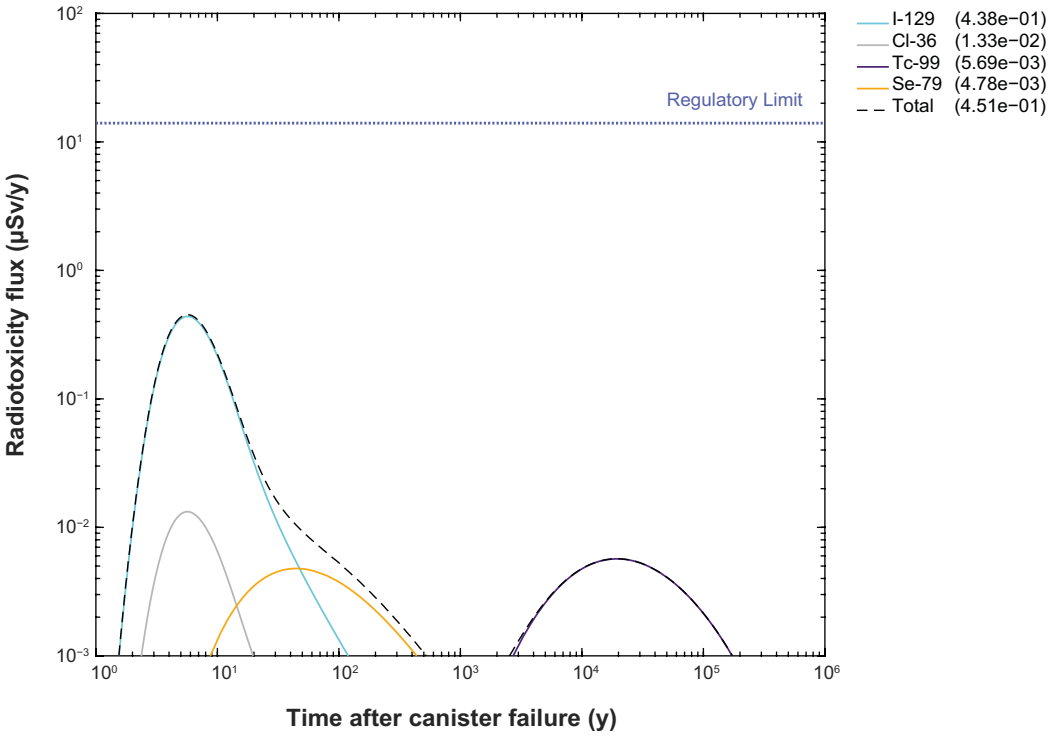

Figure 3-8. *The annual effective dose for the replicated corrosion scenario using FARF 31, for the IRF source term only. The legend is sorted by annual effective peak dose (µSv/y) within the time frame of the assessment. The time on the x-axis is relative to canister failure.*

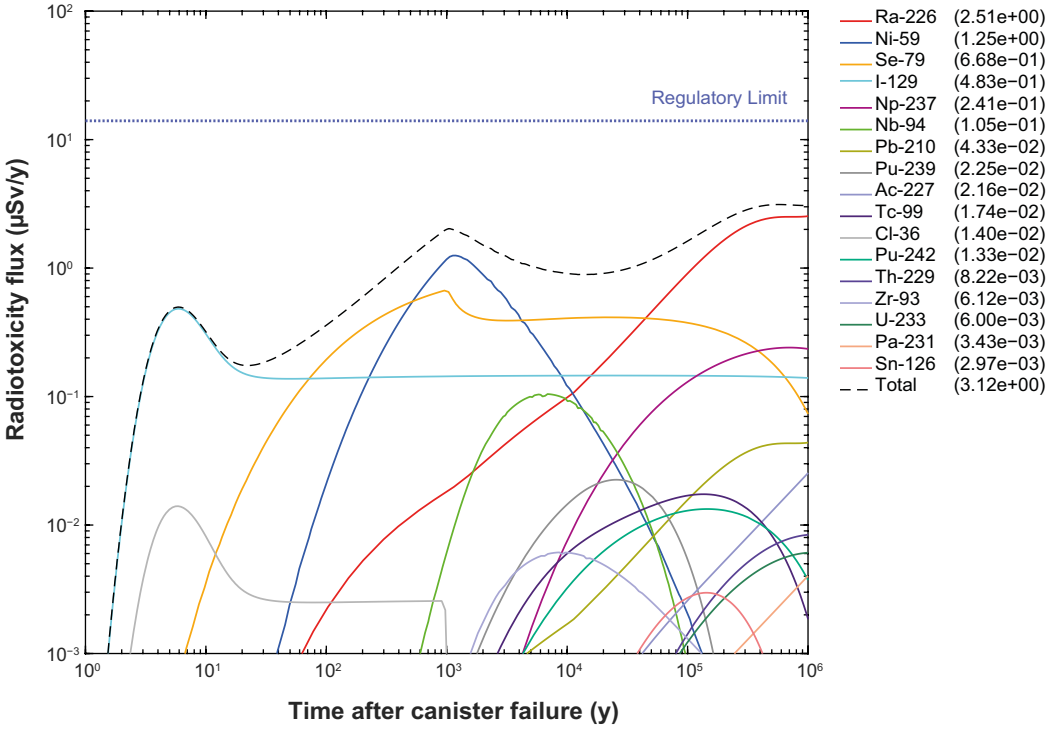

Figure 3-9. *The annual effective dose for the replicated corrosion scenario using FARF 31, for the combined IRF, CRF and DRF source terms. The legend is sorted by annual effective peak dose (µSv/y) within the time frame of the assessment. The time on the x-axis is relative to canister failure. Only those radionuclides contributing more than 0.1 % of the total radiotoxicity are plotted.*

3.2.2 MARFA Replication Case

The central corrosion case of SR-Site was also replicated with MARFA to the best of our ability using the same input data. The decision was made to include the IRF and CRF/DRF fractions in a single source term input file although as two separately specified source terms in MARFA. The practical advantage of this is that one avoids the necessity of two separate computational runs and the associated post processing of data required to superimpose the solutions. The avoidance of additional code to superimpose breakthrough curves from separate simulations is, of course, far preferable from a QA point of view as it minimises unnecessary input/output handling of data. The main drawback of this, however, is that it is not possible to distinguish between the IRF and CRF/DRF fractions in the breakthrough curves which necessitates the need to use a common LDF for both IRF and CRF/DRF fractions.

The issue of using basic LDF's versus pulse LDFs was handled by rescaling the source term thereby reducing the activity flux (Bq/y) and molar flux (mol/y) specified for the IRF as discussed in Section 3.1.4 (since IRF-specific pulse LDF values are numerically much smaller than the basic LDF's). In this way, far-field radionuclide flux exiting the geosphere could be multiplied by the basic LDF for calculation of the annual effective dose so that the correct result would be obtained when using basic LDF values in place of the pulse LDF. The breakthrough of the combined IRF and CRF/LDF fractions is shown in Figure 3-10 and exhibits some of the typical oscillatory behaviour discussed in Section 2.2.

In these calculations, 10^8 particles were used to simulate the SR-Site corrosion case using MARFA. The version of Marfa used for these calculations releases particles at different times sampled from the cumulative source term where each nuclide is assigned a number of initial particles proportional to the source term strength. In the present MARFA calculations to replicate the SR-Site corrosion case, only data points for times less than 1.1×10^6 y are considered in the source term so that particles aren't wasted on calculating radionuclide breakthrough significantly after 10^6 years. It is, however, necessary to simulate slightly beyond the upper limit of the safety assessment timescale since an artefactual early dip in breakthrough can occur that is due to the abrupt termination of the source term at 10^6 y. The dip is related to the bandwidth of the breakthrough curve reconstruction calculation, however, and can be reduced by decreasing the bandwidth of the kernel at the expense of extra stochastic noise in the breakthrough (i.e. by increasing the postprocessor sensitivity parameter "gamma"). In all simulations made in this work, the default setting of 0.2 for the gamma-parameter has been used after recommendation from the author of the MARFA code. Out of the 10^4 data points in the original source term, truncating the maximum time to 1.1×10^6 y reduces the source term to 2 773 data points.

For nuclides that dominate the source term and have relatively long half-lives or are close to the beginning of decay chains, only small amounts of oscillatory behaviour are seen in the simulation results shown in Figure 3-10. For less important nuclides and those with short half-lives near the terminal end of decay chains (such as Ac-227 and Pb-210), the noise is substantial. A considerable amount of manual fine-tuning was necessary (in close cooperation with the author of the code) for the user provided particle splitting parameters and the weighting values for individual radionuclides in the input files to obtain this level of accuracy. Considerably noisier breakthrough is obtained if using only the default values for these user defined parameters. Because of these issues, the MARFA code has been recently modified to simplify the user defined tuning parameters, although oscillatory problems still persist in the new version which appears to be an unavoidable consequence of particle-based methods.

In the SR-Site calculations, this is complicated by the presence of 37 radionuclides with a source term that extends well beyond 10^6 y which means that the particles released are spread very thinly in time. Some alternative techniques such as simulating each decay chain separately have been explored and this has been found to give somewhat better performance, although not entirely free of noise artefacts. The calculation time scales in proportion to the number of particles released. For the 10^8 particles used in these simulations, MARFA takes just over 6 hours of CPU time to compute the breakthrough curves for the entire cohort of radionuclides (compared to a few 10's of seconds for FARF31). For the calculations, a standard Dell Optiplex 9020, desktop 64-bit MS Windows 7 system was used with an Intel i5-4670 3.4 GHz processor and 8 Gb of RAM memory.

It should be noted that the oscillations in the breakthrough curves are computational artefacts that are unavoidable when using MARFA. When compared with the corresponding FARF31 results, there is also a slightly earlier first arrival of radionuclides, although only noticeable for I-129, Cl-36, Se-79, and Ni-59. This appears to be related to the breakthrough curve reconstruction algorithm and associated

kernel bandwidth for very early arriving particles as described in Section 2.2. For dose rates above 0.1 μS/yr in these calculations, however, there is little oscillation and accordingly, it has only a minor effect on the total modelled radiological risk. The annual effective peak doses calculated in the FARF31 calculations replicating the SR-Site central corrosion case and in the new modelling by MARFA are given in Table 3-7 for most significant dose contributing radionuclides.

Table 3-7. Peak doses calculated using FARF31 and MARFA in replication runs for the SR-Site central corrosion case where both the IRF and CRF/DRF fractions are included in the source term. The difference between the FARF31 and MARFA results is also given relative to the FARF31 peak dose.

	FARF31 Peak Dose (μS/yr)	MARFA Peak Dose (μS/yr)	Diff. %
Ra-226	2.51	2.76	10 %
Ni-59	1.25	1.46	17 %
Se-79	0.668	0.708	6 %
I-129	0.483	0.523	8 %
Np-237	0.241	0.263	9 %
Nb-94	0.105	0.120	4 %
Pb-210	4.33×10^{-2}	3.81×10^{-2}	−12 %
Pu-239	2.25×10^{-2}	2.61×10^{-2}	16 %
Ac-227	2.16×10^{-2}	2.02×10^{-2}	−6 %
Tc-99	1.74×10^{-2}	1.80×10^{-2}	3 %
Cl-36	1.40×10^{-2}	1.09×10^{-2}	−22 %
Pu-242	1.33×10^{-2}	1.46×10^{-2}	10 %
Th-229	8.22×10^{-3}	1.17×10^{-2}	42 %
Zr-93	6.12×10^{-3}	6.90×10^{-3}	13 %
U-233	6.00×10^{-3}	6.11×10^{-3}	2 %
Pa-231	3.43×10^{-3}	3.95×10^{-3}	15 %
Sn-126	2.97×10^{-3}	3.37×10^{-3}	13 %
Total	3.12	3.39	9 %

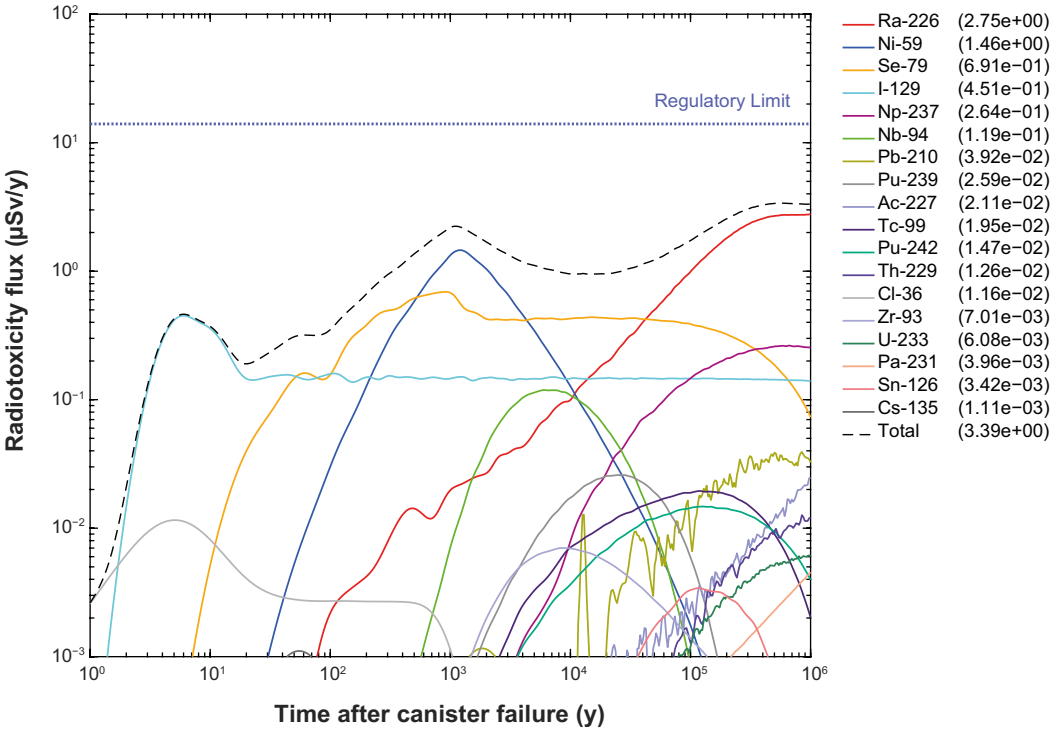

Figure 3-10. *The annual effective dose for the replicated corrosion scenario using MARFA, for the combined IRF, CRF and DRF source terms. The legend is sorted by annual effective peak dose (μSv/y) within the time frame of the assessment. The time on the x-axis is relative to canister failure. Only those radionuclides contributing more than 0.1 % of the total radiotoxicity are plotted.*

4 Rock description and setup of layered rock model

4.1 General description of fracture adjacent rock

The transport and retardation properties of crystalline rock have been investigated extensively in the Forsmark and Oskarshamn site investigations (e.g. Stephens et al. 2007, Byegård et al. 2008, Crawford 2008, Selnert et al. 2009b, Crawford and Sidborn 2009, Sandström and Tullborg 2009, Löfgren and Sidborn 2010), as well as in earlier and more recent research, e.g. at the Äspö Hard Rock Laboratory (Gnirk 1993, Winberg et al. 2003, Nilsson et al. 2010). There is also a wealth of studies performed on relevant rock formations internationally (e.g. Möri et al. 2003, Kuva et al. 2012).

From the point of view of radionuclide retardation, it is the rock in the immediate vicinity of flow bearing features that can be presumed to be of most importance. In the TRUE Block Scale project, carried out at the Äspö Hard Rock Laboratory, a schematic illustration (Andersson et al. 2002) of a transport flowpath in cross-section was produced to explain the main features of an open flow bearing fracture (reproduced in Figure 4-1). Although this image was produced with Äspö HRL specific conditions in mind, it is a useful starting point for the present discussion since it is a good illustration of our present knowledge concerning rock that surrounds flowpaths.

The lower illustration shows a water-conducting fracture zone and the surrounding rock. While water can flow in some of the water bearing fractures, others constitute dead ends. Accordingly, the water in such features would be effectively stagnant. There may also be nearby, open fractures that hold stagnant water although these are not connected to the flowing system (not shown in Figure 4-1). Black lines intersecting the surrounding rock represent minor fractures (lower illustration) and micro fractures (upper illustration). These minor- and micro fractures might be expected to hold effectively stagnant water. Presently there is no defined size limit between what is labelled a minor- or micro-fracture, but instead there is a recognised continuum of fracture lengths and widths.

The upper part of the illustration (Figure 4-1) shows an exploded view of the flowpath and fracture-adjacent rock in cross-section. As can be seen from the figure, the fractures are partially blocked by fault gouge and small rock fragments. The rock facing the fractures is also typically coated by a very thin layer of fracture mineralisation that is assumed to be highly porous. Beyond the fracture coatings, there is a hydrothermal alteration rim which might span a few centimetres into the rock matrix. This alteration rim may have been affected both mechanically and chemically, which will have altered its transport properties relative to those of the underlying rock which is labelled as fresh, unaltered rock. As is typically observed in nature (and also shown in Figure 4-1), the properties of the surrounding rock vary, not only in an orthogonal direction to the flowpath, but also along it.

Based on the numerical data given Figure 4-1 one might surmise that the illustration represents a feature in a deformation zone and that the flowpath has in the past conducted, or still conducts, significant amounts of water. Accordingly, the surrounding rock has been extensively affected by alteration processes. This is particularly apparent in the figure which features fault gauge and a relatively thick and porous alteration rim. When designing the layout of the tunnels and deposition holes of a KBS-3 repository, the intention is to stay clear of such major hydraulic structures as far as this is achievable. Consequently, rock that surrounds fractures intersecting deposition holes can be expected to feature less tectonic and chemical alteration than the TRUE Block Scale conceptualisation might otherwise imply.

Perhaps a more accurate representation of a (non-deformation zone) flow bearing fracture for the Forsmark site is that depicted in Figure 4-2 which has a considerably simpler microstructure. In Figure 4-2 we have what might be termed a stochastic background fracture featuring a discontinuous fracture coating of secondary minerals such as chlorite, calcite, and clay overlying an alteration rim which may, or may not be recognisable by ocular examination. This type of feature is characterised by an absence of multiple parallel flowpaths such as splays, and no features of tectonic origin such as fault breccia and mylonite.

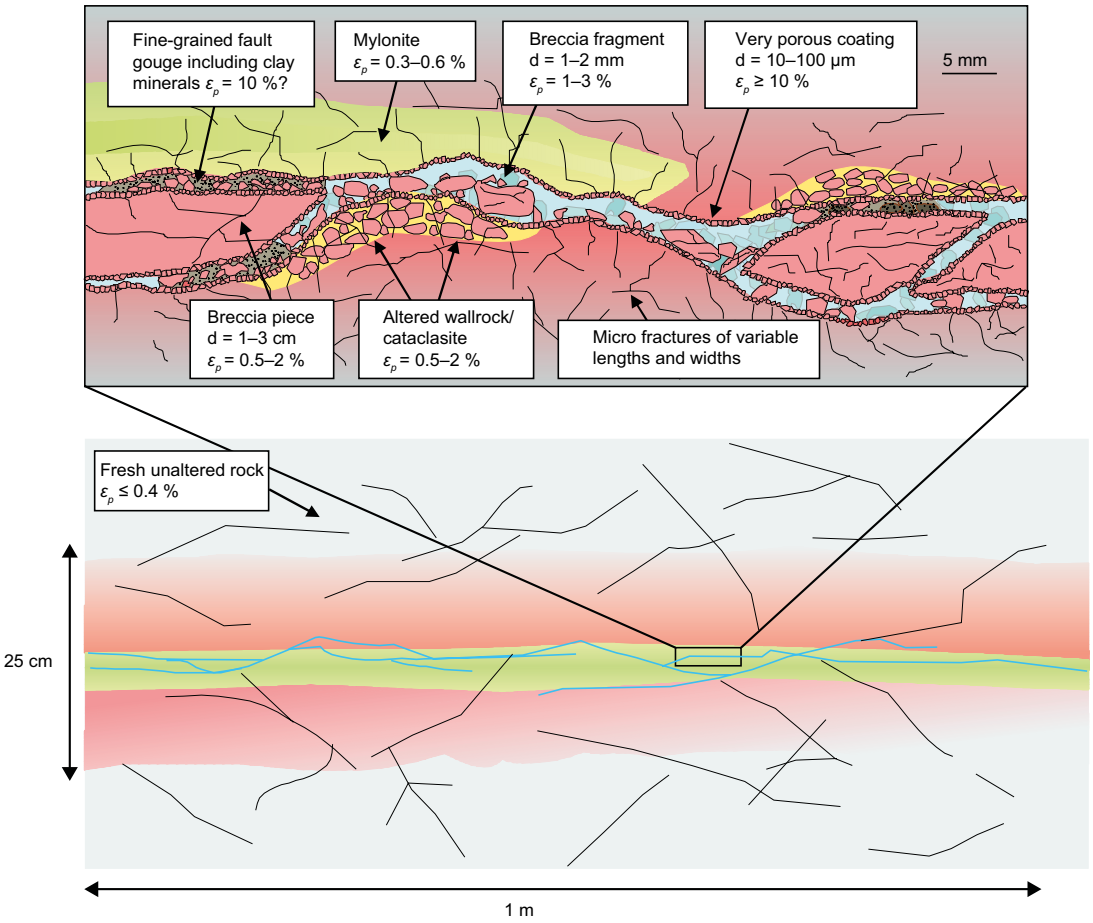

Figure 4-1. *Schematic illustration of a generalised transport path in cross-section based on the conceptual model developed in the TRUE Block Scale project for a minor deformation zone. The pathway is characteristic of a typical conductive structure involved in the tracer experiments. Since the model is site-specific for the Äspö HRL, details concerning rock types, etc may not be representative of the Forsmark site. Illustration reproduced from Andersson et al. (2002).*

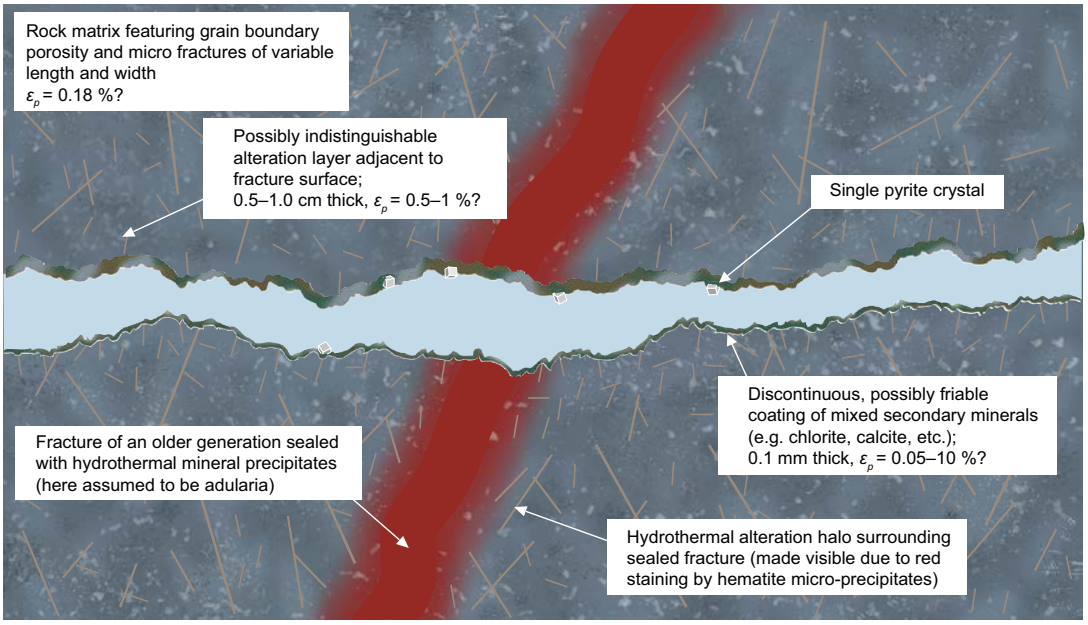

Figure 4-2. *Schematic illustration of a generalised non-deformation zone transport path thought to be reasonably representative of a background (stochastic) flow-bearing fracture that might be found in the immediate vicinity of the KBS-3 repository at Forsmark. Illustration reproduced with minor modifications from Crawford (2008).*

4.1.1 Fracture coating

There is a large body of observational evidence supporting the notion that secondary minerals often coat fracture surfaces. Within the Forsmark site investigation area, the relative frequency of different fracture minerals can be summarised as follows: calcite and chlorite/corrensite >> laumontite > quartz, adularia, albite, clay minerals > prehnite, epidote > hematite and pyrite, although there are large variations between fractures (e.g. Byegård et al. 2008, Löfgren and Sidborn 2010, Tullborg et al. 2008, Sandström and Tullborg 2008). It should, however, be highlighted that some open fractures, or parts thereof are occasionally uncoated and exhibit apparently unaltered rock surfaces (e.g. Eklund and Mattsson 2009).

Figure 4-3 shows photos of some typical fracture-adjacent rock samples from Forsmark. These are categorised into several basic fracture types, labelled A-H within the SDM-Site retardation model described by Byegård et al. (2008). Three of these (fracture type B, F, and H) have been selected as being particularly archetypal examples of the different fracture classes which are developed in Section 4.1 and are discussed below by way of example. This should not be taken to imply that the other fracture types are less common, but that these three are good examples which exhibit the most common microstructural features that the multilayer model developed in this work attempts to capture. It should also be recognised that the different classifications described in Byegård et al. (2008) essentially represent a continuum of possibilities where the photographs in Figure 4-2 are typical examples.

In the upper middle image (fracture type B) in Figure 4-3, a relatively thick layer of mainly chlorite and clay minerals covers the entire fracture surface. The thickness of the fracture coating is judged to be about 1 mm in Byegård et al. (2008, Table 2-3), which is somewhat thicker than normal at Forsmark (cf. Section 5.3). The underlying rock is judged as being altered and the thickness of the alteration rim is estimated to be about 1 cm. The middle right-hand image (fracture type F) in Figure 4-3 shows a coating of varying thickness that mainly consists of calcite and covers an underlying rock that is judged to be fresh (i.e. chemically unaltered). The bottom right-hand image (fracture type H) in Figure 4-3 shows a fracture surface without even partial coverage of fracture minerals. The rock sample is judged to be fresh and essentially unaltered to the naked eye. It is important to note that in many instances, the fresh and uncoated fracture surfaces cannot be explained in terms of accidental breakage of the drill core in the drilling process, as the extension of the fracture is observed in the borehole wall rock by the borehole camera (Claesson Liljedahl et al. 2011).

Figure 4-3. *Typical fracture surfaces of Forsmark drill core samples. Photos reproduced from Byegård et al. (2008, Table 2-3). Mineral abbreviations are: chlorite (Chl), calcite (Ca), epidote (Ep), hematite (Hm), laumontite (Lau), prehnite (Pr), pyrite (Py), quartz (Qz).*

The porosity of fracture coatings is often assumed to be relatively high (cf. Figure 4-1). Evidence supporting this claim comes from ^{14}C-PMMA impregnations of fracture-adjacent rock samples. Generally, they suggest that some of the most common fracture minerals, e.g. chlorite and clay minerals, and sometime calcite, have relatively high and accessible porosity (e.g. Penttinen et al. 2006a, b, Siitari-Kauppi et al. 2010, Widestrand et al. 2007, 2010). As the porosity is often positively correlated with the effective diffusivity this would suggest that fracture coatings have high effective diffusivities relative to the underlying rock.

In some instances, fracture minerals are discussed in terms of having very low porosities or even being impervious (armouring). There are observations from ^{14}C-PMMA impregnation studies suggesting that some fracture minerals have a non-connected, or very poorly connected, porosity. Such observations have been associated with calcite and carbonates (Siitari-Kauppi et al. 2010), as well as with fracture adjacent rock layers subjected to mylonitization (Widestrand et al. 2007, 2010). For the Forsmark site, there is no observation that could either support or disprove the notion that part of the fracture surface is covered by fracture coatings of low or poorly connected porosity.

4.1.2 Alteration rim

Beneath fracture coatings (if they exist), the underlying rock may be altered or disturbed. There is ample evidence from ^{14}C-PMMA impregnations (e.g. Siitari-Kauppi et al. 2010), and in a few instances from laboratory diffusion experiments (e.g. Vilks et al. 2005, Widestrand et al. 2007, Selnert et al. 2008) that the alteration rim has an increased porosity and effective diffusivity compared to that of undisturbed rock. A quantitative discussion on this matter this is provided in Sections 5.5 and 5.6.

Figure 4-4 shows an autoradiograph of a rock sample taken from Feature A at the TRUE 1 site at the Äspö Hard Rock Laboratory (Andersson et al. 2002). The studied fracture surface is to the left in the figure. The autoradiograph was made subsequent to ^{14}C-PMMA impregnation. Darker areas indicate porous parts of the rock matrix that were filled with ^{14}C-PMMA. The orange rectangles on the autoradiograph indicate windows at the fracture surface where the average porosity has been estimated based on image analysis of the autoradiograph intensity. The estimated porosity for each window is shown in the graph directly below the autoradiograph as a function of distance from the fracture surface. As can be seen from the figure, an increased porosity extends about half a centimetre into the rock matrix. As can also be observed from the autoradiograph, the increased intensity in micro fractures at the fracture surface plays a significant role for this increased porosity.

As shown in Figure 4-4, the alteration rim is most likely not a distinct layer featuring constant diffusive properties. It is rather, a zone of increased porosity at the fracture surface that gradually decreases with distance until it approaches the porosity of the underlying undisturbed rock matrix. The thickness of this zone is often reported to be on the order of a centimetre in terms of increased matrix diffusion properties but may be considerably larger when described in terms of other observable features, such as red staining by hematite.

In general, alteration and disturbance can have a mechanical, thermo-mechanical, or chemical origin. From a mechanical point of view, micro-fracturing of the fracture-adjacent rock may have occurred in tectonic events that subjected the rock to increases or decreases in stress. In an earthquake, for example, a slip may be induced at the fracture plane which creates micro fractures in the rock matrix. Such a slip often results in decreased rock stresses which could manifest in a locally less compressed rock matrix. This could potentially increase the overall microporosity in a similar fashion as destressing rock samples in the laboratory creates increased porosities (Jacobsson 2007) and effective diffusivities (Skagius and Neretnieks 1986). Even just the existence of an imbalanced stress distribution at the surface of a partially open fracture surface hosted in stressed rock can cause this. An increased mechanical stress at the fracture plane (e.g. during the build-up of stresses prior to the slip) may also lead to mineral recrystallization that could locally create anisotropic rock with very different microstructural characteristics. In some instances, such as in the case of mylonitized rock (as illustrated in Figure 4-1), this may decrease the effective diffusivity normal to the fracture surface. Recrystallization could also occur in thermal or thermo-mechanical events during the rock uplift. If the recrystallization gives rise to an alteration rim of finer grain size, the effective diffusivity could be decreased (or, less frequently, increased) in more than one direction.

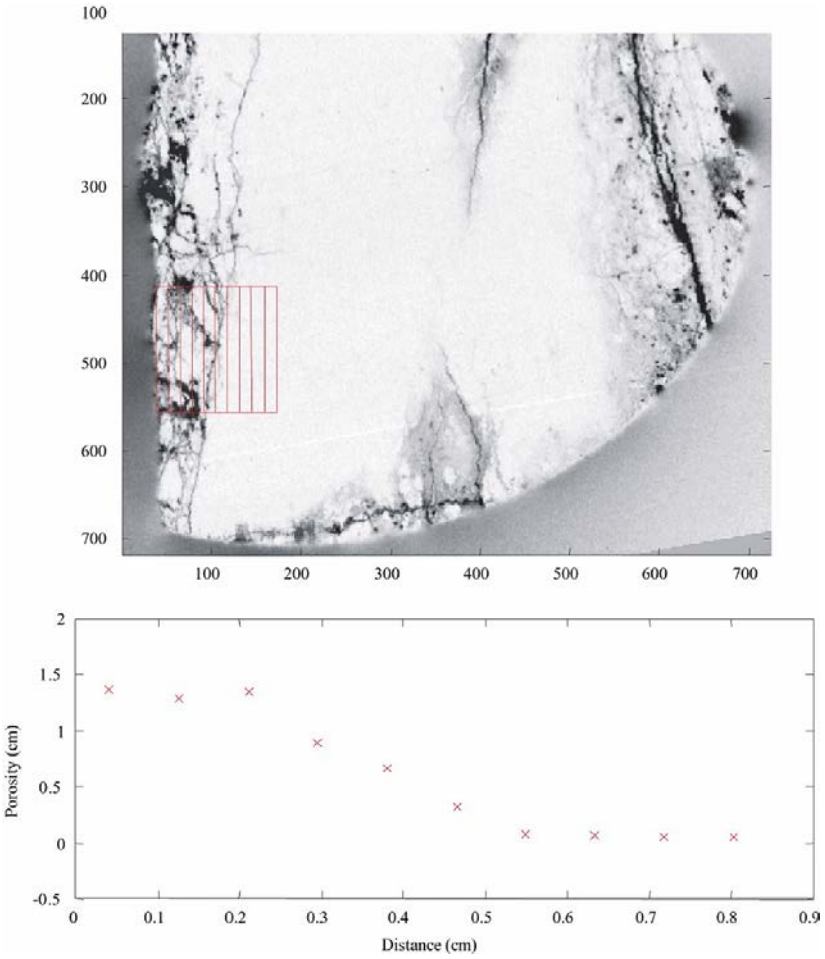

Figure 4-4. *Results of ^{14}C-PMMA impregnation of a sample of Feature A from KXTT3 (TRUE-1). Photo: Autoradiograph with averaging windows (bins) shown at different distances roughly perpendicular from the fracture surface. Graph: Porosity variation in the rock versus distance from fracture surface estimated from the autoradiographic binning analysis. Image reproduced from Anderson et al. (2002, Figure 7-6).*

From a geochemical point of view, alteration processes may have affected the fracture-adjacent rock at high temperatures in hydrothermal events, when the bedrock was at greater depth in the lithosphere during earlier stages of orogenesis. Such local alteration should not be confused with the ductile deformation that can occur in large parts of the rock mass when the bedrock was actively undergoing uplift. Weathering alteration may also occur by water-rock interactions at more moderate temperatures in geologically recent times after the bedrock uplift.

Figure 4-5 shows a few different types of altered rock samples taken from Forsmark. The upper left-hand photo, Figure 4-5(A) shows strongly altered and heavily fractured fault rock which, in the case shown, is also non-cohesive and friable. The upper right-hand photo, Figure 4-5(B) shows a sealed fracture network featuring mainly breccia and cataclasite with interstitial fracture fillings typically consisting of laumontite, calcite, epidote, or chlorite (often mixed). Byegård et al. (2008) judge that its potential impact on radionuclide retardation might be by constituting fast diffusion pathways from the fracture into the rock matrix. This would be a result of its increased porosity and effective diffusivity relative to the underlying rock matrix. The lower left-hand photo, Figure 4-5(C) shows rock that has been subjected to extensive, hydrothermally mediated quartz dissolution. This altered rock type, called “vuggy” rock, is only sparsely occurring at Forsmark. Its porosity is so high that pores can be seen by the naked eye. In fact, this rock type is sufficiently permeable that advective flow can potentially outcompete diffusive processes as a transport mechanism through the rock matrix.

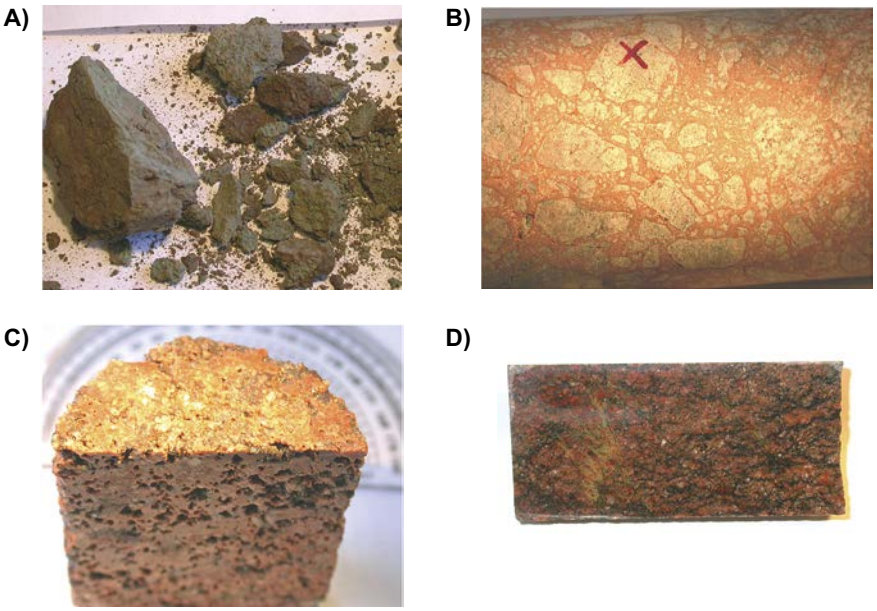

Figure 4-5. *A few different alteration types occurring at Forsmark. A) strongly altered and partly incohesive fault rock; B) sealed fracture networks consisting of cataclasite and breccia; C) quartz dissolved "vuggy" rock; D) oxidised wall rock with medium to strong alteration intensity. Photos reproduced from Byegård et al. (2008, Table 2-4).*

The lower right-hand photo, Figure 4-5(D) shows rock that has become altered by oxidation. Although oxidised rock may feature a slightly increased porosity and effective diffusivity relative to the underlying undisturbed rock, the difference is minor (e.g. Vilks et al. 2005). Accordingly, common observable characteristics of an oxidized alteration rim, such as red staining of minerals by hematite precipitates, may be of limited value for determining the thickness of the alteration rim with regard to its matrix diffusion properties. On the other hand, as noted in Byegård et al. (2008), oxidation may have an impact on the sorption properties of the altered rock, especially for radioelements that sorb by way of a surface complexation mechanism.

4.1.3 Undisturbed rock

In safety assessment calculations, one seeks to use conservative data when there are uncertainties in observed input data so radiological consequences are not underestimated. As a result, a strategy was developed for the Forsmark and Oskarshamn site investigations to focus the radionuclide retention studies on rock that is relatively undisturbed by the presence of fractures (e.g. Berglund and Selroos 2004, Widestrand et al. 2003). It should be noted that by undisturbed rock, we mean rock underlying the alteration rim. This category therefore also includes rock that has been subjected to large-scale deformation. Such rock generally has lower porosity and effective diffusivity than rock in the alteration rim and should provide a higher resistance towards matrix diffusion. Data from both laboratory investigations and in situ measurements suggest that the variation in micro porosity is small and that the variation in effective diffusivity is relatively well-constrained for the undisturbed rock matrix. This is especially true for the Forsmark site (Crawford 2008, SKB 2010c, Section 6.8) and, although to a lesser extent, also for the Laxemar site (Crawford and Sidborn 2009, SKB 2010d, Appendix A8).

In the site descriptions, the rock mass was described as being either hosted within deformation zones, or outside deformation zones. In general, rock within deformation zones tends to have higher porosity and effective diffusivity than rock outside deformation zones, even though it is not necessarily fracture-adjacent (Crawford 2008, Crawford and Sidborn 2009). It should be noted that these deformation zones may be caused by both brittle and ductile deformation and are much more extensive than the alteration rims discussed in the above section.

4.2 The layered rock model and fracture classes

In the few safety assessments that have explicitly considered a layered rock matrix microstructure, e.g. the Finnish safety assessments TILA-99 (Vieno and Nordman 1999, Section 11.5) and TURVA-2012 (Posiva 2013, Section 7.8), the rock directly adjacent to the flowpaths was assigned a larger effective diffusivity and porosity than the undisturbed rock matrix. In other safety assessments, for example the Swiss Kristallin-I (Nagra 1994) and SKI Site-94 (SKI 1996), matrix diffusion was only permitted in the fracture coatings and alteration rim around fractures, while diffusion into the undisturbed rock matrix was conservatively neglected. This indicates either an acknowledgement of much lower diffusive potential in the undisturbed rock matrix relative to the fracture adjacent rock, or that deeper penetration was not deemed necessary in the modelling to achieve the safety assessment goals. A summary of how matrix diffusion was handled in eight different safety assessments between 1983 and 1999 can be found in SKB (2004 Section 4.3).

When setting up a retardation model, the surrounding rock can in many cases be assumed to have constant retardation properties along the entire flowpath. Alternatively, as we have done in this work, the fracture adjacent rock is divided into different classes that are distributed along the flowpath. In this present work, we call these "fracture classes" where each fracture class constitutes a rock layer sequence and where each layer is assigned different properties. A conceptual image of this is shown in Figure 4-6, where a flowpath intersects two sections of layered rock.

In our layered rock model, each layer is assigned individual retention properties and the properties are assumed to be temporally and spatially constant within the layer. The layers are also assigned unique thicknesses that are assumed to not vary. Furthermore, the upper and lower rock volumes are treated as mirror images, which is a deviation from the natural situation where opposite fracture surfaces typically feature different fracture coatings (Eklund and Mattsson 2009, Löfgren and Sidborn 2010). The model is conceptually similar to the rock model introduced in the safety assessment TURVA-2012. There, the flowpaths were divided into four different transport classes including; clay fractures, calcite fractures, slickensided fractures, and other (uncoated) fractures (Posiva 2013, Section 7.8.2). The first three of these transport classes feature layered rock structures that include the fracture coating, an alteration halo (i.e. alteration rim), and unaltered rock. The fourth class was assumed to comprise unaltered host rock only.

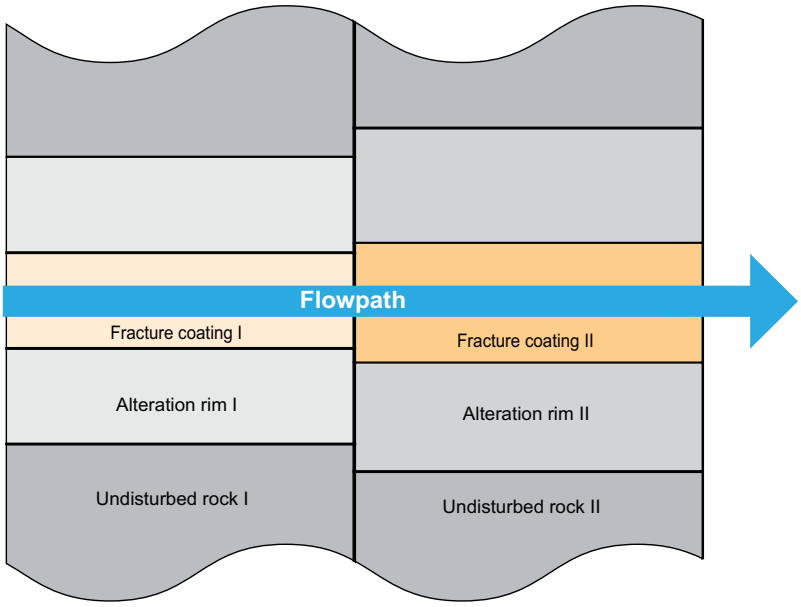

Figure 4-6. *Conceptual model of two distinct rock volumes through which a flowpath traverses; each having different layers featuring different properties. Layers such as these may constitute the building blocks of a layered rock model.*

In our modelling approach, we aim to give a more realistic representation of the repository host rock as compared to that considered in SR-Site. Despite this, some simplifications concerning the flowpath and fracture-adjacent rock remain the same as in SR-Site:

- The properties of the flowpath are the same as in SR-Site. This means that flowpaths are confined to planar structures of uniform aperture; free from fault gauge and without surface roughness, stagnant zones, and preferential flowpaths. Furthermore, the local flowpath is for each section confined to a single fracture, as opposed to being distributed between several fractures in a fracture zone, or parallel flowpaths within fracture clusters. This does not prohibit the flowpath from following a larger-scale connected fracture network.
- Each layer is treated as a homogeneous volume with uniform properties. We thereby neglect the fact that the micro porosity consists of different pore types that have different transport properties. We also neglect the possibility that different mineral types in each layer might have differing sorption properties.
- The underlying process for matrix diffusion is the same as in SR-Site (i.e. Fickian diffusion in a homogeneous medium). Linear, reversible adsorption is assumed and other non-adsorptive immobilisation processes are neglected. Only one-dimensional matrix diffusion is accounted for which means that species can only diffuse orthogonally to the flowpath direction, but not along it, nor in a radial configuration which might be more appropriate for highly channellised flow.
- Hydrodynamic dispersion within the flowpath is assumed to be the same as in SR-Site and characterised by a Péclet number of 10.
- If there are patches of fracture covered with impervious mineral coatings, the rock volume behind this spot is assumed to be unavailable for retention in our model (in the natural system, diffusion occurs in a three-dimensional pattern and this rock volume would be potentially accessible to radionuclides).

4.2.1 Setup of fracture classes

While the flowpath of Figure 4-6 is only shown intersecting two fracture classes, it is likely that the natural case would be better represented by introducing additional fracture classes and further segmentation of the flowpath. Different flowpath segments can thereby be comprised of different fracture classes, allowing them to have differing impacts on the retardation. In setting up the fracture classes, however, a few important observations and criteria were honoured as described in the following paragraphs.

Firstly, when locating the deposition tunnels of the KBS-3 repository, it is assumed that there will be a reasonably large respect distance to major deformation zones. Furthermore, when accepting or rejecting individual deposition hole locations it is generally considered advantageous to stay clear of significant hydraulic structures, even if they are not directly associated with large deformation zones. To account for this in our layered rock model, the host rock has been divided into two principal rock volumes. The first corresponds to the rock immediately surrounding the canister deposition holes and tunnels. This rock volume was labelled the immediate far-field in Crawford (2008) and roughly corresponds to the so-called hydraulic rock domain in the site descriptive models of Forsmark and Oskarshamn. In this rock volume, the flowpaths are assumed to be predominately hosted in discrete stochastic fractures. A heuristic rule which we have adopted in the modelling is that the F-factor (i.e. the flow-related transport resistance) in the immediate far-field is assumed to constitute about 90 % of the F-factor along the entire flowpath through the geosphere. This is arbitrary, although not inconsistent with typical flowpaths leading from the repository as identified using particle tracking in the site scale hydrogeological DFN modelling (e.g. Crawford 2008). As the flowpaths leave the immediate far-field, they enter what we call the distant far-field. In this rock volume, flowpaths may be hosted in larger deformation zones. In this work, it is assumed that the distant far-field constitutes the last 10 % of the cumulative flowpath F-factor.

Secondly, there is good evidence from the site investigations and supporting research that some percentage of the open fractures (or fracture planes) are covered by fracture minerals that are relatively porous. Therefore, our fracture classes should include at least one class with a relatively porous fracture coating.

Thirdly, there are good indications from the site investigations, especially at Forsmark, that a percentage of the sampled fractures are characterised by fresh wall rock that is not coated by any fracture minerals. Accordingly, at least one class should feature uncoated wall rock. This fracture class is in conformity with the fourth transport class of the safety case TURVA-2012 described as "other" (uncoated) fractures.

Finally, there are indications that some fracture mineral coatings, as well as mylonitized or highly anisotropic parts of the fracture adjacent rock, have a relatively low porosity and reduced pore connectivity. Even though such fracture coatings aren't likely to be widely distributed, they are conceptually important for safety assessment considerations, as they may hinder radionuclide retention in part of the underlying rock matrix.

In recognition of the above observations and heuristic assumptions, we use four different fracture classes in our layered rock model. These fracture classes are mostly defined based on the nature of the fracture coating, or absence of it. With the current state of site-specific knowledge, we cannot presently predict what type of altered rock is more likely to be associated with a specific type of fracture coating. This gap in knowledge is handled by; 1) varying the altered rock properties in the sensitivity studies described in Chapter 6 and Chapter 8; and 2) by assuming pessimistic material property values. The modelling in Chapter 8 demonstrates the importance of the alteration rim properties for quantification of radiological risk, and in the detailed site investigations it would therefore seem wise to focus on better characterising these.

Three of the fracture classes, denoted fracture class F1:1, F1:2, and F1:3, are assigned to the immediate far-field. Accordingly, they represent the discrete fracture network residing outside of deformation zones. The fourth class (fracture class F2:1) is assigned to the distant far-field and represents the very heterogeneous flowpaths presumed to be hosted in (major) deformation zones. Concerning rock that is undisturbed by the presence of open fractures, the large body of evidence available suggests that this rock has similar matrix diffusion properties in different host rock volumes (e.g. Selnert et al. 2008, Crawford 2008, SKB 2010c). A small difference is observed, however, between the matrix diffusive properties of apparently undisturbed rock within and outside deterministically determined deformation zones. Consequently, it is reasonable to use the same properties of the undisturbed rock for the fracture classes within the immediate far-field, while assuming different properties for the distant far-field. The resulting layered rock model is illustrated conceptually in Figure 4-7, although the order of fracture classes in the immediate far-field may be assumed to vary in specific realisations.

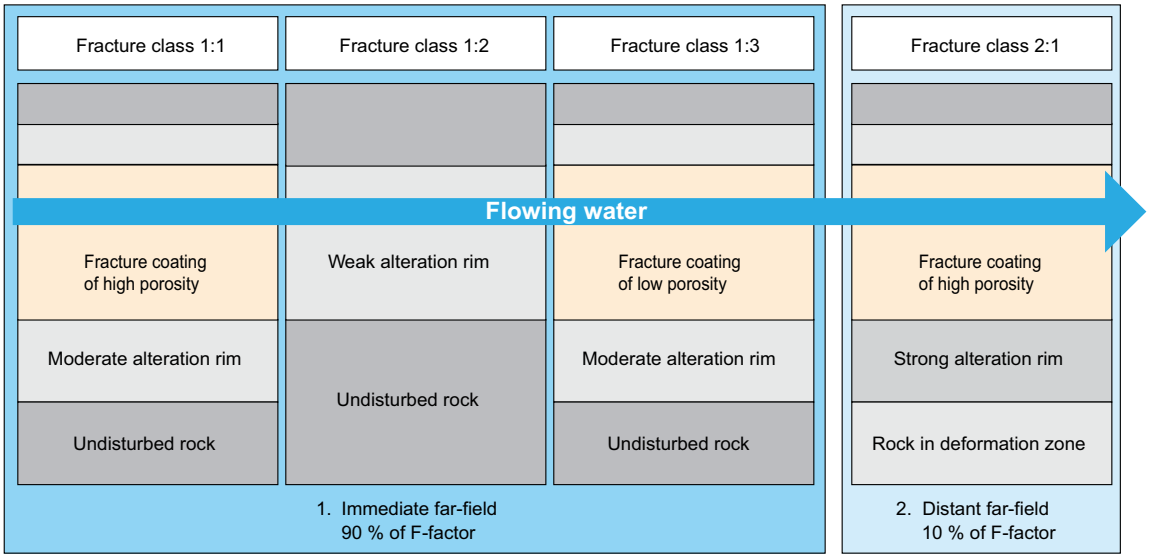

Figure 4-7. *General setup of our layered rock model. The fracture classes of the immediate far-field may be distributed in different manners along the flowpath in different modelling cases. The distribution of the hydrodynamic transport resistance (F-factor) between the different fracture classes is arbitrary in this example, although intended to be a realistic representation of what we think is reasonable.*

Fracture class F1:1

The first fracture class (F1:1) features a fracture coating of relatively high porosity and effective diffusivity. In this modelling exercise, we assume that the coating consists of a mixture of the commonly occurring fracture minerals chlorite and clay minerals, based on Byegård et al. (2008 Section 2.2.1) and Löfgren and Sidborn (2010). It can also be envisioned that calcite is intermixed in the fracture coating, as long as it has a relatively high porosity. However, this latter possibility has not been implemented in the quantifications of fracture class F1:1. This fracture class is consistent with how rock surrounding discrete fractures is usually perceived in sparsely fractured crystalline rock at depth, outside major deformation zones. Therefore, an alteration rim of moderate width is assumed to overlay the undisturbed rock.

Fracture class F1:2

The second fracture class (F1:2) features no fracture coating, which is consistent with observations of fresh fracture surfaces found when mapping the drill cores in the site investigations. The fact that the fracture surfaces are denoted as fresh in the background documentation (e.g. Stephens et al. 2007, Eklund and Mattsson 2009) indicates that they have little chemical alteration. However, the fracture adjacent rock may still have been subjected to mechanical disturbance and de-stressing. Hence a weak alteration rim is assumed to overlay the undisturbed rock.

Fracture class F1:3

The third fracture class (F1:3) features a fracture coating, or a polished fault surface, of low or poorly-connected porosity. Evaluating the consequences of such a layer is in line with the request for complementary information by SSM (cf. first bullet of Section 1.2). For the Forsmark site, there are no dedicated observations that either support or reject the possibility of such a coating or layer. However, there are general observations of both fracture minerals and, for example, mylonitized rock at fracture surfaces having low or poorly-connected porosity.

For the fracture mineral calcite, or at least for the group of carbonates, there are contradictory observations from ^{14}C-PMMA impregnations. On the one hand, many observations suggest that calcite and carbonate coatings are highly porous (e.g. Widestrand et al. 2010, Appendix 3, Kuva et al. 2012). Such observations are consistent with the quantification of the fracture coating layer of the calcite coated[4] transport class in the TURVA-2012 safety case (Posiva 2013, Table 7-14), which was assigned high porosity and effective diffusivity. On the other hand, there are also observations suggesting that some carbonate fracture minerals have a non-connected, or very poorly connected, porosity (e.g. Siitari-Kauppi et al. 2010, Kuva et al. 2012).

There are also observations of mylonitized rock at fracture surfaces having low-, poorly connected, or highly tortuous porosity, giving rise to reduced diffusion rates across the foliation (e.g. Widestrand et al. 2007). In the TURVA-2012 safety case, the slickensided transport class featured a thin layer at the fracture surface having both lower porosity and effective diffusivity than that of the underlying alteration rim (Posiva 2013, Table 7-15). Slickenside is a term for a polished fault surface formed by frictional wear during faulting, although was used in TURVA-2012 to denote any of several types of lineated fault surfaces.

As noted previously, there is little site-specific data for Forsmark supporting or rejecting the notion that part of the fracture plane is covered by a layer of low- or poorly-connected porosity. Even if it does occur, however, it is unlikely that such a layer is widely distributed. Accordingly, only a limited part of the flowpath is postulated to encounter this fracture class in our study. The alteration rim and the underlying undisturbed rock matrix of this fracture class are set to mimic those of fracture class F1:1.

[4] The full designation in Posiva (2013) is "*Calcite (and possibly clay and sulphide) coated fractures*".

Fracture class F2:1

Fracture class F2:1 is assigned to represent flowpaths in water conducting zones in the distant far-field, often coinciding with deterministically identified deformation zones. Such zones may provide fast routes for advective radionuclide transport through the geosphere. Here, the fracture surface is coated by a relatively thick and porous layer of fracture coatings and there exists a strong alteration rim of significant thickness. Underneath the alteration rim, the rock matrix may have been subjected to large-scale ductile or brittle deformation. Consequently, this fracture class has similarities to the investigated fractures in the TRUE series of experiments at Äspö (e.g. Winberg et al. 2003) and the conceptual illustration in Figure 4-1.

5 Quantification of fracture class layer properties

5.1 Material properties of the different layers

An illustration of our layered rock model, comprised of four fracture classes and eleven separately parameterised layers, is shown in Figure 4-7. For each layer, numerical values need to be assigned to the following parameters:

- Layer thickness, L (m).
- Transport porosity, ε_p (%).
- Effective diffusivity, D_e (m^2/s).
- Sorption partitioning coefficient, K_d (m^3/kg).
- Surface coverage fraction, ϕ_s (%).

In this chapter, we attempt to quantify the thickness, transport porosity, and effective diffusivity of the individual rock layers even though there is a lack of site-specific data that occasionally requires the use of coarse approximations. Concerning the K_d-values, the simplistic approach of not assigning individual values to the different layers has been taken. Instead, the best estimate sorption coefficients used in SR-Site for undisturbed rock have been used for all layers without further justification.

Additionally, for each fracture class one needs to assign a portion of the entire flowpath that encounters the particular fracture class. In this work the assumption is that the last 10 % of the flowpath, in terms of the F-factor, traverses features with transport properties characteristic of fracture class F2:1. Hence the remaining 90 % of the F-factor needs to be distributed between fracture classes F1:1 to F1:3. In this work we call this parameter the surface coverage fraction, ϕ_s and is assigned based on the considerations described in Section 5.3.

5.2 Central case quantification

Figure 5-1 shows the central calculation case parameterisation for our layered rock model. The chosen parameter values are justified in subsequent sections. In Chapter 8 a number of these parameter values are varied in sensitivity studies.

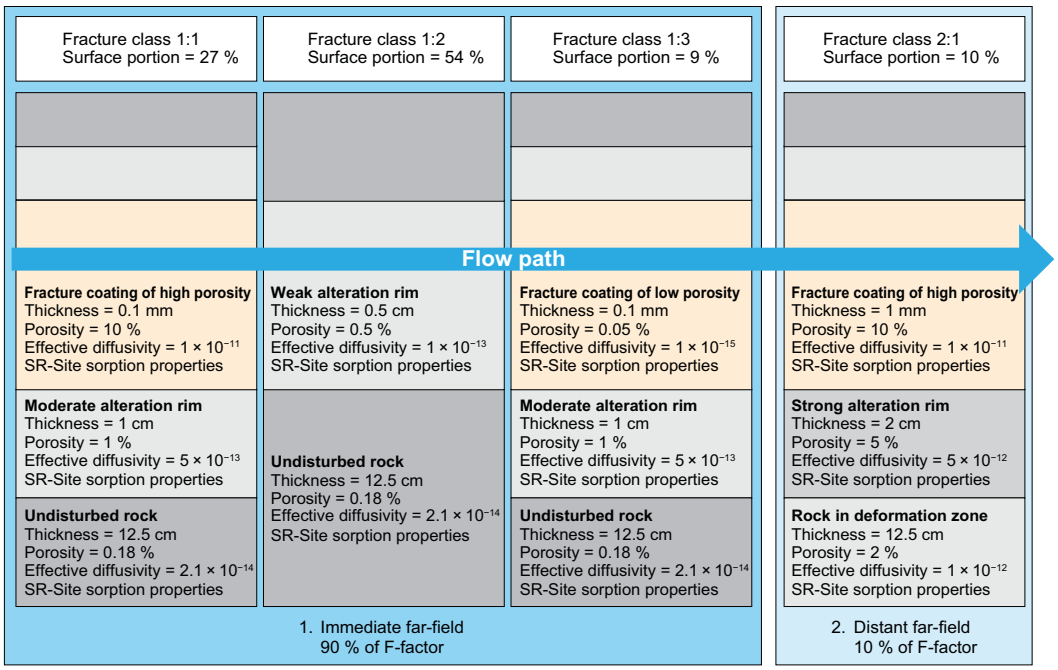

Figure 5-1. *Parameterisation of fracture classes and layers in our central case layered rock model. The upper fracture surface is assumed to be a mirror image of the lower surface.*

5.3 Surface coverage fraction

5.3.1 General considerations

As stated in Section 4.2, fracture classes are assigned largely based on observations of the fracture coating and undisturbed rock only, since there is a lack of site-specific data concerning the alteration rim. For the immediate far-field, the same properties are assumed for the undisturbed rock in each fracture class. Accordingly, the estimated surface coverage fractions for the associated fracture classes are based solely on the estimated extent of fracture coating, or its absence.

In a special site-specific campaign aimed at quantitatively mapping fracture surfaces of drill cores, the surface coverage and thickness of the most common fracture minerals were investigated (Eklund and Mattsson 2009, Löfgren and Sidborn 2010). The campaign was largely focused on local rock volumes where groundwater flow had been previously detected by the Posiva difference flow meter in the site investigation. One meter of drill core on each side of 401 flow anomalies (so called PFL-anomalies) were investigated and the fracture minerals of 2 071 open fractures were mapped. For each fracture, up to eight layers of fracture minerals on each side of the fracture surface, were recorded. Not all fracture minerals were mapped, but only the ones judged to have the greatest impact on solute transport and reaction. These minerals were calcite, chlorite, clay minerals (considered as a group), hematite, and pyrite. In addition, observations of hematite staining as well as occurrences of uncoated, seemingly fresh wall rock were recorded.

In the following paragraphs, the mapping methodology concerning the total coverage is briefly described. Since the details given are relatively sparse, the reader is recommended to review the full description of the mapping campaign given in Löfgren and Sidborn (2010). The total coverage represents the percentage of the drill core fracture surface that an individual fracture mineral layer was found to cover. Figure 5-2 illustrates a drill core sample where the rock matrix is overlaid by three different mineral layers covering a natural fracture surface. The individual layers do not have to cover the entire surface, and do not have to have a uniform thickness (as illustrated by layer A).

The total coverage of each layer is estimated based on ocular inspection of the layer occurrence at the perimeter of the drill core sample, as well as by ocular inspection normal to the fracture surface. If, for the sake of simplicity, we assume that the layers in Figure 5-2 are constant in the z-direction, layers A, B, and C have total coverages of 40 %, 60 % and 80 %, respectively. The presence of any given fracture mineral is thus not mutually exclusive with the presence of another mineral on the same patch of fracture surface. This leaves an uncoated surface of 20 %.

Judging from existing site-specific knowledge of fracture surfaces (e.g. Eklund and Mattsson 2009), fracture minerals are often found to cover small patches of the fracture surface, as illustrated in Figure 5-2. Furthermore, there are often patches of uncoated fracture surfaces. This suggests that even on the scale of the drill core's cross-sectional area (~ 0.002 m^2), different parts could conform to hypothetically different fracture classes. To acknowledge this small-scale heterogeneity when estimating the surface coverage fraction, the chosen approach is to sum all fracture surface areas conforming to a fracture class, irrespective of how small the areas of the individual patches are. From the perspective of solute transport modelling, where flowpath averaging of fracture properties is typically performed in one way or another, one is interested in the overall proportion of the flowpath associated with various representative elementary volumes featuring differing retention properties. Provided the different rock volumes on a larger scale feature similar patterns of fracture mineralisation, the local sequence of the fracture classes is presumed to be of limited importance. By analysing the distribution of the most important fracture minerals at Forsmark it was concluded that there is no great difference in fracture mineral occurrences and abundances between large-scale rock volumes (Löfgren and Sidborn 2010, 2016). Consequently, the approach of summing all surfaces conforming to a fracture class is judged as suitable for providing input data to solute transport modelling.

By using raw data from the mapping campaign described in Eklund and Mattsson (2009) and in Löfgren and Sidborn (2010), it can be determined, on average, what percentage of the fracture surface is covered by chlorite and clay minerals (fracture class F1:1) and what percentage is considered uncoated (fracture class F1:2). Determining the surface coverage fraction of fracture class F1:3 is more difficult as there

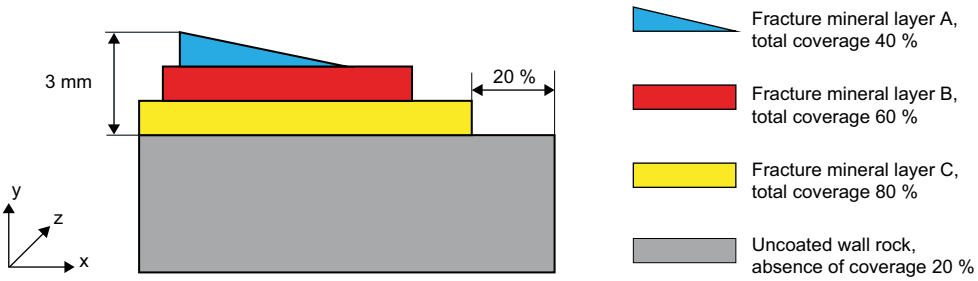

Figure 5-2. *Illustration of a rock sample covered by three fracture mineral layers that are stacked on each other, revealing an uncoated surface of 20 %.*

are no site-specific observations that can be used to associate a specific fracture mineral to this particular fracture class. This has been resolved by using the surface coverage of calcite as a proxy for fracture class 1:3, and by varying its surface coverage fraction in the sensitivity studies described in Chapter 8. Any improvement to this approach requires input data from future dedicated drill core mapping campaigns. In Löfgren and Sidborn (2010), fracture mapping data were sorted into different elevation ranges, where the range 300–500 m b.s.l. (metres below sea level) is of primary interest for the immediate far field. However, when treating raw data in this present report, input from the entire elevation range (i.e. from ground surface to the end of borehole, up to 1 000 m deep), have been used. This is deemed acceptable as only relatively small differences between pooled data sets from different elevation ranges were observed in Löfgren and Sidborn (2010).

5.3.2 Fracture class F1:1

The fracture minerals chlorite and clay minerals (as a group) are assumed to coat the fracture surfaces of fracture class F1:1. Although the minerals are treated in Löfgren and Sidborn (2010), that report does not provide data on the total coverage for combinations of these minerals. Consequently, we were compelled to revisit the raw data[5] of the 2 071 open fractures mapped in Eklund and Mattsson (2009). In Table 5-1, averaged data for the (up to) eight individually recorded fracture mineral layers of the mapping campaign are provided. The column "Population fraction" refers to the percentage of all the 2 071 fractures for which the specific fracture mineral, in the specific layer, was recorded. The column "Mean total coverage" is obtained by pooling the total coverages for the specific fracture mineral in the specific layer and by taking the arithmetic mean. The column "Mean layer thickness" concerns the thickness of the fracture mineral layers and is explained in detail later in this chapter.

Table 5-1. Arithmetic mean of total coverage and thickness of the (up to) eight layers of fracture minerals recorded for each open fracture. Data for chlorite, clay minerals and calcite are based on all 2 071 fractures mapped in Eklund and Mattsson (2009).

	Upper layer 1			**Upper layer 2**		
	Population fraction	Mean total coverage	Mean layer thickness[1]	Population fraction	Mean total coverage	Mean layer thickness
Chlorite	11 %	49 %	0.07 mm	26 %	51 %	0.11 mm
Clay minerals	17 %	42 %	0.07 mm	3 %	40 %	0.07 mm
Calcite	38 %	21 %	0.11 mm	11 %	27 %	0.12 mm
	Upper layer 3			**Upper layer 4**		
	Population fraction	Mean total coverage	Mean layer thickness	Population fraction	Mean total coverage	Mean layer thickness
Chlorite	9 %	62 %	0.09 mm	1 %	74 %	0.12 mm
Clay minerals	0.3 %	39 %	0.08 mm	0 %	-	-
Calcite	1 %	42 %	0.16 mm	0.1 %	23 %	0.08 mm

[5] Data delivery note Sicada_08_090.

Table 5-1. Continued.

	Lower layer 1			Lower layer 2		
	Population fraction	Mean total coverage	Mean layer thickness	Population fraction	Mean total coverage	Mean layer thickness
Chlorite	12 %	50 %	0.08 mm	24 %	55 %	0.10 mm
Clay minerals	18 %	45 %	0.08 mm	3 %	44 %	0.08 mm
Calcite	33 %	21 %	0.10 mm	11 %	22 %	0.14 mm
	Lower layer 3			**Lower layer 4**		
	Population fraction	Mean total coverage	Mean layer thickness	Population fraction	Mean total coverage	Mean layer thickness
Chlorite	8 %	62 %	0.09 mm	1 %	67 %	0.09 mm
Clay minerals	0.3 %	62 %	0.11 mm	0 %	-	-
Calcite	1 %	38 %	0.23 mm	0.1 %	25 %	0.10 mm

[1] For all individual mineral layers, when a mineral coverage is recorded but its thickness is below detection limit (0.1 mm), the thickness 0.05 mm is assigned (half of the detection limit).

As one can see from Table 5-1, clay minerals were found in the layer directly facing the fracture (layer 1) in 17 % and 18 % of the cases for the upper and lower fracture surface, respectively. However, on average only 42 % and 45 % of these fracture surfaces were covered by clay minerals in layer 1. In layer 2, clay minerals were only found in 3 % of the cases for both the upper and lower fracture surfaces. Their mean total coverages were 40 % and 44 %. Occurrences in layers 3 and 4 are sparse or even non-existant and these layers have been neglected when processing the data.

Based on the adopted methodology, the same fracture mineral cannot be recorded in two adjacent layers for the same fracture surface. They would then have been recorded as a single layer of greater thickness. Fracture surfaces having clay minerals recorded in the first layer are thereby separated from those having clay minerals in the second layer. When estimating the total coverage along the flowpath, one can add the contribution from these separate fracture surfaces. In practice this means adding the contribution from layers 1 and 2. This is done in the following fashion:

$$\text{Total flowpath coverage, clay minerals} = \sum\left(\frac{\text{population fraction} \times \text{total coverage}}{2}\right)$$

- $$= \left(\frac{17\% \cdot 42\% + 3\% \cdot 40\% + 18\% \cdot 45\% + 3\% \cdot 44\%}{2}\right) \approx 9\%$$

All of the percentages used in the estimation are described in the previous paragraph above. The sum is halved to account for the fact that both fracture surfaces of the fracture have been used in the calculation. For chlorite it turns out that significant occurrences are also noted in mineral layer 3, in addition to occurrences in layers 1 and 2 (cf. Table 5-1). However, for unknown reasons, there is no fracture where the occurrence of chlorite has been recorded in both layer 1 and 3 with an interspersed layer of another mineral. As previously argued in the paragraphs above, occurrences cannot be recorded in both layer 1 and 2 or in layer 2 and 3 for the same fracture surface. As a result, we can calculate the "total coverage of flowpath" for chlorite in an analogue way as for clay minerals, although incorporating data for the first three layers.

$$\text{Total flowpath coverage, chlorite} = \sum\left(\frac{\text{population fraction} \times \text{total coverage}}{2}\right)$$

- $$= \left(\frac{11\% \cdot 49\% + 26\% \cdot 51\% + 9\% \cdot 62\% + 12\% \cdot 50\% + 24\% \cdot 55\% + 8\% \cdot 62\%}{2}\right) \approx 24\%$$

All data in the above calculation can be identified in Table 5-1. The raw data, and the mapping methodology, leaves no possibility for combining the "total coverage of flowpath" for clay minerals and chlorite in a rigorous way. It can only be claimed that the combined value should be within the range of 24 %–33 %. The lower limit corresponds to a situation where chlorite and clay mineral layers are

always stacked on each other, as illustrated in Figure 5-2. The upper limit corresponds to a case where the fracture minerals are always found side by side, but never stacked. Based on this, we estimate that roughly 30 % of the fracture surfaces of the immediate far-field consist of fracture class F1:1. As the mineral patches are very small compared to the total surface area of the flowpath, we furthermore assume that fracture class F1:1 corresponds to about 30 % of the immediate far-field in terms of the F-factor. As 90 % of the total flowpath F-factor is assumed to reside in the immediate far-field, the surface coverage fraction, ϕ_s of fracture class F1:1 is given by:

- ϕ_s for fracture class F1:1 = 30 % × 90 % = 27 %.

5.3.3 Fracture class F1:2

In 18 % of the 2 071 open fractures investigated in Eklund and Mattsson (2009), both the upper and lower fracture surfaces were found to be fresh and uncoated. The hypothesis of commonly occurring open fractures lacking any fracture coating has been challenged in Claesson Liljedahl et al. (2011), where a number of fractures have been re-examined. However, for the purpose of this present report it is not the total absence of fracture coatings that is in focus, but the observation that the great majority of he fracture surface is uncoated. For fractures in the elevation range 300–500 m b.s.l., corresponding to the immediate far-field, the percentage of uncoated fractures is 25 % (Löfgren and Sidborn 2010, Table 3-16).

As described in Section 5.3.1 , we sum the contribution from fracture surfaces that are either totally uncoated or only partly uncoated. This was not done in Löfgren and Sidborn (2010) and, accordingly, the raw data obtained in the mapping campaign have been reassessed. By inspecting the raw data, it was found that in an overwhelming majority of the cases, underlying fracture minerals had a higher total coverage than overlying fracture minerals. This can be exemplified by layers A and B in Figure 5-2, where the overlying layer A has a total coverage of 40 % while the underlying layer B has a total coverage of 60 %. Based on this general observation, the assumption was made that layers are stacked on top of each other, but that layers of minor total coverage do not exist side by side with the layer of the largest total coverage. By this approach, the fraction of uncoated rock is taken as 100 % minus the total coverage of the layer having the highest total coverage, out of the possible four candidates, for fracture surface. This approach creates a bias towards a high fraction of uncoated rock and is best used to estimate the upper limit for the potentially uncoated surface area.

In Figure 5-3, a cumulative distribution function (CDF) of the total coverage of the one layer having the highest total coverage per fracture surface is provided, based on data from all of the 2 071 open fractures mapped in Eklund and Mattsson (2009).

Figure 5-3 shows that only about 10 % of the fracture surfaces are entirely coated by, at least, one layer of the investigated fracture minerals. For 23 % of the upper, as well as of the lower, fracture surface, no fracture mineral coats the wall rock. This should not be confused with the 18 % of fractures with both surfaces uncoated, as in this instance the upper and lower surfaces are treated separately. On average (arithmetic mean), the layer having the highest total coverage covers about 39 % of the fracture surface. This sets the upper boundary for the fraction of uncoated wall rock to about 61 %, which is rounded to 60 % in this work. Except for the requirement that layers are stacked and do not exist side by side, there is also the requirement that fracture minerals not mapped in the campaign pose no significant risk of interference with the numerical result. To improve the accuracy of the estimate, a dedicated mapping campaign may need to be undertaken. Presently, we can only bound this uncertainty by sensitivity case studies as outlined in Chapter 8. For the central case, it is judged that the estimate of 60 % represents the fraction of uncoated wall rock in the immediate far-field sufficiently well for the present purpose. It is furthermore assumed that the surface coverage fraction, in terms of the F-factor for the entire flowpath, is:

- ϕ_s for fracture class fracture class F1:2 = 60 % × 90 % = 54 %.

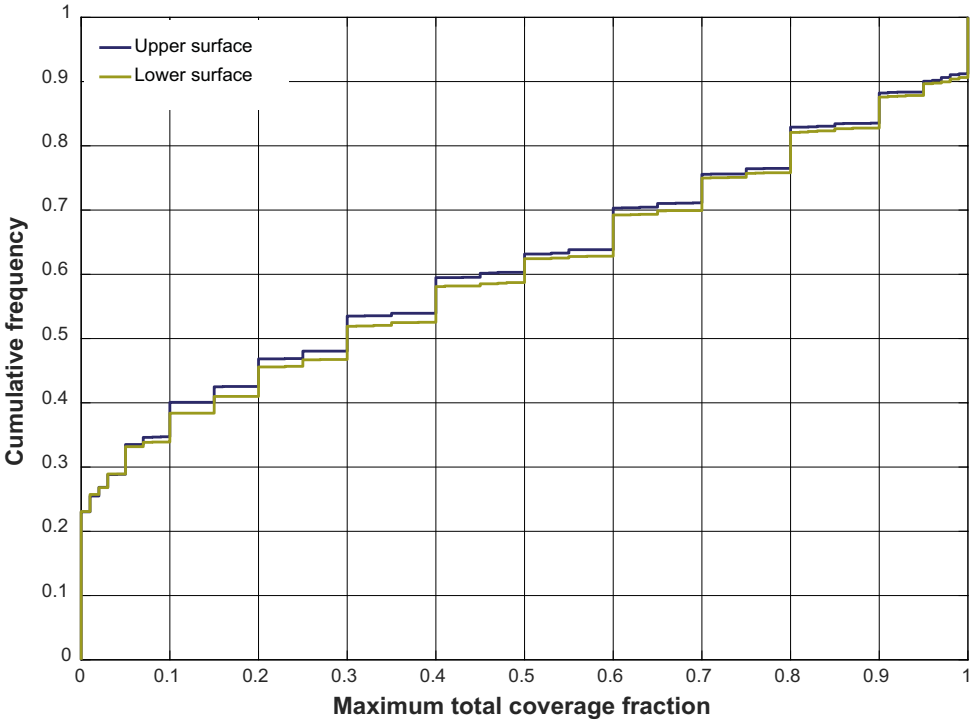

Figure 5-3. *Empirical cumulative distribution function (CDF) of the total coverage of the layer having the highest value per fracture surface for upper (dark blue) and lower (olive-tan) fracture surfaces.*

5.3.4 Fracture class F1:3

The total coverage of calcite is used as a proxy for estimating the surface portion of fracture class F1:3. Table 5-1 shows that calcite is predominantly found in layers 1 and 2, while occurrences in layers 3 and 4 can be largely disregarded. Using the same approach to calculate the "total coverage of flowpath" as for fracture class F1:1, the outcome is:

$$\text{Total flowpath coverage, calcite} = \sum\left(\frac{\text{population fraction} \times \text{total coverage}}{2}\right)$$

- $$= \left(\frac{38\% \cdot 21\% + 11\% \cdot 27\% + 33\% \cdot 21\% + 11\% \cdot 22\%}{2}\right) \approx 10\%$$

All data in the above calculation can be identified in Table 5-1. As 90 % of the total flowpath F-factor is found in the immediate far-field, the surface coverage fraction, ϕ_s is estimated to be:

- ϕ_s for fracture class F1:3 = 10 % × 90 % = 9 %.

Another, non-independent approach for estimating the surface portion of fracture class F1:3 would be to take 100 % minus the summed surface portions of the other fracture classes. Acknowledging that, by way of our assumption, the surface coverage fraction of fracture class F2:1 is 10 %, the outcome would again be 9 %.

5.3.5 Fracture class F2:1

By way of our earlier assumption, fracture class F2:1 is deemed to constitute the last 10 % of the flowpath F-factor. As previously noted, this is an arbitrary figure, although consistent with typical outcomes of particle tracking simulations of migration paths leading from individual canister positions to the surface in SR-Site.

5.4 Layer thickness

5.4.1 Fracture coating

In the fracture mapping campaign of Eklund and Mattsson (2009), the thickness of the individual fracture mineral layers was estimated. This was done by ocular inspection of the fracture surface, mainly at the perimeter of the drill core sample. The estimate was based on the average of five readings at the perimeter (if possible) where the specific layer could be observed. This can be exemplified by layers A and B of Figure 5-2. Here, for the sake of a simple illustrative example, we imagine that the thickness of each layer is 1 mm at the most. Layer A, which has the shape of a triangular wedge, is then assigned a thickness of 0.5 mm while layer B, having the shape of a rectangular prism, is assigned a thickness of 1 mm.

As for the total coverage, the layer thickness was estimated for up to eight layers for each fracture. In Table 5-1, the column "Mean layer thickness" is obtained by pooling the layer thicknesses of Eklund and Mattsson (2009) for the specific fracture mineral in a given layer and by taking the arithmetic mean. As can be seen from the table, the mean layer thickness generally is about 0.1 mm. On many occasions, a fracture mineral layer is noted to exist, having a recorded total coverage, but where the layer thickness is below the detection limit of 0.1 mm. In such cases, a layer thickness of 0.05 mm is assumed in this report, corresponding to half the detection limit.

The upper bounding value for the fracture coating thickness can be obtained by summing the layer thicknesses of the (up to four) individual layers residing on each fracture surface. In doing this, we don't discriminate between different fracture minerals that coat the surface, even in cases where they are associated with different fracture classes. Essentially, we stack the mineral layers as depicted in Figure 5-2 and disregard the possibility that layers may exist side by side. We also disregard the fact that the layers may not cover the entire fracture surface. If taking the example of Figure 5-2, the maximum fracture coating thickness in that case would be 3 mm. This approach was taken by Sidborn and Löfgren (2016) for the 2 071 mapped fractures of Eklund and Mattsson (2009) and Figure 5-4 shows the resulting maximum fracture coating thickness, $d_{c,max}$ (mm), given in terms of a cumulative distribution function.

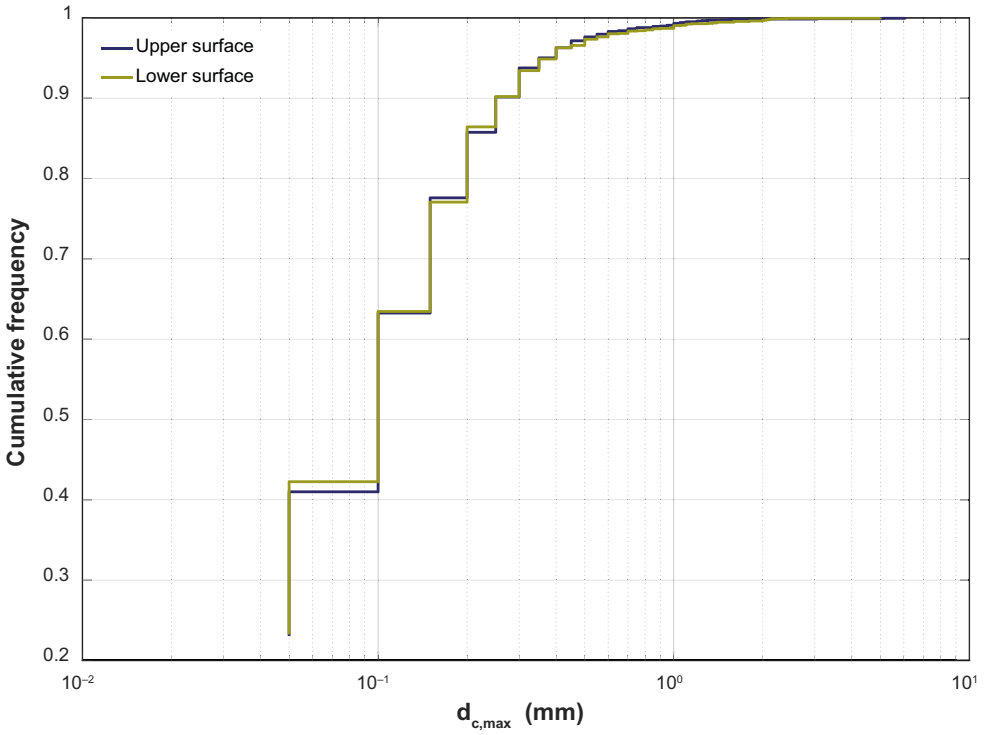

Figure 5-4. *The maximum fracture coating thickness of the upper (dark blue) and lower (olive-tan) surface. Adopted from Löfgren and Sidborn (2016).*

It should be noted that in a few instances Eklund and Mattsson (2009) recorded mineral layers consisting of minerals other than calcite, clay minerals, chlorite and hematite. Data from such mineral layers also form the basis for Figure 5-4. As can be seen, the median value of the maximum fracture coating is 0.1 mm. The results indicate that only on rare occasions, a coating thickness on the order of 1 mm can be expected. A limitation of Figure 5-4 is that it is not based on all fracture minerals existing at the surface, but only the mapped ones. The adequacy of the CDF could be improved by dedicated mapping of fracture coatings where the thickness of the entire fracture coating is quantitatively recorded, which was not the case in Eklund and Mattsson (2009).

The layer thicknesses of Eklund and Mattsson (2009), and of Table 5-1, are not averaged over the entire fracture surface, as was done in Löfgren and Sidborn (2010). This is the correct approach for this report, as the partial coverage of fracture minerals is already incorporated in the layered rock model by using different surface coverage fractions for the different fracture classes. Below, we estimate the fracture coating thickness for the individual fracture classes, based only on fracture minerals that conform to each class.

Fracture class F1:1

Clay minerals (as a group) coat fracture class F1:1, together with chlorite. Clay minerals are frequently found in layers 1 and 2 (cf. Table 5-1) but very sparsely in layers 3 and 4. Accordingly, layers 3 and 4 are disregarded when estimating the layer thickness. As the same fracture mineral cannot exist in two adjacent layers, the occurrences in layer 1 and 2 must correspond to separate fracture surfaces. If weighting the thicknesses of the two upper and lower layers with the population fraction, for the individual fracture mineral, one gets the fracture mineral thickness:

$$\text{Fracture mineral thickness, clay minerals} = \frac{\sum\left(\text{population fraction} \times \text{mean layer thickness}\right)}{\sum \text{population fraction}}$$

$$= \left(\frac{17\% \cdot 0.07\,\text{mm} + 3\% \cdot 0.07\,\text{mm} + 18\% \cdot 0.08\,\text{mm} + 3\% \cdot 0.08\,\text{mm}}{17\% + 3\% + 18\% + 3\%} \right) \approx 0.08\,\text{mm}$$

For chlorite, data from the three upper and lower layers are accounted for, as justified in Section 5.3.2:

$$\text{Fracture mineral thickness, chlorite} = \frac{\sum\left(\text{population fraction} \times \text{mean layer thickness}\right)}{\sum \text{population fraction}}$$

$$= \left(\frac{11\% \cdot 0.07\,\text{mm} + 26\% \cdot 0.11\,\text{mm} + 9\% \cdot 0.09\,\text{mm} + 12\% \cdot 0.08\,\text{mm} + 24\% \cdot 0.10\,\text{mm} + 8\% \cdot 0.09\,\text{mm}}{11\% + 26\% + 9\% + 12\% + 24\% + 8\%} \right)$$

$$\approx 0.09\,\text{mm}$$

The data in the above calculations can be identified in Table 5-1.

Once more, the raw data and the mapping methodology leaves no possibility for combining the thicknesses for clay minerals and chlorite in a rigorous way. One way of combining the data would be to sum the thicknesses 0.08 mm and 0.09 mm, resulting in a fracture coating thickness of 0.17 mm. However, this may lead to an overestimation of the combined thickness, as the two fracture minerals may not always exist in the same fracture, and if they do, they need not have the same total coverages. Therefore, the layer thickness of 0.17 mm is seen as being an upper bounding value. A second possibility for combining the data would be to take the arithmetic mean between the lower bounding value (0.08 mm) and the upper bounding value, resulting in an estimate of 0.13 mm. These two values, 0.13 mm and 0.17 mm can be compared with the CDF of the maximum fracture coating thickness of Figure 5-4. While the thickness 0.13 mm is close to the median value of the CDF, the value of 0.17 mm is in the ~ 80 % percentile. Based on these considerations, we round the layer thickness for fracture class F1:1 to 0.1 mm. This fracture coating thickness can be compared with the corresponding thickness for the clay-coated transport class in the TURVA-2012 safety case, where a layer thickness of 0.2 mm was assigned (Posiva 2013, Table 7-13).

Fracture class F1:3

As discussed previously, data on calcite are used as a proxy for fracture class F1:3, even though the surface adjacent layer may not necessarily consist solely of calcite. Based on data in Table 5-1, the same calculation can be made for calcite as for clay minerals and chlorite. As calcite occurs only sparsely in layers 3 and 4, these layers are disregarded in the calculation. The result is then:

$$\text{Fracture mineral thickness, calcite} = \frac{\sum\left(\text{population fraction} \times \text{mean layer thickness}\right)}{\sum \text{population fraction}}$$

$$= \left(\frac{38\% \cdot 0.11\,\text{mm} + 11\% \cdot 0.12\,\text{mm} + 33\% \cdot 0.10\,\text{mm} + 11\% \cdot 0.14\,\text{mm}}{38\% + 11\% + 33\% + 11\%} \right) \approx 0.11\,\text{mm}$$

This is roughly comparable with the median value of the maximum fracture coating thickness in Figure 5-4. We therefore round the layer thickness for fracture class F1:3 to 0.1 mm. This thickness can be compared with the corresponding thickness for the calcite-coated transport class in TURVA-2012, where a layer thickness of 0.2 mm was assigned (Posiva 2013, Table 7-14).

Fracture class F2:1

No specific mineral is assigned to the fracture coating of this fracture class. It is assumed that the fracture class corresponds to a major fracture zone and that the wall rock is covered by a relatively thick fracture coating. As such, this fracture class resembles the fractures investigated in the TRUE series of experiments at the Äspö Hard Rock Laboratory. From examining Figure 5-4 one can see that the 99 %-percentile of the CDF corresponds to a thickness of about 1 mm. This thickness is assumed for Fracture class F2:1 without further justification.

5.4.2 Alteration rim

In ^{14}C-PMMA impregnations, (e.g. Kelokaski et al. 2001, Penttinen et al. 2006a, b, Siitari-Kauppi et al. 2010, Widestrand et al. 2007, 2010), one can obtain the porosity distribution going from the fracture surface and into the rock matrix. The alteration rim can be seen as a zone of elevated porosity, gradually decreasing towards the background porosity of the undisturbed rock matrix, when moving away from the fracture surface. An example of such a measurement is provided in Figure 5-5, based on a sample from the Oskarshamn site.

A few samples of altered rock from the Forsmark site have been investigated with the ^{14}C-PMMA impregnation technique (Penttinen et al. 2006a). The pool of samples chosen for this study, however, may not necessarily be representative of the host rock at Forsmark from a statistical point of view. This is especially true for the immediate far-field, as heavily altered drill core samples are overrepresented in the study.

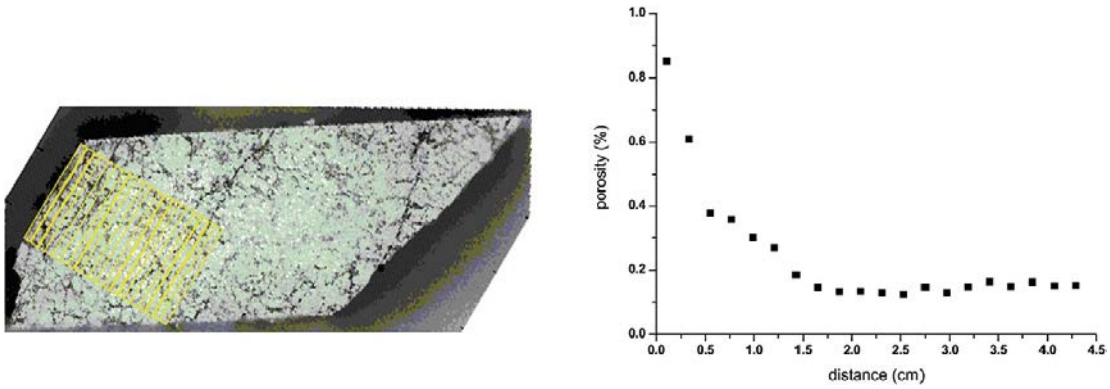

Figure 5-5. *^{14}C-PMMA porosity profile, relative to the fracture surface, for sample O11 from borehole KLX04. Reproduced from Penttinen et al. (2006b, Figure 5-40).*

Fracture class F1:1 to F2:1

Based on the overall (subjective) impression from examining a number of reports on ^{14}C-PMMA impregnations of rock types relevant for the Forsmark site (e.g. Kelokaski et al. 2001, Penttinen et al. 2006a, b; Siitari-Kauppi et al. 2010, Widestrand et al. 2007, 2010), a typical alteration rim thickness appears to be on the order of about 1 cm in cases where the underlying wall rock is not heavily deformed. This thickness is assigned to fracture class F1:1 and F1:3. For fracture class F1:2, featuring a weak alteration rim, a thickness of 0.5 cm is assumed. Fracture class F2:1 features a strong alteration rim with similarities to the generalised conceptual model from the TRUE Block Scale project, shown in Figure 4-1. In Figure 4-1, the alteration rim thickness is shown to be about 10 cm. This thickness, however, may not be relevant for the zone of increased porosity and diffusion properties. Evidence from ^{14}C-PMMA and diffusion studies (e.g. Vilks et al. 2005) does not support the use of such a thick alteration rim. Instead, we have assumed a thickness of 2 cm. An improved quantification of the alteration rim thickness would require a dedicated campaign where, for example, ^{14}C-PMMA impregnations were made to produce profiles as in Figure 5-5. This would also require samples to be chosen in such a manner that they are statistically representative of rock both in the immediate and the distant far-field. The chosen alteration rim thicknesses are summarised in Table 5-2.

Table 5-2. Alteration rim and undisturbed rock thicknesses of the central case of our layered rock model.

Fracture class	Alteration rim thickness	Undisturbed rock thickness
F1:1	1 cm	12.5 m
F1:2	0.5 cm	12.5 m
F1:3	1 cm	12.5 m
F2:1	2 cm	12.5 m

The thickness of the alteration haloes for the layered transport classes varies from 0.3 cm to 1 cm in TURVA-2012 (Posiva 2013, Tables 7-13 to 7-15), which corresponds reasonably well with our chosen values.

5.4.3 Undisturbed rock

The connectivity of the microporous network of the undisturbed rock matrix is often specified to be at least on the decimetre scale. This much has been unambiguously demonstrated in the laboratory and in situ by ^{14}C-PMMA impregnation, diffusion experiments, and electromigration methods (e.g. Birgersson and Neretnieks 1990, Möri et al. 2003, Vilks et al. 2003. Löfgren and Neretnieks 2006, Nilsson et al. 2010). Diffusion profiles from diffusion experiments performed in situ show variously that tracers can typically reach at least 40 cm (Birgersson and Neretnieks 1990), 8 cm (Vilks et al. 2003) and 7 cm (Nilsson et al. 2010) into the rock matrix on the time scale of the experiment. Beyond these depths, either no sampling was made to quantify diffusive penetration, or the detection limit of the analysis method was insufficiently low in relation to the tracer contact time to quantify greater depths of penetration. The fact that both alternating and direct electrical current can be propagated over long distances in the saturated bedrock in the relative absence of electrically conductive matrix minerals (Thunehed 2017, Löfgren 2015), has also been cited as a strong indicator that the pore connectivity is more or less, unlimited. Further supporting evidence for at least dm-scale connectivity comes from the measurements of BET surface areas and independent sorption measurements made using an electromigration method using 9 cm long and 5 cm diameter intact bore core samples (André et al. 2008, 2009).

In SR-Site, the undisturbed rock was assumed to have a microporous network that is connected on all scales relevant for the safety assessment. If unlimited pore connectivity is assumed, the maximum penetration depth for matrix diffusion can (simplistically) be set to the average half-spacing between flow-bearing features so as to not overestimate storage capacity of the rock matrix. The spacing between adjacent flow bearing features was set to 25 m in SR-Site (SKB 2010c, Section 6.7), as a statistical average for the Forsmark site at repository depth. In doing so, the small-scale heterogeneity of hydraulic features was neglected, as they were assumed to be represented by single flowpaths hosted in planar structures. Realistically, the spacing between flowpaths in fracture zones may be much shorter. This can impact, for example, short-term tracer tests.

The approach taken in SR-Site results in a thickness of the undisturbed rock layer of 12.5 m. As shown in earlier safety assessments, and in Chapter 9 of the present work, provided the thickness of the undisturbed rock is on at least a decimetre-scale or greater, the exact value is of limited importance for the overall radiological risk assessment for the typical ranges of Safety Assessment F-factors characterising the fracture-rock-flow system.

5.5 Microporosity

Very few site-specific observations exist on the microporosity of the rock directly adjacent to open fractures. The site-specific data that is available, however, is derived from six drill core samples from Forsmark that were subjected to ^{14}C-PMMA impregnation, providing information on their porosity distribution (Penttinen et al. 2006a). Due to the lack of more detailed observations, additional data from the Oskarshamn (including Äspö), and Oilkiluoto sites have been used (Kelokaski et al. 2001, Penttinen et al. 2006a, b, Siitari-Kauppi et al. 2010, Widestrand et al. 2007, 2010, Ikonen et al. 2015). These sites have some similarities in their geological settings, but also differences. The rock at the Oilkiluoto site, for example, often exhibits higher anisotropy than rock from the other sites.

5.5.1 Fracture coating

General considerations

The porosity data that exists for fracture coatings are mainly based on measurements on sealed fractures, obtained by the ^{14}C-PMMA impregnation method (e.g. Penttinen et al. 2006a). In TURVA-2012, micro porosities were assigned to the fracture coating layer of different transport classes. For the clay-coated and calcite-coated transport classes, a porosity of 6 % was assigned (Posiva 2013, Tables 7-13 and 7-14). The slickensided transport class was given a porosity of 1 % (Posiva 2013, Table 7-15).

Fracture class F1:1

In Penttinen et al. (2006a, Section 4.7), a fracture-adjacent sample from the Forsmark site was investigated by the ^{14}C-PMMA impregnation method. For this sample it was found that there existed mineral bands with a microporosity of over 5 %, and that they also seemed to consist of chloritized biotite. For another fracture-adjacent sample that appeared to be more heavily altered, mineral grains with up to 20 % porosity were detected, partly corresponding to sealed fractures (Penttinen et al. 2006a, Figures 4-24 to 4-27). The report also shows results from impregnations of other rock pieces from the Forsmark site, although they either lack sealed fractures, or the wall rock is atypical for the site.

In Penttinen et al. (2006b, Section 5.6), a fracture-adjacent sample from the Oskarshamn site is discussed, featuring a thick "clayish" fracture coating having a ^{14}C-PMMA porosity greater than 10 %. In Penttinen et al. (2006b, Section 5.7) the porosity of an unspecified fracture filling material is estimated to be about 3-5 %. In Penttinen et al. (2006b, Section 5.7) a rock sample is investigated having altered clay phases forming a connective network of highly porous veins with over 20 % porosity. The report also shows results from impregnations of other rock pieces but those summarised here are judged to be the ones of most relevance for the estimate of the fracture coating porosity. In Kuva et al. (2012, Section 3.2) the porosity of so-called "clay fractures" were investigated by the ^{14}C-PMMA impregnation method for rock samples from Oilkiluoto. The porosity of the sealed fractures varied although, on many occasions, was found to be on the order of 10 %. This was also the general impression obtained from similar investigations in Siitari-Kauppi et al. (2010). In Widestrand et al. (2010, Appendix 3) ^{14}C-PMMA impregnation results from samples taken from the LTDE-SD site at Äspö are shown. For the A03:10 sample, for example, where chlorite/epidote and/or calcite constitutes the sealed fractures, the autoradiographs were found to imply high porosities of up to 30 %.

Based on the above observations, the following guesstimate was made for the porosity of the fracture coating layer of fracture class F1:1:

- Fracture class F1:1, porosity = 10 %.

Fracture class F1:3

This fracture class (F1:3) features a fracture coating or a polished fault surface of low, or poorly-connected porosity. In Siitari-Kauppi et al. (2010), for example, sealed calcite fractures were occasionally found to be non-porous, or of very low porosity. The following conclusion was drawn:

"Fracture fillings were both highly porous and slightly or non-porous; especially carbonate and calcite fillings were found to be low or non-porous by the PMMA method. Calcite is known to be porous but it seems that the pores are isolated and not connecting to the open porosity network. In sample O7, a totally altered cordierite was non-porous contrary to the cordierite grains normally observed in the studied samples."

The hypothesis of non-porous fracture minerals is mainly based on results from the ^{14}C-PMMA impregnation method. The porosity detection limit of this method is roughly 0.05 % (Ikonen et al. 2015). We have subjectively chosen to adopt this value for the fracture class F1:3:

- Fracture class F1:3, porosity = 0.05 %.

Fracture class F2:1

The fracture coatings of deformation zones are often made of porous mixtures of chlorite and clay minerals, although other coatings are also common. We assume the same porosity for this layer as for fracture class F1:1, i.e. 10 %. This porosity equals the lower limit of the porosity range for the very porous coating of the generalised conceptual model from the TRUE Block Scale project, shown in Figure 4-1.

- Fracture class 2:1, porosity = 10 %.

5.5.2 Alteration rim

With the ^{14}C-PMMA impregnation method, (e.g. Penttinen et al. 2006a, b, Siitari-Kauppi et al. 2010, Widestrand et al. 2007, 2010), one can obtain microporosity profiles extending from the fracture surface and into the rock matrix. Such a profile of gradually changing porosity is shown in Figure 5-5. Another example, from a water conducting zone at Forsmark, is shown in Figure 5-6.

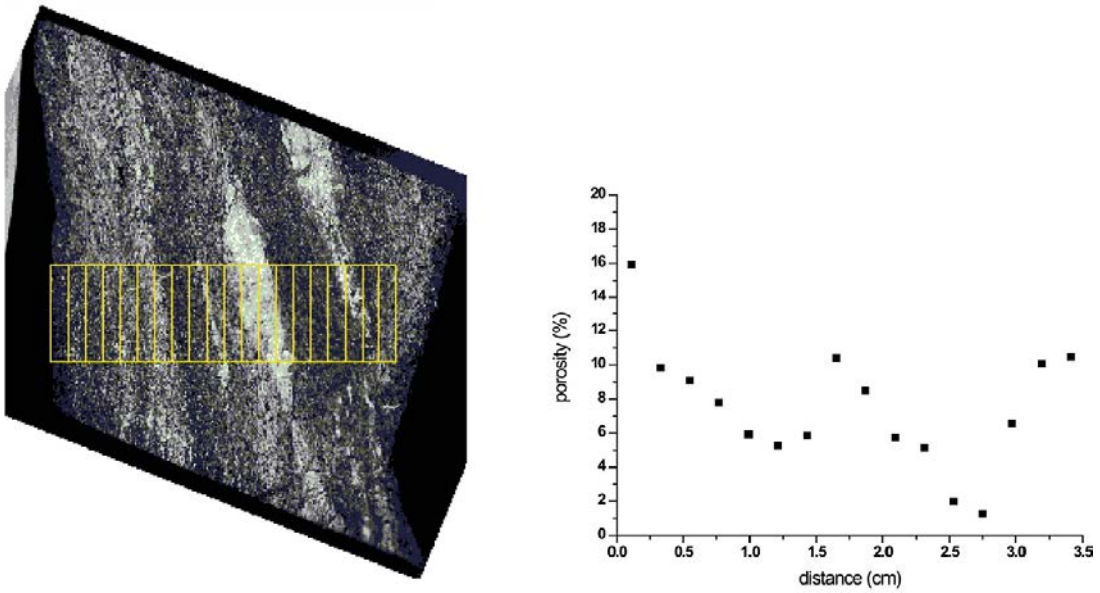

Figure 5-6. *^{14}C-PMMA porosity profile, relative to the fracture surfaces on the left and right, for a sample made of metamorphic granite, granodiorite and tonalite (fine- to medium-grained), taken from within a water conducting zone of borehole KFM 04A. Reproduced from Penttinen et al. (2006a, Figure 4-26).*

Fracture class F1:1 to F2:1

The general impression from the above-mentioned ^{14}C-PMMA impregnation studies is that the elevated porosity of the alteration rim is, on average, about 1 % in cases where the underlying wall rock is not heavily deformed. This porosity value is adopted for the alteration rim of fracture class F1:1 and F1:3. The weak alteration rim of fracture class F1:2 is assumed to have a porosity of 0.5 %. Occasionally, high porosities are found in the first millimetre of the alteration rim even outside deformation zones, although it often decreases rapidly at greater distances from the surface (cf. Figure 5-5).

In deformation zones, the high porosity of the alteration rim may persist for a few centimetres into the rock. In many instances, the underlying rock also has elevated porosities compared to the undisturbed rock outside the deformation zone (cf. Figure 5-6). For fracture class F2:1 we assume a porosity of 5 % over the first two centimetres of wall rock.

The assumed porosities agree reasonably well with the porosity range assigned to the altered wall rock in the generalised conceptual model from the True Block Scale project (cf. Figure 4-1). They are summarised in Table 5-4.

Table 5-3. Alteration rim and undisturbed rock thicknesses of the central case of our layered rock model.

Fracture class	Alteration rim porosity	Undisturbed rock porosity
F1:1	1 %	0.18 %
F1:2	0.5 %	0.18 %
F1:3	1 %	0.18 %
F2:1	5 %	2 %

These values can be compared with the alteration halo porosities of the TURVA-2012 transport classes. For the clay-coated and calcite-coated fracture classes, the porosity of the alteration halo was assumed to be 4 % and 2 %, respectively. These values are comparable with the moderate alteration rims assumed here for fracture class F1:1 and F1:3. For the slickensided transport class, often associated with faults, a porosity of 5 % was assigned to the alteration halo. This value equals the value we have assigned to fracture class F2:1. For the other (uncoated) transport class, the wall rock was assumed to be unaltered with a porosity of 0.5 % (Posiva 2013, Tables 7-13 to 7-16). This value equals the value we have assigned to the alteration rim of fracture class F1:2 in this work.

5.5.3 Undisturbed rock porosity

Fracture class F1:1 to F1:3

For the fracture classes of the immediate far-field, we adopt the value assigned to the undisturbed rock in SR-Site (SKB 2010c, Table 6-90):

- Fracture class F1:1 to F1:3, undisturbed wall rock porosity = 0.18 %.

Fracture class F2:1

For fracture class F2:1, the wall rock outside the alteration rim is assumed to have also been subjected to large-scale deformation. In Crawford (2008, Table 4-7) porosities are summarised for several drill core sample categories including deformation zones. For samples taken from within deformation zones that have been subjected to medium or strong alteration (as observable by ocular inspection), the mean porosity is 2.5 %. Pooling all samples taken from within a deformation zone, with or without observed alteration, the mean porosity is roughly 1 %. Since the average value of these observations rounded to one significant figure is 2 %, we assume this for the wall rock outside the alteration rim for fracture class F2:1:

- Fracture class F2:1, wall rock porosity = 2 %.

5.6 Effective diffusivity

5.6.1 General considerations

No site-specific measurement data exist for the effective diffusivity of fracture coatings. Also, in a limited literature study, no reliable data on the effective diffusivity of fracture minerals has been found which might be considered relevant for the geological conditions at Forsmark. Furthermore, very little site-specific data exist for the effective diffusivity of alteration rims, even when including well-investigated sites of similar geology such as Oskarshamn and Olkiluoto. As discussed in the previous section, however, some data exist on the porosity of these layers and one possibility is to estimate the effective diffusivity using empirical relations between the porosity and effective diffusivity. These relations may be useful for the very porous fracture coatings, and perhaps for highly altered crystalline rock of relatively high porosity, although they are known to perform poorly for low porosity crystalline rock. The most commonly used relations are usually some variation of Archie's law (Archie 1942), which correlates the geometric formation factor, F_f (–) and the porosity, ε_p (–) using a simple power-law relation:

$$F_f \approx \varepsilon_p^m \tag{5-1}$$

Where, m is an empirical fitting parameter that typically ranges from 1.8 and 2.0 for consolidated sandstone and as little as 1.3 for packed unconsolidated sand. The formation factor, in turn relates to the effective diffusivity by way of the expression:

$$D_e = F_f \cdot D_w \tag{5-2}$$

Where, D_w (m^2/s) is the free diffusivity of the migrating solute at infinite dilution in an unconfined fluid, and D_e (m^2/s) is the effective diffusivity in the porous medium. The free diffusivity is typically assumed to be 1×10^{-9} m^2/s for all species at in situ temperature, although this is only order-of-magnitude accurate. An exception is typically made for anions where an anion exclusion factor is used to reduce the effective diffusivity (cf. Section 5.6.5). The formation factor relates to the porosity via the expression (Neretnieks 1980):

$$F_f = \varepsilon_p \cdot \frac{\delta}{\tau^2} \tag{5-3}$$

Where, ε_p (–) is the transport porosity (i.e. the porosity that contributes to diffusive transport through the rock), δ (–) is the pore constrictivity, and τ^2 (–) is the tortuosity of the porous system. On occasion, the term effective tortuosity τ_D (–) is used instead (e.g. Vilks et al. 2005):

$$\tau_D = \frac{\tau}{\sqrt{\delta}} = \sqrt{\frac{\varepsilon_p D_w}{D_e}} \tag{5-4}$$

Archie's law was modified in Parkhomenko (1967) to improve its applicability in crystalline rock by adding a pre-factor:

$$F_f = 0.71 \cdot \varepsilon_p^{1.58} \tag{5-5}$$

Although the form of this modification was first proposed by Winsauer et al. (1952), the above version is widely cited in the literature in relation to the electrical resistivity of crystalline rocks. For the dense and low-porous Forsmark rock matrix, however, the precision of Equation 5-5 has proven to be poor (e.g. Byegård et al. 2008, Figure 3-5). Also, it may be noted that it is formally incorrect since it implies an effective diffusivity less than the free diffusivity in unconfined water (i.e. $\varepsilon_p = 1$). One might also argue that relations derived for the rock matrix are not strictly applicable to fracture coatings which have very different microstructural characteristics. As an alternative, we could use an empirical relation between the porosity and effective diffusivity of bentonite clay, which was used in SR-Site (although in a rearranged form). Combining Equations 5-1 and 5-4 in SKB (2010c) allows us to write:

$$D_e = 3.48 \cdot 10^{-9} \exp\left(2.05 \cdot 10^{-3} \cdot \rho_s \left(1 - \varepsilon_p\right)\right) \tag{5-6}$$

Where ρ_s (kg/m^3) is the crystallographic density of the solid clay mineral, which is taken to be 2 780 kg/m^3 (SKB 2010c, Section 5.1.1). This empirical relation is justified in the porosity range ~ 20 % to ~ 80 %, based on the dry density range shown in SKB (2010c, Figure 5-6). This range should be kept in mind when using this relation for our proposed fracture coatings, where the lowest

porosity is 10 %. In Figure 5-7 the various relations discussed above are plotted. The arrows are inserted to indicate the porosities of the 11 distinct layers of the present layered rock model. Grey arrows denote the fracture coating (C); blue arrows, the alteration rim (A); and yellow arrows, the underlying rock matrix (U). In the figure the fracture class is given by 1:1, 1:2, etc.

5.6.2 Fracture coating

Diffusion into fracture coatings is typically the dominant matrix diffusion process for in situ tracer tests in flowing water, performed in fractured crystalline rock. Since contact times during tracer tests are short, they tend to sample retardation properties of fracture infillings and coatings and very little penetration into the underlying rock matrix is achieved. In Zhou et al. (2007), a literature survey covering 40 field tracer tests at 15 sites is presented regarding the field-scale effective matrix diffusion coefficient (i.e. the effective diffusivity). The lower limit of the estimated effective diffusivity range, from all these field-scale tracer tests, is 3×10^{-12} m^2/s. This may be contrasted with the effective diffusivity of the underlying rock matrix, which may be orders of magnitude lower. A problem, however, with short term in situ tracer tests in flowing features is that they may overestimate the effective diffusivity of the fracture-adjacent rock. This is because tracers may diffuse into stagnant water of connected fractures that are not part of the flowpath, or into effectively stagnant zones within the plane of the fracture constituting the flowpath. Similar effects might also occur in flow channels with tapered edges giving strong variation in flow velocities across the flow channel width (i.e. if diffusive equilibrium is not attained in a transverse direction relative to the fluid flow). This can affect the tracer breakthrough curve in an analogous fashion to diffusion into a highly porous fracture coating. This is difficult to account for in inverse modelling of the breakthrough curves, as the specifics of the flowpath and surrounding fracture system are largely unknown, and the process is mathematically indistinguishable from matrix diffusion (i.e. non-Gaussian plume spreading rather than Gaussian hydrodynamic mixing dispersion). The presence of multiple parallel flowpaths with differing hydrodynamic characteristics may also give rise to non-Gaussian plume spreading behaviour (e.g. Neretnieks 2002).

We have found no effective diffusivity data relating to fracture coatings or minerals comprising presumed fracture coatings. This, in combination with the inherent difficulty of interpreting in situ tracer tests in fracture systems forces us to rely on 1) the porosity versus effective diffusivity relations of Figure 5-7, and 2) the corresponding effective diffusivities used in TURVA-2012. Without performing additional experimental studies on fracture coatings, the only way to handle this uncertainty is by making sensitivity studies, or by applying pessimistic assumptions. This is done in Chapter 8.

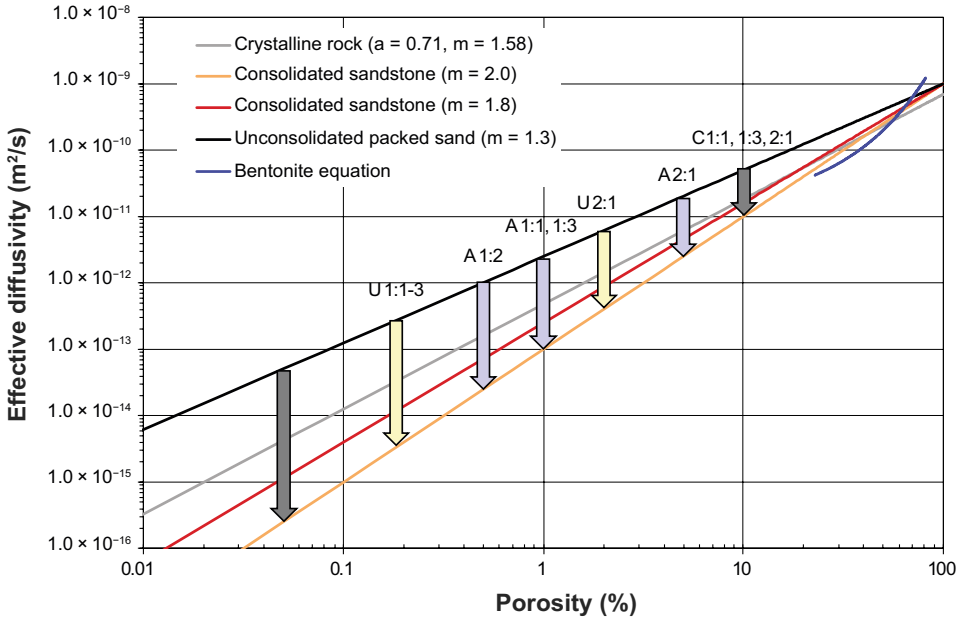

Figure 5-7. *Relations between the porosity and effective diffusivity. The first four relations are Archie's law with different fitting parameters. The fifth relation, only given for porosities above 22 %, and labelled "Bentonite equation" corresponds to Equation 5-6. D_w is here assumed to be 1×10^{-9} m^2/s when estimating D_e using Equation 5-2.*

Fracture class F1:1 and F2:1

In these fracture classes, the coatings are assigned a porosity of 10 %. Using the Archie relations shown in Figure 5-7, the effective diffusivity can be estimated to range between 1×10^{-11} m^2/s and 5×10^{-11} m^2/s. If one makes the assumption that Equation 5-6 for bentonite can be reasonably extrapolated down to porosities on the order of 10 %, the effective diffusivity would be estimated to be 2×10^{-11} m^2/s. In TURVA 2012, the transport classes with clay fracture coating and calcite fracture coating, were each assigned an effective diffusivity of 1×10^{-12} m^2/s (Posiva 2013, Tables 7-13 and 7-14), although in that case, a lower porosity of 6 % was assumed.

Based on the above discussion, we chose an effective diffusivity for these fracture classes that roughly equals the lower limit of the range given by the relations plotted in Figure 5-7, i.e.:

- Fracture class F1:1 to F1:3, effective diffusivity = 1×10^{-11} m^2/s.

For anions, we also assume that the effective diffusivity should be multiplied by an anion exclusion factor of ~ 0.32 as discussed previously (see also Section 5.6.5).

Fracture class F1:3

The fracture coating of this fracture class (or alternatively, a strongly anisotropic layer of rock) is assumed to have a very low porosity that may also be poorly connected, or at least featuring significant tortuosity. Assuming the Archie relation for consolidated or crystalline rock in Figure 5-7, with a porosity of 0.05 %, the effective diffusivity is estimated to be in the range 3×10^{-16} m^2/s to 4×10^{-15} m^2/s. We chose a value roughly corresponding to the geometric mean of this range:

- Fracture class F1:2, effective diffusivity = 1×10^{-15} m^2/s.

Given the fact that this is a hypothetical layer that may, or may not exist in nature, and that we are using empirical relations that are not at all suitable for this type of low porosity material, the estimate given here should be treated with some scepticism. For anions, we additionally assume that the effective diffusivity should be multiplied by an anion exclusion factor of ~ 0.32 as previously.

5.6.3 Alteration rim

Within the Forsmark site investigation, seven drill core samples, all taken from locations within one metre of logged hydraulically conductive features, have been subjected to laboratory through-diffusion experiments (Selnert et al. 2008). In these experiments, tritiated water (HTO) was used as the tracer. These samples have been identified in this present report by comparing the tabulated borehole positions of the samples in Selnert et al. (2008, Appendix 2) with the positions of flow anomalies detected by the Posiva flow log.

This can be exemplified by the case of borehole KFM02A. According to Selnert et al. (2008, Appendix 2), 25 drill core samples from this borehole were subjected to through-diffusion experiments. Cross-checking the positions of these samples with the positions of detected flow anomalies interpreted to be associated with flowing fractures in Rouhiainen and Pöllänen (2004, Appendix 7.1), one can see that only two of the samples are taken from within a metre of a hydraulically conductive fracture. These two positions have also been cross-checked with the Wellcad diagram associated with the boremap mapping of the drill core of borehole KFM02A (Petersson et al. 2003, Appendix 2). From this diagram one can see that at one of these positions, the rock matrix is altered, and the alteration is classified as “medium intensity, oxidised”. At the other position, the rock matrix is unaltered.

The procedure described above has been repeated for all boreholes from which samples have been taken and which were also the focus of through-diffusion experiments. The effective diffusivity, rock capacity factor, α (–), and the water immersion porosity of these samples are compiled in the upper part of Table 5-4. For the non-sorbing tracer HTO, the rock capacity factor should equal the connected porosity (e.g. Lever and Bradbury 1985) as measured by the water immersion method, even though measurement uncertainty may lead to differences. Table 5-4 also gives the effective tortuosity, where values are based on the rock capacity factor if possible and on the water immersion porosity if no rock capacity factor is available for the particular sample.

Table 5-4. Effective diffusivity, rock capacity factor, and water immersion porosity of Forsmark and Äspö samples taken in the vicinity of flowing fractures. Solute transport data reproduced from Selnert et al. (2008, Appendixes 1 and 2) and Vilks et al. (2005, Table 2).

Nr.	Borehole	Sample name/ borehole length (m)	Borehole length of flowing fractures (m)	Rock type	Alteration type of borehole section	Effective diffusivity D_e (m^2/s)	Capacity factor α (–)	Water immersion porosity (–)	Effective tortuosity (–)
1	KFM02A	300.96–300.99	299.4–301.7	101057	Medium intensity, oxidised	7.5×10^{-13}	1.8×10^{-2}	1.21×10^{-2}	6.9
2	KFM02A	481.01–481.04	480.4–481.2	101057	Unaltered	5.80×10^{-14}	2.5×10^{-3}	1.7×10^{-3}	9.3
3	KFM04A	359.45–359.48	358.2–359.8	101051	Weak to medium intensity, oxidized or chloritisized	7.9×10^{-12}	7.2×10^{-2}	–	4.3
4	KFM05A	168.34–168.37	167.2–168.7	101057	Unaltered	9.8×10^{-14}	1.6×10^{-3}	1.5×10^{-3}	5.7
5	KFM06A	331.72–331.75	330.0–332.0	101057	Intensity unknown, oxidized	1.62×10^{-12}	5.13×10^{-3}	2.36×10^{-2}	2.5
6	KFM06A	331.78–381.81	330.0–332.0	101057	Intensity unknown, oxidized	1.2×10^{-12}	1.85×10^{-2}	2.54×10^{-2}	5.6
7	KFM08A	412.30–412.33	411.6–413.1	101057	Medium or strong intensity, oxidation or quartz dissolution	1.4×10^{-13}	–	8.6×10^{-3}	11.1
8	LTDE-SD	A-1	Adjacent to fracture	Granodiorite	Alteration zone	4.61×10^{-11}	–	3.11×10^{-3}	0.4[a,b]
9	LTDE-SD	E-1	Adjacent to fracture	Granodiorite	Alteration zone	4.78×10^{-14}	1.91×10^{-3}	3.75×10^{-3}	8.9[a]
10	LTDE-SD	F-1	Adjacent to fracture	Granodiorite	Alteration zone	1.50×10^{-12}	–	2.80×10^{-3}	1.9[a]

Rock type 101057 = Granite to granodiorite, metamorphic, medium-grained.
Rock type 101051 = Granite, granodiorite and tonalite, metamorphic, fine- to medium-grained.
D_w of HTO used in effective tortuosity calculation = 2×10^{-9} m^2/s.
a) Values do not correspond to effective tortuosities in Vilks et al. (2005, Table 2) as they used a higher free diffusivity, $D_w = 9.3 \times 10^{-9}$ m^2/s.
b) This value is physically not possible and likely to be in error.

It should be highlighted that these rock samples may well have been located many centimetres or decimetres away from the fracture surface, which may be beyond the extent of the true alteration rim. Since these measurements represent the best information presently available, we use them with caution and acknowledge a degree of uncertainty associated with their use.

Vilks et al. (2005) performed laboratory through-diffusion diffusion experiments on samples adjacent to, or in very close proximity to, a known hydraulically conductive fracture. The samples were taken from the larger part of the drill core of the telescoped LTDE-SD borehole at the Äspö Hard Rock Laboratory, where the borehole intersects an open fracture[6]. The positions of the samples in the drill core, relative to the (coloured grey) fracture surface, are indicated in Figure 5-8. For core sample A, the fracture surface was coated by chlorite and minor amounts of calcite. For core samples E and F, only chlorite coated the surface. Figure 5-8 also shows the interpreted porosity and effective diffusivity profiles, relative to the distance from the fracture surface. Both iodide and titrated water were used as tracers. For further details the reader should refer to Vilks et al. (2005).

As can be seen from the data given in Figure 5-8, the effective diffusivity ranges over four orders of magnitude within this small, localised rock volume. Furthermore, they represent a sample volume that is, for the most part, located further away from the fracture surface than our assumed 0.5 cm to 2 cm thick alteration rim. The most fracture-adjacent samples of cores A, E, and F extend from the fracture surface and 3 cm into the wall rock. For these samples, located only a few centimetres or perhaps a decimetre apart, there is a great spread in the estimated effective diffusivities derived from HTO and iodide tracers. This indicates that also in respect to the alteration rim, it makes sense to have a layered

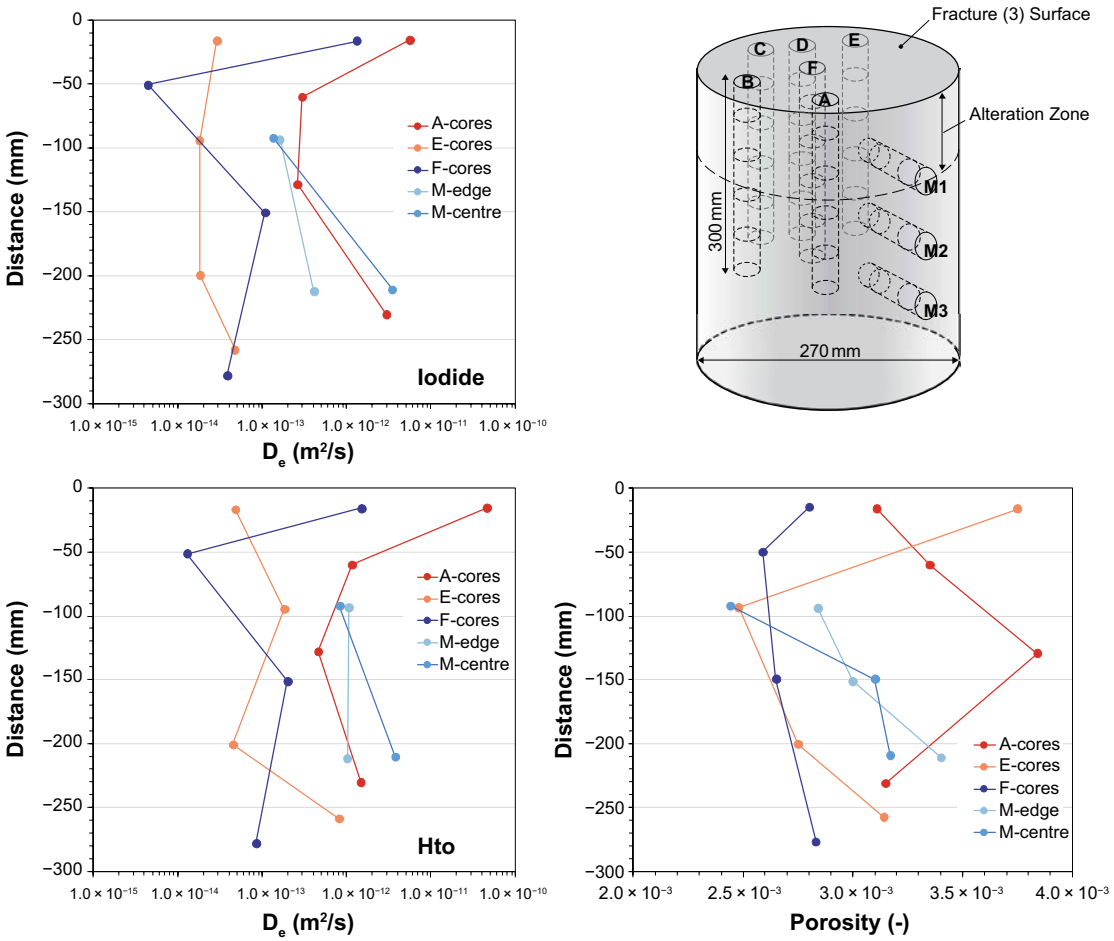

Figure 5-8. *Positions of samples in the LTDE-SD drill core, as well as resulting porosity and effective diffusivity profiles relative to the fracture surface. Adapted from Vilks et al. (2005 Figures 5, 12 and 13).*

[6] This fracture is not the one investigated by the in situ in-diffusion tracer test of the LTDE-SD campaign.

rock model where a fracture surface locally can be divided into different fracture classes. The data for these three samples are gathered in Table 5-4. The effective diffusivity for the A-1 sample seems unrealistically high for the estimated water immersion porosity and is therefore disregarded. The fact that there is such small-scale variability also raises the question whether the measurements made using short samples in through-diffusion experiments in the laboratory are truly representative of the rock volume when upscaled. To a large extent, formation factors estimated from in situ resistivity measurements are already volume-averaged in a physically meaningful manner, although there are additional methodological artefacts and features that must be considered carefully when using such data (e.g. Löfgren 2015).

The ten rock samples of Table 5-4 can be divided into two categories. Those with the lowest porosity and effective diffusivity seem to be relatively unaltered, representing fracture class F1:2. Others appear to be altered to varying degrees and have relatively high effective diffusivity, porosity, and rock capacity factor. It should be noted that there is a discrepancy in the effective tortuosity data in Table 5-4 for the LTDE-SD samples. In Vilks et al. (2005), the effective tortuosity has been calculated using a D_w of HTO of 9.3×10^{-9} m^2/s. This suggests that a diffusivity for H^+ (i.e. hydronium ion, H_3O^+) has been used rather than the self-diffusion coefficient for HTO in water, although there is no indication of this in the documentation. Furthermore, a D_w of iodide of 2.05×10^{-9} m^2/s is used when calculating the effective tortuosity for iodide, as was also used in Vilks et al. (2003), which is the normally accepted free diffusivity of the iodide anion at typical laboratory temperatures.

Figure 5-9 shows the effective diffusivities of a great number of samples obtained in through-diffusion experiments, using HTO as a tracer, versus the rock capacity factor or water immersion porosity. The data are from the Forsmark and Oskarshamn site investigations and from the LTDE-SD laboratory campaign (Selnert et al. 2008, 2009a, Vilks et al. 2005, Widestrand et al. 2010). Again, when rock capacity factors have been available these have been used in preference to water immersion porosities. The samples include undisturbed rock, rock subjected to large-scale deformation, and rock featuring varying degrees of alteration adjacent to open fractures. Most of the samples fall under the category of undisturbed rock. Samples with rock capacity factors, or porosities above 5 % predominantly come from a strongly altered volume of vuggy rock in Forsmark (cf. Figure 4-5) that has been subjected to extensive quartz dissolution, although is not representative for the site. From a ~ 6 m section of the drill core of borehole KFM02A (275 m to 281 m), 9 samples were taken for diffusion studies. Consequently, this local rock volume is greatly overrepresented in Figure 5-9.

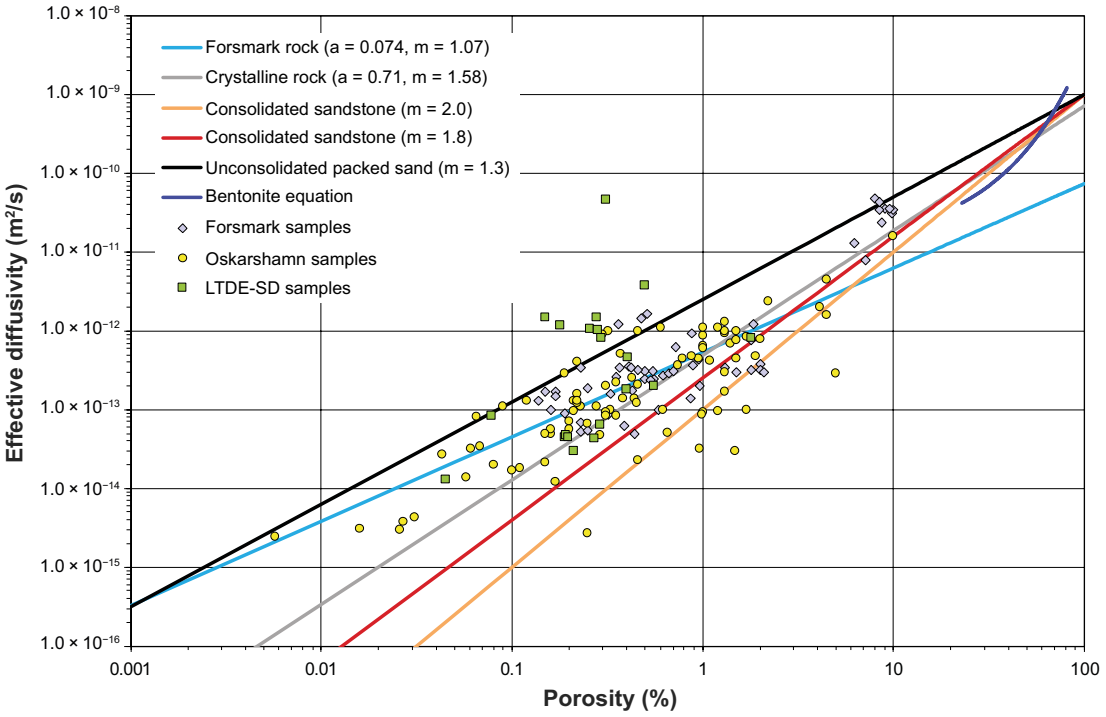

Figure 5-9. *Effective diffusivity at laboratory temperature versus rock capacity factor or porosity at the Forsmark and Oskarshamn site investigation area.*

For rock with rock capacity factors or porosities below 5 %, the effective diffusivity ranges from 2.4×10^{-15} m^2/s to 4.5×10^{-12} m^2/s (if sample A-1 of Vilks et al. 2005 is disregarded). The figure also shows plots of the effective diffusivity-porosity relations described in Section 5.6.1. In addition, a plot of Archie's relation with fitted site-specific parameters for Forsmark (Byegård et al. 2008, Figure 3-5) is shown as the light blue curve. It should be noted that the exponent of 1.07 is close to unity, indicating that the effective tortuosity is only weakly related to the porosity. Mean effective diffusivities within different porosity or rock capacity factor ranges are provided in Table 5-5.

Table 5-5. Mean effective diffusivity and tortuosity in different rock capacity factor or porosity ranges, for the samples of Figure 5-9. Sample A-1 of Vilks et al. (2005) is disregarded. Effective diffusivities apply at laboratory temperature.

Porosity or rock capacity factor range	Arithmetic mean effective diffusivity (m^2/s)	Arithmetic mean of effective tortuosity (–)	Number of samples
< 0.5 %	2.8×10^{-13}	7.5	91
0.5 to < 1 %	3.9×10^{-13}	8.4	24
1 to < 2 %	6.2×10^{-13}	9.1	27
2 to 5 %	1.4×10^{-12}	9.3	9

All effective diffusivities presented so far in this section are estimated assuming laboratory temperature (about 25 °C), with a D_w of about 2×10^{-9} m^2/s. In SR-Site, a typical D_w value of 1×10^{-9} m^2/s was used for all species in the geosphere at the in situ temperature (SKB 2010c, Section 6.8). For simplicity, one can therefore divide the effective diffusivities given in Table 5-5 by a factor of two to get an approximate value for the relatively narrow range of present day in situ temperatures.

Figure 5-10 shows the effective tortuosity versus the rock capacity factor or water immersion porosity for the samples of Figure 5-9. For samples with rock capacity factors or porosities of 5 % or below, the effective tortuosity ranges from to 1.4 to 44 with an arithmetic mean of 8 (and disregarding sample A-1 of Vilks et al. 2005). It is interesting to note that the data points do not follow the trends anticipated from the typical Archie relation, especially if the exponent is significantly higher than 1. The absence of a trend of increasing effective tortuosity with decreasing rock capacity factor or porosity is also evident in Table 5-5.

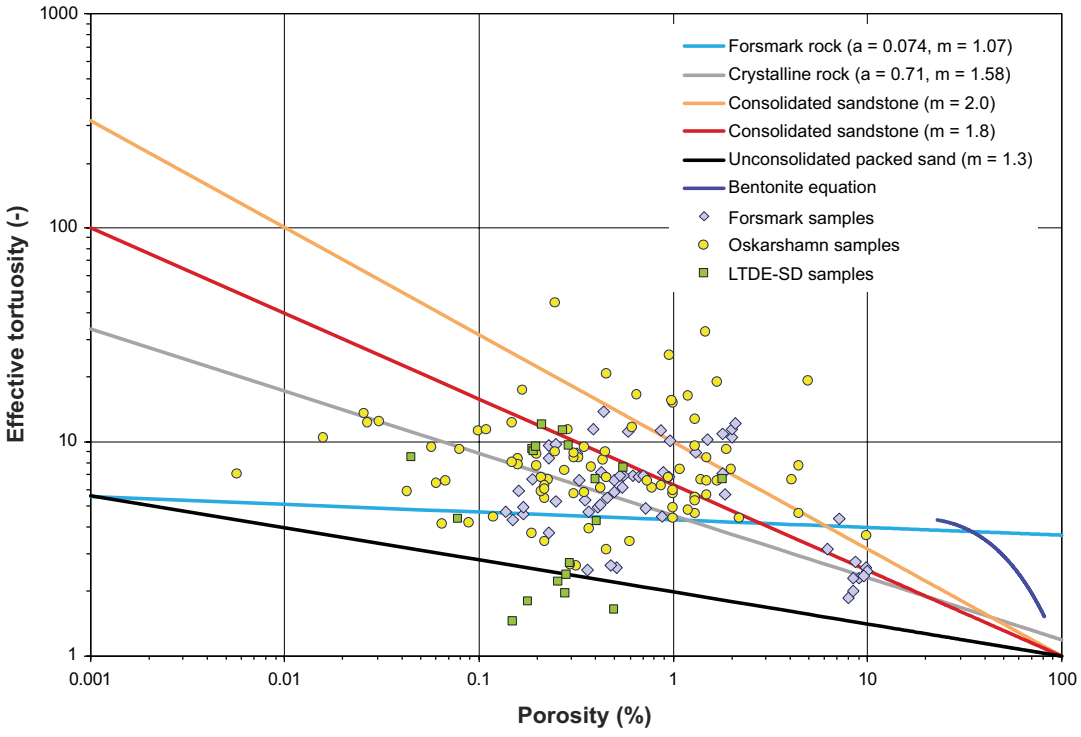

Figure 5-10. *Effective tortuosity versus rock capacity factor or porosity for samples from the Forsmark and Oskarshamn site investigation area. $D_w = 2 \times 10^{-9}$ m^2/s used for HTO in all effective tortuosity calculations.*

The rock directly facing open fractures may be subjected to considerably less stress than rock volumes at some distance from fractures. The reasoning for this is that tectonic movements at the fracture plane will have released (part of) the existing stresses. Regardless of the actual stress situation at fracture surfaces, however, the rock is most likely subjected to a significant effective stress that does not exist in the laboratory. In the quantification made below, we have not used a correction factor for stress release and excavation induced damage to reduce the effective diffusivities obtained in the laboratory (as was done for the undisturbed rock in SR-Site). This may result in a bias towards slightly too-high effective diffusivities for the alteration rim in our layered rock model. On the other hand, there is a general bias towards too-low effective diffusivities when using the through-diffusion method, due to the need to use intact rock samples. This can be exemplified by the investigation of Vilks et al. (2005) where the fracture-adjacent samples of core B, C and D (cf. Figure 5-8) were excluded from through-diffusion measurements as they were intersected by minor open fractures that might reasonably be interpreted as being part of the rock matrix. This bias is of limited importance when investigating sparsely fractured undisturbed rock. In the alteration rim, however, small fractures may be relatively frequent (cf. Figure 4-5). The greater the extent of alteration and deformation, the larger this bias may be. Given the present state of knowledge, it is not possible to say whether these two biases mutually cancel, or if one bias outweighs the other. This can only be handled by way of sensitivity studies.

It is acknowledged that other strategies might be employed to assign effective diffusivities to the alteration rim. In the absence of a dedicated experimental program that properly investigates the issue, however, only informed guesses can be provided. In TURVA-2012, effective diffusivities in the alteration halo for the transport classes having layered structures range from 3×10^{-13} to 1×10^{-12} m^2/s (Posiva 2013, Tables 7-13 to 7-15). This is consistent with our estimated range presented below for the Forsmark site.

Fracture class F1:1 and F1:3

These two fracture classes feature a moderate alteration rim. For these classes, the decision was made to primarily base the quantification of the effective diffusivity on the data in Table 5-4 and secondarily on Table 5-5. The rationale here is that the data in Table 5-5 are mostly derived from samples relatively distant to mapped open fractures. In Table 5-4, we (subjectively) chose the samples of row numbers 1, 3–7, and 10 to represent the moderate alteration rim. The mean effective diffusivity of these samples is 1×10^{-12} m^2/s at laboratory temperature and 5×10^{-13} m^2/s at in situ temperature. The porosity of the alteration rim is assumed to be 1 %. This gives an effective tortuosity of 4.5. This is slightly lower than the effective tortuosity values of Table 5-5 although broadly similar to those of Table 5-4. The higher effective tortuosity values of Table 5-4, as compared to Table 5-5, agree with our general understanding of the system, that the rock volume directly adjacent to open fractures often is subjected to a higher degree of micro-fracturing than rock distant from fractures. Microfractures typically cut straight through mineral grains and might be reasonably expected to constitute less tortuous pathways than grain boundary pores. We therefore assign the following effective diffusivity for fracture classes F1:1 and F1:3:

- Fracture class F1:1 and F1:3, effective diffusivity = 5×10^{-13} m^2/s.

As per our previous treatment, the effective diffusivity for anions should be multiplied by an anion exclusion factor of ~ 0.32.

Fracture class F1:2

Fracture class F1:2 has fresh wall rock with little alteration, although might still be affected by stress release and microfracturing. The porosity of the alteration rim is assumed to be 0.5 %. Based on Table 5-5, the corresponding effective diffusivity would be expected to be around 3×10^{-13} m^2/s at laboratory temperature and 1.5×10^{-13} m^2/s at in situ temperature. We round this down to:

- Fracture class F1:2, effective diffusivity = 1×10^{-13} m^2/s

This gives an effective tortuosity of 7.1, which is in the range presented in Table 5-4 and Table 5-5. Once again, for anions this effective diffusivity should be reduced by an anion exclusion factor of ~ 0.32.

Fracture class F2:1

The alteration rim of fracture class F2:1 is assumed to be strongly altered and have a porosity of 5 %. In the following treatment, we pool all data of Figure 5-9 in the porosity or rock capacity factor range of 4 % to 8 %, although excluding the atypical samples from borehole section 275 m to 281 m of KFM02A. This gives 6 samples with an average porosity of 5.9 % and an average effective diffusivity of 5.4×10^{-12} m^2/s at laboratory temperature. At the in situ temperature this corresponds to 2.7×10^{-12} m^2/s.

For this strong alteration rim, that presumably would be interspersed by frequent minor- and micro-fractures, this effective diffusivity is likely to be an underestimate as it is based on data from non-fractured rock. In the absence of a proper upscaling model to account for such fracturing, we subjectively increase the effective diffusivity for the in situ temperature to:

- Fracture class F2:1, effective diffusivity = 5×10^{-12} m^2/s.

This is one order of magnitude higher than the effective diffusivity assumed for the moderate alteration rim of fracture class F1:1 and F1:3. This gives an effective tortuosity of 3.2, which is in the lower range of Table 5-4. As previously, for anions the effective diffusivity should be multiplied by an anion exclusion factor of ~ 0.32.

5.6.4 Undisturbed rock

Fracture class F1:1 to F1:3

For the undisturbed rock of the fracture classes belonging to the immediate far-field, the best estimate value of SR-Site is used without further elaboration (cf. SKB 2010c, Table 6-91). In doing so, it is easier to see the effect of the fracture coating and alteration rim, by comparing the results with those of the existing SR-Site central corrosion case as reproduced in Chapter 3. We therefore have:

- Fracture class F1:1 to F1:3, effective diffusivity = 2.1×10^{-14} m^2/s.

For anions this effective diffusivity should be multiplied by an anion exclusion factor of ~ 0.32.

Fracture class F2:1

The recommendations for SR-Site are not valid for rock in deformation zones in the distant far-field, which is characterised by large-scale deformation and perhaps by an increased degree of fracturing. The porosity of this rock is assumed to be 2 % (cf. Table 5-3). Based on the data in Table 5-5, it seems reasonable to assume an effective tortuosity of about 9 for this rock. This would suggest an in situ effective diffusivity of about 2.5×10^{-13} m^2/s. This effective diffusivity is lower than expected from Table 5-5 for this porosity. The mean effective diffusivity of the 2 % to 5 % porosity range is 1.4×10^{-12} m^2/s. In deformation zones one can probably assume a lower effective tortuosity than that estimated above due to presumed impact of increased micro-fracturing. If the effective tortuosity is halved (i.e. $\tau_D \sim 4.5$, the corresponding effective diffusivity would be roughly 1×10^{-12} m^2/s. As can be seen from Figure 5-9, the effective diffusivity of 1×10^{-12} m^2/s is also observed for a number of the LTDE-SD rock samples taken from rock adjacent to a water conducting fracture, although there is some statistical dispersion in the data.

This value may be also be considered in the context of results from in situ formation factor logging by electrical methods at the Forsmark site and, in particular, the fractured rock formation factor. Here, fractures that do not conduct water at rates detectable by the Posiva flow meter (PFL) are taken to be part of the rock matrix. In site investigation reports (e.g. Löfgren and Neretnieks 2005b), histograms of the fractured rock formation factor are provided. One such histogram is reproduced in Figure 5-11. Only the uppermost part of the upper tail of the histogram would likely represent rock in heavily fractured deformation zones. From the general impression of this type of histogram (Löfgren and Neretnieks 2005a, Figure 5-3, Löfgren and Neretnieks 2005b, Figure 5-3, Löfgren et al. 2006, Figure 5-3, Löfgren 2006, Figure 5-3, Löfgren 2007, Figure 5-2) this uppermost part occurs at a formation factor of about 1×10^{-3}, corresponding to an effective diffusivity of 1×10^{-12} m^2/s.

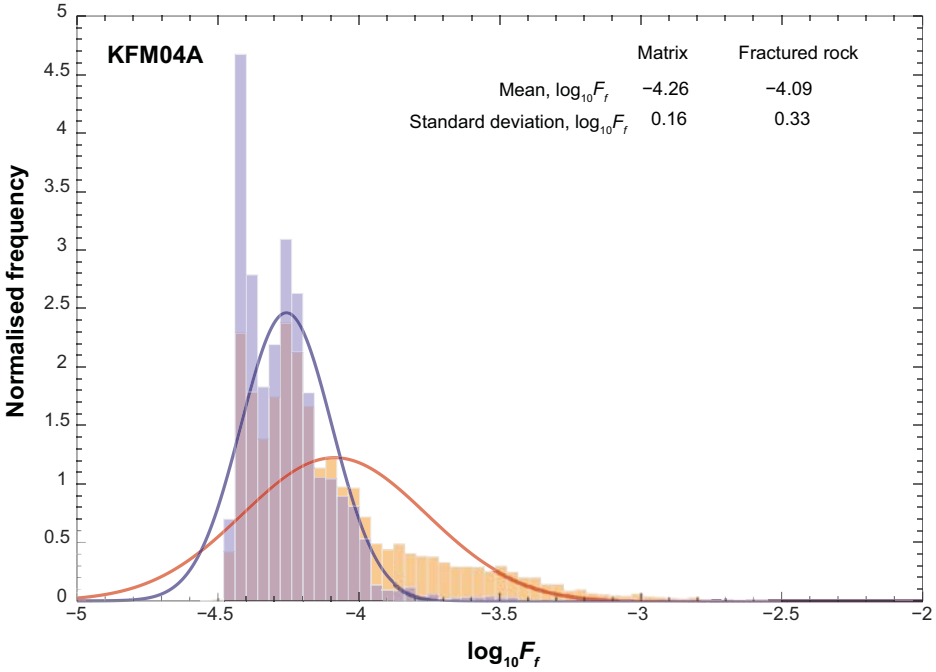

Figure 5-11. *Histogram of the fractured rock (orange), and matrix (light blue) formation factor from borehole KFM04A together with corresponding fitted probability density functions, as obtained by electrical loggings in situ. In fact, the apparent formation factor is shown in the histogram rather than true formation factor (see definition in Löfgren 2015), although for the upper tail of the histogram for fractured rock this does not affect the results appreciably. Adapted from Löfgren and Neretnieks (2005b, Figure 5-3).*

Acknowledging the difficulty in assigning a representative effective diffusivity to the wall rock of deformation zones, outside the alteration rim, we assume:

- Fracture class F2:1, effective diffusivity = 1×10^{-12} m^2/s.

For anions, this effective diffusivity should be reduced by an anion exclusion factor of ~ 0.32. The value given above is probably more appropriate for the first few decimetres of wall rock from the flowpath, subjected to increased fracturing, than for rock at some distance from fractures that is only subjected to large-scale ductile deformation. As shown in Chapter 8 and Chapter 9, however, only the first few decimetres of fracture adjacent rock, or less, influence the radionuclide breakthrough for the F-factor ranges typically encountered in safety assessment.

5.6.5 Anion exclusion factor

In this work, we use the anion exclusion factor of ~ 0.32 to lower the effective diffusivity for anions, as compared to non-charged or positively charged species. No anion exclusion factor is used to reduce the porosity. This is because the primary effect of anion exclusion is presumed to occur by way of electrical double layer overlap in pore throat constrictivities rather a direct effect of bulk transport porosity reduction. This follows the recommendations of SR-Site (SKB 2010, Section 6.8) and is based on the measurement data compiled by Vilks et al. (2005) as shown in Figure 5-12. Anion exclusion effects, however, are highly dependent on microstructure and in strongly hydrothermally altered rock, for example, secondary sericite infilling at grain boundaries and in microfractures might give rise to significant anion exclusion effects for porosity as well. While this might be the case for veined gneiss rock types at Olkiluoto, the effect appears to be absent in Forsmark rock.

In this present work, we have assumed the same anion exclusion factor for all layers, although acknowledge the speculative nature of assigning an anion exclusion factor for the fracture coating. This can be exemplified by the fracture mineral calcite. Calcite, which is a carbonate, has different surface charge properties compared to silicates and oxides. The counter ions are hypothesised to be tightly bound to the surface in a very thin and non-diffusive double layer (e.g. Fenter et al. 2000), which suggests that anion exclusion might not occur.

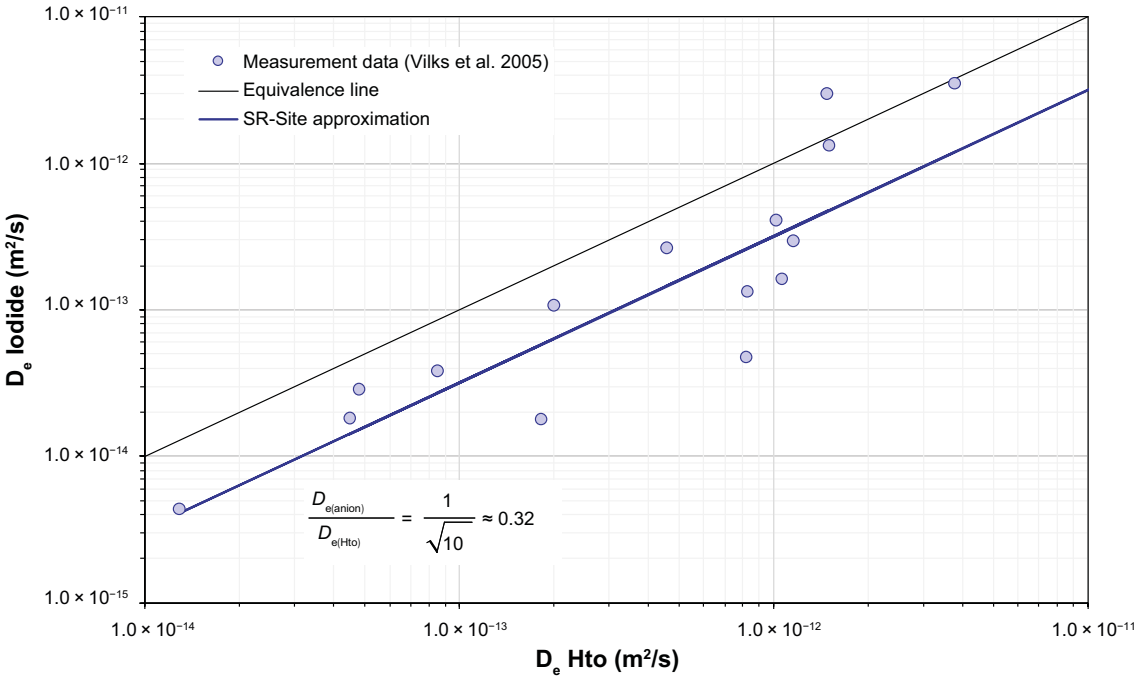

Figure 5-12. Empirical basis of anion exclusion factor of 0.32 as assumed in SR-Site based on a comparison of iodide and tritium through-diffusion data obtained simultaneously for the same samples of rock studied in the LTDE-SD project at Äspö (Data from Vilks et al. 2005).

5.7 Sorption properties

The underlying mechanism for sorption is assumed to be the same as in SR-Site, implying linear reversible adsorption as described by a conditionally constant partitioning coefficient, K_d (m^3/kg) for the prevailing groundwater composition. All other non-adsorptive immobilisation processes are thus neglected in this description as are Langmuirian site saturation effects. In SR-Site, the K_d was assumed to be spatially and temporally invariant and equal to an assumed site-specific average value derived for each radioelement, an approach that has also been used in the present work. Accordingly, the simplistic approach of not assigning individualised K_d-values to the different rock alteration layers has been adopted. Instead, the best estimate sorption coefficients of SR-Site, for undisturbed rock, have been used for all layers without further justification. The assumed K_d-values are shown in column two of SKB (2010c, Table 6-89) for the different radioelements and are reproduced in Table 5-6.

Table 5-6. Kd-values used in central case layered rock model for all layers. The predominant species for redox sensitive elements are highlighted in bold text. Data reproduced from SKB (2010c, Table 6-89).

Radionuclide (Redox State)	Best Estimate K_d (m^3/kg)	Radionuclide (Redox State)	Best Estimate K_d (m^3/kg)
Ac(III)	1.48×10^{-2}	Pb(II)	2.52×10^{-2}
Ag(I)	3.49×10^{-4}	Pd(II)	5.20×10^{-2}
Am(III)	1.48×10^{-2}	Pu(III)	1.48×10^{-2}
C, HCO_3^-	0.0	Pu(IV)	5.29×10^{-2}
C, CH_4	0.0	Pu(V)	9.14×10^{-3}
C, $-CO_2H$	0.0	Pu(VI)	9.14×10^{-3}
Cd(II)	1.10×10^{-3}	Ra(II)	2.42×10^{-4}
Cl(-I)	0.0	S(-II)	0.0
Cm(III)	1.48×10^{-2}	Se(-II)	2.95×10^{-4}
Cs(I)	3.49×10^{-4}	Se(IV)	2.95×10^{-4}
Eu(III)	1.48×10^{-2}	Se(VI)	2.95×10^{-4}
H(I)	0.0	Sm(III)	1.48×10^{-2}
Ho(III)	1.48×10^{-2}	Sn(IV)	1.59×10^{-1}
I(-I)	0.0	Sr(II)	3.42×10^{-5}

Radionuclide (Redox State)	Best Estimate K_d (m^3/kg)	Radionuclide (Redox State)	Best Estimate K_d (m^3/kg)
Mo(VI)	0.0	Tc(IV)	5.29×10^{-2}
Nb(V)	1.98×10^{-2}	Tc(VII)	0.0
Ni(II)	1.10×10^{-3}	Th(IV)	5.29×10^{-2}
Np(IV)	5.29×10^{-2}	U(IV)	5.29×10^{-2}
Np(V)	4.13×10^{-4}	U(VI)	1.06×10^{-4}
Pa(IV)	5.92×10^{-2}	Zr(IV)	2.13×10^{-2}
Pa(V)	5.92×10^{-2}		

This simplistic approach can certainly be questioned, and more realism could be included in the calculations to represent spatially variable sorptive properties. In such a case, the challenge would be to assign appropriate K_d-values to the entire set of radionuclides in the different alteration layers. If it was the intention of SSM, expressed in item 4 of SSM (2013a), that SKB should also vary retention properties associated with sorption, the layered rock model presented here would be well-suited for such a modelling exercise.

Since sorption is a surface-mediated process, the K_d-value to a good first approximation can often be assumed to be proportional to the specific surface area (i.e. BET surface area) of geological substrates. This is, at least to a certain extent, independent of mineralogy. Since different matrix minerals are known to sorb more strongly than others, however, it is generally a more accurate heuristic for estimating relative variations within a geological material sub-type than between very different materials. Measured BET surface areas of fracture minerals sampled from bore cores at Forsmark have been found to be as much as 20–600 times greater than that estimated for the intact rock, while altered rock (sealed fracture networks hosted in cataclasite/breccia pieces and oxidised wall rock) have been found to have BET surface areas about 40 times greater (Byegård et al. 2008). The greater specific surface area of these materials implies considerable potential for increased retention in the fracture mineral and alteration layers. While detailed accounting for altered sorptivity in the multilayer rock matrix model was deemed out of scope for the present work, this is being incorporated in the updated site descriptive modelling methodology currently under development by SKB which will form an important input for radionuclide transport calculations to be performed in future safety assessments.

In Section 8.4, a simple sensitivity study is made by uniformly increasing K_d-values by an order of magnitude for the altered rock in accordance with the above description. This possibility is explored in two separate variation cases for fracture class F1:1. One variation case where increased sorption occurs only in the fracture coating, and one where increased sorption occurs both in the fracture coating and alteration rim. In future work, more elaborate sensitivity studies concerning sorption are envisioned where sorptive properties could be related to other micro-structural and independently quantifiable geochemical proxies.

6 Results for individual fracture classes

In this chapter MARFA simulations are made for radionuclide transport involving the individual hypothesised fracture classes described previously in Section 4.2, although considered separately. For these calculations it is assumed that the given fracture class occupies the entire transport flowpath assuming the same hydrodynamic properties as the SR-Site central corrosion case (i.e. same F-factor, advective travel time, and Péclet number). Even though it is highly unlikely that a single fracture class would persist over an entire transport flowpath through the geosphere, these calculations provide a useful benchmark for evaluating the impact of individual rock matrix parameterisations that would be far more difficult to gauge in a simulation with mixed fracture classes even though results for such cases are also explored in Chapter 7 and Chapter 8.

For the multilayer rock matrix cases, problem-specific retention tables need to be calculated for the MARFA program using the Mathematica scripts distributed with the code. This entails creating a sub-directory for each rock type where material properties (K_d, D_e, ε_p) are pre-defined for each radioelement in separate files, individualised for each rock layer. The Mathematica scripts are then called to calculate retention tables in the format required by MARFA. Since the analytical solution (Cvetkovic 2010) is defined in the frequency domain (Laplace space) and contains recursively defined transcendental functions, it needs to be evaluated using multi-precision arithmetic to avoid infinities and divide-by-zero errors which are problematic when evaluating the solution using double precision floating-point arithmetic. Mathematica is ideally suited for this task since arbitrary-precision arithmetic is a core functionality of the program.

A consequence of the necessity to generate problem-specific retention tables for variable material properties in multilayer rock matrices is that the retention tables must be regenerated from scratch each time a material property is altered in sensitivity analyses. Due to the complexity of the input and output file structures it is therefore very important to properly automate this process for QA purposes. For this reason, we have developed a detailed scripting procedure for automatic generation of MARFA input files in this project which handles all input and output from the code together with plotting of breakthrough curves.

6.1 Fracture class F1:1

The F1:1 fracture class is assumed to have the material properties described previously in Section 5 and which are summarised in Table 6-1. The same flowpath hydrodynamic properties ($F = 5.366 \times 10^4$ y/m, $t_w = 6.401$, $Pe = 10$) and source term were assumed for this simulation as for the SR-Site central corrosion case, and the only difference is the parameterisation of the layered rock matrix.

Table 6-1. Non-sorption parameter values for the F1:1 fracture class. Kd values for sorption are assumed to be the same as the best estimate values given in Table 5-6 for the 25 radioelements considered in the calculations.

Rock layer	Layer thickness, δ_k	Transport porosity, ε_p	Effective diffusivity, D_e
fracture coating	0.1 mm	10 %	1.0×10^{-11} m^2/s
alteration rim	1 cm	1 %	5.0×10^{-11} m^2/s
undisturbed rock	12.5 m	0.18 %	2.1×10^{-14} m^2/s

The results of the MARFA simulation are shown in Figure 6-1. The main effect of the multilayer rock matrix with enhanced diffusive retardation properties in the fracture coating and alteration rim is an enhanced retardation of the leading edge of the breakthrough curve and a decrease in the peak dose rate for each of the radionuclides.

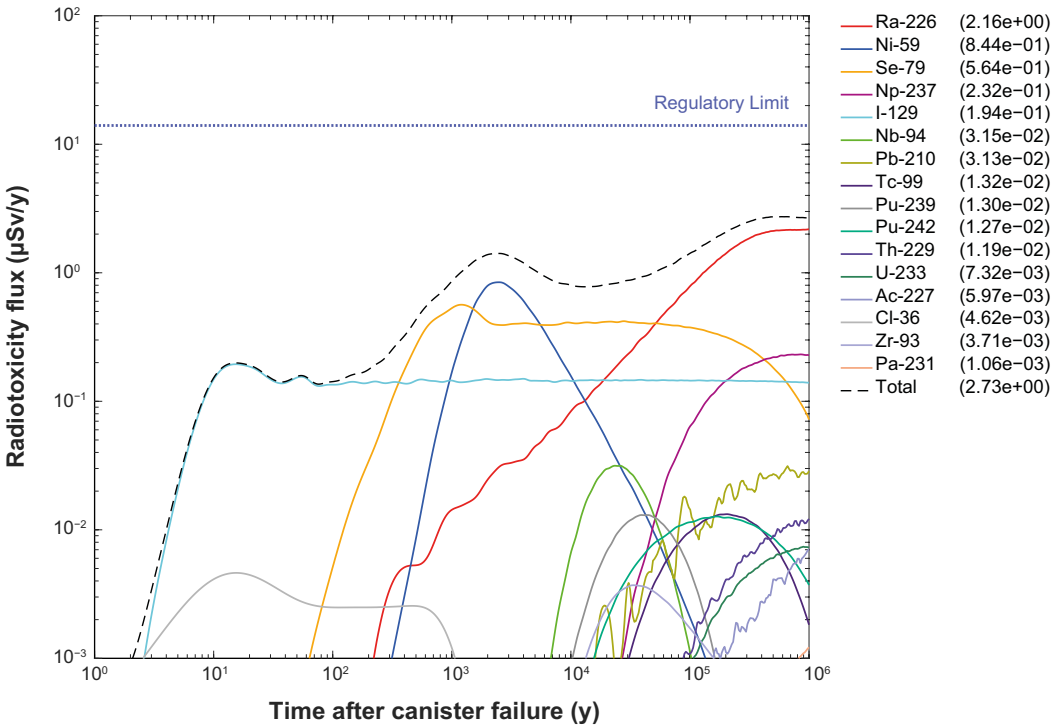

Figure 6-1. *The annual effective dose for the corrosion scenario calculated using MARFA assuming fracture class F1:1 specific material properties for the whole flowpath (combined IRF, CRF and DRF source terms). The legend is sorted by annual effective peak dose (µSv/y) within the time frame of the assessment. The time on the x-axis is relative to canister failure. Only those radionuclides contributing more than 0.1 % of the total radiotoxicity are plotted.*

6.2 Fracture class F1:2

The F1:2 fracture class is assumed to have the material properties described previously in Section 5 and which are summarised in Table 6-2. As previously, the same flowpath hydrodynamic properties and source term were assumed for this simulation as for the SR-Site central corrosion case, and the only difference is the parameterisation of the layered rock matrix.

Table 6-2. Non-sorption parameter values for the F1:2 fracture class. Kd values for sorption are assumed to be the same as the best estimate values given in Table 5-6 for the 25 radioelements considered in the calculations.

Rock layer	Layer thickness, δ_k	Transport porosity, ε_p	Effective diffusivity, D_e
alteration rim	0.5 cm	0.5 %	1.0×10^{-13} m^2/s
undisturbed rock	12.5 m	0.18 %	2.1×10^{-14} m^2/s

The results of the MARFA simulation are shown in Figure 6-2. Once again, the main effect of the multilayer rock matrix with enhanced diffusive retardation properties in the fracture coating and alteration rim is an enhanced retardation of the leading edge of the breakthrough curve and a decrease in the peak dose rate for each of the radionuclides. The impact is, however, somewhat smaller than the previous case (F1:1) mostly owing to the lower effective diffusivity and smaller thickness of the alteration rim.

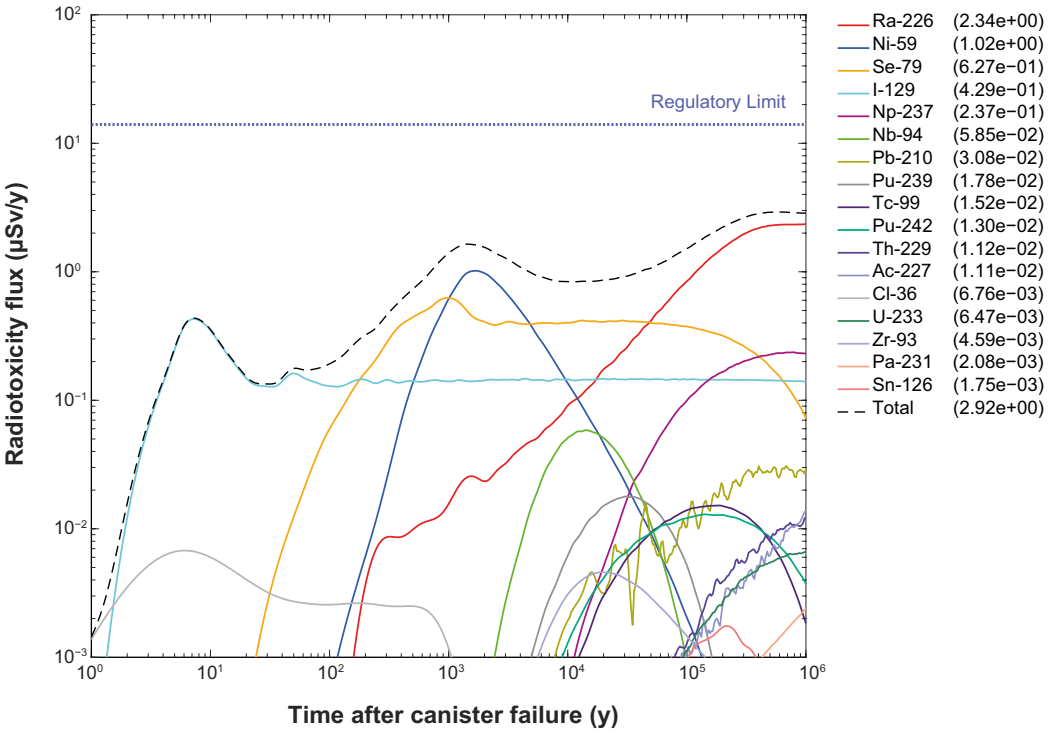

Figure 6-2. *The annual effective dose for the corrosion scenario calculated using MARFA assuming fracture class F1:2 specific material properties for the whole flowpath (combined IRF, CRF and DRF source terms). The legend is sorted by annual effective peak dose (µSv/y) within the time frame of the assessment. The time on the x-axis is relative to canister failure. Only those radionuclides contributing more than 0.1 % of the total radiotoxicity are plotted.*

6.3 Fracture class F1:3

The F1:2 fracture class is assumed to have the material properties described previously in Section 5 and which are summarised in Table 6-3. The same flowpath hydrodynamic properties and source term were assumed for this simulation as for the SR-Site central corrosion case, and the only difference is the parameterisation of the layered rock matrix.

Table 6-3. Non-sorption parameter values for the F1:3 fracture class. Kd values for sorption are assumed to be the same as the best estimate values given in Table 5-6 for the 25 radioelements considered in the calculations.

Rock layer	Layer thickness, δ_k	transport porosity, ε_p	Effective diffusivity, D_e
fracture coating	0.1 mm	0.05 %	1.0×10^{-15} m²/s
alteration rim	1 cm	1 %	5.0×10^{-13} m²/s
undisturbed rock	12.5 m	0.18 %	2.1×10^{-14} m²/s

The results of the MARFA simulation are shown in Figure 6-3. This case is interesting since it combines reduced retention characteristics in the fracture coating with enhanced retention properties in the alteration rim relative to the undisturbed rock. The impact on radionuclide breakthrough is mixed with faster breakthrough of the leading edges of the breakthrough curve for some nuclides, although also with a decreased peak dose rate that is somewhere in between that of the original SR-Site case and the results for fracture class F1:2.

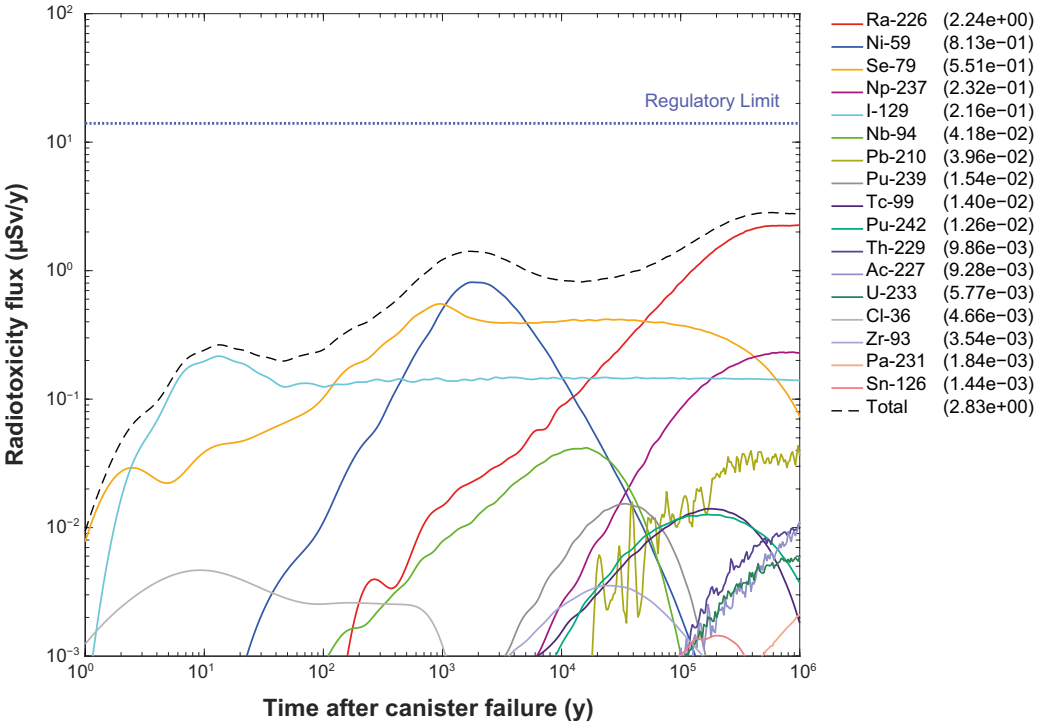

Figure 6-3. *The annual effective dose for the corrosion scenario calculated using MARFA assuming fracture class F1:3 specific material properties for the whole flowpath (combined IRF, CRF and DRF source terms). The legend is sorted by annual effective peak dose (µSv/y) within the time frame of the assessment. The time on the x-axis is relative to canister failure. Only those radionuclides contributing more than 0.1 % of the total radiotoxicity are plotted.*

6.4 Fracture class F2:1

The F2:1 fracture class is assumed to have the material properties described previously in Section 5 and which are summarised in Table 6-4. The same flowpath hydrodynamic properties and source term were assumed for this simulation as for the SR-Site corrosion case, and the only difference is the parameterisation of the layered rock matrix.

Table 6-4. Non-sorption parameter values for the F2:1 fracture class. Kd values for sorption are assumed to be the same as the best estimate values given in Table 5-6 for the 25 radioelements considered in the calculations.

Rock layer	Layer thickness, δ_k	Transport porosity, ε_p	Effective diffusivity, D_e
fracture coating	1 mm	10 %	1.0×10^{-11} m^2/s
alteration rim	2 cm	5 %	5.0×10^{-12} m^2/s
undisturbed rock	12.5 m	2 %	1.0×10^{-12} m^2/s

The results of the MARFA simulation are shown in Figure 6-4. Here, we see a very strong retardation effect that gives enhanced retardation of the leading edge of the breakthrough curve and reduces peak dose rates by a very significant amount relative to any of the preceding cases.

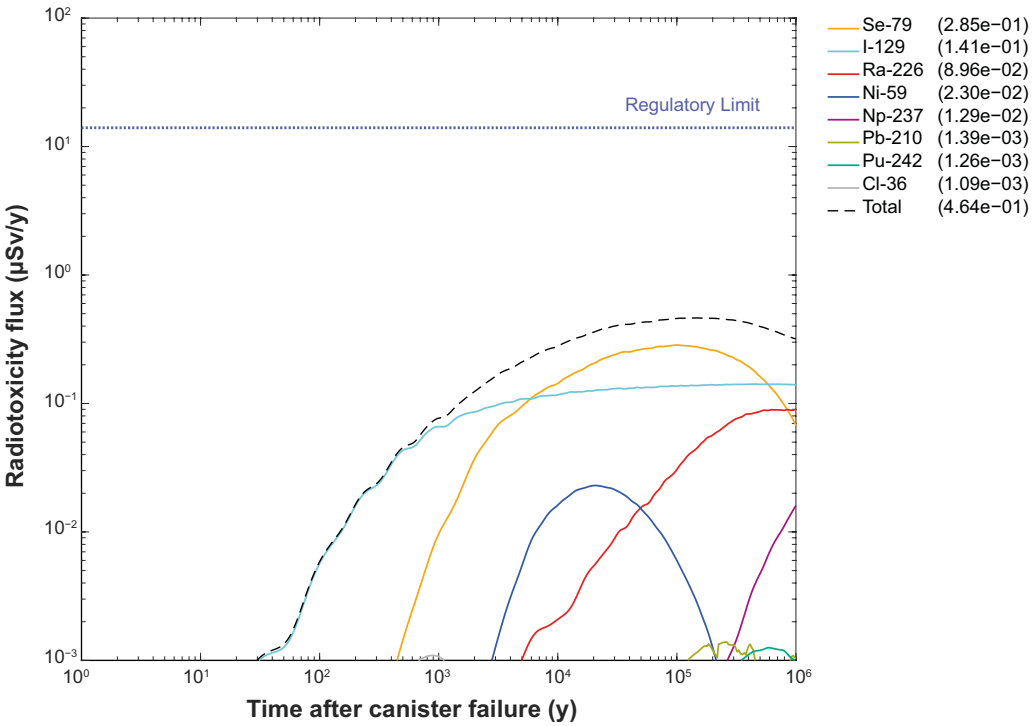

Figure 6-4. *The annual effective dose for the corrosion scenario calculated using MARFA assuming fracture class F2:1 specific material properties for the whole flowpath (combined IRF, CRF and DRF source terms). The legend is sorted by annual effective peak dose (µSv/y) within the time frame of the assessment. The time on the x-axis is relative to canister failure. Only those radionuclides contributing more than 0.1 % of the total radiotoxicity are plotted.*

7 Central case for multiple fracture classes

In this section, we present the MARFA simulation results for radionuclide transport involving a mix of different fracture classes distributed according to the schematic illustration in Figure 5-1. Here, the different fracture classes are assigned in a simple linear sequence in the ratio 9 % (F1:3): 27 % (F1:1): 54 % (F1:2): 10 % (F2:1) in accordance with the specification given in Section 5.3. The different fracture classes are distributed in proportion to the cumulative flowpath F-factor which does not necessarily map linearly to flowpath distance. The assumed 90 % of the flowpath F-factor accumulated in the immediate far-field therefore doesn't imply 90 % of flowpath length since F-factor is typically distributed in a highly non-linear fashion along the flowpath. For these calculations, we assume the same hydrodynamic properties as the SR-Site central corrosion case (i.e. same F-factor, advective travel time, and Péclet number as in previous calculation cases). The results of the calculation are shown in Figure 7-1.

In this simulation, we see that there is an enhanced retardation of the leading edges of the breakthrough curve and reduction in the peak breakthrough for most nuclides which varies from 10 %–80 % relative to the SR-Site central corrosion case (for a single layer rock matrix) as replicated in this work using MARFA (cf. Figure 3-10), although including the IRF release fractions which were previously handled separately in SR-Site. The reduction in the peak flux for the summed radionuclide fluxes is roughly 36 %. The results suggest, as previously speculated, that the neglection of matrix heterogeneity is most likely a cautious assumption that leads to a slight overestimation of radiological risk.

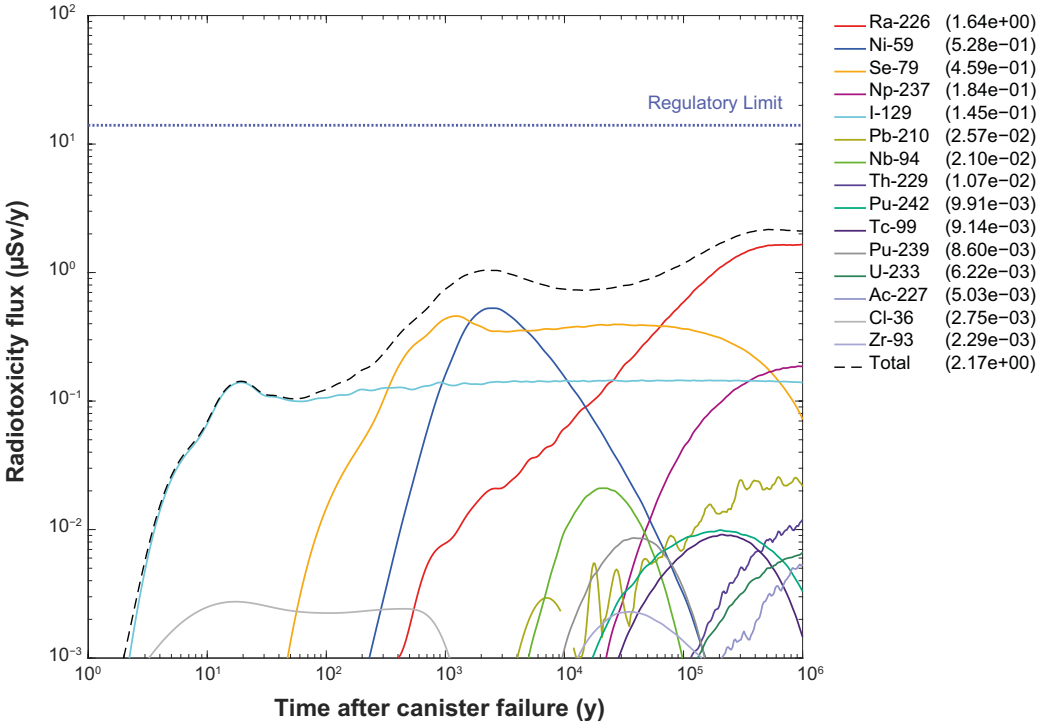

Figure 7-1. *The annual effective dose for the corrosion scenario calculated using MARFA assuming the different fracture classes distributed in proportion to cumulative F-factor along the flowpath (combined IRF, CRF and DRF source terms). The legend is sorted by annual effective peak dose (µSv/y) within the time frame of the assessment. The time on the x-axis is relative to canister failure. Only those radionuclides contributing more than 0.1 % of the total radiotoxicity are plotted.*

8 Sensitivity studies

In this section, we make a set of sensitivity analyses aimed at examining the effect of:

1) A limited maximum penetration depth (single layer rock matrix),
2) reduced effective diffusivity (single layer rock matrix),
3) single fracture classes assumed for entire flowpath (multilayer rock matrix),
4) increased sorptivity in the fracture-adjacent layers (multilayer rock matrix),
5) random versus sequential order of mixed fracture classes (multilayer rock matrix).

In making comparisons between each of the above, we focus on the total peak dose rate (summed over all radionuclides) and the peak dose rate of the six most prominent radionuclides of the SR-Site central corrosion case, i.e. Ra-226, Ni-59, Se-79, I-129, Np-237, and Nb-94. These radionuclides have a peak dose rate of at least 0.1 μS/m in the central corrosion case when also accounting for the instant release fraction (cf. Figure 3-9 and Figure 3-10).

8.1 Limited maximum penetration depth

In SSM's reasoning as documented in SSM (2013a), the possibility of a limited maximum penetration depth for matrix diffusion is brought up. This is based on concerns in Haggerty (2012) who suggest that SKB should investigate the impact of a maximum penetration depth that is much smaller than the metre-scale used in SR-Site. For the Forsmark host rock at depth, with its large spacing between hydraulically active fractures, a restricted maximum penetration depth would be associated with limited pore connectivity or a microporous system at, or below the percolation threshold (e.g. Haggerty 1999). Based on the discussion in Section 5.4.3, we argue that the microporous system is connected on at least a decimetre scale in situ, and that no significant percolation threshold effects are seen on this scale. For the sensitivity study, however, we model the impact of a 10-cm maximum penetration depth for the central corrosion case of SR-Site, where the flowpath is surrounded by undisturbed rock matrix.

In this study, we reproduce the central corrosion case of SR-Site for flowpath 1 of Table 3-2, with two modifications. Firstly, we limit the thickness of the undisturbed rock to 10 cm on each side of the flowpath. Secondly, we use the combined source term of the IRF, CRF, and DRF. This approach agrees with the modelling described in Section 3.1.4 and, accordingly, we can compare the breakthrough curves with those of Figure 3-9 and Figure 3-10. Breakthrough curves, with the limited maximum penetration depth, are modelled using both FARF31 (Figure 8-1) and MARFA (Figure 8-2).

The second column of Table 8-1 shows the peak dose rates of the six most prominent radionuclides of the central corrosion case of SR-Site, modelled with FARF31 in the present replication study (cf. Figure 3-9), as well as the total peak dose rate. Corresponding values for the limited maximum penetration depth case are shown in the third and fourth column, based on data in Figure 8-1 and Figure 8-2.

Table 8-1. Comparison between SR-Site and sensitivity study peak dose rates.

Nuclide	Peak dose rate for SR-Site replication case with IRF FARF31 (μS/yr)	Peak dose rate for limited penetration depth case FARF31 (μS/yr)	Peak dose rate for limited penetration depth case MARFA (μS/yr)
Ra-226	2.51	2.56	2.79
Ni-59	1.25	1.25	1.46
Se-79	0.668	0.672	0.698
I-129	0.483	0.484	0.470
Np-237	0.241	0.245	0.267
Nb-94	0.105	0.105	0.119
Total	3.12	3.18	3.43

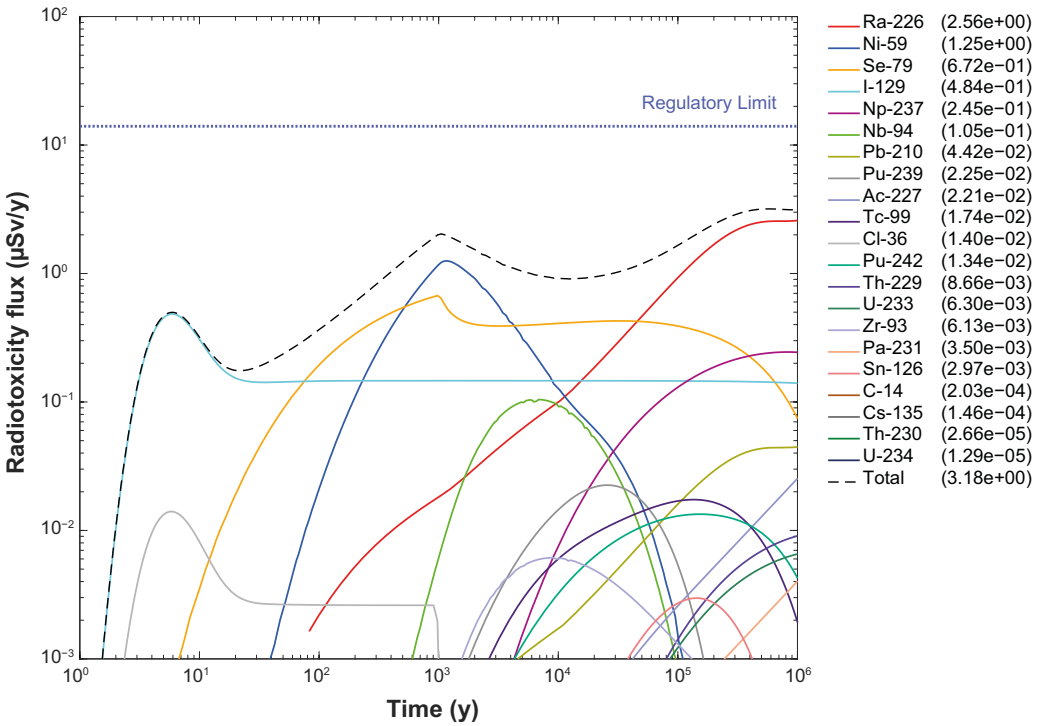

Figure 8-1. *Results from FARF31 modelling of far-field dose rate results for central corrosion case of SR-Site, with a limited maximum penetration depth, for flowpath 1. The legend is sorted by annual effective peak dose (µSv/y) within the time frame of the assessment. The time on the x-axis is relative to canister failure. Only those radionuclides contributing more than 0.1 % of the total radiotoxicity are plotted.*

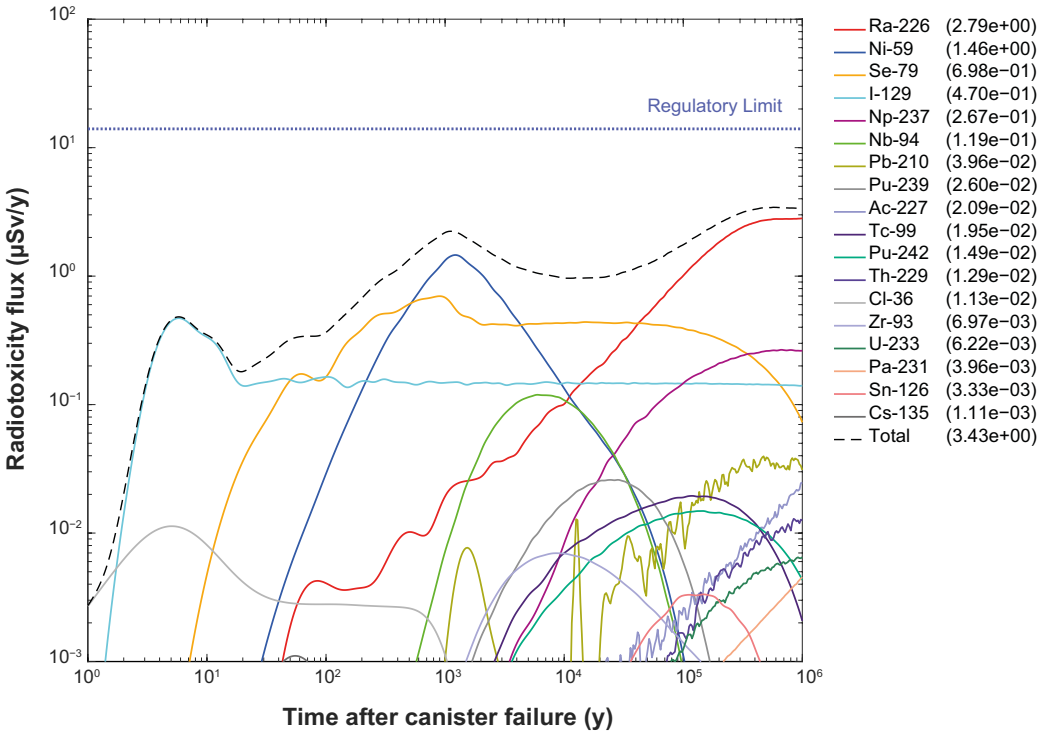

Figure 8-2. *Results from MARFA modelling of far-field dose rate results for central corrosion case of SR-Site, with a limited maximum penetration depth, for flowpath 1. The legend is sorted by annual effective peak dose (µSv/y) within the time frame of the assessment. The time on the x-axis is relative to canister failure. Only those radionuclides contributing more than 0.1 % of the total radiotoxicity are plotted.*

As can be seen from Table 8-1, the peak dose rates barely change as a result of limiting the maximum penetration depth to 10 cm. The largest differences are for Ra-226 and Np-237, the dose rates of which are still increasing or only just reach a maximum at very late breakthrough times. Comparing the shapes of the breakthrough curves, however, reveals a very limited effect by imposing this maximum penetration depth. The slightly higher peak dose rates of the MARFA simulation in Table 8-1 are also reflected in the MARFA modelling of the SR-Site case (cf. Figure 3-10), and cannot be solely attributed to the limited penetration depth in the case study.

8.2 Reduced effective diffusivity

The effective diffusivity used in SR-Site is already relatively low compared to in earlier safety assessments, as measures have been taken to ensure that that it applies under in situ conditions even if this may be over-conservative. Compared to effective diffusivities measured in the laboratory, the recommended value is reduced by about one order of magnitude. In this sensitivity study, we reduce the effective diffusivity again by an additional order of magnitude. This means that cations and non-charged species are assigned an effective diffusivity of 2.1×10^{-15} m^2/s. The corresponding value for anions is 6.6×10^{-16} m^2/s. As demonstrated later in Chapter 9, combining such low effective diffusivities with the F-factor of flowpath 1 in Equation 9-5 gives effective penetration depths of only 4 mm and 1 mm, respectively based on median retarded travel times for migrating solutes. We have made an additional case study calculation of the central corrosion case of SR-Site, with the combined source term, and with the reduced effective diffusivity discussed above. This has been done using both FARF31 (Figure 8-3) and MARFA (Figure 8-4). The transport porosity is unchanged relative to SR-Site implying that the effective tortuosity is increased by a factor of ~ 3.2.

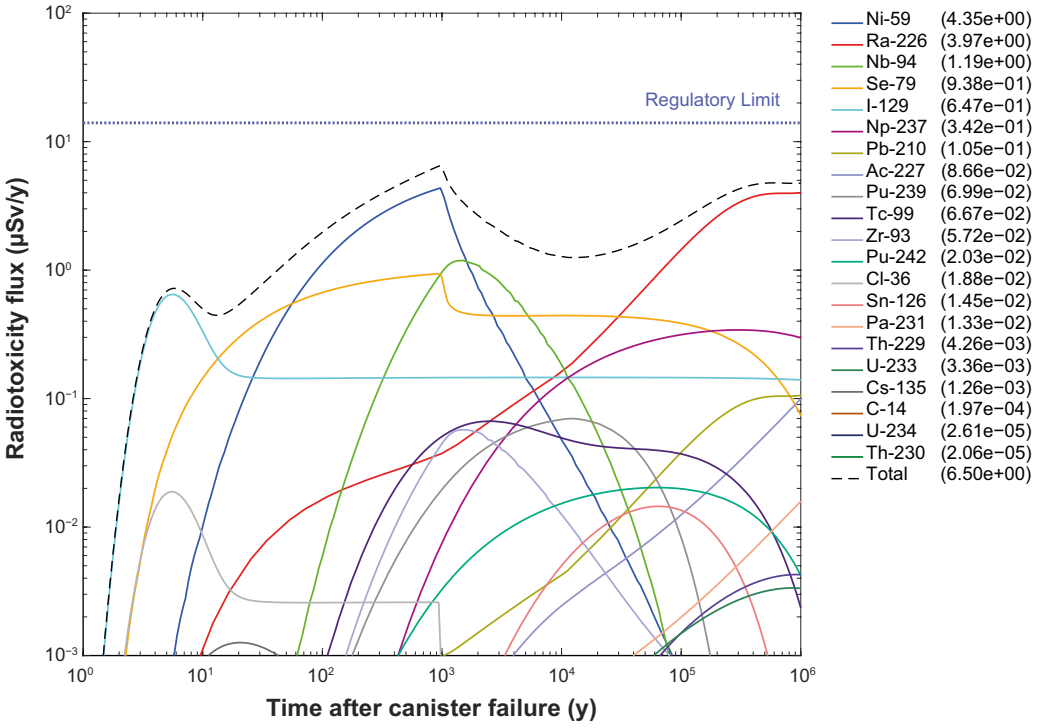

Figure 8-3. *Results from FARF31 modelling of far-field dose rate results for central corrosion case of SR-Site assuming 10 times reduced effective diffusivity for flowpath 1. The legend is sorted by annual effective peak dose (µSv/y) within the time frame of the assessment. The time on the x-axis is relative to canister failure. Only those radionuclides contributing more than 0.1 % of the total radiotoxicity are plotted.*

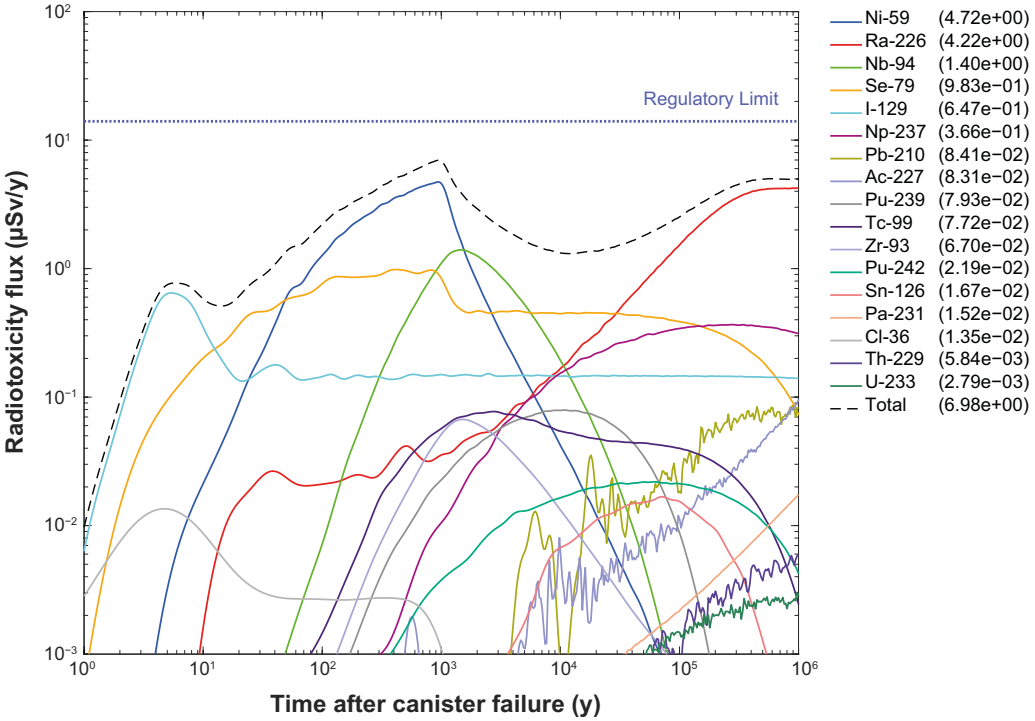

Figure 8-4. *Results from MARFA modelling of far-field dose rate results for central corrosion case of SR-Site assuming 10 times reduced effective diffusivity for flowpath 1. The legend is sorted by annual effective peak dose (µSv/y) within the time frame of the assessment. The time on the x-axis is relative to canister failure. Only those radionuclides contributing more than 0.1 % of the total radiotoxicity are plotted.*

Table 8-2 shows the peak dose rates of the six most prominent radionuclides of the central corrosion case of SR-Site, modelled with FARF31 in the present replication study (cf. Figure 3-9), as well as the total peak dose rate. Corresponding values for the reduced effective diffusivity case are shown in the third and fourth column, based on data in Figure 8-3 and Figure 8-4.

Table 8-2. Comparison between SR-Site and sensitivity study peak dose rates.

Nuclide	Peak dose rate for SR-Site replication case with IRF FARF31 (µS/y)	Peak dose rate for reduced effective diffusivity case FARF31 (µS/y)	Peak dose rate for reduced effective diffusivity case MARFA (µS/y)
Ra-226	2.51	3.97	4.22
Ni-59	1.25	4.35	4.72
Se-79	0.668	0.938	0.983
I-129	0.483	0.647	0.647
Np-237	0.241	0.342	0.366
Nb-94	0.105	1.19	1.40
Total	3.12	6.50	6.98

Of the listed nuclides, the reduced effective diffusivity affects Nb-94 the most, by a factor of about 10. Nb-94 is released as pulses in both the IRF and CRF and is absent from the DRF. The increase in peak dose by a factor of 10 is also about what would be expected from penetration depth analysis for a 10-times reduced effective diffusivity if one assumes the predominant effect is reduced matrix diffusion mediated dilution of the pulse release (see Section 9.1.1) rather than a direct effect of altered retarded travel time resulting in lower attenuation by decay. The peak dose for Ra-226, on the other hand, increases by a factor of about 1.6 in the reduced effective diffusivity case. The release of Ra-226, however, is complicated since it increases over time by ingrowth at the source (in this case DRF only) and it is also produced by ingrowth along the migration path so it is difficult to relate the difference to a change in effective penetration depth in the same fashion as one also needs to consider the limited penetration depth of the parent nuclides (U-238, U-234, and Th-230). This aspect is discussed in more

detail in Section 9.1.2. Ra-226 also has a relatively short half-life (1 600 y) relative to the timing of peak dose which just starts to stabilise at 1 My. For Np-237, the peak dose is roughly 1.4 times greater in the reduced effective diffusivity case, presumably for similar reasons to Ra-266, although Np-237 has a much longer half-life (2.144 My) than Ra-226.

For Ni-59 (half-life, 76 ky), the peak dose is about 3.5 times greater in the reduced diffusivity case. For Se-79 (half-life, 377 ky), on the other hand, the peak dose is only 1.4 times greater. The transport of Ni-59, however, is more strongly retarded than that of Se-79 and it appears that hydrodynamic dispersion might play a role for the diminished impact of reduced effective diffusivity for Se-79 relative to Ni-59. I-129 (half-life, 15.7 My) also exhibits only a very minor increase in peak dose of 1.3, although it too is very poorly retarded and may be impacted by hydrodynamic dispersion.

8.3 Entire flowpath in one fracture class

In this sensitivity study, we consider the entire flowpath as consisting of the fracture classes in turn. Modelling of the different fracture classes has only been made in MARFA, as FARF31 cannot treat layered rock. Results for the different fracture classes have already be shown in Chapter 6 (Figure 6-1 to Figure 6-4), so we only summarise the results in Table 8-3 considering the peak dose rates for the six radionuclides contributing the most to the total dose rate. The second column of Table 8-3 shows the peak dose rates of the six most prominent radionuclides of the central corrosion case of SR-Site (including both IRF and CRF/DRF source terms), modelled with MARFA in the present replication study (cf. Figure 3-10), as well as the total peak dose rate. Corresponding values for the different fracture class cases are shown in the subsequent columns, based on data in Figure 6-1 to Figure 6-4.

Table 8-3. Comparison between SR-Site corrosion case and peak dose rates for case studies where individual fracture classes occupy the entire flowpath.

	Peak dose rate (µS/y)				
Nuclide	**SR-Site, replication case MARFA**	**F1:1 MARFA**	**F1:2 MARFA**	**F1:3 MARFA**	**F2:1 MARFA**
Ra-226	2.76	2.16	2.34	2.24	0.0896
Ni-59	1.46	0.844	1.02	0.813	0.023
Se-79	0.708	0.564	0.627	0.551	0.285
I-129	0.523	0.194	0.429	0.216	0.141
Np-237	0.263	0.232	0.237	0.232	0.0129
Nb-94	0.120	0.0315	0.0585	0.0418	<0.001
Total	3.39	2.75	2.92	2.83	0.464

Cross-comparing the results given in Table 8-3 gives some insights concerning the impact of alteration layers featuring differing effective diffusivities. Compared to the SR-Site replication case, using a layered rock matrix model generally gives lower peak dose rates, although they are only significantly lowered in the case of fracture class F2:1. It should be remembered that these results only consider altered effective diffusivities since the same K_d is assumed for all rock layers, which is a significant deviation from what is considered a likely scenario in the field. Moreover, they apply for flowpaths of moderate F-factors on the order of 50 000 y/m which implies a relatively low effective penetration depth in the unaltered rock matrix and thus we might expect the alteration layer to have a significant impact on retardation.

The influence of the fracture coating and alteration rim can be discussed based on the fracture classes of the immediate far field. For the major dose rate contributor, Ra-226, the effect of these layers is very limited. At most the peak dose rate of Ra-226 is decreased by ~ 20 % for fracture class F1:1. As discussed previously with regard to the reduced effective diffusivity case study (Section 8.2), this appears to be related to the fact that the source term for Ra-226 increases with time due to ingrowth both at source and along the migration path and the peak flux only just stabilises at about 1 My. The increasing boundary condition flux for Ra-266 plus ingrowth makes attribution of retardation difficult to assess using the simple scoping calculations developed in this report. For Nb-94, on the other hand, the effect is relatively large amounting to a factor of about 4 reduction in peak flux which appears to be attributable to the increased effective diffusivity in the 1 cm thick alteration rim.

The peak dose rates for all of the key nuclides are higher for fracture class F1:2 than for fracture class F1:3, indicating that a slight reduction in thickness and diffusive properties of the alteration rim is more important than a major reduction of the diffusive properties of the very thin fracture coating layer. This is because the fracture coating is very quickly equilibrated, and it is the underlying alteration rim that stands for the bulk of the retardation effect in any case.

When comparing results from fracture class F1:1 and F1:3, the total peak dose rate is virtually the same. Introducing the hypothetical low diffusivity fracture coating layer of fracture class F1:3 only alters (decreases) the total peak dose rate by ~ 5 % in the case of Ra-226 relative to fracture class F1:2. Interestingly, the thicker alteration layer in fracture class F1:3 is more than enough to offset the impact of reduced effective diffusivity in the fracture coating with regard to peak dose for all of the key radionuclides examined. The decrease for the other radionuclides is slight to moderate. Nb-94 exhibits the largest impact with a decrease of about 30 % in peak dose for fracture class F1:3 relative to fracture class F1:2.

For fracture class F2:1, the effective diffusivity of the third layer (undisturbed rock) is 48 times greater than the undisturbed rock in the other fracture classes. Hence, one would expect a much greater effective penetration depth compared to that for the other fracture classes. The increased retardation effect that this entails brings about a very significant reduction in peak dose rate for all radionuclides.

8.4 Varying sorption properties

In this sensitivity study, we vary the sorption properties of the different layers in a simplistic manner again using the combined (i.e. including both IRF and CRF/DRF) source term and flowpath 1. We implement our layered rock model and assume that the entire flowpath consists of rock with material properties characteristic of fracture class F1:1. In the first sensitivity case study, we increase the K_d-values in the fracture coating by a factor of 10 relative to those used in SR-Site (Figure 8-5). In the second sensitivity case study, we increase the K_d-values by a factor of 10 in both the fracture coating and the alteration rim (Figure 8-6).

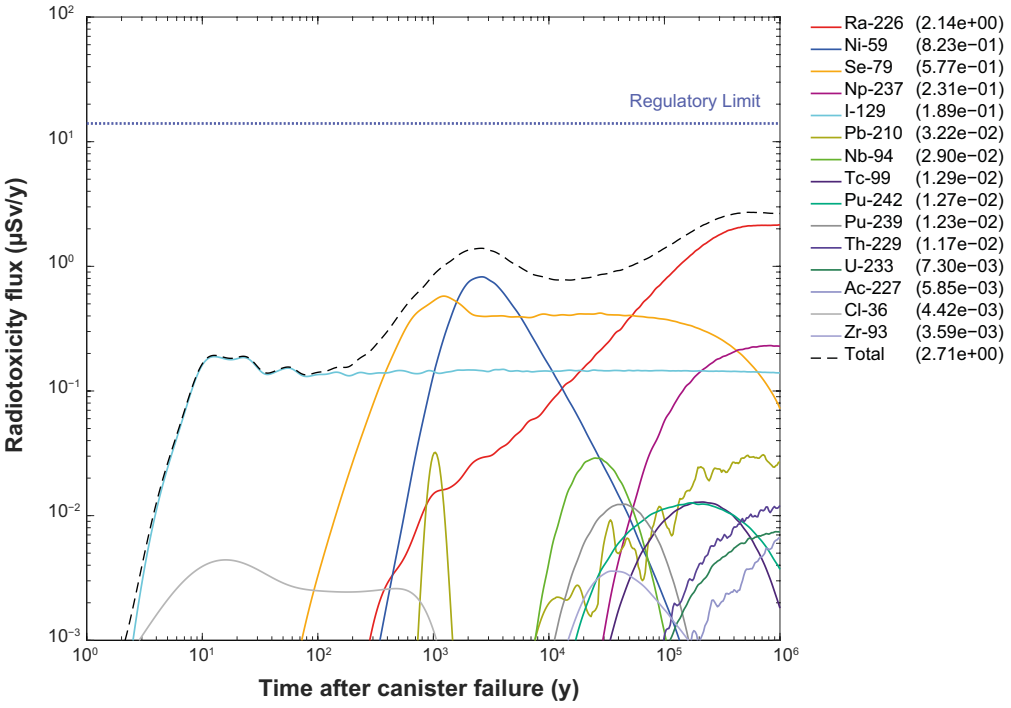

Figure 8-5. *Results from MARFA modelling of far-field dose rate results for flowpath 1 assuming material properties of fracture class F1:1, although with the K_d of the fracture coating increased by a factor of 10. The legend is sorted by annual effective peak dose (μSv/y) within the time frame of the assessment. The time on the x-axis is relative to canister failure. Only those radionuclides contributing more than 0.1 % of the total radiotoxicity are plotted.*

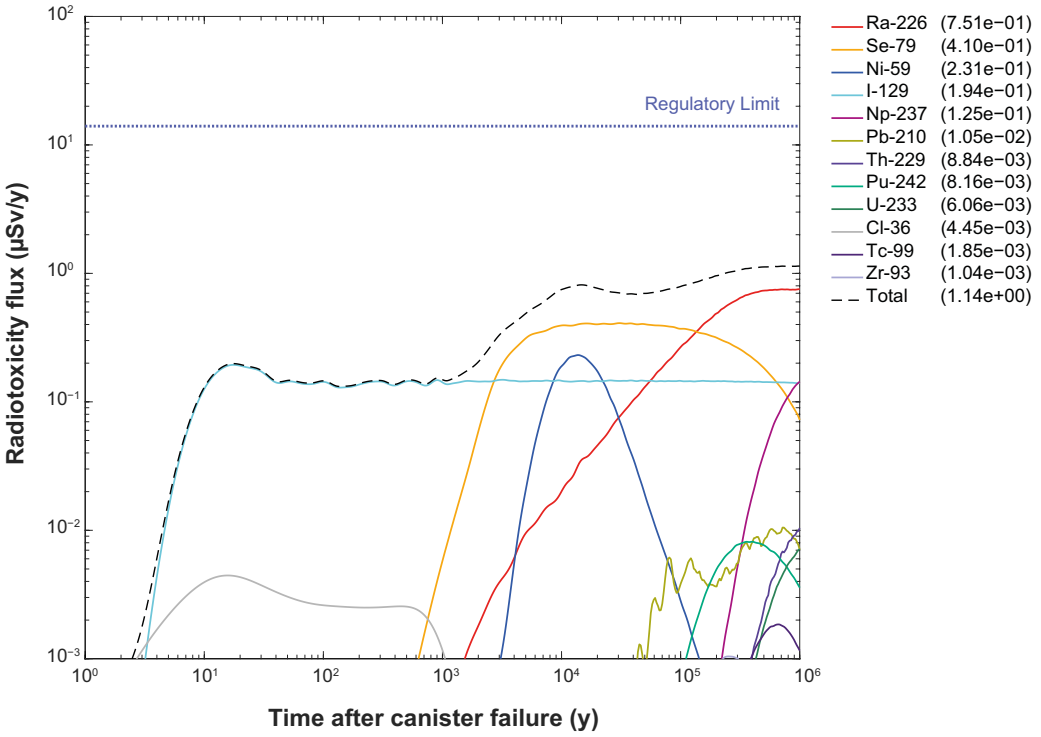

Figure 8-6. *Results from MARFA modelling of far-field dose rate results for flowpath 1 assuming material properties of fracture class F1:1, although with the K_d of the fracture coating and alteration layer increased by a factor of 10. The legend is sorted by annual effective peak dose (µSv/y) within the time frame of the assessment. The time on the x-axis is relative to canister failure. Only those radionuclides contributing more than 0.1 % of the total radiotoxicity are plotted.*

The second column of Table 8-4 shows the peak dose rates of the six most prominent radionuclides for the central fracture class F1:1 base case (including both IRF and CRF/DRF source terms), modelled with MARFA (cf. Figure 6-1), as well as the total peak dose rate. The third and fourth columns give the corresponding results for the two cases studying the impact of K_d increase in the fracture coating and alteration rim.

The results indicate that the very thin fracture coating in the F1:1 fracture class has very little impact on the results even when the K_d for sorbing radionuclides is increased by a factor of 10. There is essentially no impact on non-sorbing radionuclides (I-129 in Table 8-4) as would be expected, although there appears to be some small jitter presumably due to the stochastic nature of the MARFA simulations. It is interesting to note the very early peak for Pb-210 in Figure 8-5. This appears to be an artefact although possibly related to ingrowth from one of the parent nuclides in the decay chain being more strongly retained in the fracture coating. This is speculative, however, and further work will need to be done to properly ascertain the reasons for this. A similar artefact, although less prominent, can be seen in the limited diffusion depth case (cf. Figure 8-2).

The lack of a large impact of increased K_d does not necessarily mean that fracture coatings should not be further investigated if there is reason to believe that their retardation properties are much greater than the default values for the unaltered rock matrix. This is particularly relevant for nuclides which might have relatively low maximum depths of penetration such as Pb-210, Po-210, Ac-227, and possibly also Am-241 where the fracture coating will play a much more important role. Increasing the sorption capacity of the alteration rim, which is 100 times thicker than the fracture coating, has a much larger impact on the results as might be expected. The total peak dose rate is decreased from 2.73 to 1.14 µS/y (roughly a 60 % reduction), while the peak dose rates for the sorbing nuclides Ra-226, Ni-59, and Np-237 are decreased by 40–70 % relative to the fracture class F1:1 base case with default K_d values. Increasing the sorption capacity of the fracture adjacent layers does not only lower the dose rates, it also delays the timing of the first breakthrough and peak dose breakthrough. For radionuclides with relatively short half-lives, this might be expected to have a big impact on peak dose rate.

Table 8-4. Comparison of peak dose rates for fracture class F1:1, with different sorption properties.

Nuclide	F1:1 using default K_d values, MARFA (μS/y)	Increased K_d in fracture coating, MARFA (μS/yr)	Increased K_d in fracture coating and alteration rim, MARFA (μS/y)
Ra-226	2.16	2.14	0.751
Ni-59	0.844	0.823	0.231
Se-79	0.564	0.577	0.410
I-129	0.194	0.189	0.194
Np-237	0.232	0.231	0.125
Nb-94	0.0315	0.029	< 0.001
Total	2.73	2.71	1.14

8.5 Segment order for mixed fracture classes

As discussed in Chapters 4 and 5, it is deemed unlikely that the entire flowpath will be surrounded by the same type of wall rock. For this reason, we introduced four different fracture classes that, in (what we believe to be) a reasonably realistic fashion, span the rock microstructural types frequently observed at the site. In our central calculation case for a segmented, multi-layered rock model, we assume that the three fracture classes F1:1 to F1:3 occupy the first 90 % of the flowpath (in terms of the cumulative flowpath F-factor). The last 10 % of the flowpath, in the distant far-field, is assumed to be comprised of rock characteristic of fracture class F2:1. The quantification of our central case layered rock model is provided in Figure 5-1. The remaining issue is how to distribute the three fracture classes of the immediate far-field.

In Figure 5-1, each fracture class is assigned a surface coverage fraction. For fracture class F1:1 to F1:3, the surface fractions are estimated solely based on the existence of a fracture coating layer, or its absence. Even on the scale of the drill core sample cross-sectional area, surface coatings are observed to appear in a patch-wise manner (cf. Section 5.3) suggesting short correlation lengths. This speaks against the notion that the flowpath is characterised by a single fracture class over long distances, say over tens to hundreds of meters. It seems far more likely that the fracture classes are distributed in a patch-wise manner such that representing it on very large scales becomes infeasible for modelling purposes. Although this is partly due to limitations in computing power, it is primarily due to a lack of knowledge on exactly how the fracture coatings are distributed. The fact that sampling is done on small diameter bore core fracture surfaces also means that information on longer range correlation lengths for fracture coatings is not quantifiable which is a source of uncertainty. There is also uncertainty introduced by basing the surface fraction of the fracture classes only on the fracture coating distribution, and not also on the underlying layers for which we have even less information.

In the reference case for this sensitivity study, the patch-wise distribution of fracture coatings is represented by dividing the flowpath into 100 segments. The last 10 segments represent the distant far-field and therefore all are assigned to fracture class F2:1. Fracture classes F1:1, F1:2, and F1:3 are assigned 27, 54, and 9 segments each in a serial sequence in accordance with the designated surface coverage fractions depicted in Figure 5-1. The order of fracture classes within a group as depicted in Figure 5-1, however, is arbitrary and there are 6 different serial sequences that could be modelled by shuffling the order of fracture classes defined for the immediate far field. If we were to also include F2:1, there would be 24 different block-wise sequences that could be modelled.

Instead of modelling different ordering of the fracture classes in turn, it was judged that a segmented, randomised ordering of fracture classes might be a useful limiting case and likely to be also more physically representative. This sensitivity study therefore focuses on the impact of block-wise serial versus randomised fracture class ordering. The results of the MARFA model assuming the reference case, serial sequence of fracture classes are shown in Figure 8-8 (noting that this is the same as Figure 7-1). The coloured bar below the graph shows the order of fracture class segments.

In the sensitivity study, we once more assume a flowpath divided into 100 segments where each of the segments are assigned to different fracture classes in accordance with their surface fraction in Figure 5-1. In this case, however, the order of the segments in the immediate far-field is randomised. Figure 8-8 shows the results of this simulation with the order of the fracture classes indicated in the coloured bar below the plot.

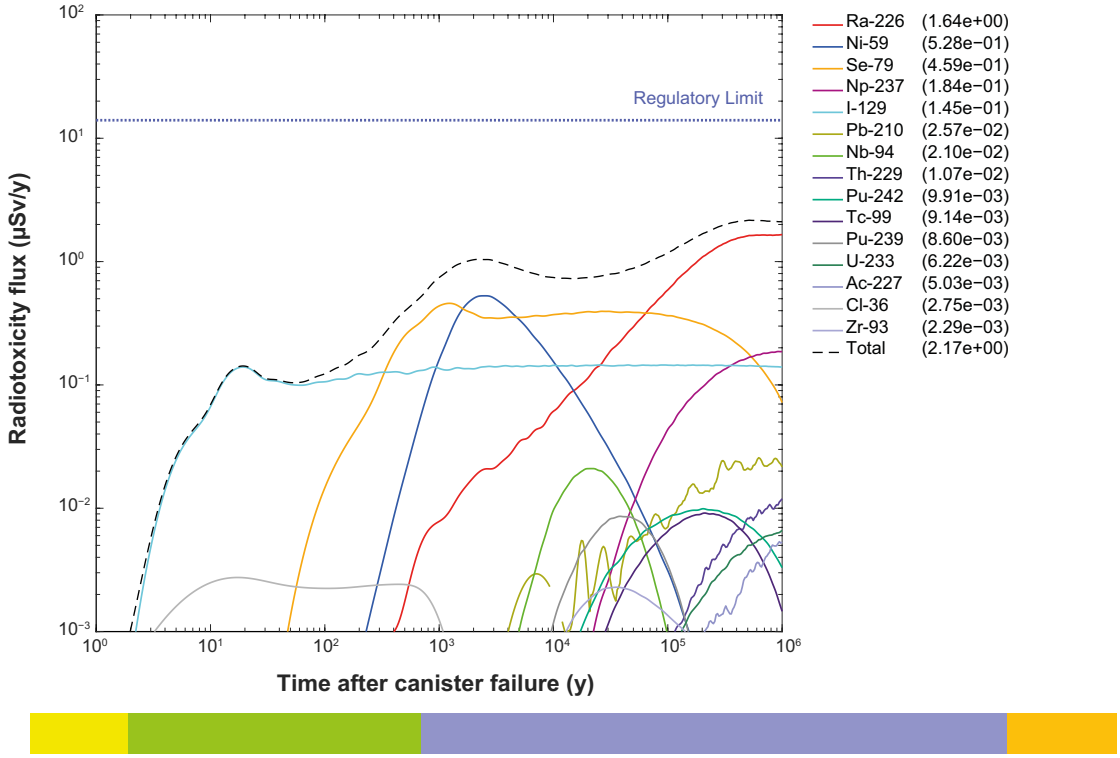

Figure 8-7. *Results from MARFA modelling of far-field dose rate results for flowpath 1 assuming linear sequence of rock-type segments. Order of segments shown in lower bar by green (fracture class F1:1), blue (F1:2), yellow (F1:3) and orange (F2:1). Time is shown relative to canister failure. Peak dose rates are given for each radionuclide in the legend.*

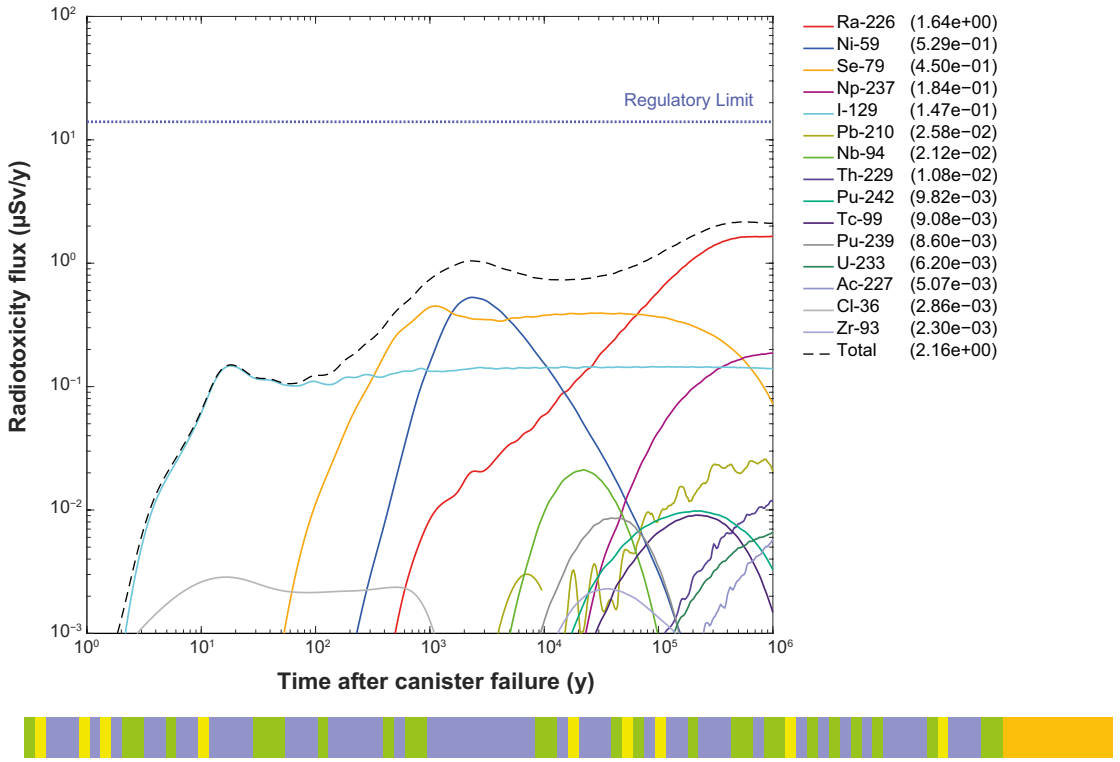

Figure 8-8. *Results from MARFA modelling of far-field dose rate results for flowpath 1 assuming randomised sequence of rock-type segments in the near-field. Order of segments shown in lower bar by green (fracture class 1:1), blue (1:2), yellow (1:3) and orange (2:1). Time is shown relative to canister failure. Peak dose rates are given for each radionuclide in the legend.*

Table 8-5 shows the total peak dose rate and the peak dose rates for the six most prominent radionuclides of the central corrosion case of SR-Site which assumed a single layer with material properties assumed to be the same as undisturbed rock. The SR-Site peak fluxes, as replicated in this work using MARFA, are taken from the legend of Figure 3-10. Data for the randomised and serial central case layered rock model are taken from Figure 8-8 and Figure 8-7, respectively.

Table 8-5. Comparison of peak dose rates for SR-Site and central case layered rock models.

Nuclide	SR-Site case, MARFA (μS/yr)	Central case, serial sequence, MARFA (μS/yr)	Central case, random sequence, MARFA (μS/yr)
Ra-226	2.76	1.64	1.65
Ni-59	1.46	0.533	0.524
Se-79	0.708	0.439	0.452
I-129	0.523	0.146	0.146
Np-237	0.263	0.186	0.185
Nb-94	0.120	0.0212	0.0210
Total	3.39	2.16	2.16

Considering the stochastic nature of the MARFA program, only very minor differences are seen when comparing serial versus random fracture class sequences. The results of the last two columns in Table 8-5 differ by less than 1 % with the exception of Se-79, which differs by roughly 3 %. Moreover, the deviations between the two cases seem approximately randomly distributed around zero indicating a stochastic effect rather than a systematic deviation. In a non-layered system, where heterogeneity is deemed to occur only along a flowpath (and not with distance into the rock matrix), the results from the different realisations should be identical based on theoretical reasoning in SKB (2004). It is, however, difficult to evaluate very small variations in simulations made using MARFA since it is a stochastic tool and, unless enormous numbers of particles are used in a simulation, there will always be some deviation.

Based on the very similar results of the two realisations, we judge that no other realisations of randomised segments, or varying the order or the fracture classes in series, are necessary at least as far as the major dose determining nuclides are concerned. Although it has already been shown in the RETROCK project (SKB 2004), that material properties can be averaged along a flowpath to give a unique result for matrix related transport retardation, this can only be established analytically for single layer rock matrix models of infinite depth. In the more general case of a multilayer rock matrix, it appears not possible to calculate a closed form estimate of the flowpath average without first simulating migration assuming full variability of material properties in the multilayer system. It should be noted that this does not imply that a flowpath average does not exist, just that it may not be computable à priori in any simple fashion.

It is still not clear whether flowpath averaging of material properties can be used to represent transport in multi-layered rock matrix models, or whether the analysis can be also extended to radionuclides that are produced mostly by ingrowth along a flowpath. Short-lived, sorbing radionuclides such as Ac-227 and Pb-210 (and Po-210 although not included in the SR-Site modelling), are more likely to be influenced by variation in material properties near the end of a migration path rather than near the beginning since they are predominantly produced by ingrowth along the migration path. In this work, we have not examined the impact of altering the material properties of the terminal sequence of fracture classes in the distant far-field, although this may (or, may not) have some impact on peak dose rates attributable to exceptionally short-lived decay chain nuclides.

If comparing the results from the SR-Site central corrosion case with our central calculation case for a layered rock model, the total peak dose rate is reduced by about one third. This modest reduction possibly speaks against the need to produce an elaborate multi-layered rock matrix model for a KBS-3 type repository, at least if only modifying the diffusive properties of the alteration layers. If assuming an initially defective canister (cf. TURVA-2012), where radionuclides associated with pulse release take on much greater significance, this conclusion may not hold. For radionuclides predominantly released as a short pulse, e.g. Nb-94, the peak dose rate is reduced by about a factor of five in Table 8-5 for a multilayer rock matrix relative to the SR-Site central corrosion case. As the retardation in fracture

class F1:1 to F1:3 is similar to that of the undisturbed rock in SR-Site (cf. Table 8-3), it seems that the impact of fracture class F2:1 is significant, even though only 10 % of the F-factor is assigned to this fracture class. If the total peak dose rate is dominated by radionuclides released by fuel dissolution as in the central corrosion case in SR-Site, changing the sorption capacity of the alteration rim gives a more significant impact (cf. Section 8.4) than introducing an elaborate multilayer system based on different fracture classes as in the central case layered rock model.

8.6 Comparison of central case and different sensitivity studies for flowpath 1

In this section, we consider the results from our sensitivity studies for flowpath 1 from the perspective of peak dose rate for individual radionuclides and the peak total dose rate (summed over all radionuclides). Here, we only show the variations for the top 5 most important radionuclides. This is done in Figure 8-9 for the eleven different cases discussed in previous chapters also including the SR-site central corrosion case.

The sensitivity study giving the highest peak dose rates is variation case study 3, which is the same single-layer model as used in the SR-Site simulations, although with one order of magnitude reduced effective diffusivity. This variant gives the highest dose rates for all radionuclides individually and for the peak total dose rate. While it may be reasonable to argue that such low effective diffusivities may be found in the undisturbed rock (at least occasionally), it is worth noting that the effective penetration depth for flowpath 1, using these very low effective diffusivities, is at most a few millimetres (see Section 9.1 for this analysis). The main retardation effect therefore takes place in the alteration rim, which typically is expected to have larger effective diffusivity than the undisturbed rock.

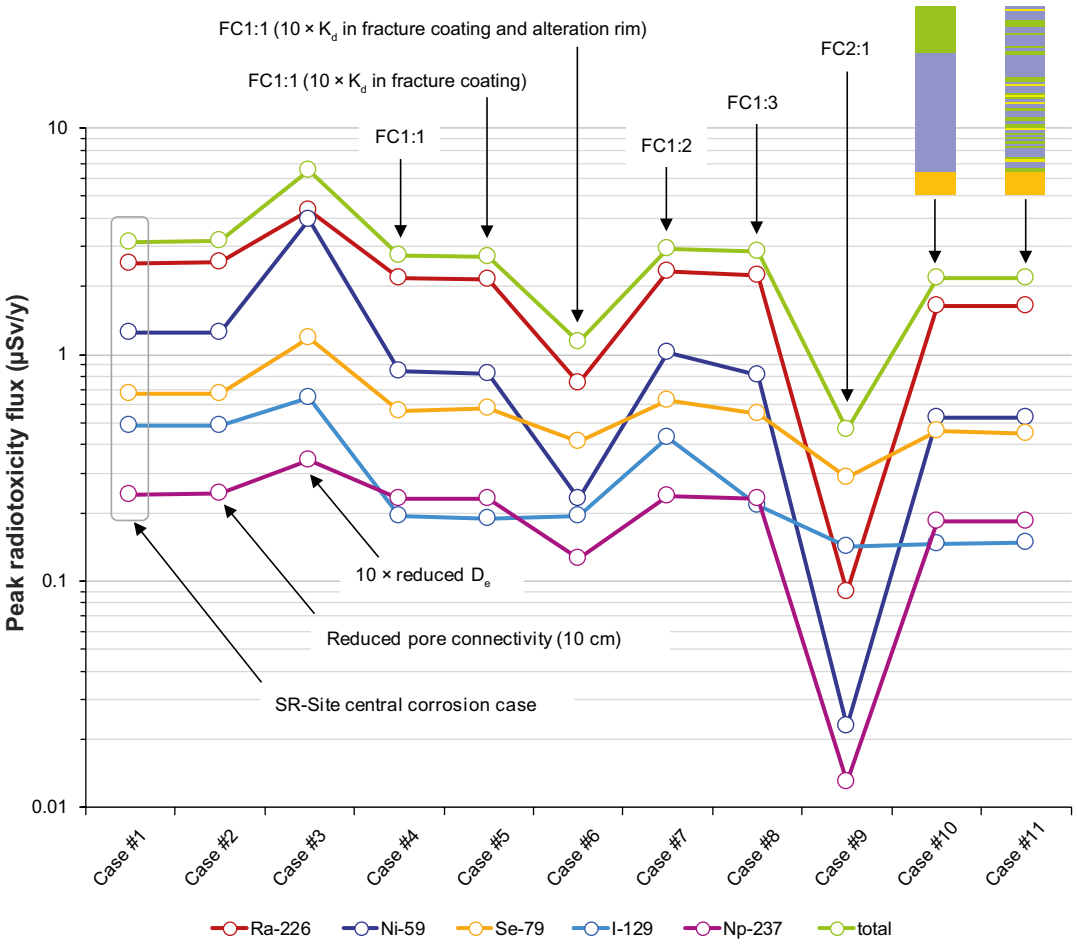

Figure 8-9. *Peak dose rates in different sensitivity studies modelled in this work.*

The sensitivity study giving the lowest peak dose rates is case 9, where the entire flowpath is assumed to have material properties corresponding to fracture class F2:1. This fracture class is associated with much larger effective penetration depths than the other sensitivity studies and, consequently a significantly stronger retardation. Interestingly, increasing the effective diffusivity in the rock beyond the alteration rim seems to give a more pronounced impact than increasing the sorption capacity of the alteration rim itself (case #6). In these specific cases, however, the increase in effective diffusivity was by a factor of 48 while the increase in the K_d-value was only a factor of 10.

8.7 Varying of flow related migration properties

8.7.1 Flowpath featuring lowest F-factor in SR-Site

In this case study, we study the impact of variation of the flow-related transport properties by examining what would happen if we were to base the calculation on the flowpath with the lowest F-Factor (flowpath 2 in Table 3-2). Although this flowpath had the worst flow-related migration properties regarding retardation potential, the canister associated with this flowpath took considerably longer to corrode (failure at 800 ky) than the canister corresponding to the central corrosion case (flowpath 1) which had a nearly 5 times larger F-factor. This was most likely due to the much lower flowrate through this canister deposition hole. In the simulation presented here, we assume the same source term (IRF, CRF, and DRF) as assumed in the other case studies to isolate the impact of flow-related transport properties only. For the comparison, we assume the same material properties as the central calculation case featuring multiple fracture classes previously described in Chapter 7. The results of this simulation are shown in Figure 8-10. It should be noted that this is not an entirely realistic calculation since the much longer failure time associated with this canister position implies that the source term for some radionuclides will be significantly less than that actually used in the calculation (which is based on the source term at 114 ky). This will have a particularly strong impact on the Ni-59 peak where the inventory at 800 ky will be ~ 600 times less than that giving rise to the peak in Figure 8-10 due to source term decay. The calculations therefore should be considered as "what if" type explorations of the consequences of flowpath hydrodynamic resistance where all other parameters are held constant.

If comparing with the reference case for multiple fracture classes, we see that the peak total dose rate is approximately doubled by decreasing the F-factor by about half an order of magnitude. Although the advective travel time is three times greater in this case than in the reference central corrosion case, this is deemed to have very minor impact on the peak dose rate and mostly influences the time of first breakthrough and leading edge of the breakthrough curves for very early arriving, non-sorbing radionuclides (I-129 and Cl-36).

8.7.2 Flowpath featuring median F-factor in SR-Site

In this case study, we study the impact of variation of the flow-related transport properties by examining what would happen if we were to base the calculation on the flowpath with the median F-Factor (flowpath 3 in Table 3-2). This canister position also was associated with a longer corrosion failure time (200 ky) than the reference case (flowpath 1 in Table 3-2) also presumably on account of a lower advective flow through the canister deposition hole. In the simulation presented here, we assume the same source term (IRF, CRF, and DRF) as assumed in the other case studies to isolate the impact of flow-related transport properties only. For the comparison, we assume the same material properties as the central calculation case featuring multiple fracture classes previously described in Chapter 7. The results of this simulation are shown in Figure 8-11.

This flowpath with an F-factor nearly double that of the reference case exhibits much stronger retardation relative to flowpath 1, and the peak total dose rate is approximately halved due to the greater flow-related transport resistance. Here also, the advective travel time is nearly three times greater than for the reference central corrosion case. In this case, however, the retarded travel time of even the non-sorbing radioelements is sufficiently long that this parameter has minimal impact.

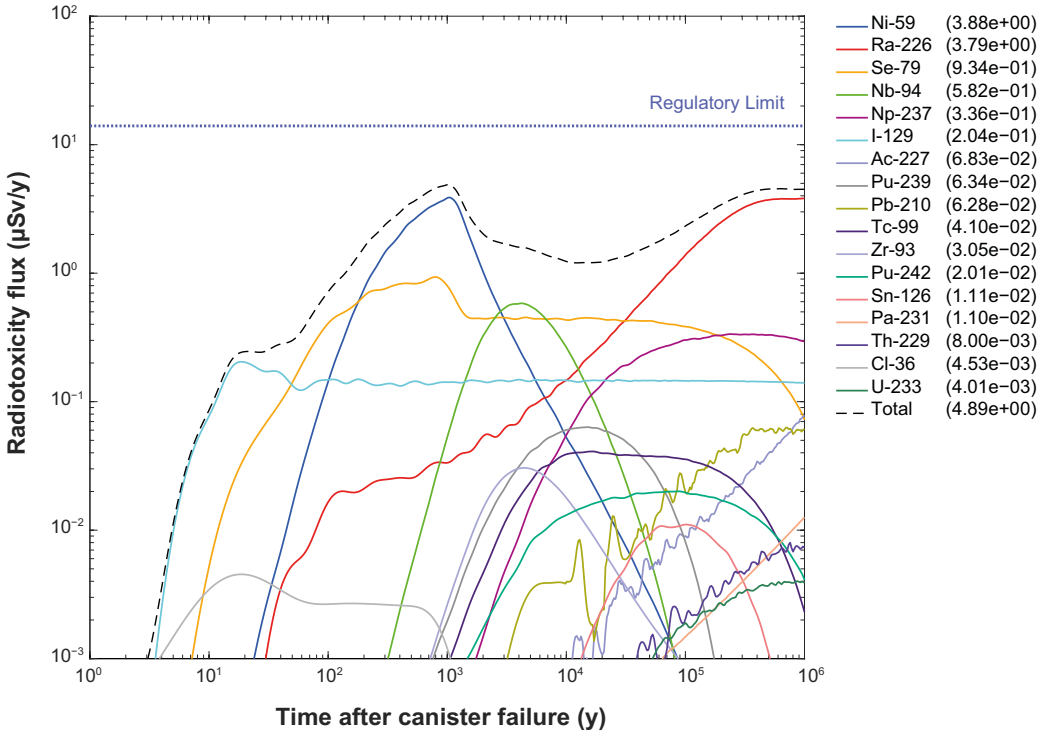

Figure 8-10. *The annual effective dose for the corrosion scenario calculated using MARFA assuming the different fracture classes distributed in proportion to cumulative F-factor along flowpath 2 (combined IRF, CRF and DRF source terms). The legend is sorted by annual effective peak dose (µSv/y) within the time frame of the assessment. The time on the x-axis is relative to canister failure. Only those radionuclides contributing more than 0.1 % of the total radiotoxicity are plotted.*

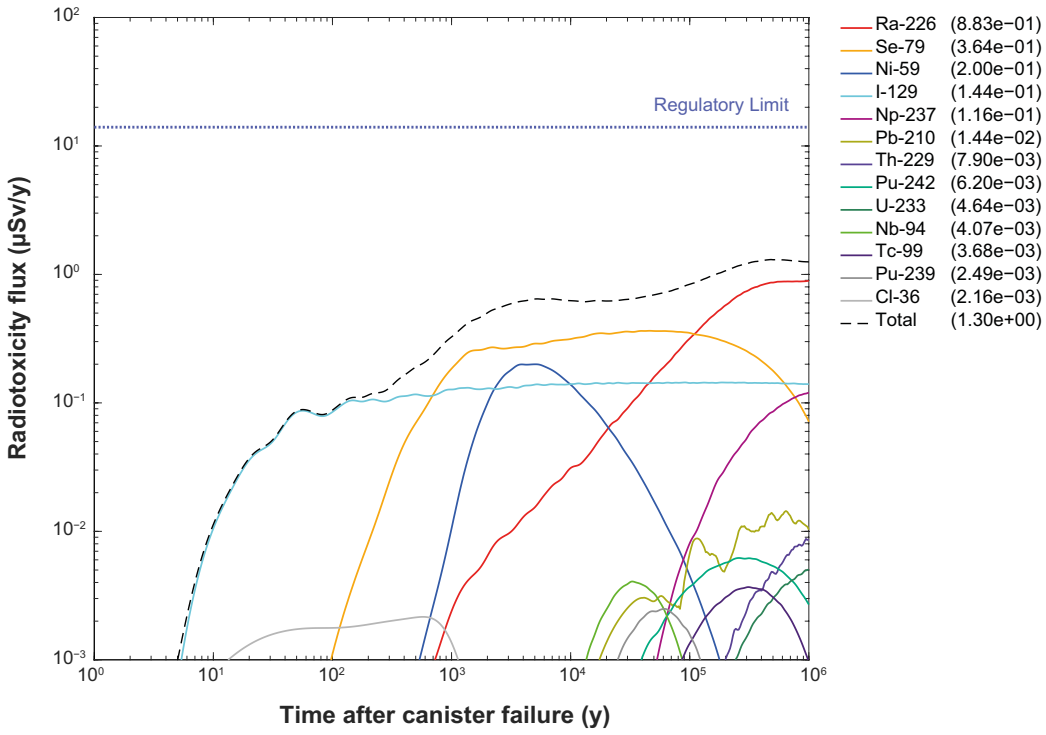

Figure 8-11. *The annual effective dose for the corrosion scenario calculated using MARFA assuming the different fracture classes distributed in proportion to cumulative F-factor along flowpath 3 (combined IRF, CRF and DRF source terms). The legend is sorted by annual effective peak dose (µSv/y) within the time frame of the assessment. The time on the x-axis is relative to canister failure. Only those radionuclides contributing more than 0.1 % of the total radiotoxicity are plotted.*

9 Attribution of retardation in single- and multilayer rock matrix systems

In this section we make a theoretical analysis to assess the extent to which transported radionuclides interact with the rock matrix. This is an important question for safety assessment since the depth of rock matrix associated with the bulk of the transport retardation effect has implications for whether chosen retardation parameters are under- or possibly over-conservative for the safety case under different hydrodynamic conditions. An estimate of the effective penetration depth also provides a quantitative yardstick with which to measure the utility of more complex multilayer rock matrix descriptions against simpler, single-layer models as have been assumed in previous safety assessments. Furthermore, the effective depth of rock matrix that provides the bulk of the retardation effect also allows us to gauge whether the maximum penetration depth based on the local average half-spacing of flow conductors is a limiting factor for radionuclide retardation and thereby a meaningful uncertainty.

In this chapter we show, among other things, that the "effective" penetration depth associated with the bulk of transport retardation can be estimated from the effective diffusivity and cumulative F-factor of the flowpath for a homogeneous and non-layered rock matrix. This penetration depth can also be shown to be independent of the sorptive affinity (K_d) of the medium for a migrating solute not subject to decay. For a radionuclide that undergoes decay, we additionally show that there is an "average maximum" penetration depth (equal to the square root of the ratio of apparent diffusivity and the decay constant of a migrating radionuclide) beyond which the presence of a limited rock matrix boundary will have limited impact on retardation.

It is also shown in this chapter that the effective penetration depth for a radionuclide undergoing decay will always be less than or equal to that for a stable solute. Finally, we show that the calculation of effective penetration depth can be extended to the multilayer case and use this to draw conclusions concerning the relative impact of fracture minerals and alteration layer on the retardation of specific radionuclides using the SR-Site central corrosion case as a benchmark.

9.1 The effective penetration depth in SR-Site corrosion case calculations

In this work, we operationally define the effective penetration depth as the equivalent depth of rock matrix that, if instantaneously equilibrated, would give a retardation factor corresponding to the travel time for a migrating solute pulse undergoing ordinary matrix diffusion. The conceptual difference between these two situations, however, is that while there is only a single retarded travel time for a solute subject to an equilibrium retardation process, the matrix diffusion problem has a skewed distribution of characteristic retarded travel times with a fat tail. The challenge then is to identify a characteristic retarded travel time that is representative of the matrix diffusion process as far as this is relevant for safety assessment.

The mean travel time (i.e. first moment of the residence time distribution) for a solute pulse is a poor choice in this context since it typically occurs far later than peak breakthrough which is arguably one of the most important metrics for safety assessment. The only exception to this is for situations involving trivially shallow depths of accessible matrix which we do not consider relevant to this work. Additionally, the effective depth of penetration corresponding to the average travel time is equal to the maximum depth of the simulated medium (for a limited matrix depth) which does not really tell us a great deal about where in the rock matrix, the bulk of the retardation effect occurs. The corollary of this, as Neretnieks (1983) also pointed out, is that the mean residence time is unbounded in an infinite rock matrix. This is clearly problematic for the computation of an effective penetration depth if using the mean travel time as a calculation basis. Identification of where the bulk of the transport retardation occurs also serves a more prosaic purpose; i.e. what depth of rock matrix (and discretization thereof) is necessary to model in numerical calculations to obtain artefact-free detail in modelled breakthrough curves.

In previous work (e.g. Crawford 2006, Moreno and Crawford 2009), we have noted that the median travel time corresponding to the first 50 % recovery of an injected Dirac pulse seems to be a good choice of characteristic breakthrough time for such a calculation. Since the residence time distribution in matrix diffusive systems exhibits a strong positive skew, the median is a useful yardstick since it identifies the extent of rock matrix that is responsible for ~ 50 % of the observed retardation effect. The choice is arbitrary, although loosely based on the idea that matrix saturation effects start to become obvious in the leading edge of breakthrough curves (i.e. ≤ 50 % solute recovery) for limited rock matrix depths roughly equal to twice the penetration depth calculated using the median retarded travel time in an unbounded rock matrix (see Figure 9-1 and Figure 9-2 for a typical example). For a maximum matrix depth set to twice the estimated effective penetration depth (in the present case, 2×3.9 cm ≈ 7.8 cm), the deviation between the cumulative residence time distribution curves for a limited and unbounded rock matrix is less than 0.3 % at the time of median breakthrough for the unbounded case (cf. vertical red broken line in Figure 9-1). For the actual residence time distribution, on the other hand, the deviation is around 4 % of the peak height (cf. vertical red broken line in Figure 9-2) for the same comparison.

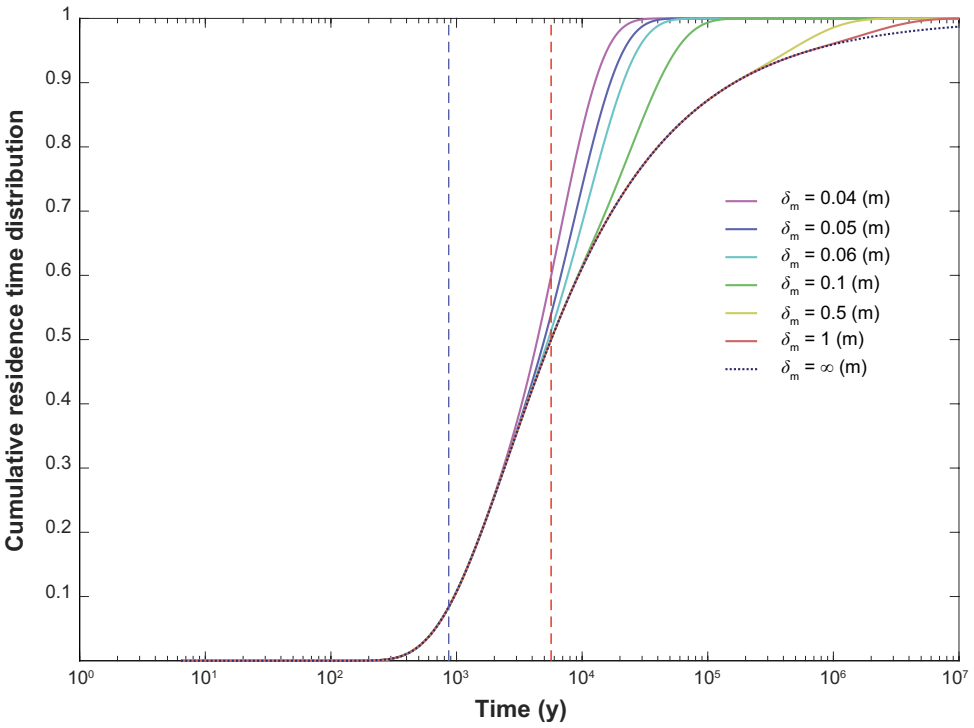

Figure 9-1. *Simulated residence time distribution (cumulative recovery time probability) for a non-decaying solute (K_d = 0.001 m^3/kg, $D_e = 2.1 \times 10^{-14}$ m^2/s) and the same hydrodynamic transport properties as in the central corrosion case of SR-Site. Curves show simulated breakthrough for different modelled matrix depths. Matrix saturation effects start to become apparent in the leading edge of the breakthrough curve (< 50 % recovered solute) for matrix depths roughly corresponding to twice the penetration depth calculated for the median retarded travel time assuming an unbounded rock matrix (~ 4 cm). The vertical blue and red lines indicate the peak (mode) and median breakthrough, respectively for transported solute assuming an unbounded rock matrix.*

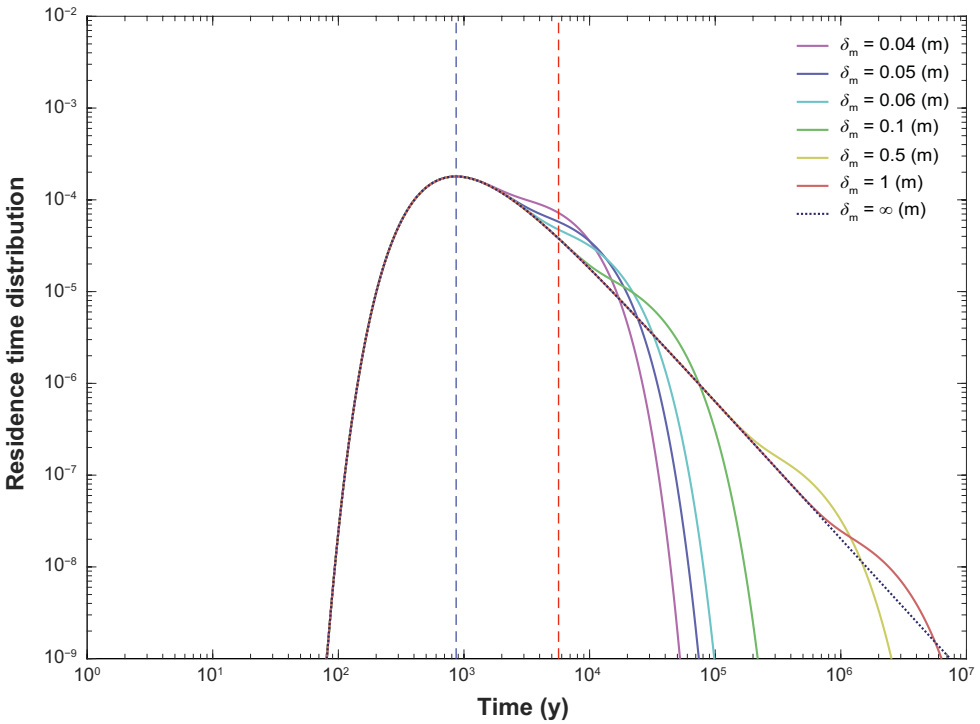

Figure 9-2. *Simulated residence time distribution (probability density function of travel times) for the same case shown in the previous figure. The vertical blue and red lines indicate the peak (mode) and median breakthrough, respectively for transported solute assuming an unbounded rock matrix.*

9.1.1 Effective penetration depth for non-decaying solutes in a single-layer, unbounded rock matrix

For an instantaneously equilibrated rock matrix (assuming linear reversible sorption), the retarded travel time, t_R can be defined directly from mass balance considerations as:

$$t_R = R_{fm} t_w = \left(1 + 2R_p \varepsilon_p \frac{\delta_m}{\delta_t}\right) t_w \tag{9-1}$$

Where, R_p is the pore retardation factor, ε_p is the matrix porosity, δ_t is the transport aperture of the flow-path, and δ_m is the effective penetration depth in the rock matrix. Also, R_{fm} is the apparent retardation factor for an equilibrium process and t_w is the advective travel time. Equation 9-1 can be rearranged to give the rock matrix depth explicitly:

$$\delta_m = \left(\frac{t_R}{t_w} - 1\right) \frac{\delta_t}{2R_p \varepsilon_p} \tag{9-2}$$

The variable, δ_m is what we refer to in this work as the effective penetration depth based on the characteristic travel time, t_R of a transport retarded solute. For an unbounded rock matrix and neglecting hydrodynamic dispersion, the solution by Neretnieks (1980) gives the median travel time for a non-decaying solute as:

$$t_{R50} = t_w + \frac{D_e R_p \varepsilon_p}{4\left(\mathrm{erfc}^{-1}\left(0.5\right)\right)^2} \cdot F^2 \tag{9-3}$$

The relation between F-factor, advective travel time, and transport aperture is given by:

$$\delta_t = 2t_w / F \tag{9-4}$$

Substituting Equation 9-3 and 9-4 into Equation 9-2 gives, after some simplification:

$$\delta_m = \frac{D_e F}{4 \cdot \mathrm{erfc}^{-1}\left(0.5\right)^2} \approx 1.0991 \cdot D_e F \tag{9-5}$$

There are, of course, alternative means of estimating an effective penetration depth. Neretnieks (1980), defines an average penetration depth based on integration of the diffusion equation (e.g. Crank 1975), thereby giving:

$$\delta_m = \frac{2}{\sqrt{\pi}} \cdot \sqrt{\frac{D_p}{R_p} t_m} = \frac{2}{\sqrt{\pi}} \cdot \sqrt{D_a t_m} \tag{9-6}$$

Where the ratio between pore diffusivity, D_p and pore retardation factor, R_p is equal to the the apparent diffusivity of a particular solute. Equation 9-6 gives a representative "average" depth to which solute will have penetrated the rock matrix as a function of contact time, t_m assuming a porewater concentration in equilibrium with that prevailing at the fracture surface (for a constant concentration boundary condition). If the rock matrix residence time corresponding to the median travel time given by Equation 9-3 is substituted into Equation 9-6 as a measure of matrix contact time, we then obtain a slightly different estimate of the effective penetration depth:

$$\delta_m = \frac{2}{\sqrt{\pi}} \cdot \sqrt{\frac{D_p}{R_p} \left(t_R - t_w\right)} = \frac{1}{\sqrt{\pi} \cdot \mathrm{erfc}^{-1}\left(0.5\right)} \cdot D_e F \approx 1.1829 \cdot D_e F \tag{9-7}$$

Although Equation 9-5 and 9-7 differ by less than 10 %, we prefer the estimate given by Equation 9-5 since it makes fewer assumptions about the form of the boundary condition at the fracture surface. For an effective diffusivity of 2.1×10^{-14} m^2/s, as used in SR-Site for cations and non-charged species, the effective penetration depth is estimated using Equation 9-5 to be less than 4 cm for the migration flowpath corresponding to the central corrosion case. As noted in the previous section (cf. Figure 9-1 and Figure 9-2), the use of a maximum matrix depth of at least twice this value (~ 8 cm) in calculations gives a very close approximation to the "true" effective penetration depth as discerned by observable breakthrough curve deviation from the unbounded case. For radionuclides experiencing anion exclusion, with an effective diffusivity of 6×10^{-15} m^2/s in SR-Site, the effective penetration depth is about 1 cm. This is in qualitative agreement with the results in Table 8-1, indicating that the storage capacity of the diffusively accessible rock matrix was only just equilibrated when limiting the maximum penetration depth to 10 cm, at least when considering median solute retardation times. If the maximum penetration depth in the calculation (cf. Figure 8-1 and Figure 8-2) was set to 2 cm or 5 cm, on the other hand, we might then expect to see larger deviations from the unbounded case. At much later times, however, the storage capacity does become completely equilibrated, although this is barely discernible from the breakthrough curves and has little to no impact on leading edge and peak breakthrough of the radionuclides.

If using an order of magnitude higher effective diffusivity, as is frequently observed in the laboratory, the effective penetration depth increases to about 40 cm for cations and non-charged species. In such a case, the breakthrough curves would be more strongly affected, compared to the case of unlimited pore connectivity if the maximum penetration depth was set to only 10 cm. In SR-Site, the maximum penetration depth was set to 12.5 m based on the average half-separation of stochastic flow conductors in the rock. To reach an effective penetration depth of 12.5 m, either the F-factor or effective diffusivity (or both) needs to be increased greatly compared to that assumed in SR-Site. Although flowpaths may exist where such penetration depths might be achievable, they would not be expected to contribute significantly to the annual effective dose rate since it is typically flowpaths featuring low F-factors (usually also high flow rates) that dominate far-field dose rates owing to their poor retardation of migrating radionuclides.

A key property of the relation described by Equation 9-5 is that the effective penetration depth is proportional to the effective diffusivity and F-factor product and independent of the pore retardation factor (and consequently, the K_d for a migrating solute). Although this might seem counterintuitive, it is a robust result that can be easily explained by the relative timescale of retardation. As outlined in Löfgren et al. (2007), while the characteristic transport time is longer for a sorbing solute, the longer transport time will allow a more strongly sorbing solute to penetrate the rock matrix to the same depth as a less strongly sorbing solute with shorter characteristic transport time. As can be seen from Equation 9-5, the sorption related retardation terms exactly cancel to give a penetration depth that is independent of sorptivity in the absence of decay. This is one of the main differences between the conceptualisation of effective diffusion depth in the context of a flowpath transport retardation effect and absolute diffusion depth which is proportional to the square root of contact time and not dependent on any flowpath retardation considerations.

There are other choices that could be used instead of the median travel time in such a calculation. For example, if we were interested in attribution of which depth of the rock matrix is responsible for a specific portion of the retarded breakthrough of a safety-assessment-critical radionuclide, we might choose the characteristic breakthrough time associated with, say the first 1 %, 10 %, 75 %, or 90 % of recovered solute, in which case we would have:

$$\delta_{1\,\%} = 0.0754 \cdot D_e F \tag{9-8}$$

$$\delta_{10\,\%} = 0.185 \cdot D_e F \tag{9-9}$$

$$\delta_{75\,\%} = 4.93 \cdot D_e F \tag{9-10}$$

$$\delta_{90\,\%} = 31.7 \cdot D_e F \tag{9-11}$$

The mode of the residence time distribution can also be shown to be associated with an effective penetration depth given by:

$$\delta_{\text{mode}} = \frac{1}{6} \cdot D_e F \approx 0.1667 \cdot D_e F \tag{9-12}$$

As can be seen from this analysis, the effective penetration depth related to different breakthrough fractions of transport solute is non-linear with the breakthrough of the first 90 % of transported solute associated with an effective penetration depth over 30 times greater than that of the first 50 % (assuming an unbounded matrix). Although Equation 9-5 gives an order of magnitude accurate spot estimate of the depth of rock matrix associated with ~ 50 % of retardation, it is also possible to calculate and plot a continuous distribution showing the depth of penetration associated with transport retardation. To do this, we substitute Equation 9-1 directly into the solution for an unbounded matrix by Neretnieks (1980). The cumulative distribution function (CDF) for different fractions, χ of the overall retardation effect can then be given as a continuous function of depth, z in rock matrix using the expression:

$$\chi(z) = \operatorname{erfc}\left(\frac{1}{2}\sqrt{\frac{D_e F}{z}}\right) \tag{9-13}$$

The corresponding probability density function (PDF) is then obtained as the derivative of Equation 9-13:

$$p(z) = \frac{\sqrt{D_e F}}{2\sqrt{\pi} z^{\frac{3}{2}}} \cdot \exp\left(-\frac{D_e F}{4z}\right) \tag{9-14}$$

As previously, both the cumulative- and probability density functions are found to be independent of sorptivity in the rock matrix. The attribution of different fractions of the overall retardation effect is plotted in Figure 9-2.

There are, of course, limitations to this kind of analysis. Chief among these is that, at least in the very simple problem formulation discussed here, it is only strictly applicable to a Dirac pulse boundary condition for a non-decaying (and non-ingrowing) solute. A more complex boundary condition, however, can be approximated as a delayed sequence of (actually, an infinite pulse train of) Dirac pulses, so the general concept of using the median transport time as a representative retarded travel time seems to be transferrable to other release situations at least with regard to identifying where the bulk of retardation occurs in the rock matrix (what we refer to in this work as retardation attribution).

Another limitation to this analysis is that it is necessary to consider the entire flowpath when discussing median, or any other characteristic travel time for the breakthrough curve (apart from the mean travel time, which we have already discussed is typically not a relevant measure for safety assessment metrics). This is because solute residence time distributions are strongly skewed for matrix diffusion processes and the sum of median travel times for a sequence of flowpath segments is always less than the calculated median travel time for the sum of flowpath segments. Since the retarded travel time is roughly proportional to the square of the F-factor (cf. Equation 9-3 for the unbounded case), this is easy to show using the quadratic identity for a sequence of n flowpath segments:

$$\left(\sum_{k=1}^{n} F_k\right)^2 = \sum_{k=1}^{n} F_k^2 + 2\sum_{j=1}^{n}\sum_{i=1}^{j-1} F_j F_i \tag{9-15}$$

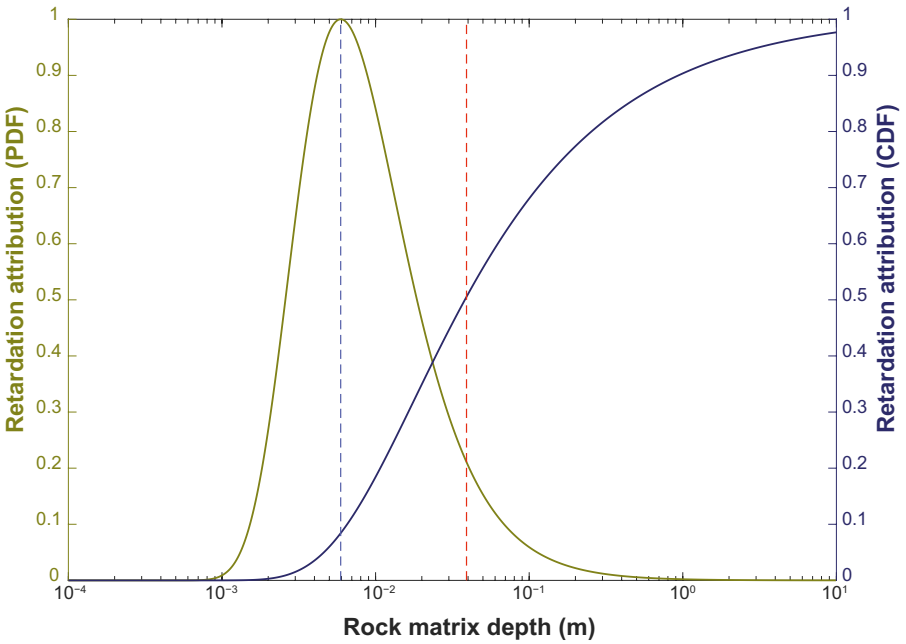

Figure 9-3. *Distribution of retardation attribution in the rock matrix for the SR-Site central corrosion case (for a non-decaying solute) shown as a cumulative density function (dark blue curve, right-hand axis), and as a normalised probability density function (olive-green curve, left-hand axis). Vertical blue and red broken lines indicate the mode and median of the distribution, respectively.*

The calculated effective penetration depth therefore is also context dependent upon whether we are considering the residence time distribution of a flowpath segment, or a sequence of flowpath segments. In this respect it differs conceptually from the notion of an absolute penetration depth which increases monotonically with the square-root of time for an unbounded matrix. Equation 9-15 may be understood as being analogous to a convolution of residence time distributions for individual segments comprising a flowpath.

While there does not seem to be any restriction that prevents retardation attribution calculations to be made for a segmented flowpath, we have not made such an analysis in this work. In fact, such an attribution calculation seems to be relatively straight-forward to perform by stochastic sampling of the underlying residence time distributions for each segment, although it is a sufficiently tedious calculation that we propose this for a future continuation project.

Retardation attribution calculations are useful in safety assessment for identifying which parts of flowpaths and of the rock matrix that dominate radionuclide retardation. Results from this type of analysis could also be useful for directing laboratory efforts for characterisation of site-specific retention properties. A particle-based code such as MARFA would also be ideal for performing such a computation, and it might be possible to introduce a calculation mode to the code whereby particle residence times in individual flowpath segments and alteration layers could be tracked and exported for retardation attribution diagnostic purposes, even for radionuclides subject to decay and ingrowth.

9.1.2 Average maximum penetration depth for decaying solutes in a single-layer, unbounded rock matrix

Unfortunately, the analysis presented in the previous section only strictly applies to non-decaying solutes and it is more difficult to apply the same concept to radionuclides which might be subject to both decay and ingrowth along a migration path. There is, however, another bounding calculation that can be used to assess the maximum accessible rock matrix for a decaying radioelement. For this calculation, we assume a constant source concentration (e.g. solubility-limited or otherwise dissolution-rate-limited) of a decaying radionuclide and estimate the effective penetration depth for transport where decay can occur along the migration path. Since the source term is assumed to be constant, this represents what might be characterised as a worst-case scenario. From the solution by Tang et al. (1981), we can write the limiting steady-state solution for the hydrodynamic dispersion-free case in an unbounded rock matrix as:

$$\frac{c}{c_0} = \exp\left(-t_w\lambda\right)\cdot\exp\left(-F\sqrt{R_p\varepsilon_p^2 D_p\lambda}\right) \tag{9-16}$$

Where, c/c_0 is the fraction of radionuclide remaining in the mobile fracture water after transport along a flowpath featuring matrix diffusive retardation. Equation 9-16 specifies the maximum geosphere attenuation for the migrating radionuclide given sufficient time for a steady-state to develop. In this case, the representative penetration depth is the equivalent depth of rock matrix that, if instantaneously equilibrated, would give the same steady-state attenuation as Equation 9-16. For an instantaneously equilibrated rock matrix of depth δ_{max} (m), we would have:

$$\frac{c}{c_0} = \exp\left(-R_{fm}t_w\lambda\right) \tag{9-17}$$

Combining Equations 9-16 and 9-17, allows us to write:

$$R_{fm} = 1+\frac{F\sqrt{R_p\varepsilon_p^2 D_p\lambda}}{t_w\lambda} = 1+\frac{2\sqrt{R_p\varepsilon_p^2 D_p}}{\delta_t\sqrt{\lambda}} \tag{9-18}$$

From the previously established definition of the retardation factor, R_{fm} given in Equation 9-1, we can then solve Equation 9-18 to obtain δ_{max} explicitly:

$$\delta_{\max} = \sqrt{\frac{D_p}{R_p\lambda}} \tag{9-19}$$

We refer to the depth of penetration calculated in this manner as the "average maximum mass balance penetration depth" to reflect the fact that it is closely related to the maximum geosphere attenuation. The physical interpretation of the penetration depth calculated in this manner is the matrix depth, beyond which the presence, or absence of a diffusive boundary will have little, or no impact on retardation as reflected in the maximum achievable attenuation of a decaying nuclide. Since we are equating an abstracted equilibrium process Equation 9-17) with a stochastic matrix diffusion process (Equation 9-16), however, this is only true in an "average" sense and the maximum penetration depth should not be interpreted to be a fixed limit in the same sense as a physical boundary for diffusion. The penetration depth calculated using Equation 9-19 is shown in Figure 9-4 for the radionuclides included in this work assuming the same material property parameters as in the SR-Site central corrosion case. Interestingly, Equation 9-19 is identical to the expression derived by Neretnieks (2013) for the average distance from which natural radionuclides generated in situ in the rock matrix (e.g. Ra-226, Rn-222, etc) might be expected to escape to the fracture water.

As can be seen from Figure 9-4, there appear to be many radionuclides that would never "sense" the presence of a limited rock matrix set to 10 cm since they decay sufficiently quickly that diffusion to such depths would not substantially alter the mass balance in the mobile fracture water regardless of the boundary condition or ingrowth along a flowpath. Taking Ra-226 as an example, we have calculated the breakthrough curves for a range of limited matrix depths to show the impact that this has on the steady-state attenuation for a constant boundary condition of 1 Bq/y. For this calculation we have neglected ingrowth from other nuclides in the 4n+2 decay chain and focus on the decay and transport of Ra-226 itself. Calculations were made in Matlab with numerical inversion of the Laplace space solution for dispersion free transport with diffusion in a rock matrix of limited depth. Numerical inversion was performed using a modified version of the de Hoog algorithm (de Hoog et al. 1982) as implemented in Matlab by Hollenbeck (1998). Results of this calculation are shown in Figure 9-5 and indicate a clear limit corresponding to about 3 times the average maximum mass balance penetration depth beyond which the presence of a diffusive boundary has no impact on breakthrough attenuation. It is relatively straightforward to demonstrate that similar results are obtained for all decaying radionuclides where ingrowth is neglected.

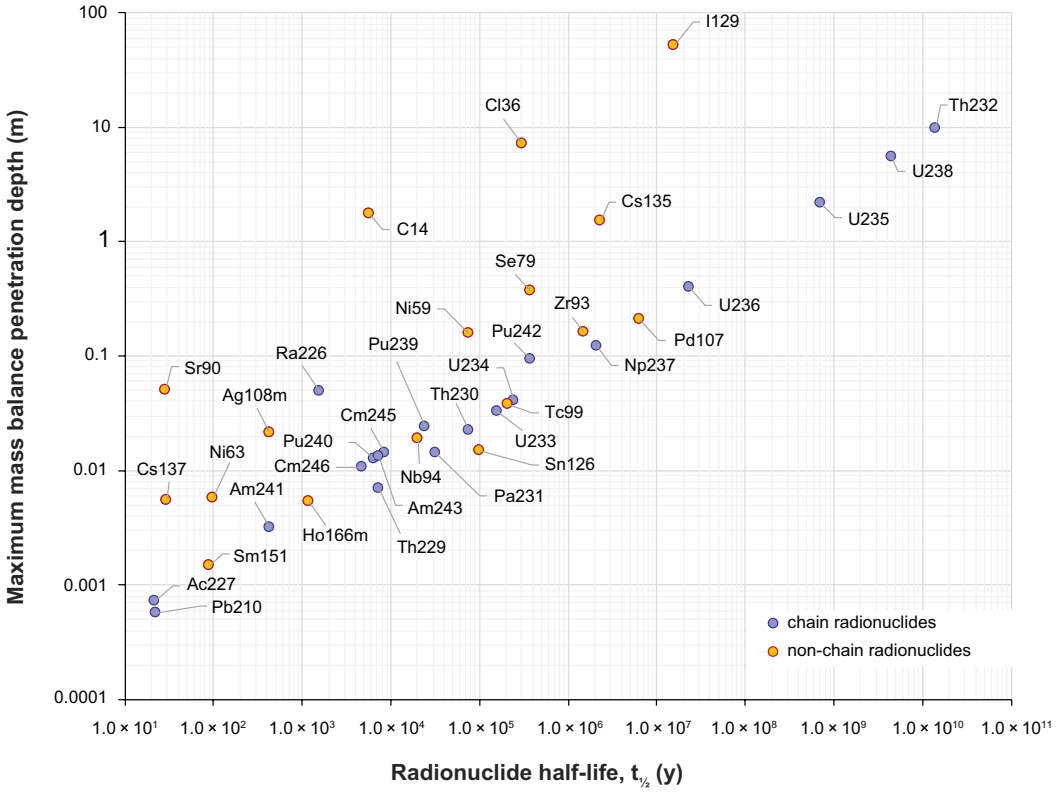

Figure 9-4. *Average maximum mass balance penetration depth versus radionuclide half-life assuming the same hydrodynamic transport and material property parameters as in the central corrosion case of SR-Site. Blue markers represent actinide chain nuclides, while red-orange markers represent non-chain fission and activation products.*

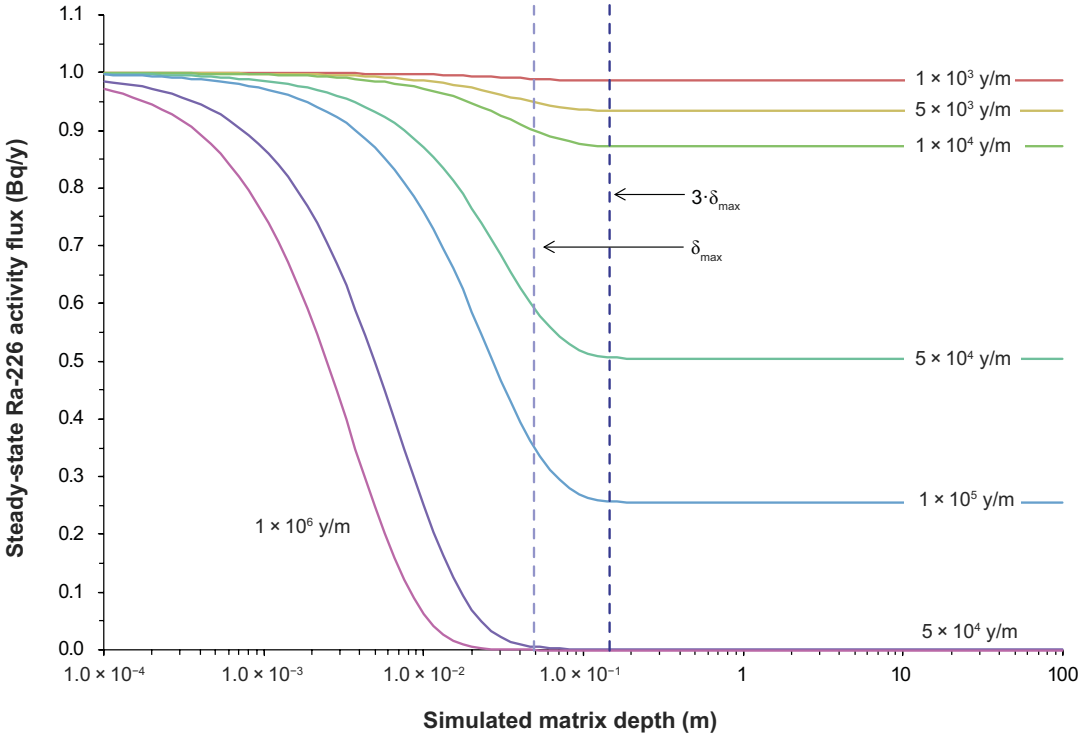

Figure 9-5. *Breakthrough curve snapshots (1 000 realisations of different matrix depths) showing the steady-state attenuation of Ra-226 for a 1 Bq/y constant flux boundary condition as a function of rock matrix depth (m) and flowpath F-factor (y/m). Also shown is the average maximum mass balance penetration depth calculated using Equation 9-19. Calculations indicate that the "true" maximum penetration depth beyond which essentially no impact can be discerned on breakthrough curves is roughly equal to 3 times the average maximum.*

For radionuclides that are part of decay chains, however, the situation is significantly complicated by the presence of parent radionuclides that contribute to ingrowth of the daughter along the migration path. To examine the dynamics of this process, we have made additional simulations for the entire 4n+2 decay chain simplified here to:

U-238 → U-234 → Th-230 → Ra-226 → Pb-210 → Po-210 (9-20)

Although Po-210 was not included in the SR-Site calculations, we have included it here since it can provide further insights into the matrix diffusion process for a decay chain and also since it is readily measured as a naturally occurring radionuclide. In the calculations, we have used the K_d for Ni(II) for Ra-226 and Po-210 since there are indications that the K_d for Pb(II) in SR-Site (cf. Table 5-6) might be unrealistically high (see discussion in Crawford 2010).

To make these calculations, we have used the Laplace-space model developed by Mahmoudzadeh et al. (2014) for hydrodynamic dispersion free flow with numerical inversion in Matlab. Since the solution contains transcendental functions that are difficult to evaluate using double precision arithmetic for some input parameter values, we have made use of the Multiprecision toolbox for Matlab (Advanpix 2017) with numerical inversion made using the Hollenbeck (1998) inversion function discussed previously (although slightly modified to function correctly with Multiprecision arguments). The results of this calculation are shown in Figure 9-6 for Ra-226 breakthrough flux.

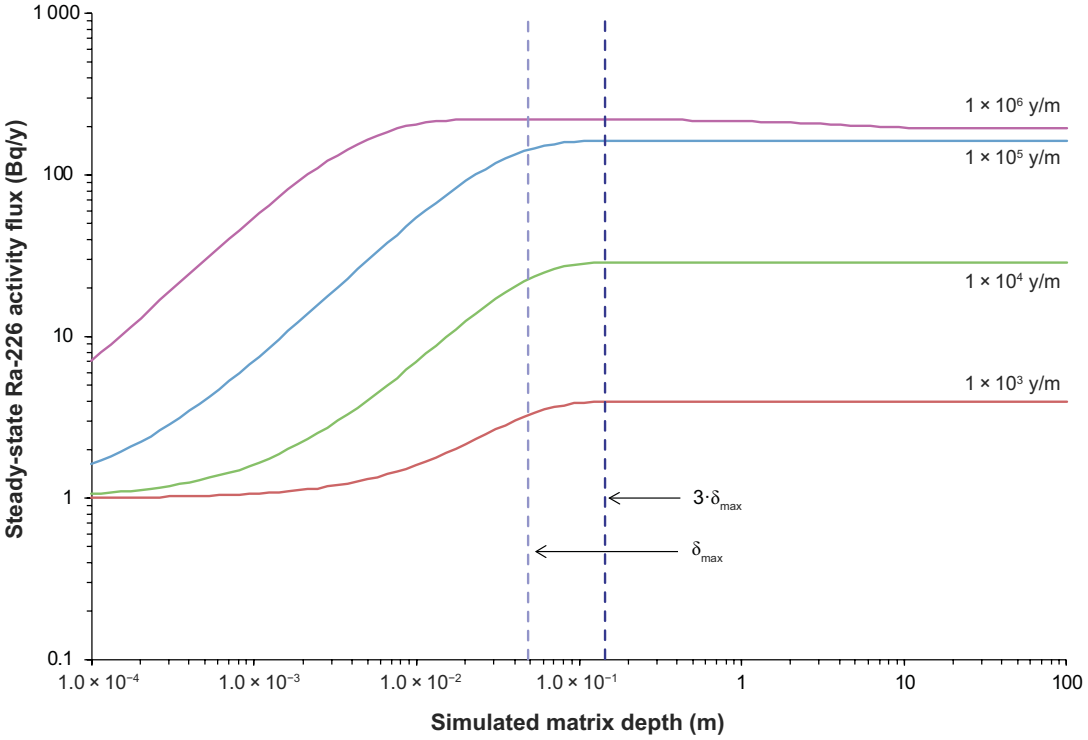

Figure 9-6. *Breakthrough curve snapshots (1 000 realisations) showing the steady-state attenuation/ingrowth of Ra-226 as a function of rock matrix depth (m) and flowpath F-factor (y/m). In this calculation we have considered a 1 Bq/y constant flux boundary condition for each of the parent radionuclides in the 4n+2 decay chain. The average maximum penetration depth and "true" maximum penetration depth beyond which essentially no impact can be discerned on breakthrough curves is also shown as described previously.*

While the results in Figure 9-6 seem to agree with those presented previously in Figure 9-5, there are some important details that are easy to overlook. Figure 9-7 shows a more detailed account of the results for the F-factor case of 10^6 y/m (cf. upper curve in Figure 9-6) where the contribution of each of the parent radionuclides is plotted separately. The curves shown in Figure 9-7 for ingrowth of Ra-226 from each parent radionuclide represents the following processes each modelled as separate cases with a 1 Bq/y flux boundary condition set for the first radionuclide in each sequence:

$$\left.\begin{aligned} &\text{U-238}\,(1\ \text{Bq/y}) \rightarrow \text{U-234} \rightarrow \text{Th-230} \rightarrow \text{Ra-226} \\ &\text{U-234}\,(1\ \text{Bq/y}) \rightarrow \text{Th-230} \rightarrow \text{Ra-226} \\ &\text{Th-230}\,(1\ \text{Bq/y}) \rightarrow \text{Ra-226} \\ &\text{Ra-226}\,(1\ \text{Bq/y}) \end{aligned}\right\} \qquad (9\text{-}21)$$

In Figure 9-7 it can be clearly seen that there is a strong coupling with the maximum penetration depth of each of the parent radionuclides. Barely visible in the steady-state profiles is a very small downturn in steady-state flux of Ra-226 for matrix depths approaching 10 m even though this is well beyond the average maximum depth of penetration for Ra-226 indicated in Figure 9-5. This is because the presence of a diffusion boundary at this depth or shallower allows U-238 to accumulate in greater concentrations at shallower matrix depths where it can have an impact on Ra-226 via the ingrowth mechanism. For ingrowth of Ra-226 from U-234 and Th-230, it is slightly more difficult to observe the systematic behaviour since they each have average maximum penetration depths of similar magnitude.

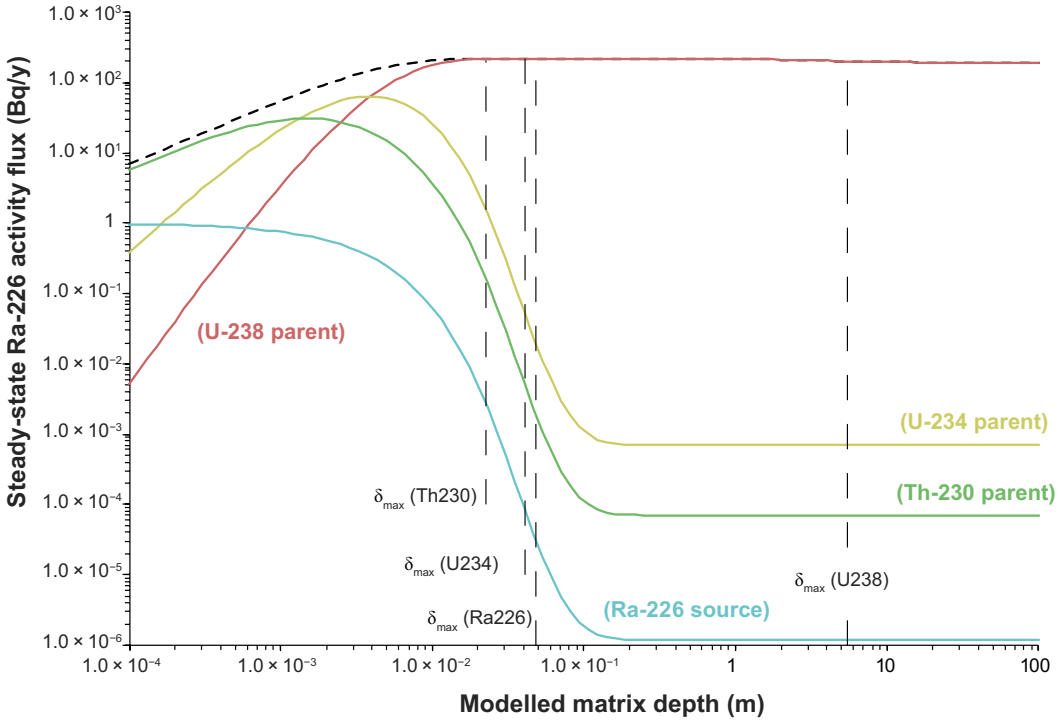

Figure 9-7. *Breakthrough curve snapshots (4 sets of 1 000 realisations) showing the steady-state ingrowth/attenuation of Ra-226 as a function of rock matrix depth (m) for a flowpath F-factor of 10^6 y/m. In this calculation we have considered a 1 Bq/y constant flux boundary condition for each of the parent radionuclides in the 4n+2 decay chain and plotted the contribution of each parent nuclide to the Ra-226 flux separately. The summed contribution of all parent nuclides and the Ra-226 boundary condition itself is shown as the thick broken curve. The average maximum penetration depth for each of the parent radionuclides is indicated in the figure.*

Plotting the corresponding curves for Pb-210, however, as in Figure 9-8 shows a very clear dependence on ingrowth from the parent radionuclides. It can be clearly seen from that the steady-state of Pb-210 is dependent on modelled matrix depth well beyond the average maximum penetration depth calculated for Pb-210 (i.e. if modelled as a single source radionuclide). Very similar behaviour is also seen for Po-210 (not shown here) which is strongly dependent on ingrowth from its parents. From these results it seems that the attenuation of the entire 4n+2 decay chain except for ingrowth resulting directly from U-238 will be barely affected by the existence of a diffusion limit at matrix depths greater than about 10–20 cm regardless of the form of the source boundary condition. At this time, we have not extended these calculations to the other actinide chains, although broadly similar results would be expected.

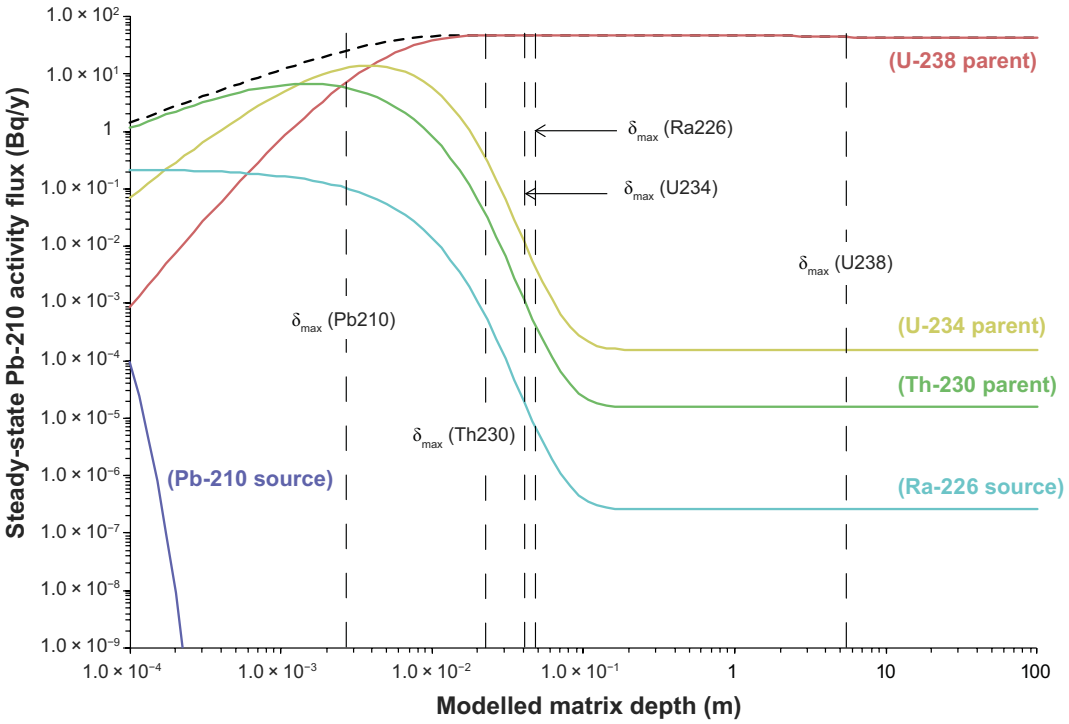

Figure 9-8. *Breakthrough curve snapshots (4 sets of 1 000 realisations) showing the steady-state ingrowth/attenuation of Pb-210 as a function of rock matrix depth (m) for a flowpath F-factor of 10^6 y/m. In this calculation we have considered a 1 Bq/y constant flux boundary condition for each of the parent radionuclides in the 4n+2 decay chain and plotted the contribution of each parent nuclide to the Pb-210 flux separately. The summed contribution of all parent nuclides and the Pb-210 boundary condition itself is shown as the thick broken curve. The average maximum penetration depth for each of the parent radionuclides is indicated in the figure.*

9.1.3 Effective penetration depth for decaying solutes in a single-layer, unbounded rock matrix

For the effective depth of penetration associated with the median travel time of a migrating radionuclide undergoing decay, we can use the transient solution also from Tang et al. (1981):

$$\frac{c}{c_0} = \frac{1}{2}\exp\left(-\lambda t_w\right)\left[\begin{array}{l}\exp\left(-F\sqrt{R_p\varepsilon_p^2 D_p\lambda}\right)\cdot\operatorname{erfc}\left(\dfrac{F\sqrt{R_p\varepsilon_p^2 D_p}}{2\sqrt{t-t_w}}-\sqrt{\lambda\left(t-t_w\right)}\right)\\ +\exp\left(F\sqrt{R_p\varepsilon_p^2 D_p\lambda}\right)\cdot\operatorname{erfc}\left(\dfrac{F\sqrt{R_p\varepsilon_p^2 D_p}}{2\sqrt{t-t_w}}+\sqrt{\lambda\left(t-t_w\right)}\right)\end{array}\right] \tag{9-22}$$

Unlike the simpler expression given by Neretnieks (1980), it is not possible to rewrite Equation 9-22 to obtain the travel time explicitly, so it must be solved numerically to obtain t_R as a function of recovery fraction, c/c_0. It should be noted that Equation 9-16 is the asymptote of Equation 9-22 in the limit of infinite contact time. Also, for a radionuclide that undergoes significant decay we are interested in the median travel time associated with 50 % of ultimately recoverable solute (i.e. 50 % of the recovery fraction given by Equation 9-16) rather than 50 % of the solute released at the source which may not even be achievable for short-lived radionuclides.

Figure 9-9 shows the effective penetration depth calculated using the transient solution (evaluated numerically using Matlab) together with the average maximum penetration depth calculated using Equation 9-19 for the steady-state condition. The green markers represent the depth of rock matrix that can be associated with 50 % of the retardation effect for transported radionuclides (neglecting ingrowth), while the yellow markers show the average maximum penetration depth calculated previously for the steady-state case using Equation 9-19. For radionuclides with long half-lives relative to travel time, the effective penetration depth asymptotically approaches that for a non-decaying solute which has already been shown to be independent of K_d (blue and red broken lines in Figure 9-9 for anions and cations, respectively).

It is not yet clear how to properly treat radionuclides that experience significant ingrowth along a flowpath in the context of a time limited pulse release (rather than the steady-state condition explored previously), although as we have shown for the 4n+2 decay chain, matrix diffusion barriers beyond a few 10's of cm are unlikely to have a significant impact on far-field radionuclide fluxes regardless of the magnitude of the F-factor or form of the boundary condition.

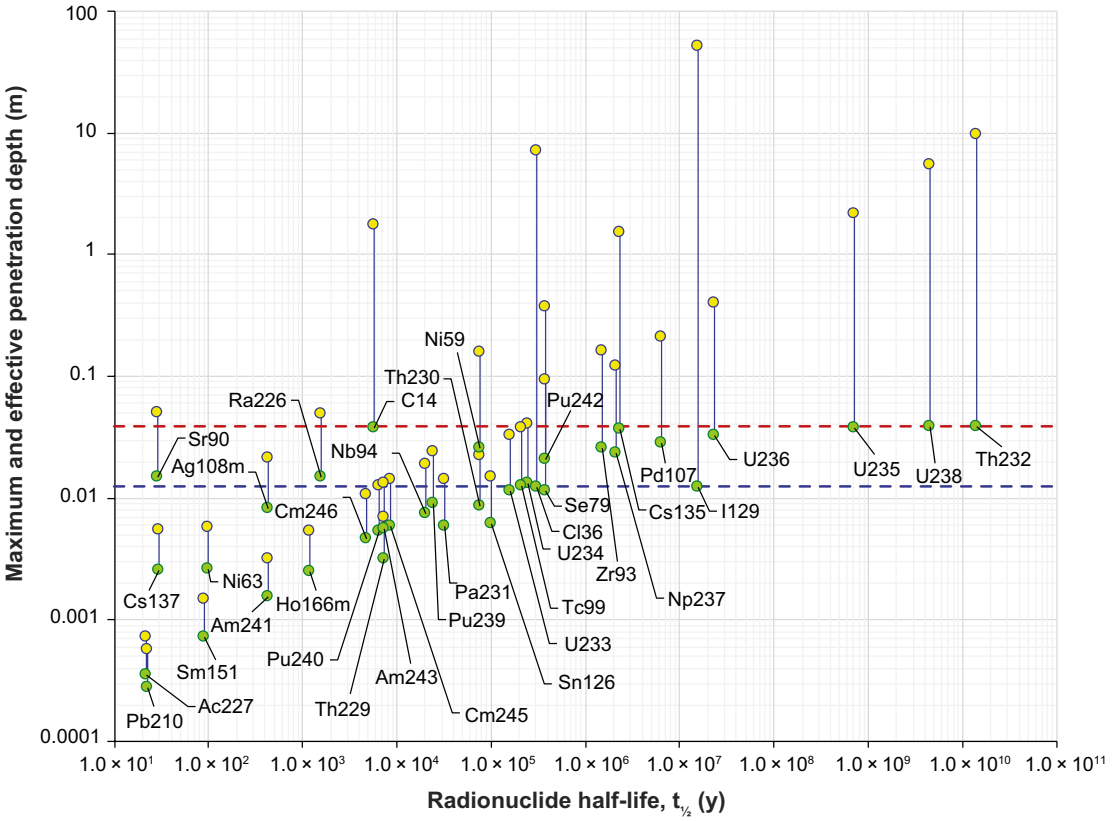

Figure 9-9. *Average maximum mass balance penetration depth (yellow markers) and effective penetration depth including decay although no ingrowth (green markers) versus radionuclide half-life: Calculations assume the same hydrodynamic transport and material property parameters as in the central corrosion case of SR-Site. The vertical tie-lines in the figure connect data points for the same radionuclide. The horizontal blue and red broken lines indicate the limiting effective penetration depth for non-decaying anionic and cationic solutes, respectively.*

By substituting Equation 9-1 directly into Equation 9-22, we can also obtain the cumulative distribution function for retardation attribution in the rock matrix. This is the analogue of Equation 9-13, although now accounting for decay:

$$\chi(z) = \frac{1}{2}\exp(-\lambda t_w)\left[\begin{array}{l}\exp\left(-F\sqrt{R_p\varepsilon_p D_e\lambda}\right)\cdot\operatorname{erfc}\left(\frac{1}{2}\sqrt{\frac{D_eF}{z}}-\sqrt{\left(R_p\varepsilon_p\lambda F\right)z}\right)\\ +\exp\left(F\sqrt{R_p\varepsilon_p D_e\lambda}\right)\cdot\operatorname{erfc}\left(\frac{1}{2}\sqrt{\frac{D_eF}{z}}+\sqrt{\left(R_p\varepsilon_p\lambda F\right)z}\right)\end{array}\right] \qquad (9\text{-}23)$$

The associated probability density function can then be obtained as the first derivative of Equation 9-23, which after some simplification is found to be:

$$p(z) = \frac{\sqrt{D_eF}}{2\sqrt{\pi}\cdot z^{\frac{3}{2}}}\exp(-\lambda t_w)\cdot\exp\left(-F\left(\frac{D_e}{4z}+R_p\varepsilon_p\lambda\, z\right)\right) \qquad (9\text{-}24)$$

Unlike the expression for a non-decaying solute, Equation 9-23 and Equation 9-24 are both dependent on the decay constant and pore retardation factor for the migrating radionuclide. The cumulative attribution distribution function for several representative radionuclides has been calculated and is plotted in Figure 9-10. The associated probability density function is plotted in Figure 9-11.

It is interesting to note in both Figure 9-10 and Figure 9-11 that the relatively long-lived radionuclides I-129 (15.7 My) and Ni-59 (76 ky) approach the limiting case calculated for non-decaying anionic and cationic solutes (Equation 9-13 and 9-14).

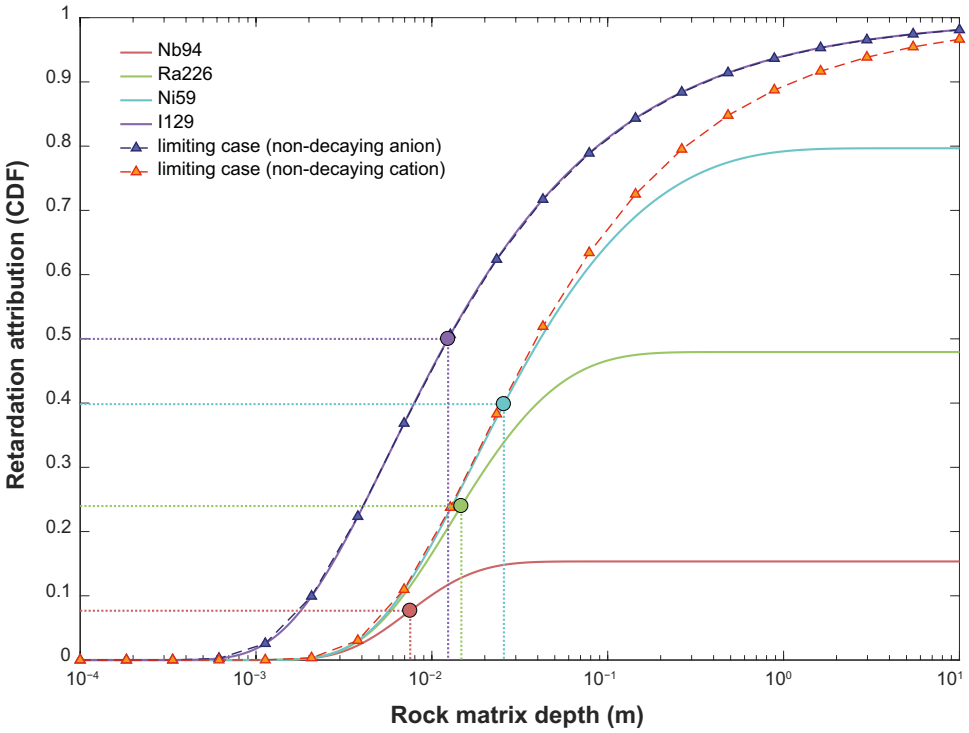

Figure 9-10. *Distribution of retardation attribution in the rock matrix for the SR-Site central corrosion case for several decaying radionuclides shown as a cumulative density function (CDF). Circular markers indicate the effective penetration depth associated with 50 % recovery for each radionuclide, respectively (same effective penetration depth as green markers in Figure 9-9).*

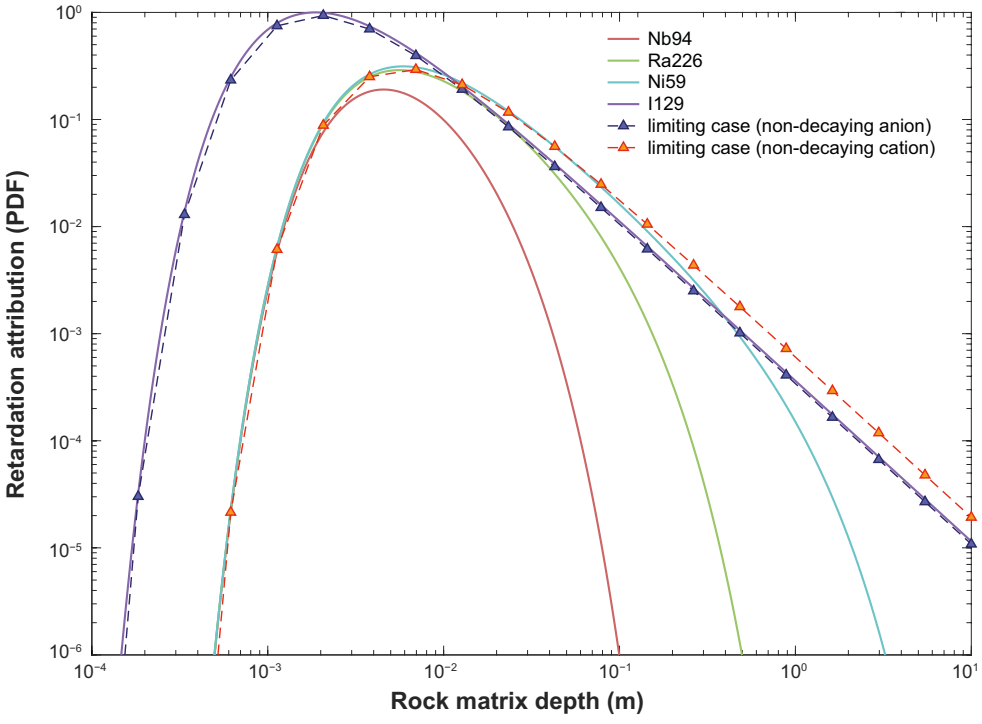

Figure 9-11. *Distribution of retardation attribution in the rock matrix for the SR-Site central corrosion case for several decaying radionuclides shown as a probability density function (PDF).*

9.2 The effective penetration depth in multilayer rock matrix calculations

In the calculations made in Section 9.1, we assume no decrease in the effective diffusivity with distance progressing further from the fracture plane and into the wall rock. In the previous chapters, however, we argue that assuming such a decrease of effective diffusivity in a layered rock model is more realistic. If we extend Equation 9-1 to the multilayer case (n-layers), the retarded travel time can be conceptualised as being equal to the net sum of contributions from the water residence time in the fracture and the retarded transport times in each rock matrix layer, i.e:

$$t_R = t_w + \sum_{k=1}^{n} t_{m(k)} \tag{9-25}$$

The maximum retarded travel time for each layer (assuming full diffusive equilibration of the layer) would then be:

$$t_{m(k)}^{\max} = \left(2R_{p(k)}\varepsilon_{p(k)} \cdot \frac{\Delta\delta_{L(k)}}{\delta_t} \right) t_w \tag{9-26}$$

Where, $\Delta\delta_{L(k)}$ (m) is the layer thickness, $R_{p(k)}$ is the pore retardation factor, and $\varepsilon_{p(k)}$ is the porosity of matrix layer k. In a time-domain random walk particle tracking framework the retarded transport times may be considered analogous to the stochastic residence times of a particle in each layer of the rock matrix. Applying the same concept as previously for a single layer rock matrix, we assume that the median travel time estimated from a simulated residence time distribution is characteristic of the effective penetration depth in the rock matrix (i.e. the depth of rock associated with ~ 50 % of the recovered solute).

In this simplified penetration depth analysis, we consider a hypothetical depth where the contacted rock matrix may be assumed to be in equilibrium with the concentration in the fracture water which is the same assumption as used previously in the single layer case. Although this is a non-physical equivalence, it is nevertheless a useful construct to visualise the depth of rock which is potentially accessible to a diffusing solute on the timescale of transport. This assumption implies that each layer must be sequentially equilibrated by diffusive transport before solute can reach the next layer. This is illustrated conceptually in Figure 9-12.

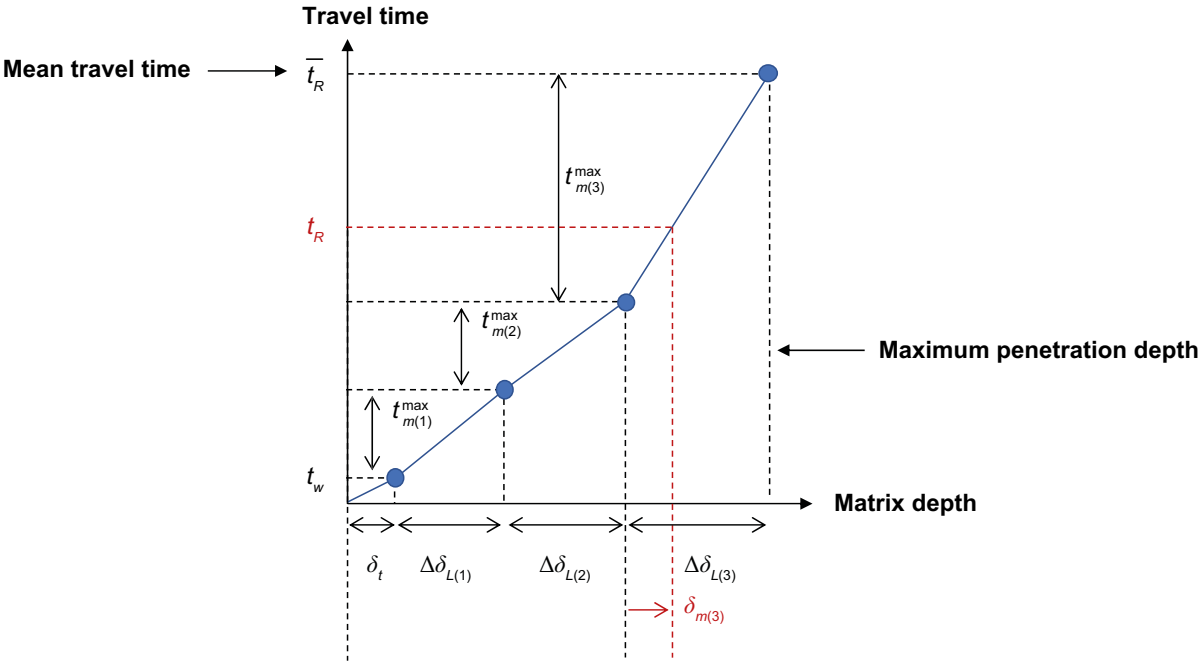

Figure 9-12. *Conceptual illustration of the effective penetration depth for a 3-layer rock matrix. The retarded travel time is equal to the sum of contributions from each layer. In this example, the fracture flow space as well as the first and second layers are fully equilibrated, whereas the third layer is only partially equilibrated.*

The retarded transport time for each layer, k can be represented in pseudo-code as:

$$t_{m(k)} = H\left[t_R - t_w - \sum_{j=1}^{k-1} t_{m(j)}^{\max} \right] \cdot \min\left[\left(t_R - t_w - \sum_{j=1}^{k-1} t_{m(j)}^{\max} \right), t_{m(k)}^{\max} \right] \tag{9-27}$$

Where, $H[\chi]$ is the Heaviside step function which takes on a value of either 0 or 1 depending on whether the argument χ is negative or positive. The value of $t_{m(k)}$ is equal to the total retarded travel time, t_R minus the sum of retarded travel times for each of the preceding layers. The retarded travel time for any layer can never exceed the maximum retarded travel time for that layer and if a layer is only partially equilibrated, all subsequent layers are deemed to have zero contact with the migrating solute.

To calculate the residence time distribution in a multilayer matrix we use the Laplace-space analytical solution described by Cvetkovic (2010). Numerically inverting the analytical solution to the time plane in Matlab allows us to estimate the median travel time associated with solute recovery. For this calculation we have also made use of the Multiprecision toolbox (Advanpix 2017) and perform the numerical inversion of the Laplace-space solution using the Matlab function developed by Hollenbeck (1998). As noted previously for the single-layer case, we are interested in the median travel time of recovered radionuclide rather than that released at the source so base the calculation on 50 % of the maximum attenuation given by Equation 9-16. Once the retarded transport times are calculated for each layer in the rock matrix it is possible to estimate the effective penetration depth for the final, partially equilibrated layer k (where, $k \le n$) using a modified form of Equation 9-2:

$$\delta_{m(k)} = \min\left[\left(\frac{t_R - \sum_{j=1}^{k-1} t_{m(j)}^{\max}}{t_w} - 1 \right) \frac{\delta_t}{2R_{p(k)}\varepsilon_{p(k)}}, \Delta\delta_{L(k)} \right] \tag{9-28}$$

And, the total effective penetration depth is then given by:

$$\delta_{m(\mathrm{tot})} = \sum_{j=1}^{k} \delta_{m(j)} \tag{9-29}$$

Based on the retarded transport times for each layer and the water residence time, we can also attribute fractional retardation in each alteration layer using the relation:

$$f_{m(k)} = \frac{t_{m(k)}}{t_R} \tag{9-30}$$

Since the penetration depths are proportional to residence times, we could also define the fractional retardation as:

$$f_{m(k)} = \frac{\delta_{m(k)}}{\delta_{m(\mathrm{tot})}} \tag{9-31}$$

The results of this analysis are presented in the following sections for each of the multilayer fracture classes considered previously in Section 6. Since the value of t_R is arbitrarily assumed to be the median travel time in this calculation, it seems that different t_R values corresponding to different recovery fractions of radionuclide could be used to reconstruct probability density functions (PDF and CDF) for attribution of retardation in a multilayer rock matrix in a similar fashion to the procedures outlined in Section 9.1. This, however, was beyond the scope of the current work and remains to be done.

9.2.1 Effective penetration depths and retardation attribution for fracture class F1:1

The effective depth of penetration for solute transport (assuming zero hydrodynamic dispersion) along a flowpath featuring material properties representative of the F1:1 fracture class is shown in Figure 9-13 based on median transport times (50 % of recovered solute). The same hydrodynamic transport resistance ($F = 5.366 \times 10^4$ y/m) and advective travel time ($t_w = 6.401$ y) is assumed as in the central corrosion case of SR-Site and the simulations described in Section 6.1. The calculated effective depth of penetration varies from as little as 4 mm in the case of Sm-151 to about 5 cm which represents an approximate limit for non-decaying cations. The effective penetration depth of anions approaches ~ 2 cm which is roughly consistent with the effective diffusivity of anionic solutes being roughly 30 % of that for cations.

It is interesting to note that the effective penetration depth of C-14 (assumed to be non-charged and non-sorbing) doesn't quite reach the same depth as that calculated for other radionuclides in the non-decay case. This appears to be related to fact that the advective travel time constitutes a larger proportion of the total transport time for this nuclide implying a lesser degree of retention in the rock matrix. The same appears to be the case for Cl-36 and I-129. For weakly sorbing Se-79, on the other hand, the advective travel time is negligible in relation to the residence time in the rock and the effective penetration depth approaches the theoretical limit for an anionic solute.

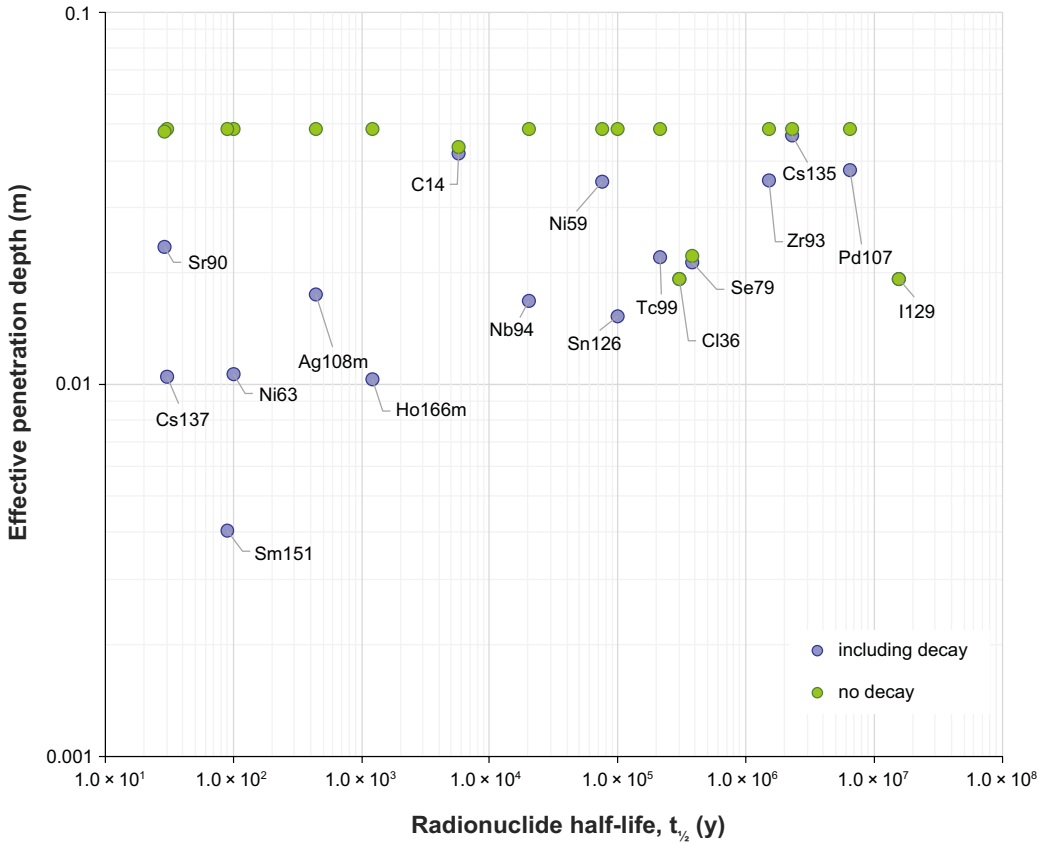

Figure 9-13. *Effective penetration depth for first 50 % of recovered radionuclide (non-chain) for transport along a flowpath assuming fracture class F1:1 material properties. The model assumes the same flowpath as the SR-Site central corrosion case (no hydrodynamic dispersion). Blue markers indicate effective penetration depths calculated for radionuclides including decay; Green markers show corresponding results when decay is neglected.*

Based on the calculated retarded transport times associated with each layer in the rock matrix the attribution of retardation in the multilayer rock matrix has been calculated using Equation 9-30 based on median transport times (50 % of recovered solute). These results are shown in Figure 9-14 for the decay case.

As noted previously, the choice of 50 % recovered solute as a calculation basis is arbitrary and we could easily choose another basis such as 75 %. When doing so, the effective penetration depth for non-decaying solute is found to be roughly 4 times greater when the calculation is based on the upper quartile retarded travel time than the median travel time. This is close to what is predicted for a single layer rock matrix (cf. Equation 9-5 and 9-10). When decay process are included, however, radionuclides with low maximum penetration depths (Equation 9-19) tend to have similar effective penetration depths for both the 50 % and 75 % recovery calculation basis. This indicates that the effective penetration depth based on median retarded travel time is already close to the limit beyond which the rock matrix does not contribute to retardation in a meaningful manner for these radionuclides. Exceptions in the present example include C-14, Cl-36, Cs-135, I-129, Ni-59, Pd-107, and Se-79, all of which have relatively large maximum average mass balance depths of penetration.

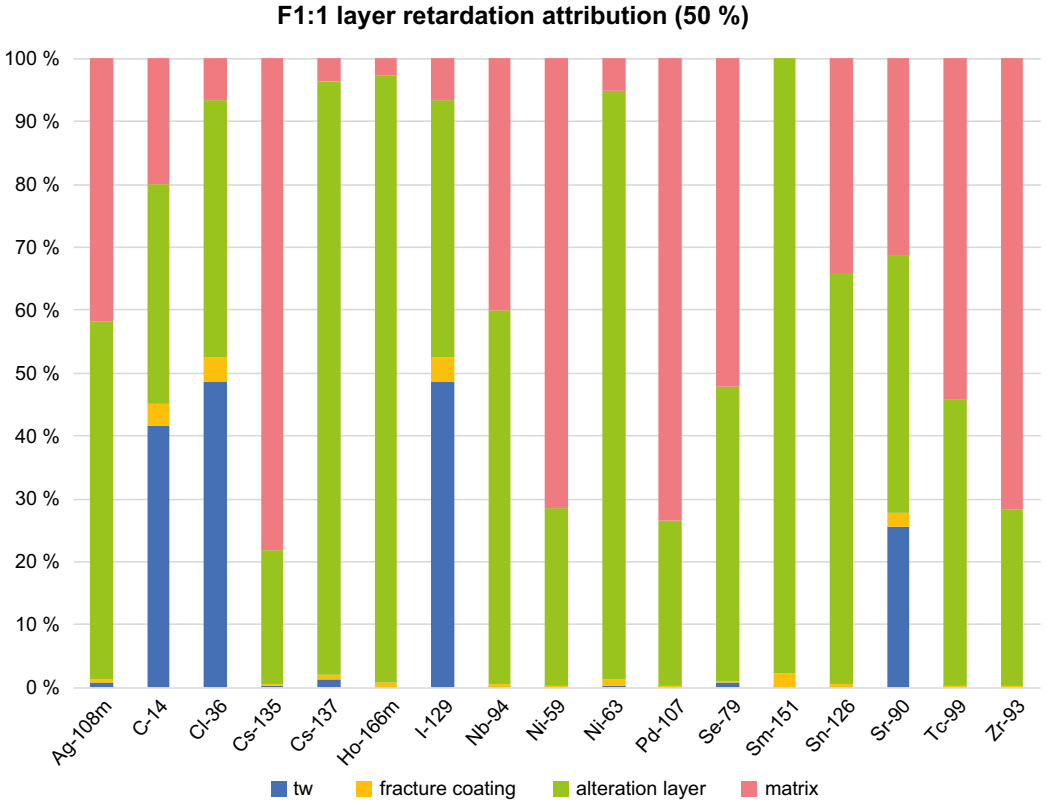

Figure 9-14. *Attribution of layer-specific retardation effects for first 50 % of recovered radionuclide (non-chain) for transport along a flowpath assuming fracture class F1:1 material properties. Model assumes same flowpath as SR-Site central corrosion case (no hydrodynamic dispersion).*

9.2.2 Effective penetration depths and retardation attribution for fracture class F1:2

Figure 9-15 shows the effective depth of penetration for solute transport assuming material properties representative of the F1:2 fracture class. The effective depth of penetration varies from as little as 1 mm in the case of Sm-151 to about 4 cm which represents an approximate upper limit for non-decaying cations. The effective penetration depth of anions is maximally about 1.4 cm which, as previously noted, is roughly consistent with the effective diffusivity of anionic solutes being about 30 % of that for cations. In this case as well, the effective penetration depth calculated for C-14, Cl-36, and I-129 fall short of the apparent theoretical limits, presumably due to the larger impact of the advective travel time for these non-sorbing solutes.

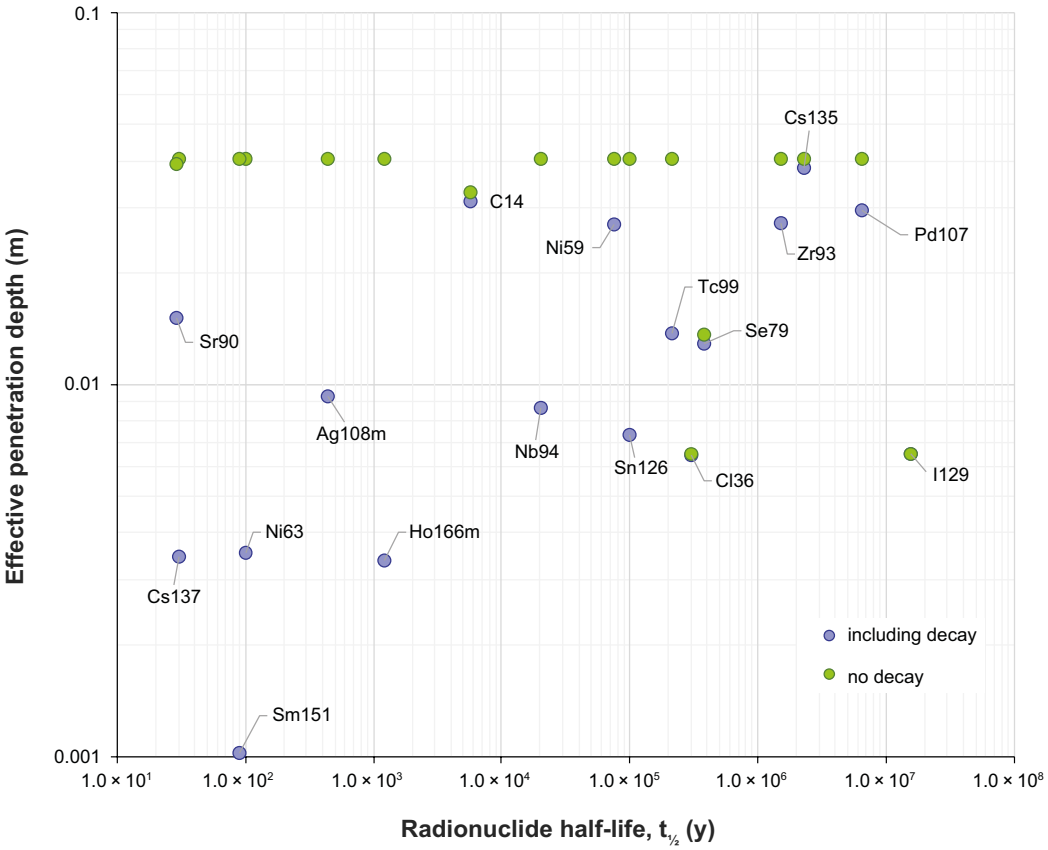

Figure 9-15. *Effective penetration depth for first 50 % of recovered radionuclide (non-chain) for transport along a flowpath assuming fracture class F1:2 material properties. Model assumes same flowpath as SR-Site central corrosion case (no hydrodynamic dispersion). Blue markers indicate effective penetration depths calculated for radionuclides including decay; Green markers show corresponding results when decay is neglected.*

Based on the calculated retarded transport times associated with each layer in the rock matrix the attribution of retardation in the multilayer rock matrix has been calculated. These results are shown in Figure 9-16.

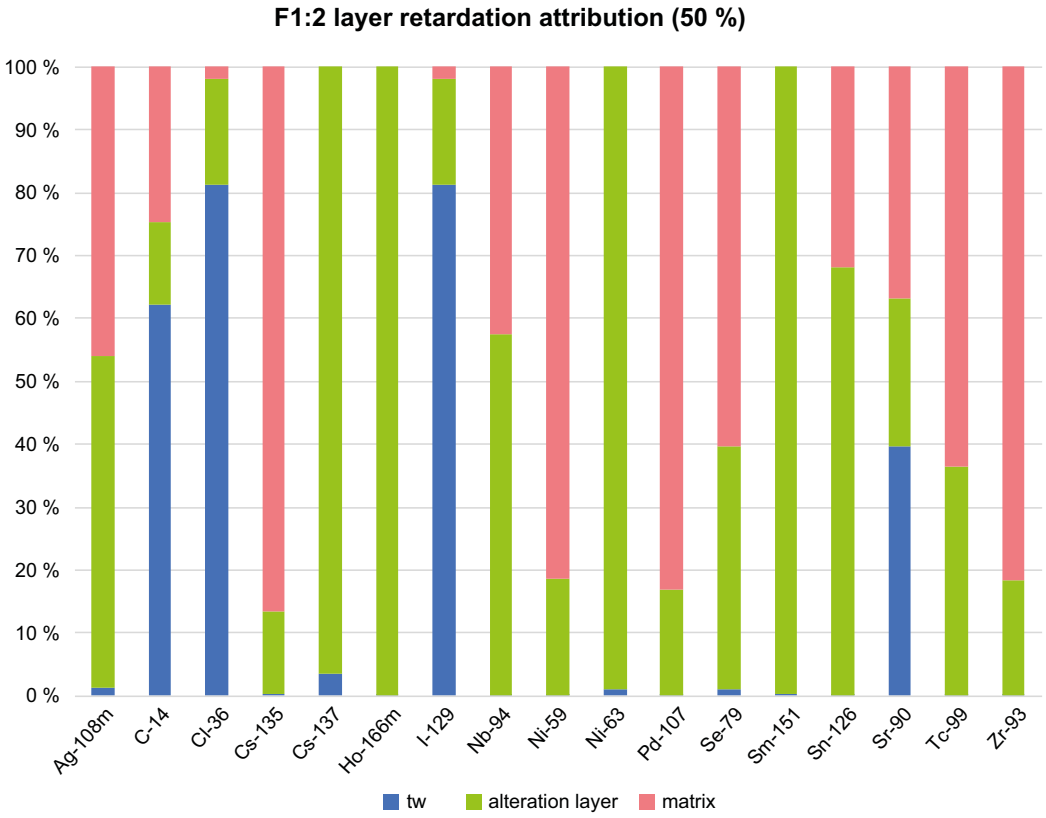

Figure 9-16. *Attribution of layer-specific retardation effects for first 50 % of recovered radionuclide (non-chain) for transport along a flowpath assuming fracture class F1:2 material properties. Model assumes same flowpath properties as SR-Site central corrosion case (no hydrodynamic dispersion).*

9.2.3 Effective penetration depths and retardation attribution for fracture class F1:3

Figure 9-17 shows the effective depth of penetration assuming material properties representative of the F1:3 fracture class. The effective depth of penetration varies from as little as 0.24 mm in the case of Sm151 to about 5 cm which represents an approximate upper limit for non-decaying cation solutes. The effective penetration depth of anions is maximally about 2.4 cm which is consistent with the effective diffusivity of anionic solutes being about 30 % of that for cations. In this case, however, the effective penetration depth is calculated to be slightly higher for I-129 and Cl-36 than for Se-79. C-14 also seems to have a slightly higher penetration depth than other cationic or non-charged solutes which is the reverse behaviour to that observed for these radionuclides in the calculations for F1:1 and F1:2 fracture classes. Once more, this appears to be related to the greater impact of advective travel time on the total travel time, although the presence of the fracture coating with reduced effective diffusivity seems to play some role as well. Although difficult to explain, this behaviour is reproducible and does not appear to be due to inaccuracies in the Laplace inversion. Further work will need to be done to fully understand the reasons for this behaviour.

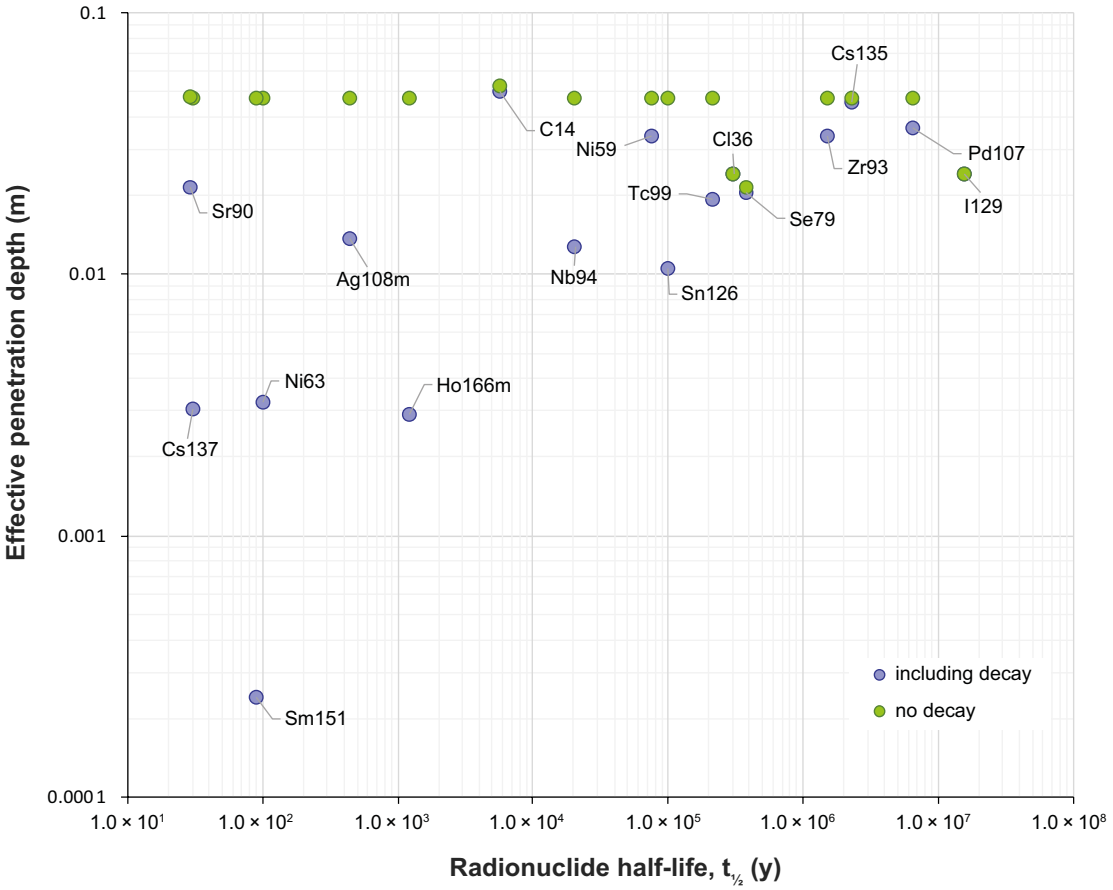

Figure 9-17. *Effective penetration depth for first 50 % of recovered radionuclide (non-chain) for transport along a flowpath assuming fracture class F1:3 material properties. Model assumes same flowpath as SR-Site central corrosion case (no hydrodynamic dispersion). Blue markers indicate effective penetration depths calculated for radionuclides including decay; Green markers show corresponding results when decay is neglected.*

Based on the calculated retarded transport times associated with each layer in the rock matrix the attribution of retardation in the multilayer rock matrix has been calculated. These results are shown in Figure 9-18.

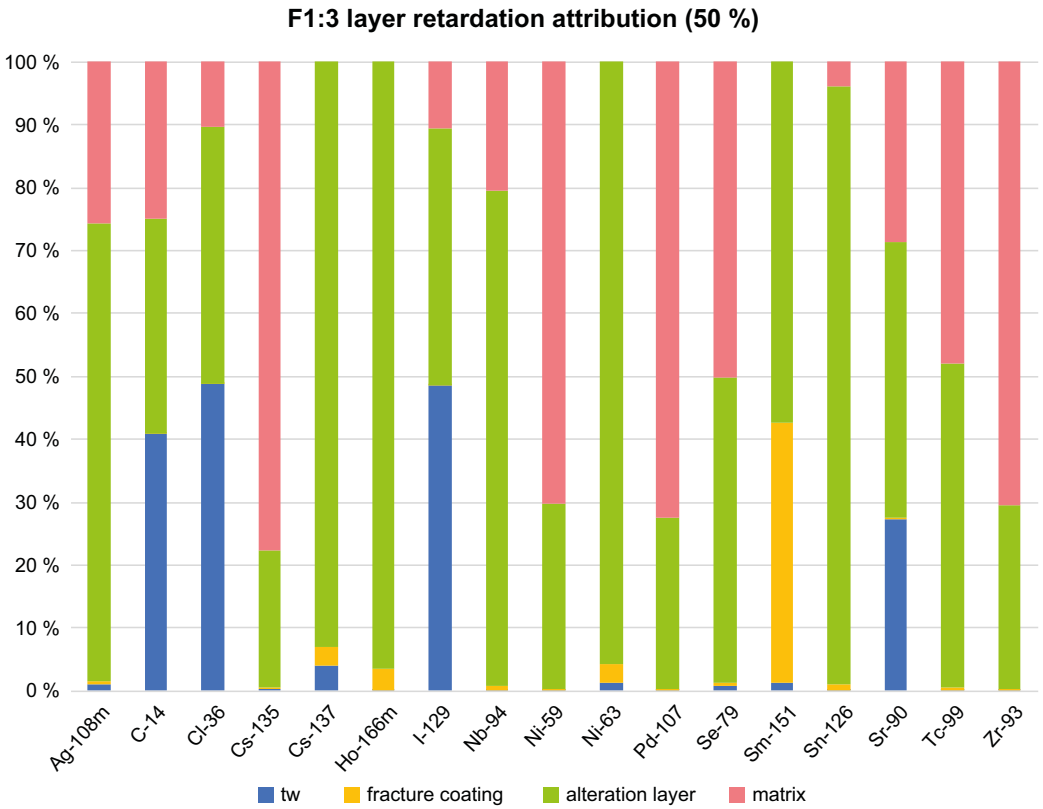

Figure 9-18. *Attribution of layer-specific retardation effects for first 50 % of recovered radionuclide (non-chain) for transport along a flowpath assuming fracture class F1:3 material properties. Model assumes same flowpath as SR-Site central corrosion case (no hydrodynamic dispersion). Blue markers indicate effective penetration depths calculated for radionuclides including decay; Green markers show corresponding results when decay is neglected.*

9.2.4 Effective penetration depths and retardation attribution for fracture class F2:1

Figure 9-19 shows the effective depth of penetration for material properties representative of the F2:1 fracture class. The effective depth of penetration varies from as little as 1.3 cm in the case of Sm-151 to just short of 2 m which represents an upper limit for non-decaying cation solutes. The effective penetration depth of anions is maximally about 60 cm which is consistent with the effective diffusivity of anionic solutes being about 30 % of that for cations.

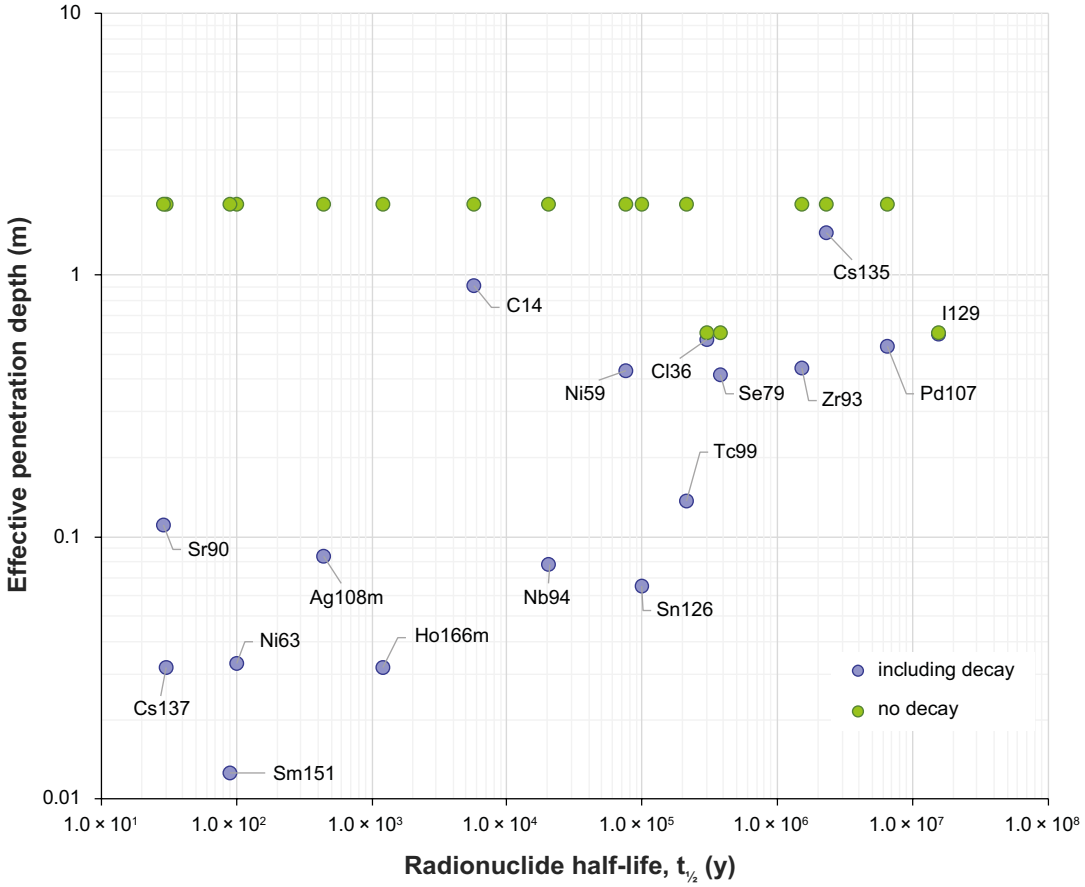

Figure 9-19. *Effective penetration depth for first 50 % of recovered radionuclide (non-chain) for transport along a flowpath assuming fracture class F2:1 material properties. Model assumes same flowpath as SR-Site central corrosion case (no hydrodynamic dispersion). Blue markers indicate effective penetration depths calculated for radionuclides including decay; Green markers show corresponding results when decay is neglected.*

Based on the calculated retarded transport times associated with each layer in the rock matrix the attribution of retardation in the multilayer rock matrix has been calculated. These results are shown in Figure 9-20.

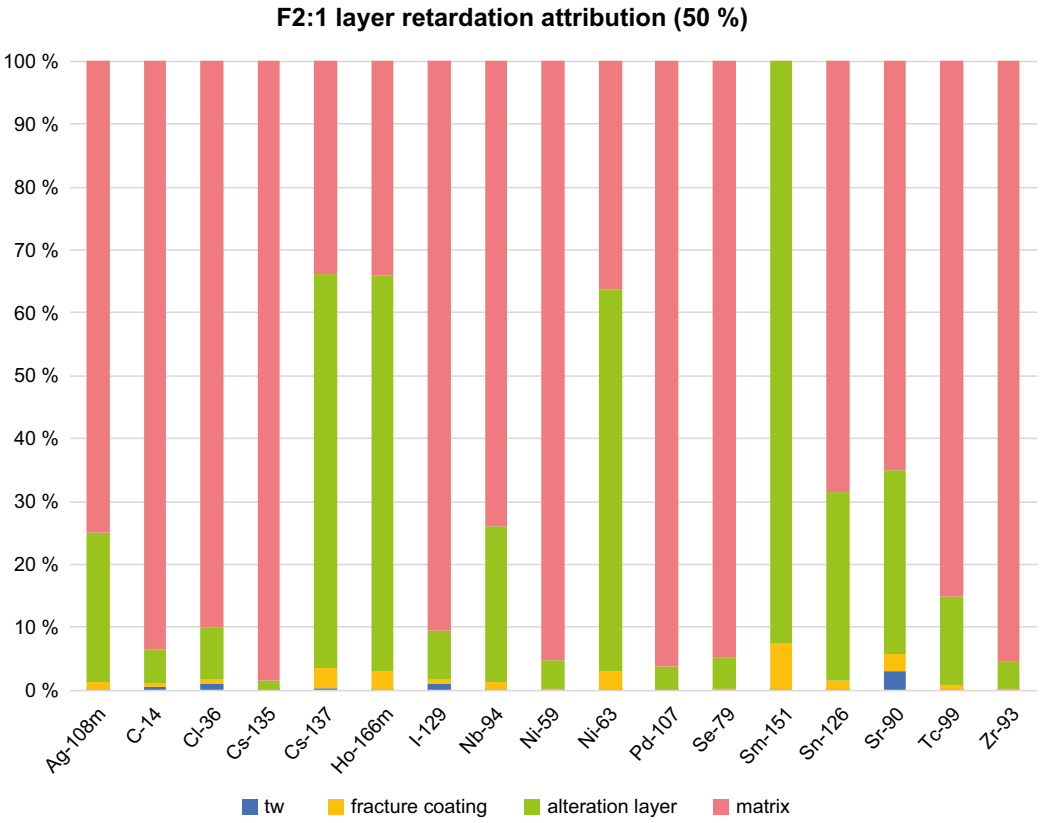

Figure 9-20. *Attribution of layer-specific retardation effects for first 50 % of recovered radionuclide (non-chain) for transport along a flowpath assuming fracture class F2:1 material properties. Model assumes same flowpath properties as SR-Site central corrosion case (no hydrodynamic dispersion). Blue markers indicate effective penetration depths calculated for radionuclides including decay; Green markers show corresponding results when decay is neglected.*

10 Conclusions

In this work, a more complex representation of rock matrix diffusive properties has been used than that previously adopted in SR-Site. Flowpaths in the rock matrix are assumed to encounter a number of different rock volumes with differing matrix retention properties conceptualised as a discretely layered rock matrix (here taken to include fracture coatings). By introducing layers featuring different material properties, a much larger range of matrix diffusion properties is accounted for than in SR-Site. Accordingly, we have increased the natural variability (which is sometimes discussed in terms of input data uncertainty) of the porosity and effective diffusivity as requested in SSM2011-2426-110.

Generally, the fracture surface is assumed to be bounded by fracture-adjacent layers of higher porosity and effective diffusivity than the undisturbed rock. This is expected to give a more pronounced transport retardation compared to the SR-Site case, where the flowpaths were assumed to be bounded by undisturbed rock. The modelling results support this notion, as the modelled peak equivalent dose rates are generally lower in the central calculation case study compared to the SR-Site corrosion case. In safety assessment, the peak release rate takes on special importance due to its relationship to regulatory compliance. The results show that by introducing the layered rock model with realistic parameter values, the peak release rate (radiotoxicity equivalent) is lowered by about 30 %, for the main flowpath considered. While this may be significant for the safety assessment, the reduction in dose is still minor and might be reasonably neglected by appealing to arguments of conservatism.

The consideration of a range of different F-factors, representative of fast migration paths associated with failed canisters in the central corrosion case of SR-Site, revealed that the F-factor impacts different radionuclides differently, with respect to retention by matrix diffusion. This has partly to do with sorption properties of the nuclides considered and partly to do with the shape of the near field release source term. A small deviation in F-factor, say differing by a factor of about five, would seemingly impact the far field release rate more than our changes of the matrix diffusion properties, going from the SR-Site case to the central calculation case study.

In the central calculation case presented in this work for a multilayer rock matrix, unknowns concerning the diffusive properties of calcite coatings required us to incorporate a calcite coating layer of lower porosity and effective diffusivity than the undisturbed rock, as fracture class F1:3. However, as calcite covers such a small part of the fracture surface (10 %), this had little impact on the results. Decreasing the effective diffusivity by three orders of magnitude for this single layer, although very thin, only had a very small impact the equivalent dose rates of the far field release.

As the central calculation case study with a multilayer rock matrix produces lower far-field release rates than the SR-Site central corrosion case, a small number of variant cases were modelled, with the aim of applying pessimistic assumptions compared to either the SR-Site central corrosion case or the central case study. Limiting the maximum accessible matrix depth to 10 cm was found to have little impact on the release rates, a result which can be explained by detailed retardation attribution and penetration depth calculations presented in Chapter 9. Reducing the effective diffusivity of the undisturbed rock by one order of magnitude in a sensitivity study of the SR-Site corrosion case resulted in an approximate doubling of the far field radiotoxicity release. The effective diffusivity used in SR-Site for the undisturbed rock in situ, however, is already conservatively low compared to what is used in other, equivalent, safety assessments (e.g. Posiva 2013, Section 7.8.2) so this scenario seems unlikely.

In summary, it is reasonable to say that the SR-Site approach of assuming flowpaths directly bounded by undisturbed rock is pessimistic relative to the adoption of a more realistic, layered rock matrix microstructure in radionuclide transport calculations. This conclusion regards retention by matrix diffusion only, and not necessarily the combined retention due to matrix diffusion and sorption. Generally, weathering and alteration effects are mostly expected to increase the sorptivity of the fracture adjacent alteration rim, so additional enhanced sorptivity in this zone might give even more pronounced results demonstrating the conservatism of the SR-Site modelling approach. This was tested in a limited way by uniformly increasing the K_d value in the fracture coatings and alteration rim by an order of magnitude resulting in a further 50 % reduction of far-field radiotoxicity fluxes for the F1:1 fracture class.

Importantly, even under these limitations, the modelling results in combination with the conceptual understanding of matrix diffusion strongly indicate that the benefit of using a layered rock retention model, compared to using the SR-Site approach, is small. This is not an unexpected conclusion and is in broad agreement with previous work (e.g. Cvetkovic 2010, Selroos and Painter 2012). Both approaches produce similar retention results, although the simplified SR-Site approach produces slightly higher doses. Consequently, in respect to radionuclide retention by matrix diffusion, the SR-Site approach is judged to be pessimistic and, hence, adequate.

References

SKB's (Svensk Kärnbränslehantering AB) publications can be found at www.skb.com/publications. SKBdoc documents will be submitted upon request to document@skb.se.

Advanpix, 2017. Multiprecision computing toolbox for MATLAB. Version 4.3.3.12185. Advanpix LLC, Yokohama, Japan.

Andersson P, Byegård J, Dershowitz B, Doe T, Hermanson J, Meier P, Tullborg E-L, Winberg A (ed), 2002. Final report of the TRUE Block Scale project. 1. Characterisation and model development. SKB TR-02-13, Svensk Kärnbränslehantering AB.

André M, Neretnieks I, Malmström M E, 2008. Measuring sorption coefficients and BET surface areas on intact drillcore and crushed granite samples. Radiochimica Acta 96, 673–677.

André M, Malmström M E, Neretnieks I, 2009. Determination of sorption properties of intact rock samples: New methods based on electromigration. Journal of Contaminant Hydrology 103, 71–81.

Archie G E, 1942. The electrical resistivity log as an aid in determining some reservoir characteristics. Petroleum Transactions of AIME 146, 54–62.

Avila R, Ekström P-A, Åstrand P-G, 2010. Landscape dose conversion factors used in the safety assessment SR-Site. SKB TR-10-06, Svensk Kärnbränslehantering AB.

Berglund S, Selroos J-O, 2004. Transport properties site descriptive model. Guidelines for evaluation and modelling. SKB R-03-09, Svensk Kärnbränslehantering AB.

Bienvenu P, Cassette P, Andreoletti G, Bé M-M, Comte J, Lépy M-C, 2007. A new determination of ^{79}Se half-life. Applied Radiation and isotopes 65, 355–364.

Birgersson L, Neretnieks I, 1990. Diffusion in the matrix of granitic rock: Field test in the Stripa mine. Water Resources Research 26, 2833–2842.

Byegård J, Selnert E, Tullborg E-L, 2008. Bedrock transport properties. Data evaluation and retardation model. Site descriptive modelling, SDM-Site Forsmark. SKB R-08-98, Svensk Kärnbränslehantering AB.

Catlow S, Troyer G, Hansen D, Jones R, 2005. Half-life measurement of ^{126}Sn isolated from Hanford nuclear defense waste. Journal of Radioanalytical and Nuclear Chemistry 263, 599–603.

Chu S Y F, Ekström L P, Firestone R B, 1999. WWW Table of Radioactive Isotopes, database version 1999-02-28. Available at: http://nucleardata.nuclear.lu.se/nucleardata/toi/

Claesson Liljedahl L, Munier R, Sandström B, Drake H, Tullborg E-L, 2011. Assessment of fractures classified as non-mineralised in the Sicada database. SKB R-11-02, Svensk Kärnbränslehantering AB.

Crank J, 1975. The mathematics of diffusion. 2nd ed. Oxford: Oxford University Press.

Crawford J, 2006. Modelling in support of bedrock transport property assessment. Preliminary site description. Laxemar subarea – version 1.2. SKB R-06-28, Svensk Kärnbränslehantering AB.

Crawford J, 2008. Bedrock transport properties Forsmark. Site descriptive modelling, SDM-Site Forsmark. SKB R-08-48, Svensk Kärnbränslehantering AB.

Crawford J, 2010. Bedrock K_d data and uncertainty assessment for application in SR-Site geosphere transport calculations. SKB R-10-48, Svensk Kärnbränslehantering AB.

Crawford J, 2013a. Memorandum: Retardation of radionuclide transport in cement affected groundwater – response to the request by SSM for supplementary information on retention of radionuclides (SSM2011-2426-110), item 1. SKBDoc 1421672 ver 1.0, Svensk Kärnbränslehantering AB.

Crawford J, 2013b. Quantification of rock matrix K_d data and uncertainties for SR-PSU. SKB R-13-38, Svensk Kärnbränslehantering AB.

Crawford, 2018. Screening of radionuclides for radionuclide and dose calculations. Report for the safety evaluation SE-SFL. SKB P-16-09, Svensk Kärnbränslehantering AB.

Crawford J, Sidborn M, 2009. Bedrock transport properties Laxemar. Site descriptive modelling SDM-Site Laxemar. SKB R-08-94, Svensk Kärnbränslehantering AB.

Cvetkovic V, 2010. Significance of fracture rim zone heterogeneity for tracer transport in crystalline rock. Water Resources Research 46, W03504. doi:10.1029/2009WR007755

de Hoog F R, Knight J H, Stokes A N, 1982. An improved method for numerical inversion of Laplace transforms. SIAM Journal on Scientific and Statistical Computing 3, 357–366.

Eklund S, Mattsson K-J, 2009. Forsmark site investigation. Quantitative mapping of fracture minerals in Forsmark. SKB P-08-47, Svensk Kärnbränslehantering AB.

Elert M, Gylling B, Lindgren M, 2004. Assessment model validity document FARF31. SKB R-04-51, Svensk Kärnbränslehantering AB.

Fenter P, Geissbühler P, DiMasi E, Srajer G, Sorensen L B, Sturchio N C, 2000. Surface speciation of calcite observed in situ by high-resolution X-ray reflectivity. Geochimica et Cosmochimica Acta 64, 1221–1228.

Gnirk P, 1993. Stripa Project Overview Report. Volume II: Natural barriers. OECD/NEA International Stripa Project 1980–1992. Svensk Kärnbränslehantering AB.

Haggerty R, 1999. Application of the multirate diffusion approach in tracer test studies at Äspö HRL. SKB R-99-62, Svensk Kärnbränslehantering AB.

Haggerty R, 2012. Review of matrix diffusion and related properties of intact rock in SKB's licence application for a spent nuclear fuel repository in Forsmark, Sweden. Technical Note 2012:44, Swedish Radiation Safety Authority.

Hollenbeck K, 1998. INVLAP.M: A Matlab function for numerical inversion of Laplace transforms by the de Hoog algorithm. Available at: https://www.mathworks.com/matlabcentral/answers/uploaded_files/1034/invlap.m

Ikonen J O, Sammaljärvi J K W, Siitari-Kauppi M K, Voutilainien M A, Lindberg A, Kuva J, Timonen J, 2015. Investigation of rock matrix retention properties supporting laboratory studies I: Mineralogy, porosity and pore structure. Posiva Working Report 2014-68, Posiva Oy, Finland.

Jacobsson L, 2007. Forsmark site investigation. Boreholes KFM01A and KFM02B. Micro crack volume measurements and triaxial compression tests on intact rock. SKB P-07-93, Svensk Kärnbränslehantering AB.

Jörg G, Bühnemann R, Hollas S, Kivel N, Kossert K, Van Winckel S, Gostomski C L, 2010. Preparation of radiochemically pure ^{79}Se and highly precise determination of its half-life. Applied Radiation and Isotopes 68, 2339–2351.

Kelokaski M, Oila E, Siitari-Kauppi M, 2001. Äspö Hard Rock Laboratory. TRUE Block Scale project. Investigation of porosity and microfracturing in granitic fracture wall rock and fault breccia specimens using the PMMA technique. SKB IPR-01-27, Svensk Kärnbränslehantering AB.

Kuva J (ed), Myllys M, Timonen J, Kelokaski M, Ikonen J, Siitari-Kauppi M, Lindberg A, Aaltonen I, 2012. Microstructure, porosity and mineralogy around fractures in Olkiluoto bedrock. Posiva 2012-02, Posiva Oy, Finland.

Lan B L, 2002. Enrico Fermi: a great teacher. European Journal of Physics 23, 29–31.

Lever D A, Bradbury M H, 1985. Rock-matrix diffusion and its implications for radionuclide migration. Mineralogical Magazine 49, 245–254.

Lindgren M, Gylling B, Elert M, 2002. FARF31 Version 1.2 – User's guide. SKB TS-02-03, Svensk Kärnbränslehantering AB.

Lindgren M, Lindström F, 1999. SR 97. Radionuclide transport calculations. SKB TR-99-23, Svensk Kärnbränslehantering AB.

Löfgren M, 2006. Forsmark site investigation. Formation factor logging in situ by electrical methods in KFM07A and KFM08A. SKB P-06-187, Svensk Kärnbränslehantering AB.

Löfgren M, 2007. Forsmark site investigation. Formation factor logging in situ by electrical methods in KFM01D and KFM08C. SKB P-07-138, Svensk Kärnbränslehantering AB.

Löfgren M, 2015. Artefacts associated with electrical measurements of the rock matrix formation factor. With comments on handling in, and potential consequences for, the safety assessment SR-Site. SKB R-14-20, Svensk Kärnbränslehantering AB.

Löfgren M, Crawford J, 2014. Modelling of radionuclide retention by matrix diffusion in a layered rock model. Response to the request by SSM for supplementary information on retention of radionuclides (SSM2011-2426-110), items 4 and 6. SKBDoc 1421960 ver 1.0, Svensk Kärnbränslehantering AB.

Löfgren M, Neretnieks I, 2005a. Forsmark site investigation. Formation factor logging in situ by electrical methods in KFM01A and KFM02A. Measurements and evaluation of methodology. SKB P-05-29, Svensk Kärnbränslehantering AB.

Löfgren M, Neretnieks I, 2005b. Forsmark site investigation. Formation factor logging in situ by electrical methods in KFM03A and KFM04A. SKB P-05-108, Svensk Kärnbränslehantering AB.

Löfgren M, Neretnieks I, 2006. Through-electromigration: a new method of investigating pore connectivity and obtaining formation factors. Journal of Contaminant Hydrology 87, 237–252.

Löfgren M, Sidborn M, 2010. Statistical analysis of results from the quantitative mapping of fracture minerals in Forsmark. Site descriptive modelling – complementary studies. SKB R-09-30, Svensk Kärnbränslehantering AB.

Löfgren M, Sidborn M, 2016. Quantitative mapping and statistical evaluation of fracture minerals in the granitic bedrock at Forsmark, Sweden. Mineralogy and Petrology 110, 663–680.

Löfgren M, Pettersson M, Widén H, Crawford J, 2006. Forsmark site investigation. Formation factor logging in situ by electrical methods in KFM05A and KFM06A. SKB P-06-91, Svensk Kärnbränslehantering AB.

Löfgren M, Crawford J, Elert M, 2007. Tracer tests – possibilities and limitations. Experience from SKB fieldwork: 1977–2007. SKB R-07-39, Svensk Kärnbränslehantering AB.

Mahmoudzadeh B, Liu L, Moreno L, Neretnieks I, 2014. Solute transport in a single fracture involving an arbitrary length decay chain with rock matrix comprising different geological layers. Journal of Contaminant Hydrology 164, 59–71.

Moral L, Pacheco A, 2003. Algebraic approach to the radioactive decay equations. American Journal of Physics 71, 684–686.

Moreno L, Crawford J, 2009. Can we use tracer tests to obtain data for performance assessment of repositories for nuclear waste? Hydrogeology Journal 17, 1067–1080.

Möri A, Mazurek M, Adler M, Schild M, Siegesmund S, Vollbrecht A, Ota K, Ando T, Alexander W R, Smith P A, Haag P, Bühler C, 2003. Grimsel Test Site. Investigation Phase IV (1994–1996). The Nagra-JNC in situ study of safety relevant radionuclide retardation in fractured crystalline rock. IV: The in situ study of matrix porosity in the vicinity of a water conducting fracture. Nagra Technical Report 00-08, Nagra, Switzerland.

Nagra, 1994. Kristallin-I. Safety assessment report. Nagra Technical Report NTB 93-22, Nagra, Switzerland.

Neretnieks I, 1980. Diffusion in the rock matrix: An important factor in radionuclide retardation? Journal of Geophysical Research 85, 4379–4397.

Neretnieks I, 1983. A note on fracture flow dispersion mechanisms in the ground. Water Resources Research 19, 364–370.

Neretnieks I, 2002. A stochastic multi-channel model for solute transport – analysis of tracer tests in fractured rock. Journal of Contaminant Hydrology 55, 175–211.

Neretnieks I, 2013. Some aspects of release and transport of gases in deep granitic rocks: possible implications for nuclear waste repositories. Hydrogeology Journal 21, 1701–1716.

Nilsson K, Byegård J, Selnert E, Widestrand H, Höglund S, Gustafsson E, 2010. Äspö Hard Rock Laboratory. Long Term Sorption Diffusion Experiment (LTDE-SD). Results from rock sample analyses and modelling. SKB R-10-68, Svensk Kärnbränslehantering AB.

Norman S, Kjellbert N, 1990. FARF31 – A far field radionuclide migration code for use with the PROPER package. SKB TR-90-01, Svensk Kärnbränslehantering AB.

Painter S, Mancillas J, 2009. MARFA version 3.2.2 user's manual: migration analysis of radionuclides in the far field. SKB R-09-56, Svensk Kärnbränslehantering AB.

Painter S, Mancillas J, 2013. MARFA user's manual: migration analysis of radionuclides in the far field. Posiva Working Report 2013-01, Posiva Oy, Finland.

Parkhomenko E I, 1967. Electrical properties of rocks. Moscow: Institute of Physics of the Earth, Academy of the Sciences of the USSR.

Penttinen L, Siitari-Kauppi M, Ikonen J, 2006a. Forsmark site investigation. Determination of porosity and micro fracturing using the ^{14}C-PMMA technique in samples taken from Forsmark area. SKB P-06-60, Svensk Kärnbränslehantering AB.

Penttinen L, Siitari-Kauppi M, Ikonen J, 2006b. Oskarshamn site investigation. Determination of porosity and micro fracturing using the ^{14}C-PMMA technique in samples taken from Oskarshamn area. SKB P-06-62, Svensk Kärnbränslehantering AB.

Petersson J, Wängnerud A, Ståhle A, 2003. Forsmark site investigation. Boremap mapping of telescopic drilled borehole KFM02A. SKB P-03-98, Svensk Kärnbränslehantering AB.

Posiva, 2012. Safety case for the disposal of spent nuclear fuel at Olkiluoto – Performance assessment 2012. Posiva 2012-04, Posiva Oy, Finland.

Posiva, 2013. Safety case for the disposal of spent nuclear fuel at Olkiluoto – Models and data for the repository system 2012. Posiva 2013-01, Posiva Oy, Finland.

RETROCK, 2005. Treatment of radionuclide transport in geosphere within safety assessments. Final report of the RETROCK Concerted Action. EUR 21230, European Commission.

Rouhiainen P, Pöllänen J, 2004. Forsmark site investigation. Difference flow logging in borehole KFM02A. SKB P-04-188, Svensk Kärnbränslehantering AB.

Sandström B, Tullborg E-L, 2009. Episodic fluid migration in the Fennoscandian Shield recorded by stable isotopes, rare earth elements and fluid inclusions in fracture minerals at Forsmark, Sweden. Chemical Geology 266, 126–142.

Schrader H, 2004. Half-life measurements with ionization chambers – A study of systematic effects and results. Applied Radiation and Isotopes 60, 317–323.

Selnert E, Byegård J, Widestrand H, 2008. Forsmark site investigation. Laboratory measurements within the site investigation programme for the transport properties of the rock. Final report. SKB P-07-139, Svensk Kärnbränslehantering AB.

Selnert E, Byegård J, Widestrand H, 2009a. Oskarshamn site investigation. Laboratory measurements within the site investigation programme for the transport properties of the rock. Final report. SKB P-07-179, Svensk Kärnbränslehantering AB.

Selnert E, Byegård J, Widestrand H, Carlsten S, Döse C, Tullborg E-L, 2009b. Bedrock transport properties. Data evaluation and retardation model. Site descriptive modelling. SDM-Site Laxemar. SKB R-08-100, Svensk Kärnbränslehantering AB.

Selroos J-O, Painter S, 2012. Effect of transport-pathway simplifications on projected releases of radionuclides from a nuclear waste repository (Sweden). Hydrogeology Journal 20, 1467–1481.

Siitari-Kauppi M, Lindberg A, Ikonen J, Kauppi L, 2010. Investigation of porosity and pore structure adjacent to fractures by PMMA method; samples taken from drill cores at Olkiluoto. Posiva Working Report 2010-66, Posiva Oy, Finland.

Silverman B W, 1986. Density estimation for statistics and data analysis. London: Chapman and Hall.

Skagius K, Neretnieks I, 1986. Diffusivity measurements and electrical resistivity measurements in rock samples under mechanical stress. Water Resources Research 22, 570–580.

SKB, 2004. RETROCK Project. Treatment of geosphere retention phenomena in safety assessments. Scientific basis of retention processes and their implementation in safety assessment models (WP2). Work package 2 report of the RETROCK concerted action. SKB R-04-48, Svensk Kärnbränslehantering AB.

SKB, 2006. Long-term safety for KBS-3 repositories at Forsmark and Laxemar – a first evaluation. Main report of the SR-Can project. SKB TR-06-09, Svensk Kärnbränslehantering AB.

SKB, 2010a. Radionuclide transport report for the safety assessment SR-Site. SKB TR-10-50, Svensk Kärnbränslehantering AB.

SKB, 2010b. Geosphere process report for the safety assessment SR-Site. SKB TR-10-48, Svensk Kärnbränslehantering AB.

SKB, 2010c. Data report for the safety assessment SR-Site. SKB TR-10-52, Svensk Kärnbränslehantering AB.

SKB, 2010d. Comparative analysis of safety related site characteristics. SKB TR-10-54, Svensk Kärnbränslehantering AB.

SKB, 2010e. Spent nuclear fuel for disposal in the KBS-3 repository. SKB TR-10-13, Svensk Kärnbränslehantering AB.

SKB, 2011. Long-term safety for the final repository for spent nuclear fuel at Forsmark. Main report of the SR-Site project. SKB TR-11-01, Svensk Kärnbränslehantering AB.

SKI, 1996. SITE-94. Deep repository performance assessment project. SKI Report 96:36, Statens kärnkraftinspektion (Swedish Nuclear Power Inspectorate).

Soler J M, Neretnieks I, Moreno L, Liu L, Meng S, Svensson U, Trinchero P, Iraola A, Ebrahimi H, Molinero J, Vidstrand P, Deissmann G, Říha J, Hokr M, Vetešník A, Vopálka D, Gvoždík L, Polák M, Trpkošová D, Havlová V, Park D-K, Ji S-H, Tachi Y, Ito T, 2019. Evaluation and modelling report of Task 9A based on comparisons and analyses of predictive modelling results for the REPRO WPDE experiments. Task 9 of SKB Task Force GWFTS – Increasing the realism in solute transport modelling based on the field experiments REPRO and LTDE-SD. SKB R-17-10, Svensk Kärnbränslehantering AB.

SSM, 2013a. Begäran om komplettering av ansökan om slutförvaring av använt kärnbränsle och kärnavfall – Retardation av radionuklider. SSM2011-2426-110, Swedish Radiation Safety Authority. (In Swedish.)

SSM, 2013b. Begäran om komplettering av ansökan om slutförvaring av använt kärnbränsle och kärnavfall – Radionuklidtransport och dosberäkningar. SSM2011-2426-103, Swedish Radiation Safety Authority. (In Swedish.)

Stephens M B, Fox A, La Pointe P R, Simeonov A, Isaksson H, Hermanson J, Öhman J, 2007. Geology Forsmark. Site descriptive modelling Forsmark stage 2.2. SKB R-07-45, Svensk Kärnbränslehantering AB.

Tang D, Frind E, Sudicky E, 1981. Contaminant transport in fractured porous media: Analytical solution for a single fracture. Water Resources Research 17, 555–564.

Thunehed H, 2017. Compilation of earth current measurements in the Forsmark area. SKB R-14-34, Svensk Kärnbränslehantering AB.

Trinchero P, Ebrahimi H, Colas E, Fernàndez-Garcia D, 2018. Assessing nickel and molybdenum transport in the bedrock at SFL using a dynamic K_d approach. Report for the safety evaluation SE-SFL. SKB R-17-03, Svensk Kärnbränslehantering AB.

Tullborg E-L, Drake H, Sandström B, 2008. Palaeohydrogeology: A methodology based on fracture mineral studies. Applied Geochemistry 23, 1881–1897.

Vahlund F, Hermansson H, 2006. Compulink. Implementing the COMP23 model in Simulink. SKB R-06-86, Svensk Kärnbränslehantering AB.

Vieno T, Nordman H, 1999. Safety assessment of spent fuel disposal in Hästholmen, Kivetty, Olkiluoto and Romuvaara − TILA-99. Posiva 99-07, Posiva Oy, Finland.

Vilks P, Cramer J J, Jensen M, Miller N H, Miller H G, Stanchell F W, 2003. In situ diffusion experiment in granite: Phase I. Journal of Contaminant Hydrology 61, 191–202.

Vilks P, Miller N H, Stanchell F W, 2005. Laboratory program supporting SKB's long term diffusion experiment. Report No: 06819-REP-01300-10111-R00, Ontario Power Generation, Nuclear Waste Management Division, Canada.

Widestrand H, Byegård J, Ohlsson Y, Tullborg E-L, 2003. Strategy for the use of laboratory methods in the site investigations programme for the transport properties of the rock. SKB R-03-20, Svensk Kärnbränslehantering AB.

Widestrand H, Byegård J, Cvetkovic V, Tullborg E-L, Winberg A, Andersson P, Siitari-Kauppi M, 2007. Sorbing tracer experiments in a crystalline rock fracture at Äspö (Sweden): 1. Experimental setup and microscale characterization of retention properties. Water Resources Research 43, W10413. doi: 10.1029/2006WR005278

Widestrand H, Byegård J, Selnert E, Skålberg M, Höglund S, Gustafsson E, 2010. Long term sorption diffusion experiment (LTDE-SD). Supporting laboratory program – Sorption diffusion experiments and rock material characterization. With supplement of adsorption studies on intact rock samples from the Forsmark and Laxemar site investigations. SKB R-10-66, Svensk Kärnbränslehantering AB.

Winberg A, Andersson P, Byegård J, Poteri A, Cvetkovic V, Dershowitz W, Doe T, Hermanson J, Gómez-Hernández J J, Hautojärvi A, Billaux D, Tullborg E-L, Holton D, Meier P, Medina A, 2003. Final report of the TRUE Block Scale project. 4. Synthesis of flow, transport and retention in the block scale. SKB TR-02-16, Svensk Kärnbränslehantering AB.

Winsauer W O, Shearin H M, Masson P H, Williams M, 1952. Resistivity of brine-saturated sands in relation to pore geometry. American Association of Petroleum Geologists (AAPG) Bulletin 36, 253–277.

Wood, 2018. ConnectFlow Technical Summary. Release 12.0. Wood PLC, Harwell Oxford, UK.

Zhou Q, Liu H-H, Molz F J, Zhang Y, Bodvarsson G S, 2007. Field-scale effective matrix diffusion coefficient for fractured rock: Results from literature survey. Journal of Contaminant Hydrology 93, 161–18.

Appendix A

The NuDec-Farf31 Matlab interface

Background

For a number of years, the code FARF31 (Norman and Kjellbert 1990) has been used for radionuclide transport calculations in Safety Assessment (SA). With the recent adoption of the more flexible, particle-based MARFA code (Painter and Mancillas 2013), FARF31 has become largely obsolete for this purpose. Although FARF31 cannot simulate as wide a range of physical scenarios as MARFA, it is still considered a competent code on account of its fast execution speed and general reliability for simple transport calculations involving decay chains and a single layer rock matrix of limited depth. For this reason, it was proposed that the code could continue to be used in a supporting role for making parameter sensitivity scoping calculations and for scenario screening. In order to render the code more flexible for such applications, a Matlab based interface (**NuDec-Farf31**) was created. This appendix details the main features of the interface program.

About the NuDec code family

The **NuDec** code family has been developed largely as an in-house project at Kemakta based upon an identified need to make scoping calculations in support of various analyses in SA. Such analyses in the past have included estimating temporal evolution of radionuclide inventories, testing sensitivity of far-field dose rates to migration parameter uncertainties, and testing migration properties related to different design alternatives for near-field containment structures.

Originally **NuDec** was intended as a simple Matlab based replacement for the MS Excel hosted Decay Macro program which was developed as an in-house proprietary code at Kemakta Konsult AB during the very early 1990's. Although this was a relatively sophisticated tool and was used successfully in a number of historical projects in an informal supporting role, the lack of formal documentation meant that it could not be properly cited and therefore not used in present day SKB projects. The initial motivation for replicating the functionality of the Decay code in Matlab was to be able to take advantage of the flexibility of the Matlab scripting environment for applications where making radionuclide inventory calculations using the MS Excel version is unnecessarily tedious. From a QA perspective, there are also clear advantages to using a procedural script-based code with clearly defined input and output files and transparent numerical procedures unlike the MS Excel version where these are at least partially hidden in Visual Basic scripts.

More recently, a need was identified for a suite of tools for making simplified and fast scoping calculations integrating the calculation of radionuclide inventories, near-field release (source term), and far-field migration simulations. To this end the **NuDec** code family has been developed. **NuDec** consists of three main core components. These are:

- NuDec-Inventory
- NuDec-Source
- NuDec-Farf31

The original Decay program was based on a full numerical solution of the decay chain ordinary differential equations using a stiff ODE solver. The **NuDec-Inventory** program, on the other hand, is based on a matrix algebraic solution described by Moral and Pacheco (2003) and calculates the temporal evolution of a radionuclide inventory. Being based on an Eigen vector approach it is subject to the same restriction as the Bateman equation method; namely that no two decay processes are permitted to have the same decay constant. This requirement, however, is generally fulfilled for all real-world decay processes of relevance in radioactive waste management. The Matlab based algorithm is fast, it permits additional pre- and post-processing operations to be performed and can easily accommodate converging and diverging chains.

The **NuDec-Source** program is, as the name suggests, a simplified near-field migration code that simulates release of radionuclides from repository containment structures. The **NuDec-Source** code is still in a very early stage of development and will be reported in a later project if deemed to be a

useful tool. The aim is to make a code which requires a minimum of input parameters to perform simplified scoping simulations that are more tedious to perform in more sophisticated codes such as COMP23 and similar.

The present description in this appendix, however, concerns the development of the **NuDec-Farf31** program which is essentially a driver script that calls the FARF31 code as an external program with automatic input and output management via shell commands in a scratch directory. The creation of a Matlab interface for FARF31 was driven in part by the need to make simplified far-field transport scoping calculations of radionuclide decay chains. Using the release version of the stand-alone FARF31 code to make numerical calculations was considered desirable from the point of view of the fast execution speed of the native program relative to what could be achieved using internally scripted Matlab functions and to avoid QA issues related to the creation of a purpose written code in Matlab for functionality that already pre-existed in the FARF31 program.

Description of NuDec-Farf31

Presently, **NuDec-Farf31** requires the user to supply a predefined source term. It is intended that in the future this functionality will be provided by integration with **NuDec-Source**. For the purposes of the present project, the source term was taken from the central corrosion case of the SR-Site safety assessment and used to replicate the far-field dose rate predictions detailed in SKB (2010a). The results of the replication study are documented in Chapter 3 of this report.

The current release version of the standalone FARF31 code is subject to a number of limitations. Chief among these is that simulations are limited to a maximum of 48 radionuclides consisting of no more than 32 distinct elements and no individual chain is permitted to have more than 8 members. Moreover, the code is not capable of simulating converging or diverging radionuclide chains. In most cases, diverging chains may be considered trivial since they typically involve very short-lived nuclides that can be assumed to be in approximate secular equilibrium in their respective decay chains. Converging chains cannot be neglected, however, since they can contribute in a non-negligible fashion to the ingrowth of daughter nuclides and therefore need to be properly accounted for. In previous safety assessments including SR-Site this problem was circumvented in an approximate fashion by directly adding the inventory of the (relatively fast decaying) parent nuclide to the inventory of the daughter to avoid the necessity to consider the converging chain explicitly.

Since very fast decaying radionuclides residing in decay chains can be considered to be in secular equilibrium with their parents, considerable simplifications are feasible for the relevant decay chains encountered in nuclear waste management. The main actinide decay chain simplifications for the thorium ($4n$), neptunium ($4n+1$), radium ($4n+2$), and actinium ($4n+3$) series were discussed previously in Chapter 3 (Figure 3-4 and Figure 3-5) in the context of the SR-Site replication case study. In the SR-Site replication case study there were 37 radionuclides consisting of 25 unique elements and no explicitly modelled converging chains. This set of nuclides comes in just under the technical limit of what is possible to simulate using Farf31. This is not surprising, however, since the list of prioritised radionuclides was already screened for the purpose of finding a minimum set of radionuclides that could be used to simulate far-field dose rates with the FARF31 code in SR-Site.

In the screening of radionuclides for the SFL preliminary safety assessment (Crawford 2018), on the other hand, a minimum set of 57 radionuclides representing 39 elements was required to account for the evolution of the waste inventory over time as well as 4 additional converging chains. Removing the trivially short-lived or very low inventory nuclides gave a total of 53 radionuclides which is certainly a greater number than FARF31 is capable of handling in a single simulation.

As noted in Section 2.1, many of the restrictions associated with the standalone FARF31 code can be circumvented by smart pre- and post-processing with the aid of the NuDec-Farf31 interface. This is achieved by splitting the problem up into a number of sub-problems and then recombining and summing the results in post-processing. In order to do this each of the non-chain, short chain, and actinide chain subsets are simulated separately as well as additional converging subsets where relevant. In the case of the SFL radionuclide inventory, this gives a total of 10 separate simulations necessary to account for the far-field transport using FARF31. For the converging chains where the same progeny appear in multiple simulations, care must be taken to ensure that the initial source term for the daughter nuclide is included only once (i.e. ingrowth is only considered for the subsequent converging chains).

Since the **NuDec-Farf31** code has evolved in parallel with the requirements of several concurrent projects, additional functionality has been added at different times according to the needs of the task at hand. For the present work, the possibility of explicitly incorporating the instant release fraction in the far-field migration simulations has been included. Such a calculation was not done in SR-Site (SKB 2010a) and the far-field dose arising from the instant release fraction from the central corrosion case was evaluated separately. In this code implementation, the instant release fraction (IRF) is defined separately from the corrosion and dissolution release (C/DRF) source term since there are different landscape dose factors associated with the different release modes. The FARF31 code is called once for the C/DRF source term and once for the IRF source term and the resulting far-field dose rates are added in a post-processing step. Although the full functionality was not used in the current work, it can be noted that the current version of **NuDec-Farf31** allows the user to simulate a greater number of nuclides and elements than the stand alone FARF31 is capable of and it also permits the simulation of converging chains.

Arkitektkopia AB, Bromma, 2020

SKB is responsible for managing spent nuclear fuel and radioactive waste produced by the Swedish nuclear power plants such that man and the environment are protected in the near and distant future.

skb.se